Towards Understanding Transitional Structures in Droplet-laden Pipe Flow

An Experimental Investigation

A Dissertation

SUBMITTED TO THE FACULTY OF THE

UNIVERSITY OF MINNESOTA

BY

Kyle J. Winters

IN PARTIAL FULFILLMENT OF THE REQUIREMENTS FOR THE DEGREE OF

DOCTOR OF PHILOSOPHY

Ellen K. Longmire, Advisor

October, 2019

Dedicated in honor of

Rachel K Franchi-Winters

For twenty years of friendship, love, and support

and

Dedicated in memory of

M. Verne Joy

Engineer, Tinkerer, Collector

A man who was never too busy to inspire his grandson

My most sincere gratitude to the late Dr. Gustavo Nunez and Nano Dispersion Technologies for the financial and intellectual support that sparked this investigation and to the National Science Foundation (CBET 1605719) for their generous support of the research contained in this dissertation.

I would like to acknowledge the inspiration, tutelage, and encouragement I have received from so many faculty, classmates, and family throughout my education, particularly those mentioned below.

I am extremely grateful to my advisor, Prof. Ellen Longmire, not only for sharing her expertise in experimental fluid mechanics to aid this research, but for her fantastic ability to ask the pivotal questions that helped me link together the physical insights compiled in this dissertation. Finally, for helping me develop as a presenter and writer.

I would also like to express my deepest thanks to the members of my committee, Prof. Filippo Coletti, Prof. Michele Guala, and Prof. Joe Nichols, for their service and their feedback.

Support from Mr. Dave Hultman was critical in the development of the initial iterations of the experimental facility that was built for this research. I am grateful for his help and the simple, effective, and budget friendly solutions that he suggested and ultimately fabricated.

Thanks to Mr. Kale Hedstrom for his help designing the fail safe mechanism for the experimental facility and his generosity in lending departmental equipment.

To the wonderfully supportive and inspiring fluid mechanicians I have had the pleasure of calling lab mates, I am forever grateful for the long hours I've shared with each of you; Dr. Yan Ming Tan, Mr. Dan Krizan, Mr. Alonso Alvarado, Dr. Deepak Adhikari, Dr. Ankur Bordoloi, Dr. Yi Hui Tee, Prof. Diogo Barros, Mr. Sagnik Paul, Mr. Jeshwanth Kundem, Dr. Zhengzhong Sun, Dr. Andras Nemes, Prof. Omid Amili, Mr. Tristan Van de Moortele, Dr. Sahar Jalal, Dr. Alec Petersen, Ms. Luci Baker, Dr. Kee Onn Fong.

For his help proofreading, my thanks to Dr. Kyle Viator.

Finally, this endeavor would have been entirely impossible without my family. To Rachel, Francis, Eamon, and Leonard, through all the missed meals, flights, late evenings, and delayed plans, your support was unwavering. To my parents, thank you for showing me what hard work looks like and for always being a phone call away.

Abstract

A facility was constructed to investigate the transition to turbulence in single-phase and droplet-laden pipe flow. A water-glycerin mixture in the facility was driven by a positive displacement pump, and custom flow conditioning components were developed to smooth the forcing from the pump. A disturbance ring was placed in the inlet of a 220D test section that was 44.8mm in diameter, D. The flow at the inlet and the frequency at which turbulent puffs occurred was characterized and compared to previous literature.

Puffs were sensed 170D downstream of the disturbance using a differential pressure transducer. The transducer signal was used to trigger downstream particle image velocimetry (PIV) at 180D. The transitional structures in the single-phase flow were investigated at Re = 2100 using planar-PIV (PPIV) in a streamwise-wall-normal plane and stereo-PIV (SPIV) in a circular cross-section. The structures in the droplet-laden flow, which consisted of 10 micron droplets of silicone oil at 3.8% volume fraction, were investigated using index-matched PPIV at Re = 2150 and Re = 2250. A registration method was developed to recognize strong ejections of fluid from the wall near a puff's trailing edge. These ejections and the accompanying decelerated flow were used to determine a puff's axial location and azimuthal orientation. The method was employed to determine ensemble averages of multiple puff occurrences. Both individual puff reconstructions and the ensemble average revealed that these ejections were accompanied consistently by a hairpin vortex that was, in turn, frequently part of a streamwise-aligned hairpin sequence. This sequence was associated with a region that started near the wall one diameter upstream of the puff's trailing edge and spread to the center of the pipe at the trailing edge before shrinking back towards the wall over the next three diameters downstream. PPIV results showed that the heads of hairpin vortices in the sequence propagated downstream faster than the puff. The vortices were

found to initiate, strengthen, spawn new hairpins, and reorient into more complex structures as they traveled a distance close to two diameters. Analysis of the kinetic energy found in the cross stream velocity components confirmed the presence of high-energy motions that were confined to extremely short segments of pipe. Further, examination revealed that individual hairpins could sometimes generate these strong localized motions, but a more general configuration for these motions was that they occurred in an axial location between two cross-stream-oriented swirling structures.

The puff data were also used to search for azimuthal modal patterns within streamwise velocity variations. These modal patterns were shown to be a robust feature of experimental puffs. Upstream patterns were typically disrupted by the trailing edge ejection and hairpin, resulting in downstream patterns of different mode and character. On average, modal patterns existed over longer distances than those identified previously in numerical simulations. PPIV in the droplet-laden flow revealed that structures qualitatively similar to puffs occur at the concentration and droplet size investigated. Detailed examination of the droplet-laden puffs showed the formation of hairpin vortex sequences that developed in a manner similar to those found in the single-phase flow. Analysis of axial velocity contours at various axial locations in the droplet-laden puffs revealed similar trends when compared to single-phase puffs.

Contents

List of Tables

List of Figures

Nomenclature

Superscripts, subscripts and operators

$\diamond^*$	nondimensional quantity
$\diamond^i$	local quantity at a single (x,y,z) or (r, ,z) location
$\tilde{\diamond}$	dimensional quantity having units
$\vec{\diamond}$	three dimensional vector quantity
$\hat{\diamond}$	unit vector
$\diamond'$	fluctuating quantity
$\overline{\diamond}$	time averaged quantity
$[\diamond]_g$	average of over the range of g
$\langle\diamond\rangle$	ensemble average quantity

Abbreviations

PIV	particle image velocimetry
SPIV	stereoscopic particle image velocimetry
PPIV	planar particle image velocimety
LOS	line of sight

FOV	field of view
BNC	Berkley Nucleonics Corporation

Greek symbols

α	angle between camera LOS and pipe axis
γ	distortion fit angle
δ_x	uncertainty estimate of a quantity, x
$u_{r,bias}$	uncertainty estimate of the distortion induced radial bias velocity
ϵ	perturbation energy norm
E	state space boundary between laminar and turbulent basins
$\frac{\epsilon}{D}$	relative pipe roughness
ρ	fluid density
μ	fluid viscosity
Π	constant axial pressure gradient
μ_e	modified viscosity
ϕ	particle volume fraction
ϕ_m	maximum close-packing volume fraction
∇	gradient operator
λ^*_{3D}	three dimensional swirling strength normalized using the bulk velocity
λ^*_{2D}	two dimensional swirling strength normalized using the bulk velocity
ω^*_z	z-component of normalized vorticity
Σ	surface boundary between laminar and turbulent solutions
σ_T	uncertainty in temperature from RTD

σ_w	axial rms velocity
θ_e	azimuthal angle of radial ejection at trailing edge
θ^*	registered azimuthal coordinate, $\theta - \theta_e$
τ	mean decay/split time constant

Roman symbols

$[U]$	velocity scale
$[L]$	length scale
$[T]$	time scale
$[M]$	mass scale
A_e	normalized ejection area
A_λ	percentage of vectors in a cross section with sufficient λ^*_{3D} normalized by the maximum percen
A	generic linear operator
C	normalized autocorrelation of axial fluctuations
C_m	projection of autocorrelation to sinusoidal mode , m
D	pipe diameter
dt	time between particle images
dT	time between vector fields
d_p	particle diameter
d_{piv}	PIV particle diameter
E	perturbation matrix
f	friction factor
f_R	rotational frequency of the pump rotor
g	acceleration due to gravity

h_f	dimensionless head loss due to friction
k^*_{ip}	local, normalized, in-plane kinetic energy at a single vector location
k_z	axial wave number
k_θ	azimuthal wave number
L_n	Eigenvector n
L_{tot}	Eigenvector sum
m	sinusoidal mode number
M	magnification factor
n	vector field index
N	number of image pairs in puff run
n_0	vector field containing trailing edge
N_{puff}	number of puff realizations
p	pressure
p_0	pressure field responsible for mean flow
q	in-plane kinetic energy, the cross-sectional average of $u^2 + v^2$
q^*	average in-plane kinetic energy normalized by the square of bulk fluid velocity
q^*_{max}	global maximum of q^* for a given record
Q	volumetric flow rate
Q_{peak}	PIV average peak ratio
r	radial cylindrical coordinate
R	pipe radius
r^*	normalized radial coordinate r/D
Re	Reynolds number based on bulk velocity and pipe diameter
R_n	rotational symmetry of order n

t	time
u	x-direction velocity component (laboratory frame)
$\vec{u}$	three-dimensional velocity vector
V	Voltage
u_θ	azimuthal velocity component
u_r	radial velocity component
$u_{r,bias}$	distortion induced radial bias velocity
v	y-direction velocity component (laboratory frame)
w	z-direction (axial) velocity component
w^*	w normalized by the bulk fluid velocity
w'	fluctuating z-component of velocity (laboratory frame)
w_b	bulk fluid velocity
w_{CL}	velocity at pipe centerline
w_{lam}	laminar velocity field
w^*_{rms}	axial root mean square velocity
w^*_{core}	axial propagation velocity of swirling core
$\overline{w}$	time averaged velocity field
x	Cartesian coordinate 1 (laboratory frame)
x^*	x normalized by the pipe diameter
y	Cartesian coordinate 2 (laboratory frame)
y^*	y normalized by the pipe diameter
z	pipe center line axis, Cartesian coordinate 3, axial cylindrical coordinate
z^*	z normalized by the pipe diameter
z^*_0	trailing edge location

Chapter 1

Introduction

1.1 Motivation

Newtonian fluid moving through a pipe at low flow rates will develop a parabolic velocity profile with the fluid moving only in the axial direction. At higher flow rates, the flow can deviate from the strictly axial flow observed in the laminar condition. These deviations can include fully turbulent flow and transitional structures that lie dynamically between turbulence and laminar flow. In either case, non-laminar flow contains significant fluid motion that is not in the axial direction. The swirling non-axial flow will result in strong velocity gradients which cause an increased proportion of the kinetic energy in the flow to be dissipated as heat. As flow rate increases, beyond the laminar condition, the very first transitional structures encountered are called puffs. The presence of puffs can cause the average pressure drop in a section of pipe to increase by 60% or more (Samanta et al., 2011). In industrial applications, where this pressure drop must be overcome by a pump, preserving the laminar character of the flow, can result in sizable energy savings. Conversely, in applications where maintaining the suspension of solids or the dispersed nature of immiscible

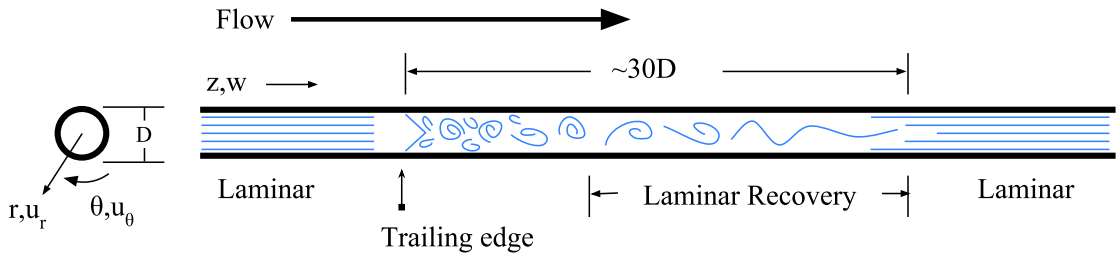

Figure 1.1: Schematic of transitional pipe flow with coordinate system and a puff labeled with its critical features.

fluids is important, the initiation of puffs or fully turbulent flow may be desirable. In this case, promoting turbulence and its increased energy cost could be ultimately beneficial. The addition of small spheres, either solid particles or liquid droplets, to pipe flow has been observed to have profound effects on the flow rate at which a given flow will start to exhibit transitional behavior (Matas et al., 2003a,b; Pouplin et al., 2011).

Figure 1.1 shows a schematic view of a transitional pipe flow where a pipe with diameter, D, having a cylindrical coordinate system contains flow with bulk velocity, w_b, and flows from left to right. The radial, azimuthal, and axial coordinates are shown as r, θ, and z, respectively. The respective velocity components are similarly shown as u_r, u_θ, and w. Puffs (shown in Figure 1.1) consist of swirling fluid confined to a section of pipe about $30D$ in axial length that propagate downstream close to the bulk fluid velocity. They are characterized by a sharp laminar-to-turbulent-like transition at their trailing edge, and a gradually decaying turbulent-to-laminar transition at the leading edge. (Wygnanski and Champagne, 1973) Only recently, through modern numerical and experimental techniques, have details emerged about the internal structure of puffs, advancing the discussions regarding the dynamical processes by which they initiate and sustain themselves. Advancing this discussion still further could create a sufficient knowledge base that allows for evaluating and optimiz-

ing methods employed to strategically modify a system's natural transition behavior.

Over 70 years ago, dilute polymer additives were discovered to interfere with head loss in turbulent pipe flows (Toms, 1948). Investigations into modifying the turbulent transition of flows using a dispersed second phase of either solid particles (Matas et al., 2003a,b) or fluid droplets have been more recent (Pal, 1993; Pouplin et al., 2011). Results have shown that it is possible, based on a number of factors, for the dispersed phase to promote or inhibit transition from the flow rate at which it would otherwise occur in a single-phase flow. While these studies investigated transition and pressure drop as time-averaged quantities, no investigation of individual transitional structures was presented. It is unknown how these structures are altered or suppressed in these types of flows. The purpose of this work is to further the understanding of the flow structure inside single-phase puffs by examining and analyzing high resolution velocity measurements inside many puffs. Furthermore, this work explores preliminary attempts to generate and measure a transitional pipe flow using an oil-in-water dispersion.

1.2 Previous work on single-phase pipe flows

Osborne Reynolds collected his observations from an experiment in which a siphon was used to drive flow through a section of pipe with a trumpet shaped inlet, and published them with his analysis. (Reynolds, 1883). He did this for various velocities, pipe diameters, and water temperatures. Reynolds first observed streaks of color added to the centerline of an unperturbed flow. As the velocity of the pipe increased above some critical value, the streak of color went from moving in a "beautiful straight line" down the pipe to abruptly "all at once mix[ing] up" at some distance downstream of the inlet.

Furthermore, the distance from the inlet at which the color began mixing decreased as

the flow rate increased. Lastly, he observed that, when briefly illuminated, the colored water could be seen to move as a mass of "distinct curls," which he identified as eddies.

When a coil of wire was added to the entrance of the pipe, Reynolds found that, for low velocities, the initial disturbance created by the coil would die out. Again he increased the velocity and found that the critical velocity decreased when compared to the unperturbed flow. This led to the conclusion that the critical velocity was sensitive to changes in the initial conditions of the flow.

In both the perturbed and unperturbed case, Reynolds observed that for the smaller diameter pipes, the swirling disturbances would appear not only suddenly, but intermittently over a limited section of pipe, as they passed downstream. As the velocity increased, the time between these "flashing" structures decreased until finally the "disturbance became general" (Reynolds, 1883).

In addition to his observations, Reynolds suspected that the birth of eddies would depend on some "definite value" of the ratio,

$$\frac{R\rho[U]}{\mu}$$

where R is the pipe radius, [U] is some characteristic velocity parameter, ρ and μ are the density and viscosity of the fluid respectively. Today, terms collected in this manner are referred to as a Reynolds number and for pipes, commonly expressed as,

$$Re = \frac{\rho w_b D}{\mu} \tag{1.1}$$

where D, is the pipe diameter, and w_b is the bulk velocity calculated as the volumetric flow rate divided by the pipe cross-sectional area. It should be noted that any combination of

velocity, length, density and viscosity can be referred to as a Reynolds number, and is used in many fluid applications other than pipes. However, in this work Reynolds number will always refer to the ratio containing w_b and D.

Familiar for many, Eqn. 1.2 describes the dimensional momentum equation for an incompressible Newtonian fluid element without a body force.

$$\rho\left(\frac{\partial\tilde{\vec{u}}}{\partial\tilde{t}}+\tilde{\vec{u}}\cdot\tilde{\nabla}\tilde{\vec{u}}\right)=\tilde{\nabla}\left(\tilde{p_0}-\tilde{p}\right)+\mu\tilde{\nabla}^2\tilde{\vec{u}} \tag{1.2}$$

where spatial and temporal derivatives of the pressure, $\tilde{p_0}-\tilde{p}$, and the velocity, $\tilde{\vec{u}}$, are used in conjunction with intrinsic fluid properties; the density, ρ, and the kinematic viscosity, μ, to describe the fluid motion. Note in this representation, the pressure is split into $\tilde{p_0}$ and $\tilde{p}$, where $\tilde{p_0}$ represents the pressure field responsible for the bulk fluid flow through the pipe. Distributing the gradient into the pressure terms and requiring that the only non-zero component of $\tilde{\nabla}\tilde{p_0}$ be $\partial\tilde{p_0}/\partial\tilde{z}=\Pi$ we arrive at:

$$\rho\left(\frac{\partial\tilde{\vec{u}}}{\partial\tilde{t}}+\tilde{\vec{u}}\cdot\tilde{\nabla}\tilde{\vec{u}}\right)=\Pi\hat{e_z}-\tilde{\nabla}\tilde{p}+\mu\tilde{\nabla}^2\tilde{\vec{u}} \tag{1.3}$$

where $\hat{e_z}$ represents the unit vector in the axial direction.

In order to generalize fluid motion across different scenarios, techniques to non-dimensionalize the equation are employed where the dimensional dependent variables, $\tilde{\vec{u}}$ and $\tilde{p}$, in Eqn. 1.3 are expressed as some non-dimensional fraction of a characteristic quantity, and the dimensional parameters pertinent to a given scenario are lumped together in a single dimensionless formation. To arrive at the non-dimensional form of Eqn. 1.3, we first define scales of mass, time, and length to normalize the dependent variables. The most natural starting place is to normalize length using the diameter of the pipe, D. Next, we can use ρD^3 as a mass scale.

Less obviously, but for reasons that will readily become apparent, we normalize time using $\frac{4\mu}{\Pi D}$. In other words,

$$[L] \equiv D, \quad [M] \equiv \rho D^3, \quad [T] \equiv \frac{4\mu}{\Pi D}$$

Next, we replace the dimensional independent and dependent variables in Eqn. 1.3 with nondimensional ones multiplied by the appropriate scaling factors, namely,

$$\tilde{t} \equiv t\,[T], \quad \tilde{\nabla} \equiv \nabla\,[L]^{-1}, \quad \tilde{\vec{u}} \equiv \vec{u}\frac{[L]}{[T]}, \quad \tilde{p} \equiv p\frac{[M]}{[L][T]^2}$$

arriving at,

$$\rho\left(\frac{[L]}{[T]^2}\frac{\partial \vec{u}}{\partial t} + \frac{[L]}{[T]^2}\vec{u}\cdot\nabla\vec{u} = \right) = \Pi\hat{e_z} - \frac{[M]}{[L]^2[T]^2}\nabla p + \frac{1}{[L][T]}\mu\nabla^2\vec{u}$$

Collecting the scaling terms and simplifying,

$$\frac{\partial \vec{u}}{\partial t} + \vec{u}\cdot\nabla\vec{u} = \frac{[T]^2}{[L]}\frac{\Pi}{\rho}\hat{e_z} - \frac{[M]}{[L]^3}\frac{1}{\rho}\nabla p + \frac{[T]}{[L]^2}\frac{\mu}{\rho}\nabla^2\vec{u}$$

Replacing the scaling terms with the dimensional parameters,

$$\frac{\partial \vec{u}}{\partial t} + \vec{u}\cdot\nabla\vec{u} = \frac{16\mu^2}{\Pi D^3\rho}\hat{e_z} - \nabla p + \frac{4\mu^2}{\Pi D^3\rho}\nabla^2\vec{u} \tag{1.4}$$

By solving the Hagen-Poiseuille equation for w_b we can express Reynolds number in the following way,

$$Re = w_b\frac{\rho D}{\mu} = \left(\frac{\Pi D^2}{32\mu}\right)\frac{\rho D}{\mu} = \frac{\rho\Pi D^3}{32\mu^2}$$

Thus, Eqn 1.4 becomes,

$$\frac{\partial \vec{u}}{\partial t} + \vec{u} \cdot \nabla \vec{u} = \frac{1}{2Re} \hat{e_z} - \nabla p + \frac{1}{8Re} \nabla^2 \vec{u} \tag{1.5}$$

In this way, flow in a circular pipe of an incompressible Newtonian fluid is completely generalized across pipes of different size, and fluids of different viscosity and density.

Prior to Reynolds' work, the ratio of parameters that constitute the Reynolds number, Re, had been shown to appear in the non-dimensional equations, but Reynolds' contribution was to show that the value of this ratio could suggest attributes of the flow's character. Reynolds found that the lowest value at which he could find evidence of instability was Re = 2,000. Furthermore, by reducing initial disturbances, he could keep the flow laminar up to Re = 12,000. The values of Reynolds number associated with different aspects of the flow behavior continue to be of interest today.

The work by Reynolds established a platform for further study. He established the abrupt nature of the transition away from laminar flow. He discovered the temporal intermittency and spatial boundaries associated with the transitional regime structures. Finally, he not only connected the dimensionless parameter now known as Reynolds number to the behavior of the flow, but showed how its critical values depend on the initial state of the pipe entry.

From the eighteenth into the mid-nineteenth century the Darcy-Weisbach equation, shown as Eqn 1.6, was developed to predict head-loss due to friction in a pipe (Weisbach, 1845; Darcy, 1857; Brown, 2002)

$$h_f = f \frac{L}{D} \frac{w_b^2}{2g}. \tag{1.6}$$

The head-loss due to friction, h_f, is expressed as a function of a friction factor, f, the length-to-diameter ratio of the pipe, L/D, the bulk velocity, w_b, and gravity, g. At the

time it was developed, the nature of the friction factor was unknown, and thus little use was made of the Darcy-Weisbach equation. It was not until 1944, that Moody helped this equation become a useful tool for engineers working with pipes. Moody published a chart that allowed for straightforward prediction of head-loss due to friction along a length of pipe. His chart is shown in Fig 1.2. The horizontal axis represents the Reynolds number of the pipe flow. The vertical axis represents the friction factor. Iso-curves for various values of relative roughness are plotted. Flow regimes are divided by dotted lines and are shown as Laminar, Critical, Transition, and Complete Turbulence.

Assuming fully developed, steady flow in a long pipe, Moody's chart allows an engineer to predict the friction factor based on the Reynolds number of the pipe flow, and the relative roughness, e/D of the pipe. The head-loss for flows in the laminar regime, regardless of roughness can be predicted by using $64/Re$ for the friction factor. This is a result of the so-called Hagen-Poiseuille flow solution to the momentum equation for pressure gradient along a cylindrical pipe. Irrespective of relative roughness, the friction factor and thus head-loss is increased when a fluid transitions from the universal laminar curve to the curve defined for its specific relative roughness value.

One noticeable feature is the hashed region in the so-called critical zone from Re = 2000 to Re = 3000 or 4000. Moody uses this to convey that no reliable friction factor can be acquired in this region due to possible variations in the upstream conditions of the pipe section being considered. In addition to being a useful engineering tool, the Moody chart represents well the Reynolds number range over which transition can happen, and the ambiguity of flows in the so-called critical zone.

The pipe flows in Moody's so-called critical and transition regions have been investigated continuously since his chart was published. Particular attention has been paid to much of what Reynolds originally observed, namely, the stability/sensitivity of these flows

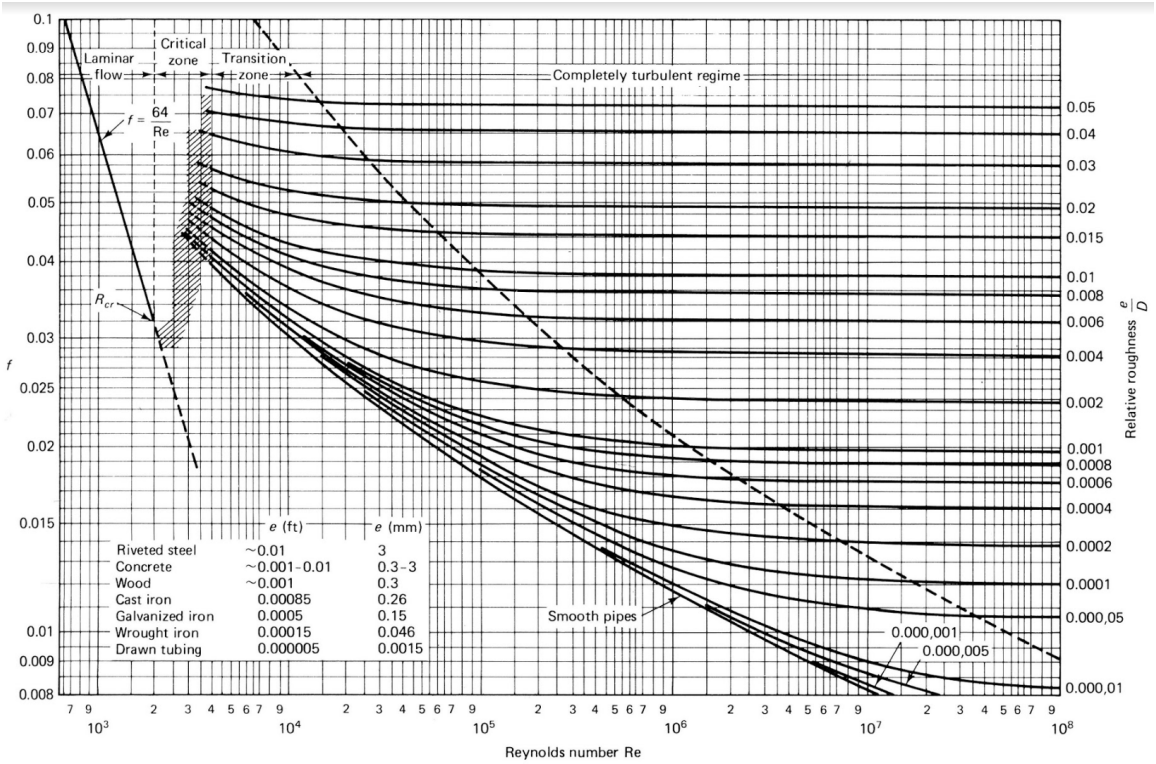

Figure 1.2: Moody chart displaying friction factor as a function of Reynolds number for varying roughness values. Moody (1944)

to perturbation, the intermittency of transition flows, and the structure and behavior of these intermittent regions.

1.2.1 Stability dynamics

Prior to, concurrent with, and after the development of Moody's chart, other researchers were conducting increasingly complex theoretical and numerical investigations centered on determining the stability of an axisymmetric velocity profile for incompressible viscous fluids.

Initially, the approach to investigating stability involved infinitesimally perturbing the dimensionless Navier-Stokes and continuity equations about the steady Hagen-Poiseuille

solution, then linearizing the equations with respect to the perturbation (Lessen et al. 1964). Assuming various exponential dependence on z, r, θ, and t results in an eigenvalue problem in which the so-called Orr-Somerfeld operator linearly maps the perturbations to their growth rates. The growth rates can then be examined with the idea being that positive real parts of the resulting eigenvalues correspond to perturbation forms that grow and are unstable.

To start, global axisymmetric disturbances to the base flow were examined. From Sexl (1927) to Pekeris (1948) to Corcos and Sellars (1958) to Schensted (1960) refinements to this method were made, resulting in the conclusion that an infinite and complete set of eigenfunctions exists that describe axisymmetric disturbances to the base flow. Davey and Drazin (1969) verified the stability of the first 27 eigenvalues for the least stable global axial mode at Reynolds number up to $1.5x10^4$. Gill (1965) examined the stability of the Poiseuille solution to axisymetric perturbations using a different approach, one where the perturbation is localized in the axial direction, and its amplitude is examined with distance along the pipe's axis. He found that while these perturbations were linearly stable, they could take long distances to decay to half their original amplitude, namely distances of the order $Re/100$. Lessen (1968) extended the study of global perturbation to azimuthally periodic disturbances and found no evidence of instability in the first azimuthal mode (assumed by the authors to be the least stable) for Reynolds number up to $3x10^4$. Garg and Rouleau (1972) extended the work on localized perturbation to non-axisymmetric perturbations and found only stable eigenvalues.

As computing techniques have advanced, larger sets of eigenvalues have been found and shown to be stable. Meseguer and Trefethen (2003) considered combinations of azimuthal wave number 1 with axial wave numbers 0 and 1 and found the flow to be stable up to Reynolds number 10^7.

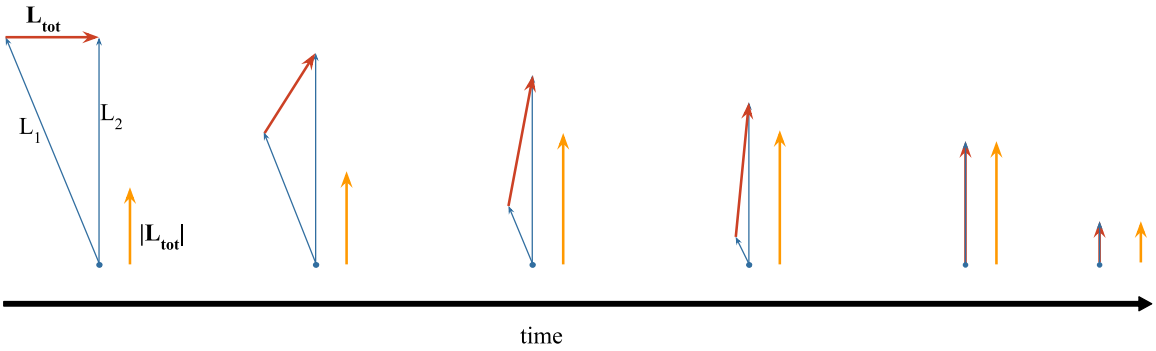

Figure 1.3: Schematic representation of monotonically decaying, non-normal vectors generating a resultant which experiences transient growth.

Despite formal proof in the case of a three dimensional disturbance, the general consensus among researchers is that the Hagen-Poiseuille flow profile is linearly stable to all infinitesimal disturbances. This previous work suggests that transition in pipe flows does not grow out of infinitesimal disturbances of the assumed form as time goes to infinity.

While the eigenvalues of the linearized perturbation problem have all been shown to decay towards the base solution at long times, it was discovered that the eigenfunctions of the linearized NS operator are not mutually orthogonal and as a result can create large transient growth factors prior to the long time decay.

The problem with the typical method for evaluating eigenvalues as stability criteria for a nonnormal operator is that, in the superposition of eigenmodes, multiple vectors can contribute to each directional component of the superposed solution. Fig 1.3 shows this concept for a reduced model with two eigenvectors, L_1 and L_2. The solution, L_{tot}, is represented by the vector subtraction of L_1 from L_2, in other words, $L_{tot} = L_2 - L_1$. As L_1 and L_2 decay, $|L_{tot}|$ can increase before finally decaying along with the mode that has the longest characteristic time. The point of showing that these large transient growth factors can be observed is to demonstrate a plausible scenario where an infinitesimal perturbation, through

completely linear growth, becomes large enough that nonlinear effects become important and the eventual decay of the linear modes is no longer applicable to the physical situation.

In addition to their eigenvalue calculations of the linearized pertubation equations, Meseguer and Trefethen (2003) also examined in detail the ϵ-pseudospectra (Reddy and Trefethen, 1990; Reddy et al., 1993; Trefethen et al., 1993) of the linearized NS operator in order to uncover transient growth factors that arise due to the non-orthogonal nature of the eigenfunctions that solve the linearized problem. The ϵ-pseudospectra is the collection of eigenvalues of a matrix that is slightly perturbed from the linearized NS operator. More formally, a value, k_ϵ is a pseudoeigenvalue of a matrix A if it is an eigenvalue of the matrix $A + E$, where E is a perturbation whose energy norm is less than the value, ϵ. When plotted in the complex plane, the pseudospectrum manifests as a domain that expands from each eigenvalue of A that can, depending upon the value of ϵ, extend into the real-positive half of the complex plane, indicating positive transient growth. Using the pseudospectum, a maximum amplification factor can also be calculated for each mode. The optimal perturbation, shown schematically in Figure 1.4 that arises from the linear nonmodal analysis is a pair of counter rotating vortices that generate a region of high momentum fluid and a region of low momentum fluid as they pull slow fluid away from the wall towards the center and fast fluid from the center towards the wall. (Pringle and Kerswell, 2010; Trefethen et al., 1993; Schmid and Henningson, 1994) The evolving nature of the initial disturbance into its final shape is a key difference between nonmodal stability and linear modal stability analysis where the initial perturbation maintains its shape as it grows or decays. Meseguer and Trefethen (2003) show that the growth factors associated with the optimal perturbation can be calculated as $Re/117.7$, and the norm of the initial perturbation required to make the $A + E$ operator unstable shrinks as Re^{-2}.

As theoretical and computational efforts in stability progressed, so too did experimental

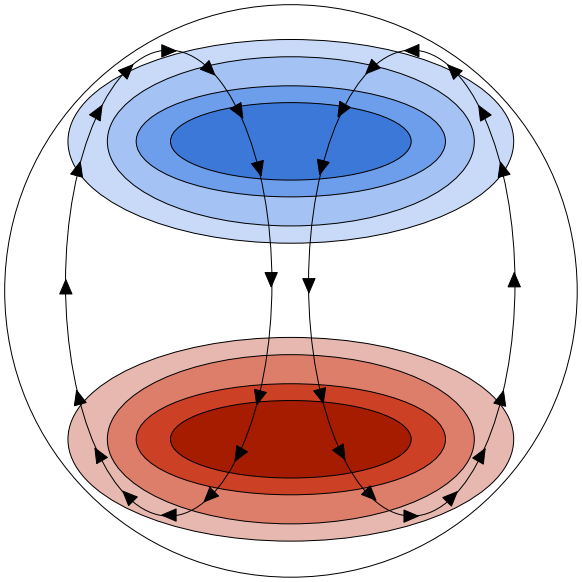

Figure 1.4: Schematic of the developed linear nonmodal optimal showing a large vortex pair indicated by the black arrowed lines and increasingly high (red) and decreasingly low (blue) momentum regions

investigations of stability. Researchers have explored in detail, the nature of the finite perturbations required to destabilize pipe flows in laboratories. Darbyshire and Mullin (1995) investigated perturbation form and amplitude by using a piston apparatus to drive flow through a pipe at constant flow rate to study four types of disturbance,

1. a single jet oriented perpendicular to the pipe axis pushing fluid into the pipe
2. a single jet oriented perpendicular to the pipe axis pulling fluid out of the pipe
3. an array of 6 evenly spaced jets oriented tangentially to the pipe wall pushing fluid
4. same as 3 but with alternating jets pushing and pulling fluid

Each type of disturbance was used to perturb a well-developed pipe flow and examined the resulting character of the flow downstream. Each disturbance type except 2 was exam-

ined for a Reynolds number range from 1800-2600. Their experiment allowed for control of the amplitude (total volume) and rate of the injection. Their criteria for decay or transition was based on hot wire measurements of the flow 70D downstream. Their findings support the existence of a critical amplitude threshold that must be exceeded for transition to occur for Reynolds numbers between 1800 and 2600. Disturbances below this threshold would decay. This critical amplitude is generally found to be a decreasing function of Reynolds number. For example, for the single jet pushing fluid into the pipe, the volume of fluid required to induce puffs decreased from 0.4% of the mean flow rate to about 0.25% over the Reynolds number range where puffs were seen to occur (1800-2700). While the general behavior with Reynolds number was similar, and absolute value of the critical amplitude was found to be of similar order, the azimuthal push and push/pull cases required successively less amplitude to trigger transition across the range of Reynolds number investigated. Further, their results also suggested that for a given value of Reynolds number, increasingly strong disturbances have an increasing probability of producing turbulent motion. At the determined critical Reynolds number value, the flow had a 50% probability of transition.

The work of Darbyshire and Mullin (1995) highlights the difficulty associated with characterizing and analyzing aspects of the disturbance that are most important to the stability. In their disturbance generating mechanism, a circular wheel drove a piston which forced fluid into the pipe. This created a situation such that, for a given injection volume, the speed of the disturbance jet, and the duration of the injection were coupled and inversely related i.e. in order to get a faster disturbance jet velocity, the wheel must spin faster and the duration of the injection must decrease. As the finite amplitude stability of pipe flows was investigated further, it became typical to describe the disturbance using one of two methods; 1) the ratio of disturbance jet flux to the flux of the mean flow, or 2) the ratio of the mean disturbance jet velocity to the mean pipe flow velocity.

Hof et al. (2003) endeavored to improve on the methods of Darbyshire and Mullin (1995) (DM95) by introducing a new shape to the velocity profile of the disturbance. They were able to generate a so-called boxcar profile, a rectangular pulse, which allowed them to prescribe a disturbance velocity (jet exit pressure) and duration independently. They confirmed and expanded upon the results of DM95. First, they showed that using the flux amplitude ratio, a Re^{-1} relationship with Reynolds number could be extracted to describe the critical disturbance amplitude for the Reynolds number range of 2,000 to 20,000, at even longer observation lengths than DM95. They showed that this Re^{-1} behavior applies to both the single cross flow, and azimuthal array push disturbance types used by DM95, listed above as cases 1 and 3. The ability to generate a constant amplitude disturbance lasting a prescribed time also allowed Hof et al. (2003) to develop a length scale over which the disturbance affects the mean pipe flow. This length scale was found to be important. Hof et al. (2003) showed that at both Re = 2170 and Re = 4000, the volume flux required to trigger transition decreased rapidly with increasing injection length scales up to length scales greater than 6D, which required a constant flux with increasing length scale. This is evidence, Hof et al. (2003) claimed, that the scaling of the critical disturbance by mean flow parameters is correct.

While Hof et al. (2003) looked only at push type disturbances, Peixinho and Mullin (2007) examined in detail the push-pull type disturbances first suggested by DM95. Borrowing from boundary layer research, they examined perturbations where the line connecting the push and pull orifices was oriented spanwise, streamwise, and 45-degrees oblique to the flow. One objective was to use the smallest possible localized push/pull disturbance coupled with an optimized jet angle to try and identify flow states where there was not a catastrophic transition into a puff. Their work resulted in a few conclusions. First, while the Re^{-1} scaling was confirmed for push type disturbances, a $Re^{-1.3}$ scaling was found for

streamwise, and spanwise push-pull disturbances, and a $Re^{-1.5}$ scaling for oblique and anti-oblique push-pull disturbances. Finally, the authors showed flow visualization results from injecting oblique, push-pull disturbances in the range of the critical amplitude. The result was a packet of horseshoe shaped vortices that appeared at an approximate 0.5D spacing that would either decay as they were swept downstream, or develop a secondary structure and rapidly create a puff.

Up to here, the methods discussed in this dissertation, both theoretical and experimental, have centered around perturbing a fully developed laminar flow. However, around the turn of the millennium, researchers began attempting to approach the stability of pipe flow from a dynamical systems perspective. This centered on the idea that the pipe flow exists in some state space with all possible values of velocity and pressure. In that state space, the laminar solution is an attractor. That is, it has some space over which it pulls a perturbed solution towards itself. As long as the solution remains in what is called the basin of attraction, the disturbance will decay to nothing as the system approaches the laminar solution, even if it experiences transient amplification as described above. Researchers were looking for a way to systematically explore the state space that lies away from the laminar basin, specifically, the region where the system is on the verge of tipping towards a turbulent solution. In order to search for these locations, or edge states, researchers developed a method by which they start at a certain stable solution that is not Hagen-Poiseuille pipe flow. It could be a problem in which the geometry is rotating, or the pipe has a different shape (e.g. an elliptical cross section), or there is some other forcing to the problem. Then in a controlled way, the problem is morphed back towards pressure driven flow in a circular pipe. The most common method involved using a careful choice of body force that was informed by research into the mechanisms that sustain turbulent motions in fluid flows.

In a series of papers, Waleffe with others, developed a framework for a general self-

sustaining mechanism to drive turbulence in wall bounded flows (Hamilton et al., 1995; Waleffe, 1997, 1998, 2001, 2003). This self-sustaining process (SSP) consists of three elements, each of which feeds another. The three elements are streamwise rolls, low momentum streaks, and spanwise (or azimuthal) wavy streak modulations. The idea is that the streamwise rolls "redistribute the mean shear" in the laminar flow, moving low momentum fluid away from walls and conversely moving high momentum fluid down towards the walls. This process creates streaky regions of fluid, at a given wall-normal distance, which have a different streamwise velocity than the surrounding flow. These streaks, Waleffe argued, will have "strong spanwise inflections," from which two types of instabilities can be expected to occur, a "fundamental sinusoidal mode," and a "subharmonic 'sinucose' mode". These modes are responsible for so-called staggered row vortices, and hairpin structures respectively. These instabilities were said to feed energy back into the streamwise rolls and thus sustain them against viscous decay.

Faisst and Eckhardt (2003) and Wedin (2004) used these insights into the general mechanisms that sustain turbulence to set up a condition where streamwise vortices were maintained via a body force provided to the initial flow.

Eventually, as the body force was removed and *Re* increased, a series of flows was found each containing three key components, streamwise rolls, streaks of high and low momentum fluid, and streamwise dependent waves as outlined by Waleffe. These flow structures organize with n-fold rotational symmetry where n will be the number of high momentum streaks, dominant streamwise vortices, and 2n will be the number of low momentum streaks These resulting flow structures travel at a constant speed, such that, when viewed in a frame of reference traveling at that speed, the solutions would appear stationary. Kerswell and Tutty (2007) found that at Re = 2400 these traveling waves were linearly unstable and could be found as two types, upper branch (high wall shear) and lower branch (low wall shear).

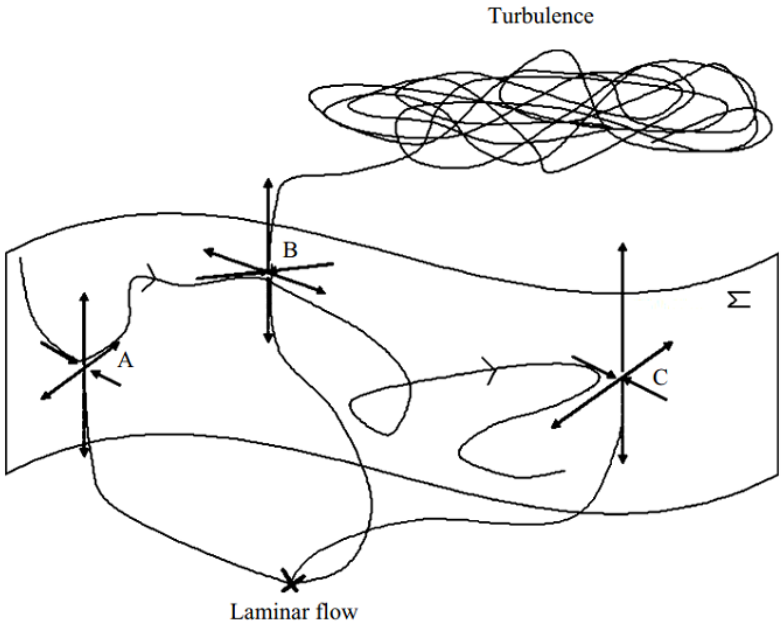

Figure 1.5: Schematic of pipe flow as a dynamical system taken from Duguet et al. (2008b) Here, the flow state starts in the upper left corner of Σ and is attracted to edge state A whose saddle-like behavior is represented by the thick black arrows. Instead of being ejected away from A to settle to the laminar flow, the flow state is attracted towards another edge state, B. From B, three possibilities are shown, decay to laminar, breakdown to turbulence, or ejection towards a still third edge state, C.

Upper branch solutions always tended toward turbulence, while lower branch solutions, when perturbed, could trend ultimately to the turbulent or laminar solutions depending on the nature of the perturbation.

The picture (see Fig 1.5) of pipe flow that arises from this dynamical systems approach is summed up well by Duguet et al. (2008a) where Σ represents the boundary between the laminar attractor and the turbulent state. The domain, Σ itself is populated by lower branch traveling wave solutions. These solutions behave like saddle points that can attract the flow towards themselves in some states and then repel the system toward the laminar basin, the turbulent state, or another edge state along Σ depending on their initial trajectory.

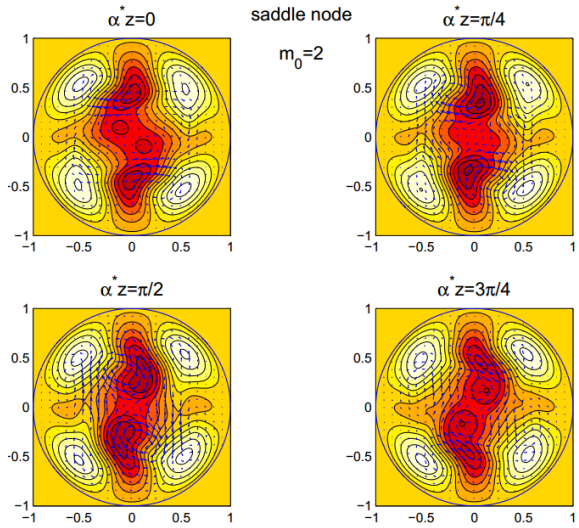

Figure 1.6: Contours of streamwise velocity variation from laminar at four evenly spaced intervals inside an R_2 traveling wave solution at $Re = 1358$ as shown by Wedin (2004). Red shows slow moving fluid while white shows fast moving fluid when compared to the laminar velocity field.

Some important observations have been made in numerical simulations. Wedin (2004) found traveling wave solutions that have rotational symmetry from what he called $R_1 - R_6$ where R_n refers to the order of the shift-and-reflect symmetry of the solution. The lowest Reynolds number for which he found a solution was 1251, where he found a solution of order 3 symmetry. Fig 1.6 shows a R_2 solution for $Re = 1358$. As with all of the solutions found, the high speed regions appear relegated to the edge of the flow and correspond to areas where the in-plane vortices introduce high momentum fluid into regions close to the wall. In general, the high-speed regions vary less along the streamwise wave length of the traveling wave solution than the high-speed regions. The low speed regions near the center meander much more over their wavelength.

Additionally, experimental evidence has been found suggesting that traveling waves are found in physical flows. The first to present this evidence were Hof et al. (2004). Their

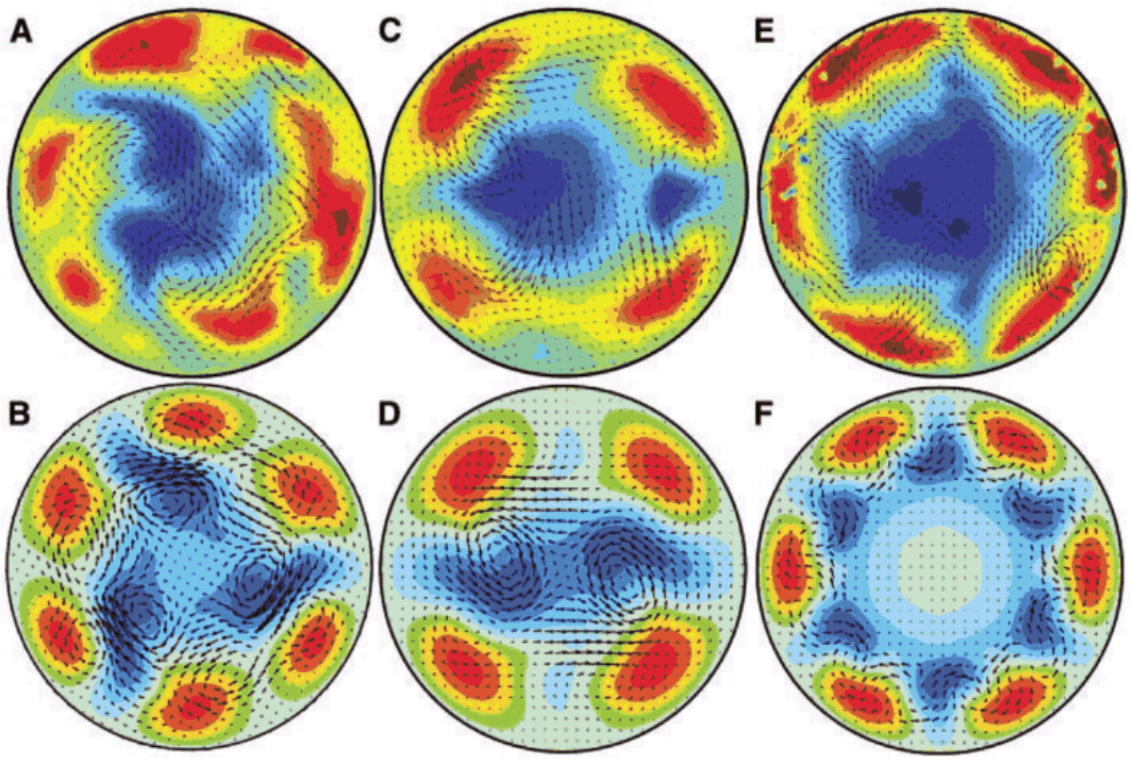

Figure 1.7: Comparison of (top) experimental and (bottom) numerical results for traveling wave solutions from Hof et al. (2004). Regions of yellow/red and cyan/blue indicate where the axial velocity of the fluid is faster or slower than the laminar case, respectively.

data, with corresponding traveling wave simulation results are shown in Fig 1.7. While the Reynolds numbers at which each traveling wave were found do not match up between experiments and simulations, the qualitative shapes of the profiles is striking, and the overall trend of finding higher order symmetry at higher Re is consistent across experiments and simulations.

Willis and Kerswell (2008) conducted a few separate numerical simulations of puffs at $Re = 2000, 2400$, and 2800. For each axial location in their domain at a given time, they examined axial velocity profiles along a circle at a fixed radius of $0.4D$. They then searched for sinusoidal patterns in the velocity profiles from 600 snapshots in time, each spaced in

time by $5D/w_b$. Strong sinusoidal patterns were found both upstream and downstream of the trailing edge in the range $-4 < z^* < 8$, where z^* is the normalized distance from the trailing edge location, z_0, defined as,

$$z^* = \frac{z - z_0}{D} \tag{1.7}$$

The authors verified that the strong sinusoidal patterns with m periods corresponded to cross-sections with m fast streaks equally spaced around the azimuth creating an m-fold modal symmetry. Axial regions for which a given m-fold symmetry was continuously strong were taken to correspond to 3D modal structures with m-streaks. Structures with m-fold modal symmetry, $m = 3$ or 4 were found twice as frequently as those where $m = 2$ or 5. The authors computed the energy contained within both the streaks themselves and the rolls presumed necessary to sustain the streaks. This energy was then compared to the streak and roll energy found in traveling waves. Willis and Kerswell found that only those structures found near $z^* = -2$, and $z^* = 4$ had amounts of energy in their rolls and streaks similar to those found in traveling waves. The authors noted that the axial velocity in structures found near these less energetic regions of the puff contained well defined fast and slow streaks and resembled traveling wave solutions. By contrast, the axial velocity contours inside the most turbulent region of the puff contained a strongly decelerated core and fast streaks near the wall, but lacked well-defined low speed streaks. This led to the conclusion that traveling waves occupy a region of phase space between the laminar and turbulent states. They found that the modal structures where $-2 < z^* < 4$ had energy which is similar to structures found in the turbulent state.

More recently, progress has been made to link the transient growth discovered via non-modal analysis that lies in the laminar basin to the abilities of the dynamical systems approach to explore flow states outside the basin using the fully nonlinear incompressible

Navier-Stokes equations. In 2012, Pringle et al. 2012 extended the linear analysis for transient perturbation growth to the full nonlinear case to consider perturbations of finite energy for a simulation domain length of $\frac{\pi D}{2}$. They found at low input energies, the optimal perturbation for energy growth is very similar to those found from nonmodal analysis. However, at higher input energies, they found a new optimal perturbation for the fully nonlinear case with a fundamentally different structure than that which experiences maximal growth in the linear case. This optimal perturbation could trigger turbulence at perturbation energy levels 10-100 times less than in the linear case. The optimal, in the case of $Re = 1750$, shown in Figure 1.8 is a more complicated structure whose strongest velocity perturbations both in-plane and axially are localized to one side of the pipe. This structure, while not axially invariant, was axially periodic over the entirety of their domain. Figure 1.8a shows isosurfaces of fast and slow moving fluid inclined into the flow moving towards the pipe wall with downstream distance. Fig 1.8b shows a cross-section of the perturbation that details the opposing layered streaks that make up the structure along with the in-plane velocity vectors whose azimuthal components change sign rapidly in the regions of strongest axial perturbation near the wall. Over a time corresponding to the mean flow traveling $7 - 15D$, this perturbation grows as it experiences the mean shear of the laminar flow, evolves into a helical wave pattern, and finally is dominated by a strong pair of counter-rotating vortices that create similarly strong streaks. This evolution corresponds to an $O(100)$ increase in energy. Pringle et al. (2012) conducted a similar process for a $5D$ long pipe. They found that the optimal perturbation at $Re = 2400$ was similar to that in the shorter pipe at $Re = 1750$, streaks and rolls that are both localized to one side of the pipe, but in this case with its strongest velocity values localized to an $O(1D)$ axial section of pipe. The growth of this perturbation follows a similar sequence as that of the shorter domain. Finally, in Pringle et al. (2015), the localization of the optimal perturbation at $Re = 2400$ continues to the point that, in a $25D$

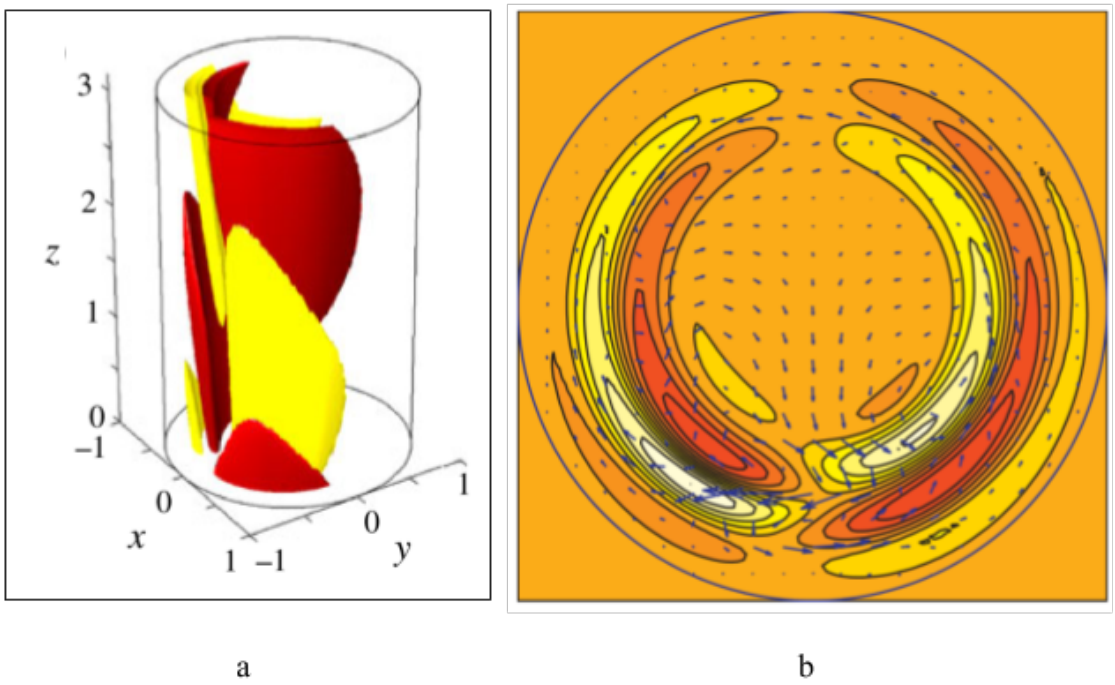

a b

Figure 1.8: The form of the optimal perturbation found by Pringle and Kerswell (2010) (as shown in Pringle et al. (2012) for $Re = 1750$ is shown as (a) a three-dimensional isosurface plot, and (b) a cross-section contour plot of the streamwise perturbation velocity. The yellow and red isosurfaces in (a) represent 50% of the maximum (fastest) and minimum (slowest) velocities. The contours in the cross-section, (b), use the same color scheme to show 10 contour levels of the streamwise perurbation velocity evenly spaced along $-0.005w_b$ to $0.005w_b$ with the maximum in-plane velocity arrows indicating $0.009w_b$.

domain, 99% of the perturbation energy is confined to a $7D$ section. The shape, amplitude, and evolution of the perturbation is similar to those found in both shorter domains. The authors point out the length scale similarities between the $7D$ of the optimal perturbation and the similar length scale for which experimental jet perturbations exhibited a minimum in the required flux to trigger transition in the results of Hof et al. (2003). Figure 1.9 shows the vorticity isosurfaces at $\pm$30% of the maximum inside the perturbation. The vortical structures weave and twist around one another as they travel downstream from left to right.

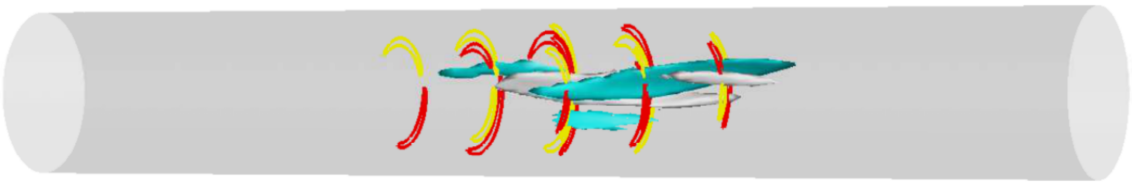

Figure 1.9: The form of the optimal perturbation in a pipe of length 25D at $Re = 2400$ taken from Pringle et al. (2015). White and blue isosurfaces show +30% and −30% of the maximum vorticity values, while the yellow and red lines show fast and slow moving fluid respectively.

1.2.2 Topology and mechanics of transitional structures

Regardless of how a flow is tripped into transition, once the transitional structures noted by Reynolds emerge, a rich set of phenomena worthy of investigation occur.

As recognized by Reynolds (1883), intermittent volumes of disorganized flow appear in flows whose Reynolds number is around 2000 or higher. These volumes, which extend over the entirety of the cross-section of the flow and span some axial distance, are referred to as slugs and puffs (Wygnanski and Champagne, 1973). Slugs and puffs, which occur under different flow conditions, are two distinct phenomena. Fig 1.10 shows a schematic of the *Re* and disturbance conditions that give rise to both slugs and puffs.

Puffs

Puffs are characterized by a region of disorganized flow whose strongest fluctuations extend roughly three to five diameters in the axial direction with transition zones/interfaces extending further in both the upstream ($3-4D$) and downstream ($20-30D$) directions (Wygnanski and Champagne, 1973). Bandyopadhyay (1986) described puffs as having three regions; the upstream region or so-called trailing interface, the downstream region called the 'relaminarizing' region, and the middle region described as fully turbulent. The interface at the

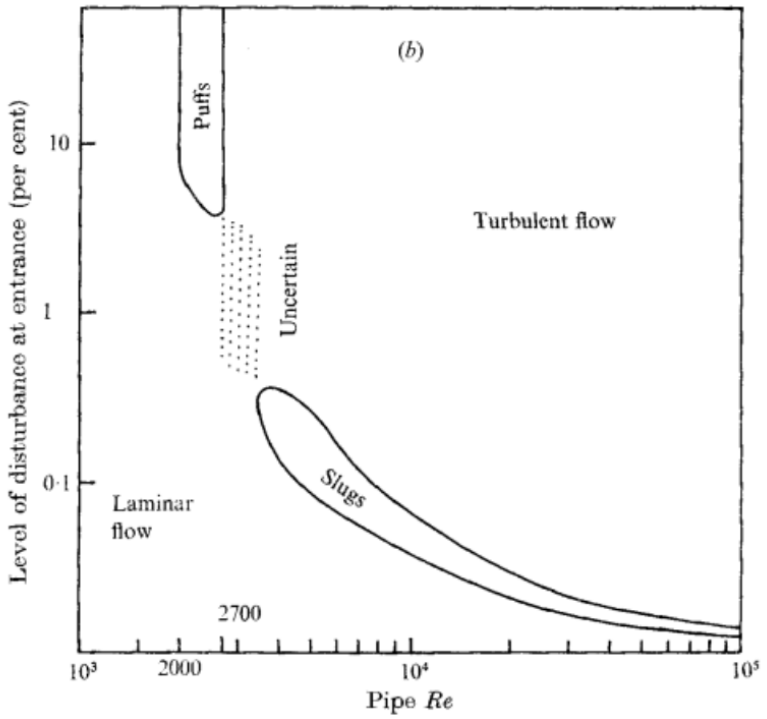

Figure 1.10: Flow regimes containing puffs and slugs from Wygnanski and Champagne (1973)

upstream edge of the puff is a roughly conical core of laminar flow penetrating downstream into the puff, sometimes including a helical motion. The downstream end of the puff is not as sharply defined as the upstream end, but exhibits a gradual recovery to the laminar velocity profile.

Figure 1.11 shows a representation of a typical normalized centerline velocity trace, w_{CL}/w_b, for a puff as experienced by an observer at a fixed axial location in the pipe. From left to right, the laminar centerline velocity gradually and smoothly decreases from its laminar value before exhibiting several long wavelength oscillations for times corresponding to $20D/w_b$. The velocity then continues to fluctuate with increasing magnitude and decreasing wavelength for collective time of $3-4D/w_b$. Finally, the velocity fluctuations become very

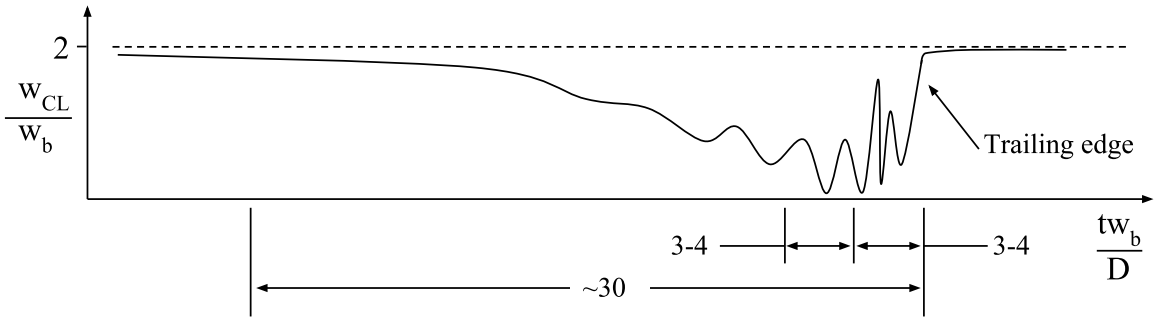

Figure 1.11: Schematic of a typical centerline velocity signature in a puff.

short in wavelength and reach their largest magnitude for a time corresponding to an additional $3 - 4D/w_b$. The strongest of these can be close to w_b in magnitude and last for times corresponding to $0.1D/w_b$. Then there is an abrupt return to the laminar centerline velocity with few velocity perturbations if any. (Wygnanski and Champagne 1973, Wygnanski et al. 1975, Darbyshire and Mullin 1995, van Doorne 2004).

Wygnanski and Champagne (1973) used various stationary objects to perturb the flow at the inlet of their test section, and noticed that regardless of how the disturbance was generated, a puff's structure was consistent at the location where they were measured downstream. The independent nature of puff structure compared to the perturbation from which it initiated was supported by later work of Wygnanski et al. (1975) where a cross-stream jet was used to perturb the flow and the resulting puffs were identical to those made by physical obstructions. Subsequent studies have also confirmed this 'memoryless' characteristic of puffs (Faisst and Eckhardt, 2004; Mukund and Hof, 2018).

When puffs form, they are destined either to decay to the laminar profile or split to form two secondary puffs. The process by which the decay or split occurs is stochastic. Fig. 1.12 taken from Avila et al. (2011), shows a decaying/splitting time constant vs Reynolds number for experiments and simulations. Therefore, mean lifetimes before decay or splitting are

derived from multiple realizations. This time is then normalized by the bulk fluid velocity and pipe diameter. The dotted line is a fit to data where decaying puffs were observed. Similarly the solid line is a fit to puffs that were observed on average to split after some time. Near $Re = 2040$, puff time constants become very large. On average, puffs in this region travel over a million pipe diameters before splitting or decaying. Additionally, puffs in this Reynolds number range have an equal probability to decay or split at any time. At very low Reynolds numbers, around 1750-1800, in addition to the relatively large perturbations required to initiate a puff, the average lifetime of a puff is less than $100D$. These puffs have a vanishingly small probability of splitting. Similarly, at $Re \approx 2400$, puffs will on average last a few hundred diameters before splitting and would nearly never decay. In the studies that examine puff lifetimes, the interactions of puffs are neglected.

To investigate the effect of puff interactions on the long-time behavior of the pipe flow, Mukund and Hof (2018) devised an experiment that capitalized on the memoryless nature of puffs to experimentally simulate pipes of extreme axial length. The inlet flow of a long pipe ($8000D$ and $2500D$) was perturbed to create an initial series of puffs. Those puffs were monitored downstream and when a puff exited the test section, a new one was added via the perturbation mechanism. These newly created puffs and their interactions with their neighbors should statistically behave identically to those that exited the test section. Mukund and Hof (2018) found for $Re = 2020$ that two initial puff sequences each with a different initial turbulent fraction (number of puffs) decayed completely to the laminar solution at times corresponding to the mean flow traveling $50x10^6$ pipe diameters (advective time units). At $Re = 2060$, however, three initial turbulent fractions all converged to a steady state turbulent fraction by $20x10^6$ advective time units. When the Reynolds number was increased to 2100, the initial conditions converged to a higher turbulent fraction sooner, by $5x10^6$ advective time units.

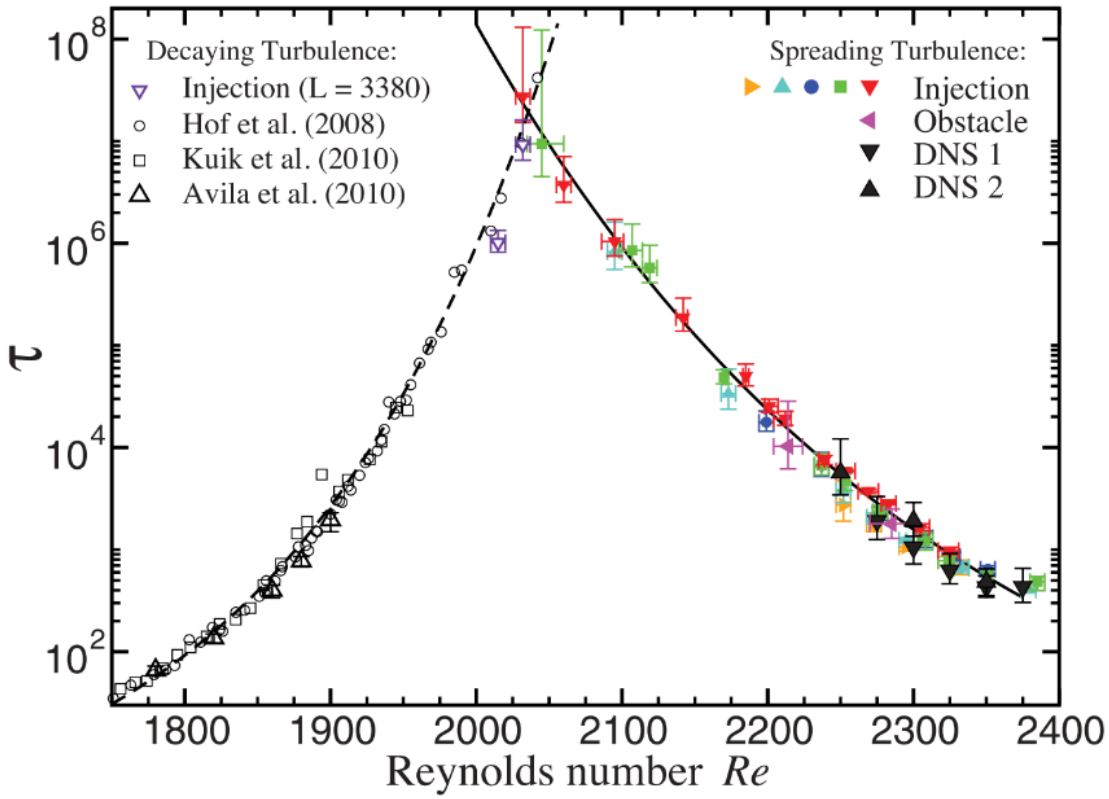

Figure 1.12: Mean decay/split time constant, τ, for turbulent spots as a function of Reynolds number from Avila et al. (2011). τ is calculated as the average length of time a puff will exist before it either decays or splits.

The mechanism by which turbulent puffs originate seems intimately tied to the region of abrupt velocity change near the upstream end of the puff. van Doorne (2004) showed that downward velocity spikes near the centerline correspond to a sharp interface between nearly laminar fluid on the upstream end and highly disorganized, swirling fluid on the downstream end. This interface was associated with large increases in the non-axial velocity contribution to kinetic energy, and sharp decreases in the kinetic energy contribution of the axial component of velocity.

Shimizu and Kida (2009) used a curve fit of the centerline velocity to define and track the leading and trailing edge of a puff in a numerical simulation at $Re = 2226$ for a time corresponding to $1000D/w_b$. They found that the instantaneous propagation velocity of puffs varies, as well as the length between the leading and trailing edges. Puffs do not travel at the same speed as the mean flow. However, on average they travel down the pipe at a velocity that decreases monotonically with Reynolds number starting around 10 – 15% faster than the bulk fluid velocity at the lowest Reynolds numbers to around 10% slower at the highest Reynolds numbers where puffs exist (Hof et al., 2005; Kuik et al., 2010). Holzner et al. (2013) used a numerical simulation to investigate the mass flux through the leading and trailing edges of a puff at $Re = 2200$ in order to discern the net exchange of fluid between the puff and the laminar flow that surrounds it. They set a threshold on the instantaneous enstrophy distribution marking an isosurface that defined the leading and trailing edges of the puff as well as isolated islands of laminar and turbulent flow inside and outside of the puff, respectively. Their results agreed with previous studies by showing there was a net flux of fluid into the puff at the trailing edge, and a net flux out of the puff at the leading edge overall, i.e. it was traveling slower than the bulk fluid velocity. Additionally, while the overall net flux at the trailing edge was positive into the puff, the average radial profile of flux was positive at the center of the puff where $r/D < 0.38$ and negative near the wall where $r/D > 0.38$. This trend was reversed at the leading edge, but still crossed zero at $r/D = 0.38$. Samanta et al. (2011) found through experiments, evidence of a minimum spacing between puffs of $20 - 30D$. Attempts to introduce disturbances at shorter intervals resulted in puffs actually annihilating one another and decaying rapidly.

Barkley (2016) constructed a theoretical model in an attempt to reproduce many of the aforementioned macroscopic behaviors of puffs. Barkley presented puffs in pipe flow as a linearly stable excitable medium that mimics the behavior of electrical impulses traveling

along a nerve cell. A sharp reversal in membrane voltage potential from quiescent to excited occurs in a neuron and is accompanied by a refractory region that cannot be excited. This phenomenon was compared directly to the trailing edge of the puff, with its slowly relaminarizing downstream region that cannot be excited into a new puff. Using this analogy, Barkley constructed his theoretical model for puff behavior based on the centerline velocity and turbulence intensity. The model was able to reproduce the preferred spacing between puffs, puff propagation speed trends, and the tendency for puffs to split or decay based on Reynolds number.

Additional work has examined the detailed structure of puffs, especially at the trailing edge, using both experiments (Wygnanski et al. 1975, Bandyopadhyay 1986, van Doorne and Westerweel 2009) and numerical simulations (Kuik 2011, Holzner et al. 2013). Wygnanski et al. (1975) used X-hotwire probes to record velocity inside a puff at various radial positions. Using a high-pass filter, the fluctuating axial and transverse velocity components were computed as w' and v', respectively. Then, by setting a threshold on the quantity,

$$log(\frac{dw'}{dt}) + log(\frac{dv'}{dt})$$

a trailing edge was determined for each record. Records were then aligned according to their trailing edges and ensemble averaged. From this average, Wygnanski et al. concluded that the trailing edge of a puff contains a toroidal eddy that drives the turbulent motion inside the puff.

Bandyopadhyay (1986) conducted an experimental investigation using PLIF in an axial-radial plane, and found that the trailing edge of a puff exists as a conical shaped 'plug' of laminar flow with a helical motion and whose boundary continually sheds a series of organized 'wake-like' vortices. Bandyopadhyay (1986) found no instantaeous toroidal vortex at the trailing edge. Instead he suggested the toroidal eddy hypothesized by Wygnanski et al.

(1975) was the result of their setup's inability to account for the three dimensional nature of the trailing edge transition process and thus was not phase-averaged in a way that preserved the vortical structure. Further, Bandyopadhyay (1986) attributed the large magnitude variations (spikes) in velocity noted by Wygnanski and Champagne near the wall at the trailing edge of puffs to the presence of the wake-like vortex sequences.

van Doorne and Westerweel (2009) presented a series of time resolved stereo-PIV measurements taken in a puff at $Re = 2000$. They noted similar spikes in w_{CL} at the trailing edge and reported their typical axial length to be $0.095D$ by measuring their full width at half maximum. The authors noted that the spikes in w_{CL} corresponded to strong, and similarly short upward spikes in the in-plane kinetic energy, given by,

$$q^*(z) = \frac{\left[u_\theta^2 + u_r^2\right]_{r,\theta}}{w_b^2}, \tag{1.8}$$

Here, $[.]_{r,\theta}$ represents averaging over the circular (r, θ) cross-sectional plane.

van Doorne and Westerweel (2009) found that some of the spikes in q^* corresponded to an energetic hairpin vortex that created a strong ejection of fluid normal to the pipe wall, which significantly disrupted w_{CL}, and sustained turbulent fluctuations downstream. The magnitude of global peak in q^*, q^*_{max} found in the puff analyzed by van Doorne and Westerweel (2009) was 0.024 and occurred at $z^* = 0.74$ based on the trailing edge identification method employed. At the q^*_{max} location, van Doorne and Westerweel (2009) noted a "very large... cross flow extends over the entire cross-section of the pipe and is directed away from [a] hairpin vortex." They noted that quasi-periodic regeneration of streamwise vortices at the puff's most upstream end developed into strong hairpin vortices similar to the auto-generating hairpin packet process (Zhou et al., 1999). van Doorne and Westerweel suggested that puffs persist by the repeated generation of hairpins in the region around the trailing edge. The hairpins work to extract energy from the incoming upstream laminar flow

near the center of the pipe that is traveling faster than the puff. A few diameters downstream of the trailing edge, the kinetic energy in the flow has been redistributed in such a way that no more energy can be extracted from the now plug-like mean axial flow. Therefore, the fluctuations must decay due to viscosity, returning the laminar profile.

In his thesis, van Doorne (2004), also presented PLIF sequences taken of a circular cross-section of puffs at 2100 and 2300. To accomplish this, the fluid in the disturbance generator jet used a fluorescent dye that could be tracked visually in the resulting puff images as it passed a laser illuminated cross-section. In the Re = 2100 sequence, van Doorne (2004) noted a series of three streamwise oriented vortex pairs upstream from the trailing edge. The vortex pairs existed at a common azimuthal position and the size of each pair increased compared to the pair which was upstream of it. The vortex pairs passed the observation plane with a time spacing roughly equal to $1D/w_b$. Within each vortex pair, one vortex dominated over the other in terms of its size. Further, the side of the dominant vortex seemed to alternate from the pair that preceded it. In the $Re = 2300$ sequence, a similar train of three vortex pairs was observed upstream of the trailing edge.

Noting the work of van Doorne, Kuik (2011) hypothesized that no previous numerical studies reported spikes in q^* because the axial resolution required to realize them in a simulation was finer than what any had previously attempted. He used an axial resolution of 0.024D which, while finer than in previous numerical studies, was slightly coarser than van Doorne's axial spacing of 0.019D based on Taylor's Hypothesis. Kuik not only reported the presence of q^* spikes similar to those reported by van Doorne for the first time in simulation, but tracked them as they evolved both forward and backward in time. Kuik found that spikes associated with q^*_{max} frequently appeared as a local maximum near the trailing edge and traveled 0.5D downstream within the puff, but sometimes traveling as far as 3.5D from the time they became recognizable as local maxima to the time they decayed. Kuik also found

that these spikes traveled faster relative to the puff as Reynolds number increased, but slower relative to the bulk fluid velocity as Reynolds number increased. The average peak velocity decreased from $1.35w_b$ at $Re = 1800$ to $1.25w_b$ at $Re = 2100$. Over a time corresponding to $t^* = 30$, Kuik identifies 25 global peaks in q^* in the range $0.019 < q^*_{max} < 0.045$. Using the second invariant of ∇u, Q, as a vortex identifier, Kuik was unable to find hairpins at the locations that corresponded to peaks in q^* (Jeong and Hussain, 1995). Instead he found "vortical structures... with an orientat[tion] normal to the pipe axis. They were about one diameter long and aligned along the azimuthal direction."

Shimizu and Kida (2009) calculated the average propagation velocity of axial velocity fluctuations by finding the time difference that minimizes the squared error between velocity time series at axially-spaced points $\pm\pi/4D$ from a given point. By registering the puff location using the average velocity of the puff, then averaging over the azimuthal coordinate, they built a map of propagation velocities over the radial-axial half plane of their simulation. At a location that was $1D$ upstream of the average trailing edge location, Shimizu and Kida (2009) found that the propagation velocity of fluctuations increased from $0.82w_b$ at $r^* = 0.42$ to $1.50w_b$ at $r^* = 0.18$. At the average trailing edge location, the propagation velocities decreased to $0.68w_b$ at $r^* = 0.44$ to $1.1w_b$ at $r^* = 0.19$. The largest decreasing gradients in propagation velocity across the whole domain are concentrated along a line that extends from $r^* = 0.35$ at $1D$ upstream of the average trailing edge location to $r^* = 0$, at the average trailing edge location. Shimizu and Kida (2009) outlined a self-sustaining process whereby turbulent fluctuations inside the puff create low speed streaks and streamwise vortices near the wall. Because these regions are near the wall and moving slowly, they are left behind by the puff as it propagates downstream at a velocity close to the bulk fluid velocity. This low speed fluid interacts with the oncoming laminar flow to create strong shear. From this shear, a Kelvin-Helmholtz instability develops and rolls up the shear layer into new

fluctuations that lift up into the fast moving fluid near the center of the pipe in regions near the line of strongly decreasing propagation velocities. These new fluctuations are carried downstream through the trailing edge into the puff to interact and sustain the turbulent fluctuations present inside the puff's core. Duguet et al. (2010) confirmed the presence of this process in their own simulations. They tracked the propagation speed of individual vortices identified upstream of the trailing edge that moved into the puff, and found that on average, they propagated downstream near $1.4w_b$, at velocities ranging from slightly greater than w_b to nearly $2w_b$. They mentioned that a link between these vortices and hairpins should be investigated.

Slugs

Turbulent slugs in pipe flow differ from puffs in a few critical ways. First, the flow inside them is more highly disordered than what is found in a puff. Darbyshire and Mullin (1995) described it as indistinguishable from flow found in a fully turbulent pipe flow. Further, they described slugs as having sharply defined interfaces at both ends. Finally, slugs have a velocity difference between their leading and trailing edges, which are faster and slower than the bulk velocity respectively. This means that slugs expand as they propagate. As they expand, they entrain new fluid elements inside themselves. Slugs are found at Reynolds numbers greater than 3000 (Wygnanski and Champagne, 1973; Darbyshire and Mullin, 1995). In the regime between 2700 and 3000, the difference between splitting puffs and slugs was difficult to distinguish, as puffs that split then merged farther downstream, and in some instances, agglomerated into slugs (Wygnanski and Champagne, 1973).

Slugs, like puffs, also evolve after they initiate. As mentioned above, the slugs expand as they travel downstream. The leading edge will travel faster than the bulk fluid velocity and the trailing edge will travel slower. How much faster or slower depends on the Reynolds

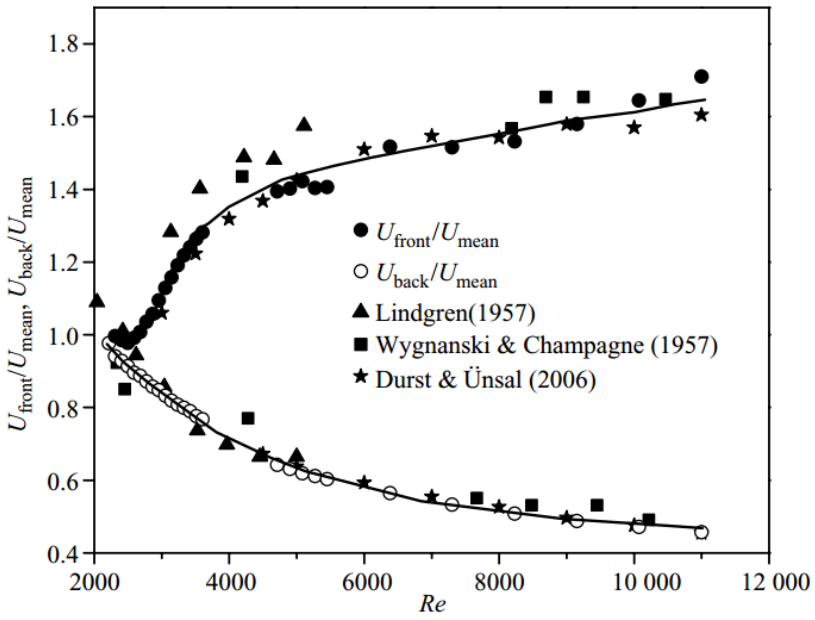

Figure 1.13: Leading and trailing edge velocities of puffs and slugs as a function of Reynolds number from Nishi et al. (2008)

number. Fig 1.13, from Nishi et al. (2008), shows a plot of the mean velocity of leading and trailing edges for puffs and slugs versus Reynolds number. Each point in the presented data was gathered via hotwire probe over approximately 100 slug realizations. For Reynolds numbers greater than $Re = 3000$, the leading edge velocity varies from $1.05w_b$ to $1.6w_b$ as Re increases. Conversely, the trailing edge velocity lags behind the the bulk flow at $0.8w_b$ at $Re = 3000$ and decreases to $0.45w_b$ at very high Reynolds number.

1.3 Turbulent transition in dispersed multi-phase flows

While laminar and fully turbulent flows containing dispersed particles and droplets have been the subject of much investigation, insight into turbulent transition in these flows is limited Balachandar and Eaton (2009). Efforts have been made to verify the validity of

applying the Krieger and Dougherty and Eilers models for modified viscosities to predict turbulent transition in pipe flows (Matas et al., 2003a,b; Pouplin et al., 2011). Both the Krieger-Dougherty and Eilers models solve for the expected viscosity of a particle laden fluid based on the viscosity of the carrier-phase fluid and the concentration of particles.

$$\frac{\mu_e}{\mu} = \left[1 - \frac{\phi}{\phi_m}\right]^{-\phi_m[\mu]} \tag{1.9}$$

$$\frac{\mu_e}{\mu} = \left[1 + \frac{2.5\phi}{2(1 - \phi/\phi_m)}\right]^2 \tag{1.10}$$

Eqns 1.9 and 1.10 show the Krieger-Dougherty, and Eilers models for modified viscosity respectively. In each, the expected viscosity of the particle laden fluid, μ_e, is a function of the dynamic viscosity of the carrier-phase, μ, the volume fraction of the particles, ϕ, and the maximum close-packing volume fraction for rigid spheres, $\phi_m = 0.68$.

Matas et al. (2003a), recorded time series of the pressure drop along a length of pipe. They noticed that as Reynolds number increased, low frequency content began to appear in the spectra of pressure time series. By defining a threshold on the low frequency content, they were able to study how the turbulent transition Reynolds number changed with not only ϕ, but the pipe-to-particle diameter ratio, D/d_p, for particles of four different diameters. In a second publication, Matas et al. (2003b) extended these results by repeating their experiment in a second pipe with a smaller diameter. This allowed them to investigate eight diameter ratios in total. The key findings from their extended study are shown in Figure 1.14a. They found that small particles ($D/d_p \geq 65$), act to monotonically increase the critical Reynolds number with increasing particle concentration. Further, they found that for these small particles, only volume fractions below 0.25 could effectively be described by modified viscosity equations. For larger particles ($D/d_p \leq 65$), the particles act to ini-

tially decrease the critical Reynolds number over a range of volume fraction. The Reynolds number domain and magnitude of the decrease depends on particle diameter. Larger particles decrease the critical Reynolds number to a lower minimum value and result in a larger domain of decreased critical Reynolds number. Further analysis of their results yielded the conclusion that modified viscosity models might explain the delayed transition for flow in which small particles make up 25% or less of the volume, but for larger particles, and larger concentrations, the modified viscosity models were inadequate.

Pouplin et al. (2011) used pressure and PIV measurements to study buoyant polydispersed liquid droplets in a liquid flow whose droplets were on average 2000 times smaller than the pipe diameter. Fig 1.14b, shows friction factor for values of Reynolds number which is modified to account for the density of the mixture and the Krieger-Dougherty viscosity. The solid line represents the laminar friction factor and the dashed line represents the Blasius solution. The dotted line represents a single-phase flow, and each marker type corresponds to a different volume fraction. It would be expected that, if the Krieger-Dougherty model was appropriate, the data points for various volume fractions would line up with the dotted single-phase curve. Due to limitations of the experiment, the only data sets containing points in what is expected by the Krieger-Dougherty model to be the transition region correspond to volume fractions of 0.31, 0.36, 0.43, 0.45. The only value of volume fraction close to agreement with the single-phase data is 0.31. The other three show strong departures from the single-phase curve. This led to the conclusion that the modified viscosity equations do not account for the modification in transitional Reynolds number at the volume fractions studied. These results were consistent with those of Matas et al. (2003b) which, for such small particles, predicted a monotonic increase in transitional Reynolds number with increasing volume fraction that outpaces that which is predicted by the modified viscosity models.

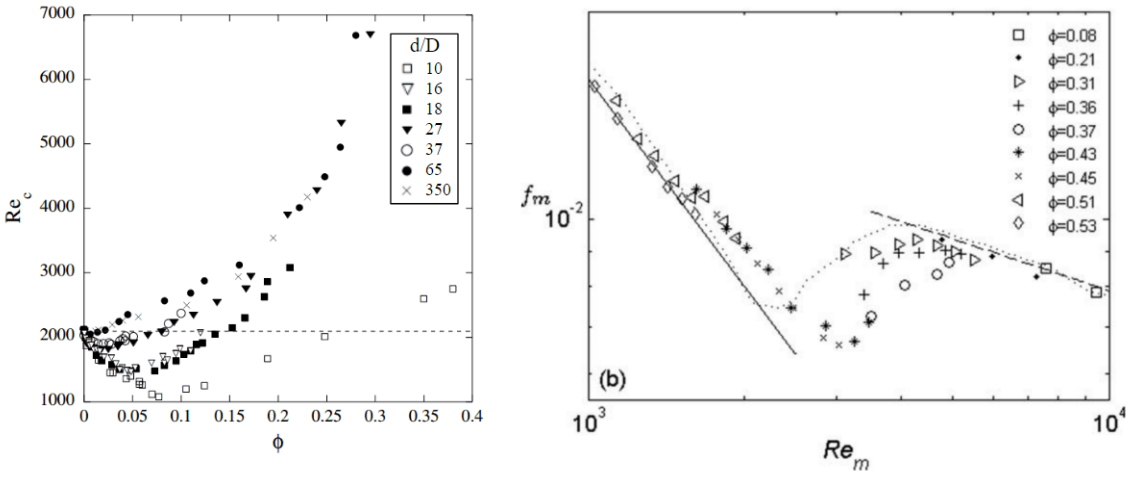

Figure 1.14: (a) The modification of critical Reynolds number with increasing particle volume fraction for various particle diameters. (Matas et al., 2003b) (b) Friction factor for increasing Reynolds number for various droplet volume fractions. (Pouplin et al., 2011)

Recently, Hogendoorn and Poelma (2018) and Agrawal et al. (2019) studied the effects of neutrally buoyant solid particles with D/d_p of 19 and 20 respectively. Hogendoorn and Poelma (2018) used measurements from a pressure transducer to monitor the friction factor of a $125D$ section of pipe for various volume fractions. The results shown in Figure 1.15 show the friction factor plotted against Reynolds number with lines representing the expected results for laminar and turbulent single-phase flow. It is evident that for the volume fractions of 1%, 5%, and 14%, the trends in behavior resemble those described by Matas et al. (2003b). The data diverges from the laminar solution at lower Re than the single-phase fluid for a volume fraction of 1%. Then at 5%, the flow diverges from laminar at an even lower Re value. Finally, at 14%, the location of divergence increases back toward the laminar value. Interestingly though, at a volume fraction of 17.5%, the friction factor plot does not exhibit a jump, but instead decreases smoothly with increasing Reynolds number. Near $Re = 1200$ the 17.5% curve begins to deviate significantly from the laminar data.

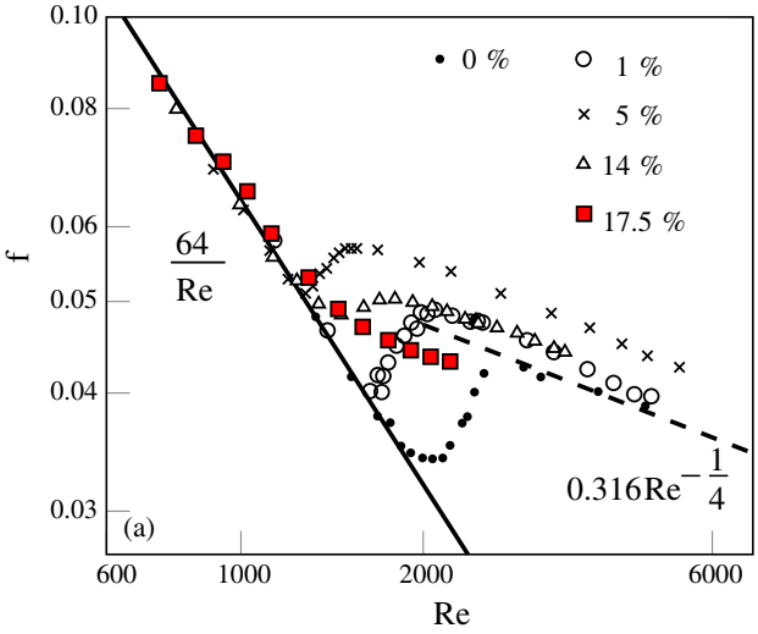

Figure 1.15: Friction factor plots against Reynolds number for various volume fractions of solid particles taken from Hogendoorn and Poelma (2018)

For reference, $\phi = 0.175$ is very close to the concentration in Matas et al. (2003b) where particles of this diameter would be predicted to have a transitional Reynolds number equal to that of single-phase flow. It is also known that, in single-phase flows, the region where the friction factor sharply increased is associated with the presence of puffs.

Using ultrasonic image velocimetry, Hogendoorn and Poelma (2018) investigated the velocity of the fluid within particle-laden flows at increasing Reynolds number and found that, while puffs developed in flow with $\phi = 1\%$, nothing resembling puffs developed for $\phi = 14\%$. This can be seen in Figure 1.16 where contours of transverse velocity are shown along the pipe radius as time passes. Figure 1.16a corresponds to the 1% volume fraction with five plots corresponding to increasing Reynolds number. At $Re = 1690$, two localized regions of strong transverse velocity appear in the pipe. When compared to the centerline velocity (black), the two structures appear to have signature characteristics of a

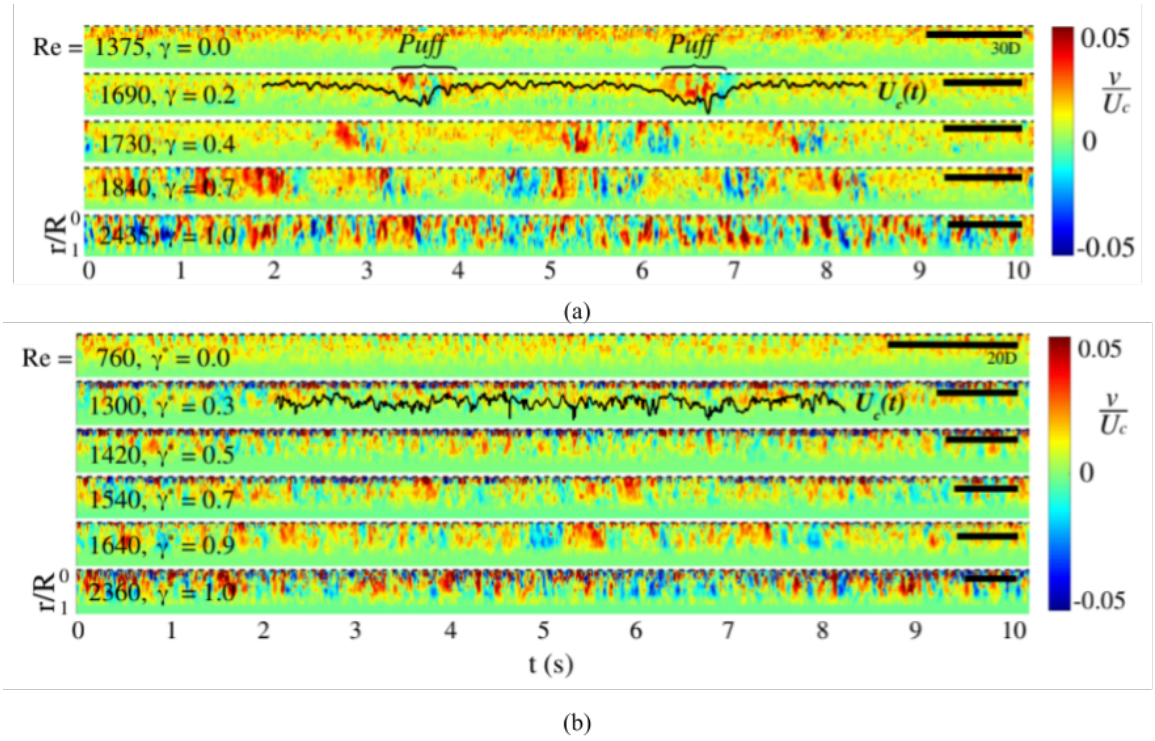

Figure 1.16: Contours of the transverse velocity components at various Reynolds numbers over time for volume fractions of (a) 1% and (b) 14% taken from Hogendoorn and Poelma (2018). The black lines in (a) and (b) correspond to the centerline velocity signal at the time and Reynolds number shown.

puff. For the 14% volume fraction data shown in Figure 1.16b, no puffs are apparent as the Reynolds number increases despite a clear departure from the laminar friction factor. What appear instead are disorganized and non-localized transverse velocity fluctuations beginning at $Re = 1300$ that increase in intensity up to $Re = 2360$. Additionally, the non localized deviations from the laminar centerline velocity are observed for $Re = 1300$ (black line).

Using pressure measurements across a $120D$ section of pipe, Agrawal et al. (2019) found similar friction factor results to those shown by Hogendoorn and Poelma (2018). Additionally, Agrawal et al. (2019) examined the transition behavior at various volume fractions and viscosity-modified Reynolds number. This was done by calculating the standard deviation

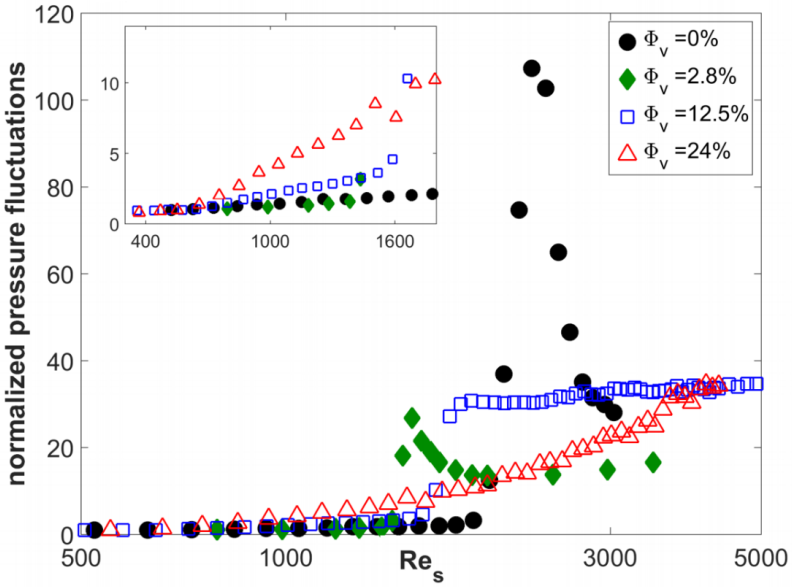

Figure 1.17: The normalized standard deviation of the pressure drop along a section of pipe plotted against the viscosity-modified Reynolds number for various values of ϕ taken from Agrawal et al. (2019).

of the pressure fluctuations along a $5D$ section at various combinations of Re and ϕ and normalizing them by the background noise in the pressure fluctuations. Figure 1.17 shows the normalized pressure fluctuation results for four volume fractions that demonstrate different fundamental behavior. First, the single-phase data is shown in black dots as a baseline. The single-phase data show a sharp increase and local peak in pressure fluctuations associated with the Reynolds number region known to correspond with puffs. The $\phi = 2.8\%$ data exhibits similar behavior to that of the single-phase fluid. At a critical value of Reynolds number, a sharp increase in pressure fluctuations was observed. This sharp increase, caused by the presence of intermittent regions of high fluctuation levels, creates a localized peak at a slightly higher Reynolds number. The $\phi = 12.5\%$ data (see inset) shows a smoothly and gradually increasing trend in the pressure fluctuations before a sharp increase. In the gradually increasing region, the authors note that the particles induce uniform weak fluctuations

that increased with Reynolds number. As with the lower values of ϕ, the sharp increase in pressure fluctuations was associated with regions of localized strong fluctuations, except they were found to appear atop the uniformly fluctuating flow. For $\phi = 24\%$, the data show a gradual smooth increase in pressure fluctuations along the entire Reynolds number domain. In this case, no localized regions of increased perturbations were observed in the pressure.

The three types of transition scenarios noted in Figure 1.17 were mapped for all of the volume fractions tested. The resulting map is shown in 1.18. At volume fractions of 5% and below, a puff-like transition scenario played out. As Reynolds number increased above some critical value, localized patches of turbulent-like flow appeared. When the volume fraction was greater than 5% but less than 12.5%, a second type of behavior arose. As the Reynolds number increased above some critical value, a constantly fluctuating background perturbation appeared in the pressure signal. This continued until a second Reynolds number threshold was reached where puff structures appeared on top of the continuously fluctuating pressure signal. At volume fractions above 12.5%, in agreement with Hogendoorn and Poelma (2018), no puff signatures were observed at any Reynolds number and continual fluctuations dominated the transition behavior. In agreement with Matas et al. (2003b), the Reynolds number at which puffs occur dropped initially, then rebounded at higher volume fractions. The fact that only the behavior of the blue squares was reflected in the results of Matas et al. (2003b) suggests that their threshold criteria did not reflect the presence of the continual pressure fluctuations appearing at increasingly lower Reynolds numbers.

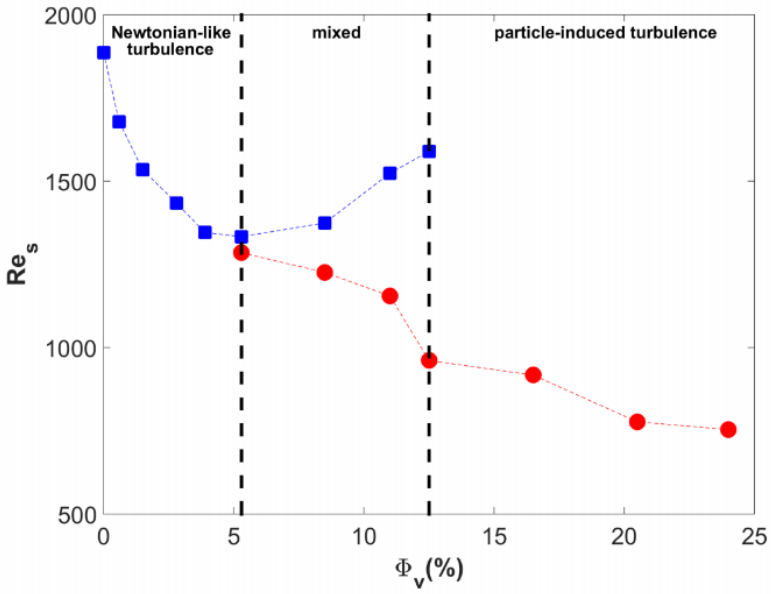

Figure 1.18: Map of the transition behavior across viscosity-modified Reynolds number and volume fraction for solid spherical particles taken from Agrawal et al. (2019). The blue squares indicate the lowest value at which puffs were observed for a given particle volume fraction. The red dots indicate the presence of uniform particle-induced pressure fluctuations.

1.4 Objectives of the research

The phenomenon of turbulent transition in single-phase pipe flows has been studied using many approaches, from modal and nonmodal techniques to dynamical systems and traveling waves to direct investigations of pressure and velocity in flow perturbations and the transitional structures from which they arise. From these works a finely detailed picture of pipe flow transition, and specific to this work, of puffs has emerged. This includes details about the Reynolds number range where puffs are found, their splitting and decaying behavior, their propagation velocities, the traveling wave structures that precede and commingle with them, the process by which a flow can be perturbed to leave its laminar basin of attraction and form a puff, and the actual velocity and vortical structure that exists inside puffs

once they have been formed. Particular attention has been paid to the investigations that observed streamwise vortices, hairpins, and the associated effects on various flow quantities inside puffs. It is still an open question regarding how common vortical structures like hairpins are inside puffs. While some evidence of periodic streamwise organization of vortical structures has been noted, there has been little investigation into the dominant organizational behavior of these structures. Similarly, while Willis and Kerswell (2008) and Hof et al. (2004) found that flows containing puffs also contain structures with modal symmetry, such structures have yet to be quantified in experimental flows with broadband disturbance levels. Detailed characterizations of both vortical and modal structures could serve as a basis for detailed quantitative comparison to transitional structures found in flows containing dispersed media.

For flows with a dispersed second phase, the traditional Reynolds number behavior of transition wherein laminar flow gives way to increasingly frequent puffs, is modified. For relatively small particles, the stability of the laminar flow is increased. For larger particles, a more complex transition scenario can play out. For diameter ratios close to twenty, the concentration controls whether the fluid will transition with isolated structures like a single-phase fluid, with global fluctuations, or a combination of both. Apart from the recent ultrasonic image velocimetry results presented by Hogendoorn and Poelma (2018), no detailed velocity measurements have been presented inside transitional structures containing a dispersed second phase. It is not known how the general velocity structure of puffs is altered by the presence of the dispersed phase.

Given the current state of knowledge, the present study was conducted with the following objectives:

1. Design, construct, and qualify a pipe flow facility to investigate transitional structures

in single-phase and droplet-laden flow.

2. Investigate puff frequency as a function of Re and ϕ.

3. Characterize coherent structures within puffs including hairpins, and modal patterns found in streamwise velocity perturbations.

4. Present the progress made in investigating the transition to turbulence of droplet-laden flows.

Chapter 2

Facility and methods

Parts of Sections 2.1, 2.3, and 2.4 are presented exactly as they appear in Winters, K. J., & Longmire, E. K. (2019). PIV-based characterization of puffs in transitional pipe flow. Experiments in Fluids, 60(4), 60.

Parts of Section 2.3.4, 2.3, and 2.4 are presented exactly as they appear in Winters K.W., & Longmire, E.K. (September, 2015) Searching for transitional structures in droplet-laden pipe flow. Paper presented at the 11th International Symposium on Particle Image Velocimetry – PIV15, Santa Barbara California.

This chapter describes the pipe flow facility that was built to achieve Objective 1 in Chapter 1. The facility evolved over time and two versions are reflected in this chapter in order to accurately describe the facility as it existed when each set of measurements was taken. The flow inside the pipe was measured using two modalities of particle image velocimetry and a differential pressure transducer in order to fulfill Objectives 2-4 in Chapter 1. This chapter also details the equipment and methods used to obtain the PIV and pressure measurements.

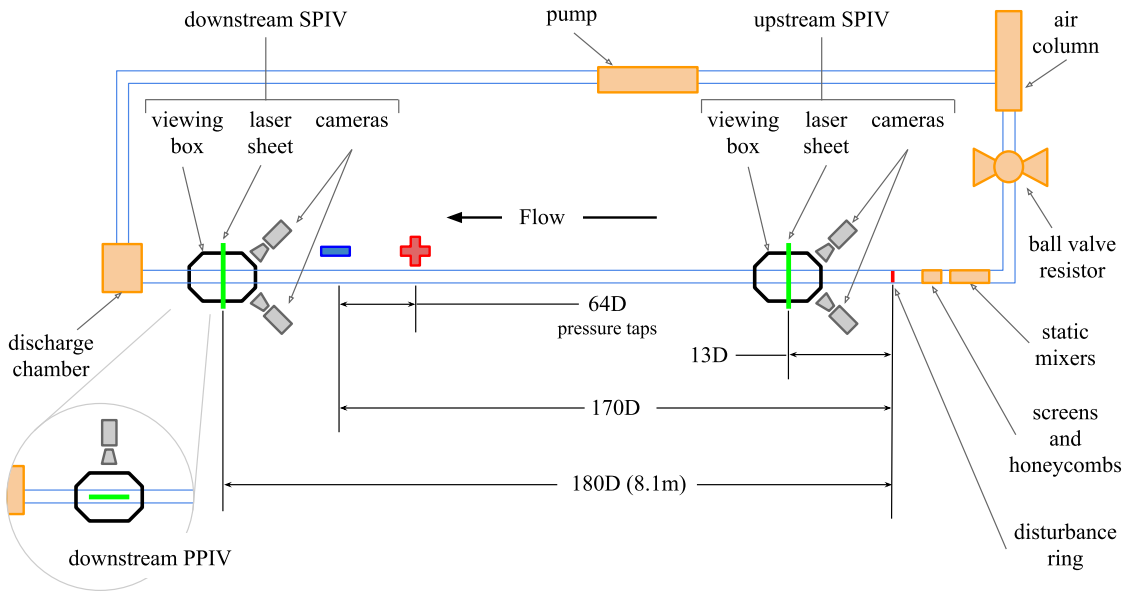

Figure 2.1: Flow circuit schematic including the upstream and downstream SPIV systems and the downstream PPIV system (see inset).

2.1 Facility for measurements of single-phase pipe flow

2.1.1 General description

The flow facility is a closed circuit shown schematically in Figure 2.1. The fluid was forced through a Moyno 1000 series positive displacement pump into an air-filled capacitor, immediately followed by a partially closed ball valve whose pressure and resistance were tuned respectively to damp the unsteady forcing from the pump. The fluid then turned 180° through a long smooth bend and entered a flow conditioning section comprised of six 3D printed mixing elements followed by honeycombs and a fine mesh screen. Next, the fluid flowed through a test section of 44.8mm diameter glass tubing (1.6mm wall thickness) that is 220 diameters in length. A disturbance generator ring, shown in Figure 2.8, was placed in the

test section 10D downstream of the flow conditioning.

The fluid used in the circuit was a 51.1% by volume mixture of glycerin in water. This fluid combination was selected in order to increase the viscosity such that the flow rate required to reach the target Reynolds number resulted in smoother delivery from the pump. Since glycerin is an energy dense nutrient for some species of algae, bacteria, and yeast, a concentration of 5-10ppm of free chlorine was maintained though regular checks and the addition of chlorine bleach when required. If the chlorine concentration was not monitored and dipped too low, a biofilm would rapidly develop in the fluid. In the event of a biofilm, the remedy was to discard the working fluid, disassemble and clean the facility, and refill with distilled water and glycerin. The pH was monitored, and held close to 7.5 for the duration of the experiments. When necessary, the pH was lowered using hydrochloric acid.

2.1.2 Components

This section provides detailed descriptions of the individual components of the flow loop, their purpose, and, where appropriate, the way they were manufactured.

Pump

The Moyno 1000 pump shown in Figure 2.2 was a close coupled model B1F CQD SAA, with a cast iron housing, tool steel internals, a chrome plated tool steel rotor (see Figure 2.2), and a nitrile stator. The suction and discharge ports were both 4" ANSI flanges. The rotor was coupled to a 3HP 170 RPM Baldor motor via a 5:1 reducer manufactured by NORD. The cast iron housing was given a custom epoxy coating to resist corrosion courtesy of Valmont Industries. Additional two-part epoxy paint was applied in-house to the tool steel internals. The motor was controlled by a Toshiba Tosvert-130G2+ transistor inverter which was in

turn controlled via an external voltage input. The control voltage source to the inverter was output from a National Instruments BNC-2110 that was controlled by a custom LabView virtual instrument (VI). The helical shaped rotor rotates inside the stator creating sealed cavities that progress the length of the stator and are forced out of the discharge end of the pump. Because of the shape of the cavities, the flow rate is a sinusoidal function of time whose period corresponds to the angular frequency of the pump shaft. Despite this drawback, this pump was chosen over a centrifugal type pump because once the Moyno pump was set to discharge a specified average flow rate, it would do so regardless of the back pressure caused by varying amounts of turbulence in the test section felt at the discharge end. Additionally, the progressing cavities of the Moyno create relatively low shear on the fluid when compared to the rapidly rotating vanes of a centrifugal pump. Immediately after leaving the pump, the fluid was accelerated through a conical contraction which reduced the diameter from 4 inches to 2 inches.

Capacitor

The air-filled capacitor shown in Figure 2.3 was used in combination with a partially-closed 2" ball valve to dampen the unsteady forcing from the Moyno pump. The capacitor was constructed from 6" PVC pipe and consists of a T-junction oriented such that the flow from the pump would impinge on the back wall and be encouraged to compress the air column in the portion of the capacitor which extends upwards 1.25m from the center of the T-junction. Midway up this section, a flexible coupling was installed to allow the capacitor to be disassembled easily for cleaning. Small pipes and tubing were fitted to the top and bottom of the capacitor to allow for pressure measurement, liquid level monitoring, and draining.

The capacitor was tested to evaluate its efficacy in reducing the fluctuating forcing from

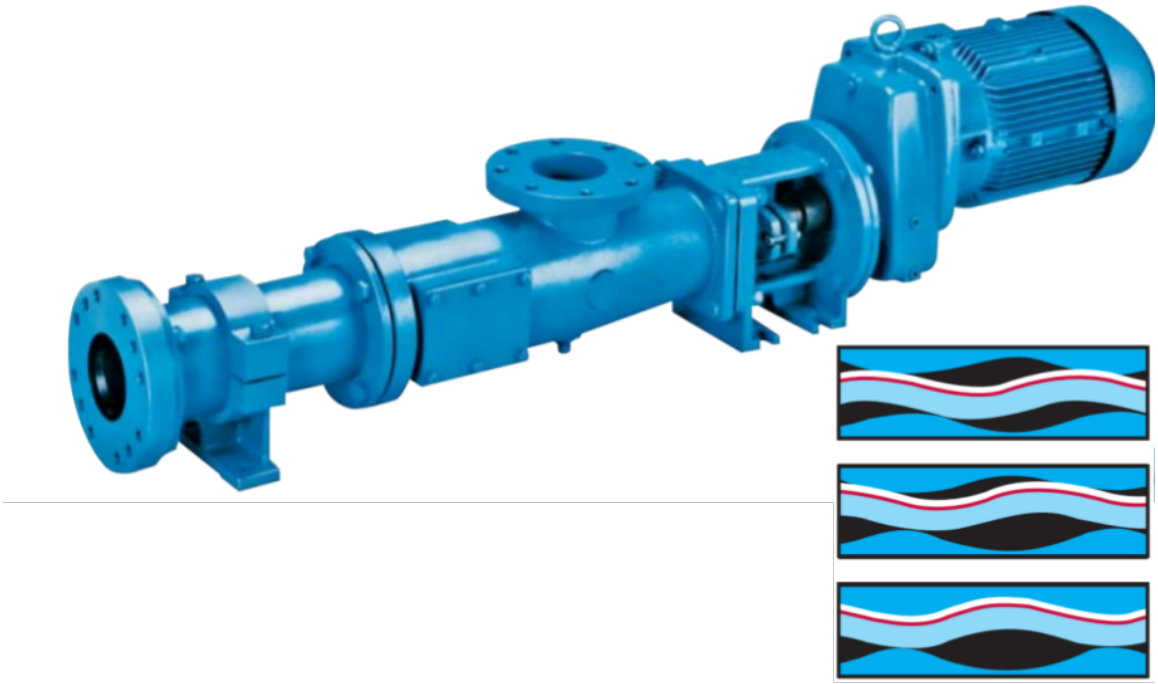

Figure 2.2: The Moyno 1000 series pump used in the facility shown with a schematic of the rotor and stator creating progressing cavities that move fluid through the pump.

the pump. The pump was driven at two different speeds while the liquid level in the capacitor was varied. Figure 2.4 shows the power spectral density of the voltage signal acquired at $1000Hz$ along a $21cm$ section of fully developed flow. The drive frequencies from the Toshiba inverter used to drive the pump were $2.5Hz$ and $4Hz$. This corresponded to rotational frequencies of the pump rotor, f_R of $0.5Hz$ and $0.8Hz$ ($w_b \approx 0.07m/s$ and $0.19m/s$), respectively. Each curve in the sub-figures of Figure 2.4 is shown in its corresponding legend with its inverter frequency and capacitor level as a percentage of full. The red curve in each sub-figure of Figure 2.4 shows the frequency response of the facility when the capacitor is completely full of liquid. The purple dotted curves show the effect of decreasing liquid levels until the blue curve shows the minimum liquid level tested for each speed. The

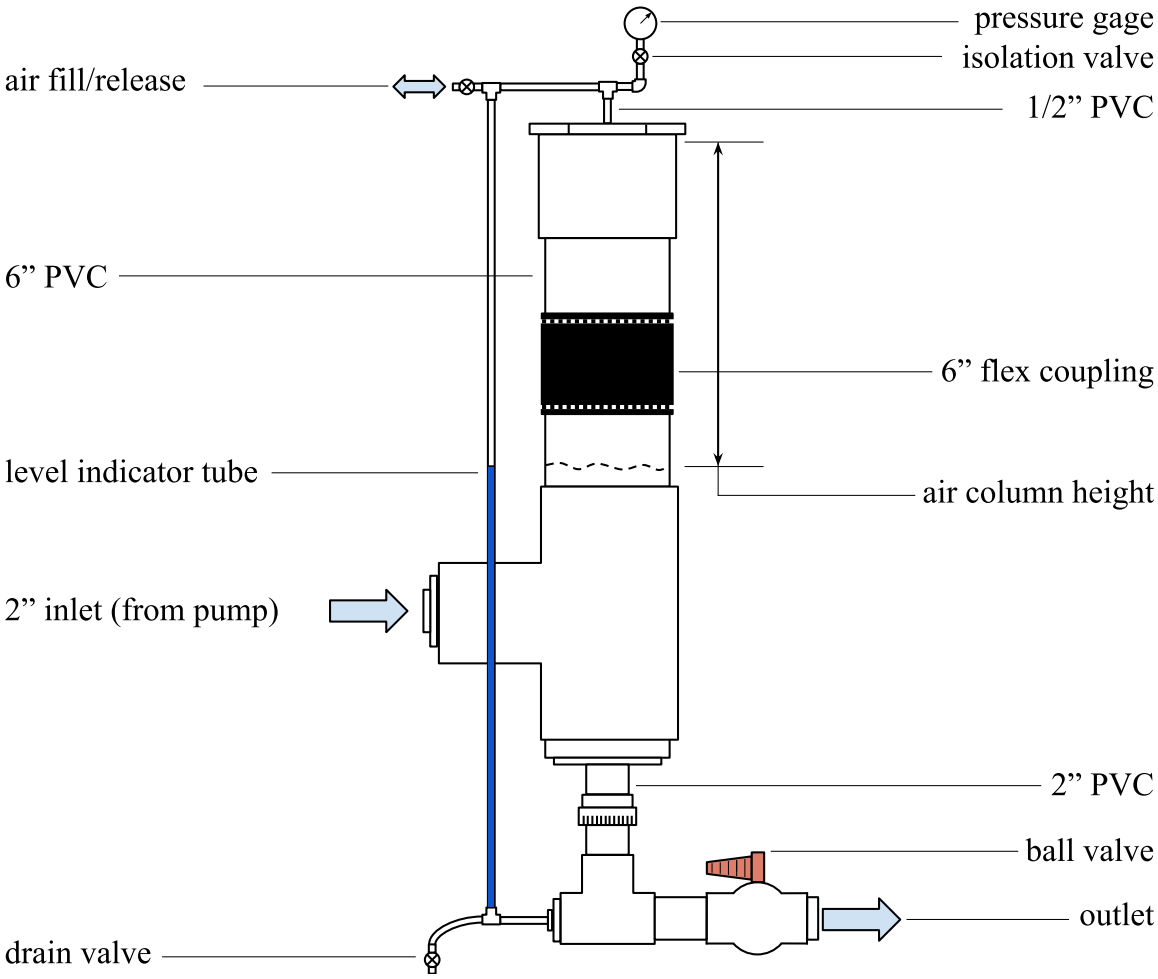

Figure 2.3: The custom-built capacitor-resistor system used to dampen the sinusoidal fluctuations in volume flow rate discharged from the pump.

capacitor level was taken from the top of the T-junction to the top of the 8” pipe section. In each Figure 2.4a and b there is a strong peak at f_R. There are also strong peaks at the harmonics corresponding to multiples of $0.5f_R$. This is due to the sinusoidal geometry of the rotor which discharges two compartments of fluid with each rotation. The amplitudes of the harmonic peaks decrease monotonically with decreasing liquid level. The degree with which the capacitor attenuates the peaks was greater for greater flow rates. While in the case of the $2.5Hz$ driving frequency, the peaks were decreased by an order of magnitude, in the

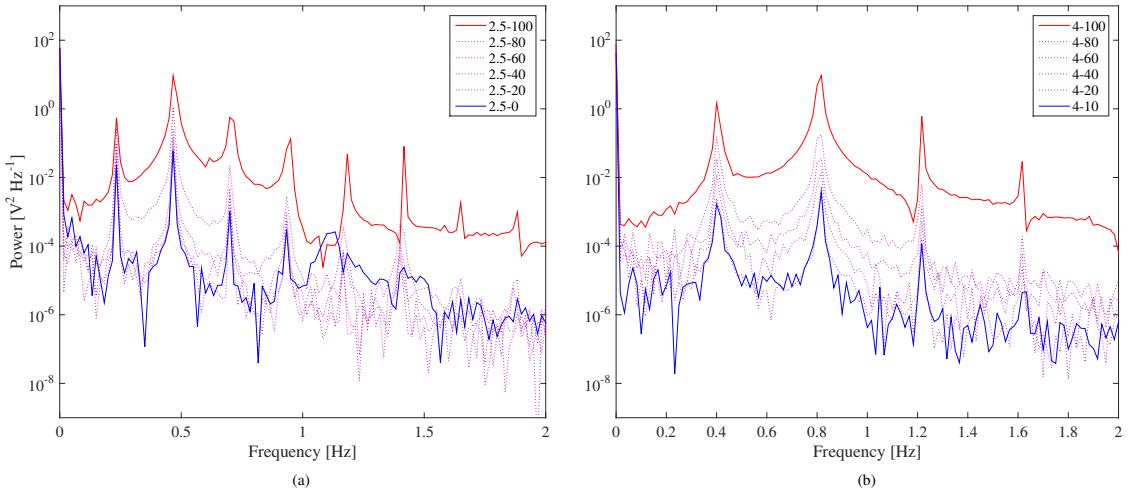

Figure 2.4: The power spectral density of the pressure transducer raw voltage signal with the facility driven at an inverter frequency of (a) $2.5Hz$ ($f_R = 0.5Hz$) and (b) $4Hz$ ($f_R = 0.5Hz$) with the capacitor at various levels. The solid blue and red curves in each sub-figure denote the minimum and maximum fill levels respectively, while the dotted magenta curves are included to show the general behavior of the increasing fluid level.

case of the $4Hz$ driving frequency, the peaks were decreased by more than three orders of magnitude. As a result of these findings, the capacitor liquid level was maintained at $140mm$ above the centerline of the T-junction inlet, the minimum liquid level for all investigations.

Flow conditioning

Immediately downstream of the 2" ball valve, 2" tubing was used to turn the fluid 180 degrees around a turn of radius, $0.75m$. Then the fluid passed through 8 static mixing elements that were 3D printed out of ABS filament. Figure 2.5a shows a 3D view of the model used to print the mixing elements. Each element consisted of two perpendicular sets of three layers of criss-crossing vanes. All of the vanes in each element were oriented at ± 45 degrees to the pipe axis. The mixing elements were sized and manufactured to fit snugly into a clear polycarbonate section whose inner diameter was equal to the glass tubing and

Figure 2.5: The static mixers used to condition the flow shown (a) as an elevation view of the model, and (b) inside the pipe section that holds them.

was attached to the 2" tubing using hose clamps. As they were inserted, each mixer was rotated by 90 degrees to the previous element.

A second piece of polycarbonate tubing with a length of 8D was attached to the section containing the mixing elements via threaded PVC pipe unions that were epoxied to the polycarbonate. This section was used to hold the honeycomb and screen sections for further flow conditioning. Each 6.4mm thick honeycomb section had a blockage ratio of 22.4%. The flow straightener was constructed by aligning 15 honeycomb sections using a 3mm hexagonal rod (Allen wrench) and welding them together around their circumference using SciGrip Weld-On 4^{TM}.

The screen supports shown in Figure 2.7 were laser cut from 6.4mm thick acrylic and had a blockage ratio of 12.9%. Plastic mesh screen with 500μm gaps and a blockage ratio of 62% was sandwiched between the supports using cyanoacrylate glue. Seven 6.4mm thick spacers were placed between the flow straightener and the screen to create a gap of length, $1D$. The spacers were 1.25mm thick rings whose outer diameter matched the inside of the pipe. These too were laser cut from acrylic.

At the most downstream end of the polycarbonate flow conditioning section, three small holes were drilled at evenly spaced azimuthal locations and tapped (8-32) to receive nylon socket head cap screws fitted with silicone washers. The screws were tightened to bear onto the most downstream end of flow conditioning segments until they held were held in place

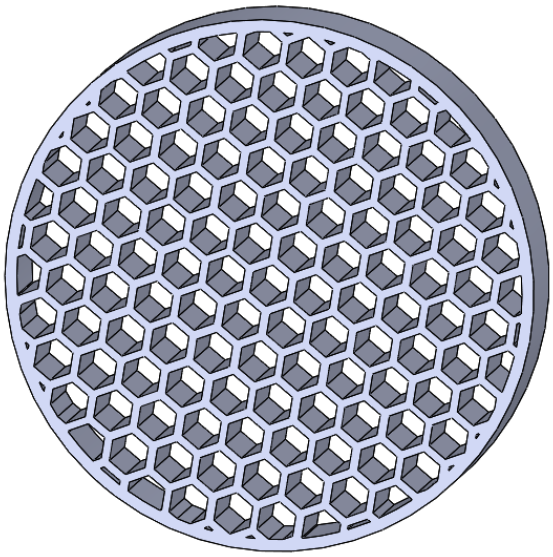

Figure 2.6: An elevation view of the 3D model used to program the laser cutter that manufactured the honeycomb sections from acrylic sheet that were later welded together.

against the flow.

Disturbance mechanism

The disturbance generator ring is shown in Figure 2.8, and was supported by four 5mm posts that friction fit against the inside wall of the test section. The thickness of the ring in the radial direction was 2mm and the thickness in the axial direction was 3mm. The continual disturbance generated by the ring was selected due to its simplicity and similarity to the type of disturbances encountered in industrial flows. The ring was was placed $10D$ from the last flow conditioning element, and was designed to disrupt the flow at similar radial locations to other experiments that used stationary obstructions to trigger transition (e.g. Wygnanski and Champagne 1973). With the ring present, the flow contained intermittent puffs at the target Reynolds number (2100), which was chosen to be in the range where puffs are not likely to split or decay for extremely long times, following Avila et al. (2011).

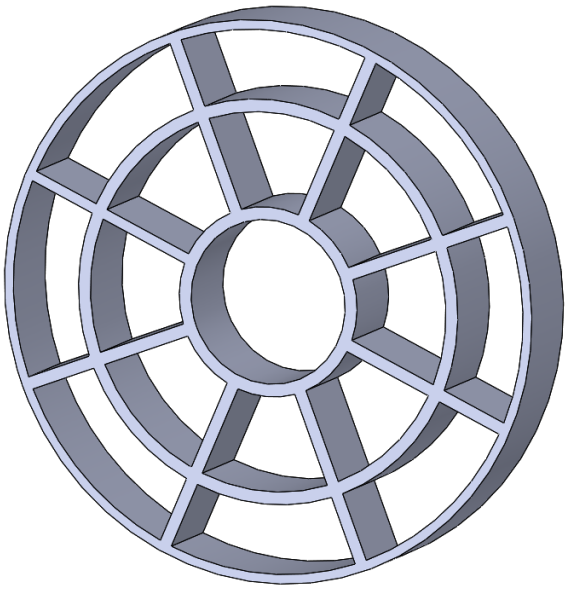

Figure 2.7: An elevation view of the 3D model used to program the laser cutter that manufactured the screen supports from 6.4mm thick acrylic sheet.

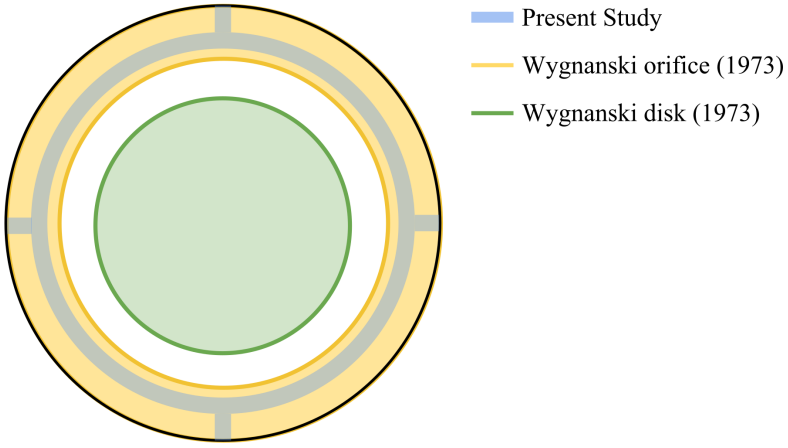

Figure 2.8: The profile of (blue) the disturbance generator used in the present study along with (yellow and green) those used by Wygnanski and Champagne (1973) for reference.

Pipe, couplings, and support structure

The glass tubing used in the test section was Simax standard wall borosilicate tubing with an inner diameter of 44.8mm and 1.6mm wall thickness. Each section was 1.5m long, with flame polished ends to prevent them from cracking. Sections were joined using custom manufactured couplings shown in Figure 2.9. A photograph of a coupling is shown in Figure 2.9a. Two different versions of the custom couplings were constructed. For the couplings where no pressure tap was required (see Figure 2.9b) , acrylic spacers were laser cut to fit snugly between a piece of two inch diameter PVC pipe and the glass test section. Three spacers were used in each side of the union. A thicker spacer, whose inner diameter matched the test section, was placed in between the glass test sections to locate the center of the union and prevent the glass tubes from butting against one another. For couplings that required a pressure tap, the PVC pipe and spacers were replaced by a single piece of PVC that was turned on a lathe from a solid two-inch diameter rod (see Figure 2.9c). After the piece had been turned, a 1/16" drill bit was used to drill a hole radially from the outer surface at a depth of 5mm. Then stainless steel tubing (purple) was epoxied into the hole. Finally a 1/32" drill bit was passed down the stainless tubing and used to drill through the remaining 1mm of PVC creating access to the flow for pressure measurement.

Figure 2.10 shows a photograph of the supports that were constructed to align and secure the test section. Each section rested on two polypropylene vibration damping clamps, marked as 'A'. These clamps were bolted to 1/4" steel upper plates (marked as 'B') that were spaced off a wider bottom plate (marked 'C') using 1/4" threaded rod that allowed for vertical adjustment (marked 'D'). The bottom plate was fastened to Unistrut rails that ran the length of the test section via bolts (marked 'E') that passed through oversized holes in the lower plate that allowed for lateral adjustment perpendicular to the pipe axis. To align the

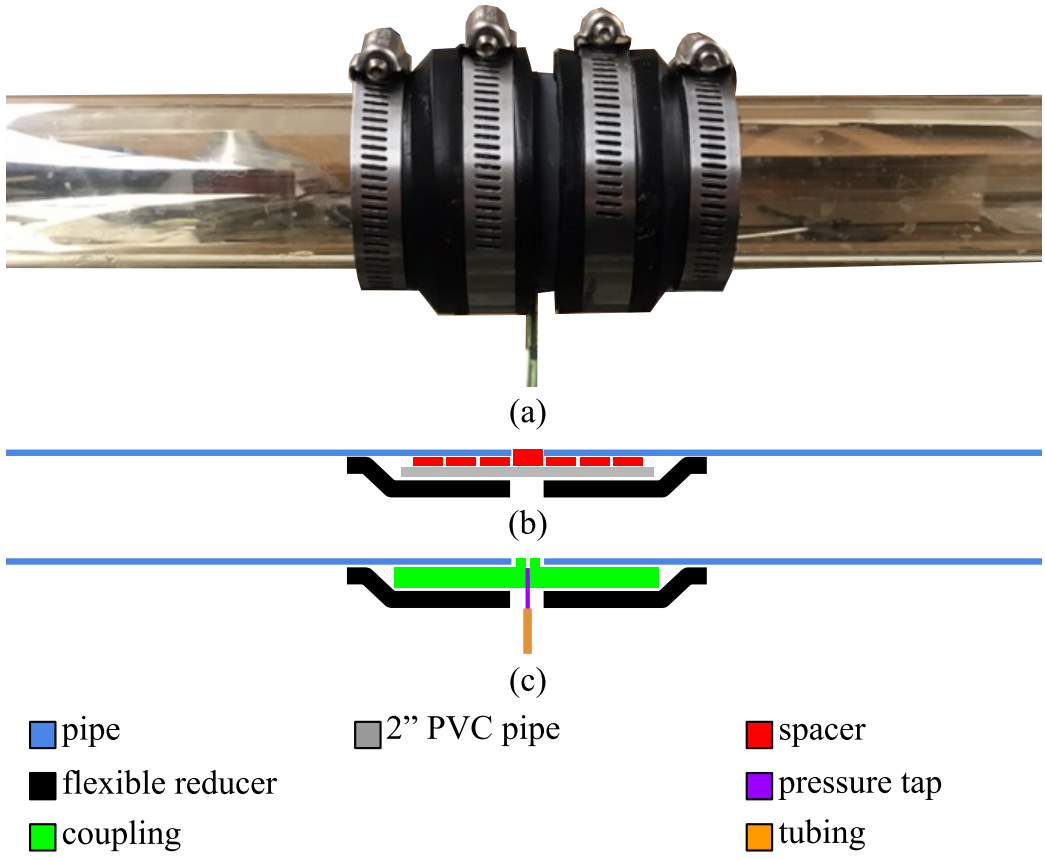

Figure 2.9: The couplings manufactured to join the glass sections are (a) shown as a photograph were made in two versions, (b) a version used simply to join sections, and (c) a version used to allow access to the flow for a pressure tap.

test section, the glass tubes were placed into the clamps and light from a laser level (Stanley SPK) was shone along the desired path centered a few millimeters above the top of the pipe's intended path. The position of each pipe clamp was adjusted using the threaded rods until the glass tubing section was parallel to the laser level and the tops of both ends of the tube was measured to be a consistent distance from the beam. Then the threaded rods and lower plate were locked into place using the nuts and bolts that secure them, respectively.

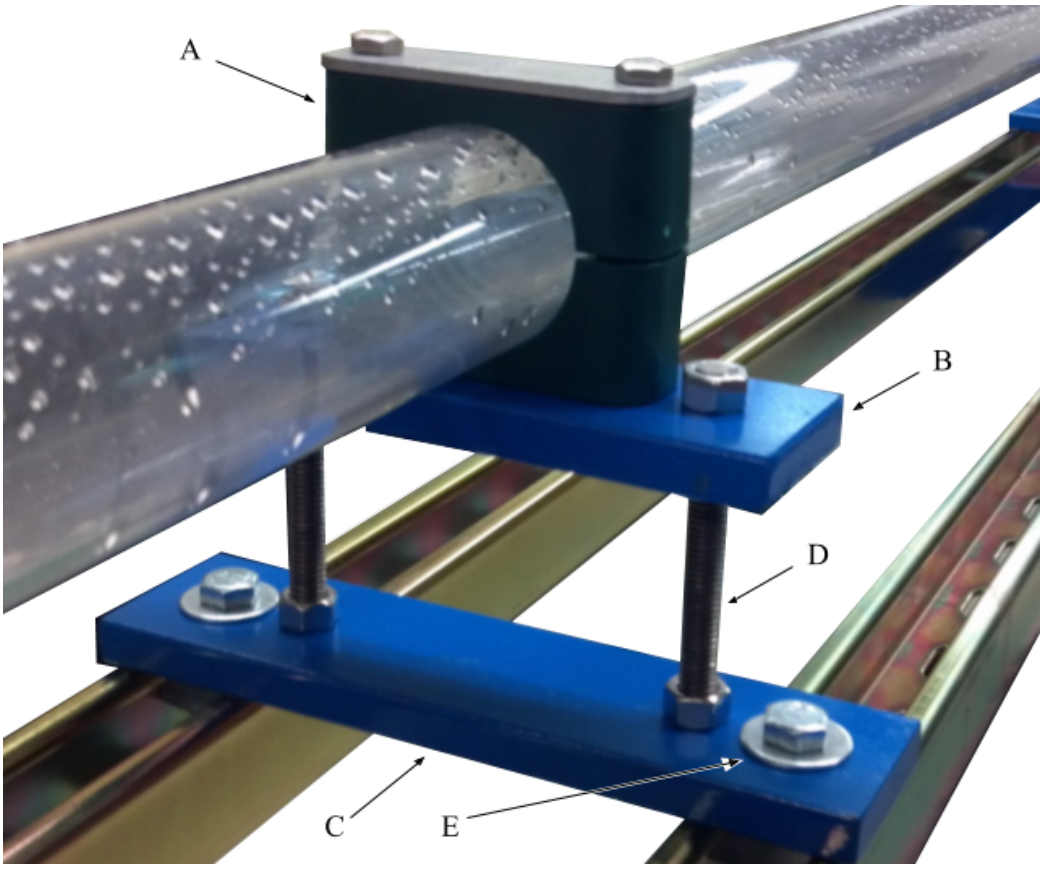

Figure 2.10: A photograph of the pipe supports manufactured to adjust and secure the ends of each pipe section.

Discharge tank

After the fluid exits the test section it enters into a discharge tank with a large volume. The purpose of the tank is to dynamically uncouple the fluid returning to the pump from that in the test section as much as possible, much like the capacitor located upstream if the test section. Figure 2.11 shows an exploded view of the components that make up the tank. To assemble the tank, a hole was drilled into the side of the polypropylene container. This hole allowed for the attachment of the 2-inch bulkhead fitting. A 2-inch adapter was threaded into the bulkhead fitting so that a small section of 2-inch PVC pipe could be welded to the

Figure 2.11: Exploded view of the components used to create a secure connection between the glass tubing and the discharge tank.

adapter. Finally, a flexible reducing coupling was fixed to the pipe section. The test section was passed into the small end of the flexible coupling up to the bulkhead fitting to ensure that the test section discharged into the largest cross-sectional area possible.

2.1.3 Pressure measurements

To sense puffs in the test section as they passed, pressure lines were attached to the custom couplings show in Figure 2.9c at the locations shown as (+) and (-) in Figure 2.1. Figure 2.12 shows the two pressure lines each connecting via a coupling to a three-way valve. One outlet of each three-way valve led through stainless steel pipe to a Validyne DP40-14, while the other outlet led to a bleed line. When both valves were opened to the bleed lines, a syringe was used to withdraw then re-inject fluid through the bleed line in such a way that the air is removed from the three-way valve and pressure line. This allowed for the cumbersome process of bleeding fluid from the transducer itself to be undertaken as infrequently as possible.

The voltage signal from the pressure transducer was low-pass filtered by a signal pro-

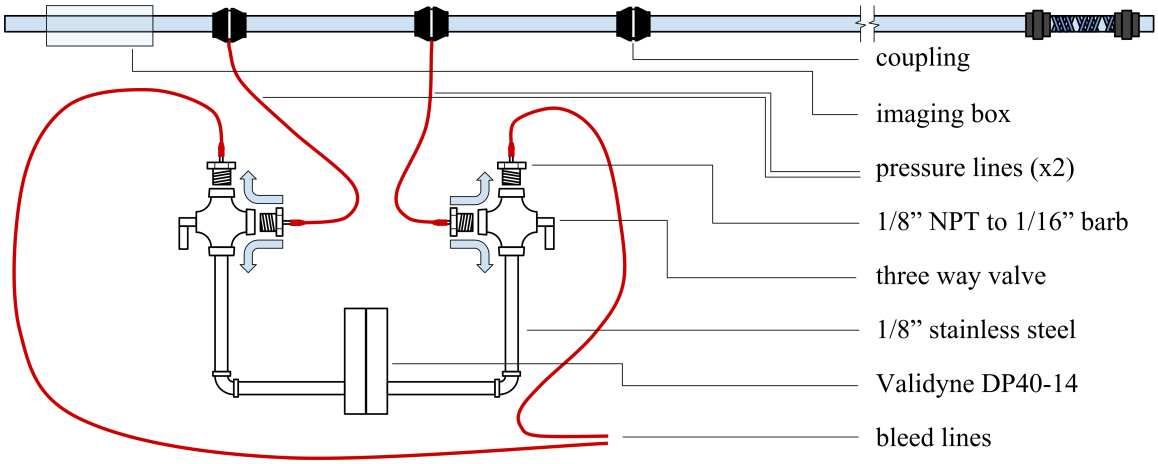

Figure 2.12: A schematic of the plumbing used to connect the pressure taps to the transducer along with the valves used to bleed the lines when necessary.

cessing box with cut off frequency set to $5Hz$ before being recorded by the custom LabView VI at $10Hz$. Two configurations of the VI were developed. The first, “Visual Monitoring Station Long Records w control and vision.vi” captured long voltage records from the pressure transducer of arbitrary length at a fixed frequency. The second, “Visual Monitoring Station Triggering w control.vi”, continuously monitored the voltage in order to trigger the SPIV system downstream to capture puffs for analysis. The two different configurations were developed because the interruption of the signal acquisition to check the triggering conditions in the second VI resulted in slightly uneven temporal sampling of the voltage.

2.1.4 Temperature measurements

The temperature was monitored in the facility using an Omega 100Ω, Class A, sealed RTD (model HSRTD-3-100-A-80-E). The sensor’s tolerance can be calculated as,

$$\sigma_T = 0.15 + 0.002T. \tag{2.1}$$

At a nominal temperature, $T = 20^{\circ}C$, $\sigma_T = 0.19^{\circ}C$. The temperature was monitored for drift during the duration of data acquisition sessions to ensure a constant Reynolds number.

2.1.5 Reynolds number calculation

In order to calculate the Reynolds number of the investigations, the density and viscosity were calculated using measurements of temperature and refractive index, and the bulk velocity was calculated using the known pipe diameter, and measurements of weight and time.

The density and viscosity of the water-glycerin mixture was a function of the mass fraction of the constituent liquids and the mixture temperature. To measure the mass fraction, pump was turned on to a flow rate close to the desired Reynolds number. After at least 30 minutes, the temperature measurement was recorded along with a measurement of the index of refraction taken from a manual refractometer whose scale is marked in Brix. When converted to index of refraction, the scale resolution of the refractometer corresponds to 0.0004. A Matlab function, IndexTemp2Visc() was written in order to bilinearly interpolate the mass fraction for each of the constituent liquids from tabulated data of mass fraction and index of refraction at $20^{\circ}C$ (Hoyt, 1934), and $30^{\circ}C$ (Koohyar et al., 2012). With the mass fraction and temperature as inputs, a second Matlab function, GlycerolMixCalc() was written in order to implement the empirical equations obtained by Cheng (2008).

In order to calibrate the volumetric flow rate, the output from the pump at various inverter frequencies, was collected into a bucket for a measured time (stopwatch), and weighed on a scale whose resolution was 0.1lbs. The temperature and index of refraction were then used to calculate the density. From the density and weight a volume was calculated that together with the time, yielded a flow rate. The computed flow rates, Q, are shown against

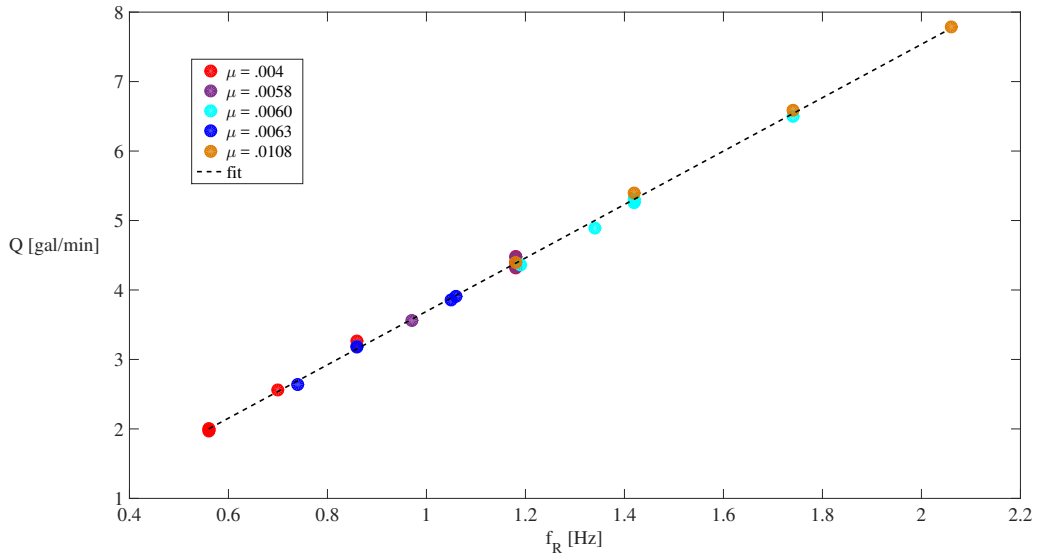

Figure 2.13: A plot of the calibration data taken from the flow rate test. The dashed line represents the linear best fit to the data.

f_R in Figure 2.13. To test that Q was insensitive to the pump head, a set of five total viscosity values were tested whose range was inclusive of those used in all investigations. The dashed line in Figure 2.13 represents a best fit line used to calculate Q from f_R. The error in Q based off of the fit error was estimated to be less than one percent for the flow rates used in all investigations. The bulk velocity, w_b was calculated from Q using the cross-sectional area of the pipe.

The Reynolds number for each investigation was calculated from the parameters described in this section, and the associated uncertainty was calculated using local gradients and the uncertainty in each parameter. The estimated uncertainty corresponding to $Re = 2100$ was ± 30.

2.2 Facility used for droplet-laden flow measurements

The investigation of droplet-laden flows was conducted in an earlier version of the facility. In that version, the pipe sections were of the same diameter as the glass, but were made from polycarbonate, and custom couplings were epoxied on to the section ends in order to mate them together. The polycarbonate allowed for pressure taps to be drilled at any location. In this version the pressure taps spanned a $13D$ length whose downstream end was $120D$ from the final flow conditioning element. There was no disturbance generator ring installed. Additionally, the through-wall fitting in the discharge tank had not been installed and the test section was fitted with a 3D printed conical nozzle that discharged a jet onto the free surface of the discharge tank. The fluid in the facility was a 43.2% by volume mixture of glycerin in water. This was necessary to match the index of refraction of the droplet phase which was of Dow Corning 200 5cSt silicone oil. In this case, ϕ was measured to be 0.038, and d_p was measured to be $10\mu m$. The droplet size was determined by removing a sample of fluid from the flow, adding water to reduce the refractive index of the water-glycerin solution, and then adding many PIV seed particles of known diameter. The resulting liquid was photographed under 40X magnification under a microscope. The known particle diameter mean was used to compute a magnification factor for the images, from which, each droplet could be sized in real space and a mean diameter could be computed. The droplets ranged in size from $d_p = 7 - 15\mu m$. From the sample taken, the standard error of the mean of the particle diameter as measured in pixels was estimated to be 3%. This propagates to an error estimate in the magnification factor, which ultimately combines with the error in the estimate of the mean of the particle diameters in pixels to yield an error estimate of 5% in the mean droplet diameter.

2.3 Particle image velocimetry

Both SPIV and PPIV measurements were used in the present work (see Figure 2.1). In general, these measurement systems consist of the following components; a light source, optics, camera(s), and particles. The light source and optics are used to create a light sheet that illuminates passing particles that are imaged twice by the camera(s) over a fixed time period, dt. The particle images are then processed into two dimensional, two component, vector fields by cross correlating sub-regions of the two particle images. In the case of SPIV, two cameras capture images of the same light sheet along different lines-of-sight (LOS). The two resulting vector fields computed from from each camera are then reconstructed to obtain a two dimensional vector field where each vector has three components, with the third component being normal to the light sheet.

SPIV measurements were taken in the single-phase flow in order to analyze the flow immediately downstream of the disturbance generator ring, as well as the flow inside passing puffs registered by the pressure measurements. PPIV measurements were taken in the single-phase flow of passing puffs in two configurations that correspond to different fields of view (FOV). Puffs in the droplet-laden case were measured using PPIV as well. In all of the PPIV configurations, the light sheet illuminates the (r,z) plane. In the single-phase case, one of the two FOV maximizes the number of vectors on the r-direction, while the second captures a longer distance in the z-direction at a reduced resolution in the r-direction.

2.3.1 Viewing Box

Conducting PIV measurements of pipe flow requires a viewing box to minimize the distortions created by the curved pipe wall. This was achieved by filling the box with the same fluid as the pipe. The viewing box constructed for the present work was built from laser

cut acrylic segments that were welded together to create recessed pockets for 7 borosilicate glass windows. The box has a glass window on the bottom through which the laser sheet was shone into the flow, and six viewing windows that allow a camera to view the flow at $\pm 60^\circ$, $\pm 45^\circ$, and $\pm 90^\circ$ from the pipe axis. Figure 2.14 shows a model of the box assembly which was constructed from 10 unique parts. First a bottom plate (1), consisting of an outline of the box and a rectangular hole for the bottom window, was cut to act as a base for assembly. Next, a locating plate (2) was welded to the base. This plate had a larger rectangular hole in order to create a recess for the bottom window, as well as cutouts to locate the rest of the parts necessary to build the walls. Eight towers were built by welding repeating stacks of four unique (3-6) corner bracket pieces. Together with the locating plate, these towers create a slot where glass panes can be inserted and sealed with silicone. Then, inner and outer end plates were welded together to create two end walls (7) through which the test section was inserted. The inner and outer plates were identical except that the outer plate had a larger hole. The larger hole created a groove for an o-ring. The end walls had through holes to receive bolts from the seal caps (8), which consisted of a plate similar to the inner plate of the end wall, and a ring which fit into the o-ring groove. When bolted together, the seal cap and end wall compressed an o-ring that sealed the wall to the pipe section, keeping the fluid inside the box.

2.3.2 Single-phase stereo PIV

SPIV measurements were taken $10D$ and $180D$ downstream of the disturbance generator ring. These measurements were conducted at $Re = 2100$. Figure 2.15 shows a rendering of the SPIV measurement systems, with the laboratory coordinate system, which was chosen such that the z-axis was coincident with the cylindrical coordinates of the pipe. The x-axis

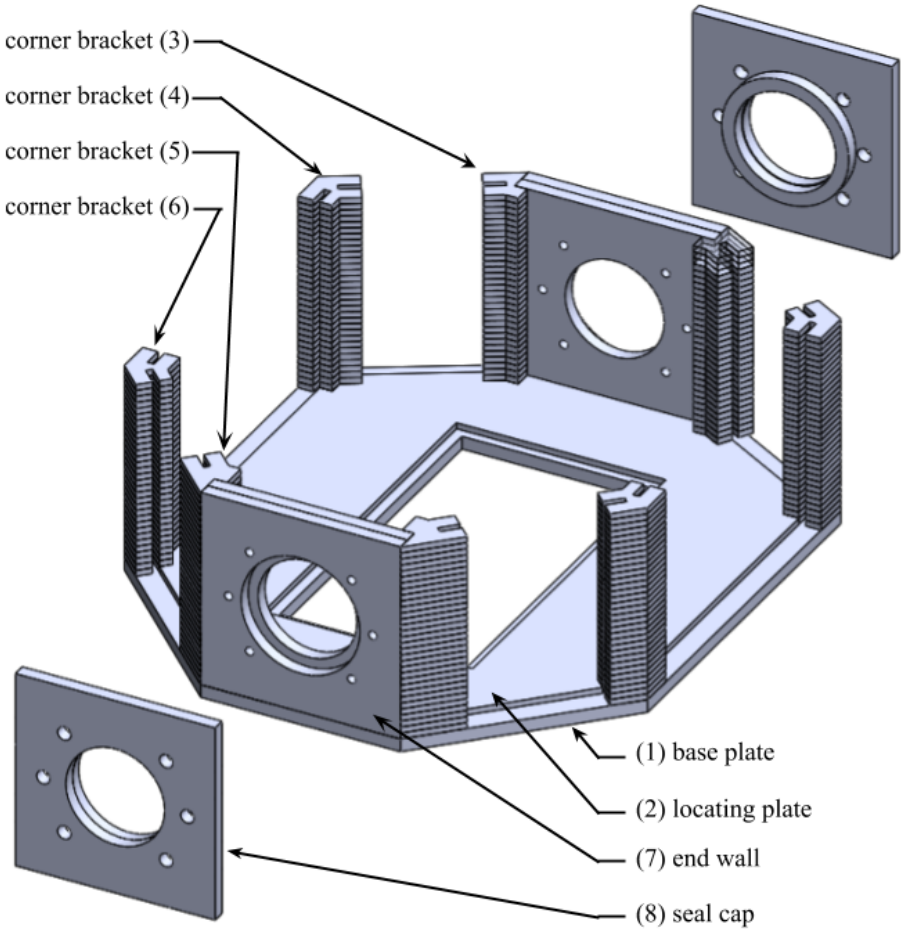

Figure 2.14: A model of the viewing box

was chosen to correspond with the line where $\theta = 0$.

The cameras were mounted at $\alpha = \pm 30°$ from the pipe axis in the (x,z) plane. Scheimpflug adapters were used to rotate the plane-of-focus of the camera lenses to be co-planar with the light sheet. The cameras' lines-of-sight were oriented perpendicular to the facets of the box angled at $\pm 120°$.

In order to calibrate the system, a circular calibration plate was 3D printed, mounted on a rod, and inserted into the test section to be imaged. The calibration plate, shown in Figure 2.16, had alternating rows of 1mm-spaced steps in the z-direction. Each row was populated

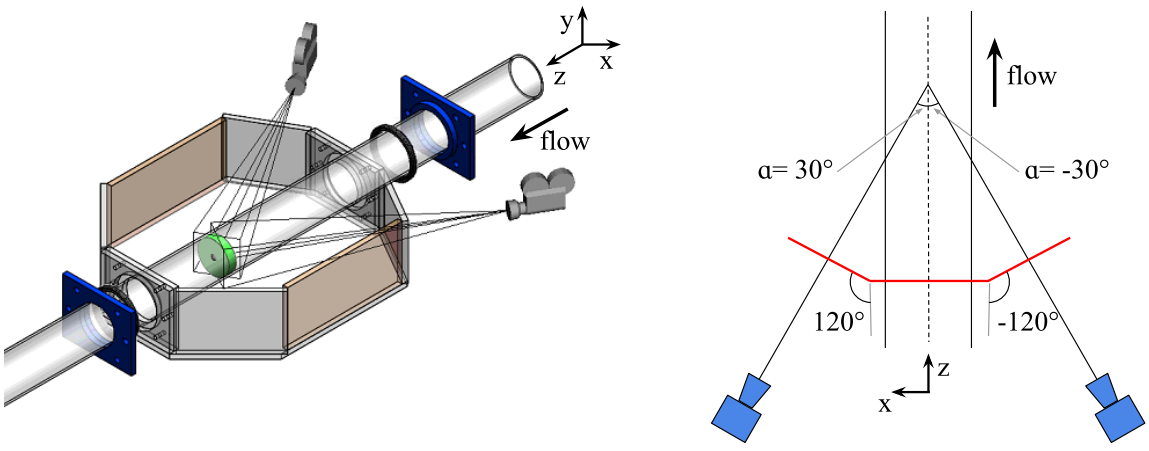

Figure 2.15: The general set up of the SPIV systems used both upstream and downstream. (a) The cameras focus through a fluid-filled visualization box with facets that are perpendicular to the line of sight of each camera. (b) Lines of sight for the cameras are oriented 30° from the pipe axis facing downstream and focus through a fluid-filled visualization box (red) with facets that are perpendicular to the line of sight of each camera.

by 1mm dots spaced 4mm apart.

The upstream SPIV system used to interrogate the inlet flow included a New Wave Solo II dual head 15Hz Nd:YAG laser to create a laser sheet that illuminated a circular cross section of pipe of 1mm thickness. To achieve the desired sheet, the laser light was focused through two spherical lenses and one cylindrical lens. The sheet was checked to ensure that the thickness was similar throughout the illuminated cross-section. The laser issued dual pulses to illuminate silver-coated hollow glass spheres (Potters Industries LLC Conduct-O-Fil SH400S20) that were dispersed into the flow. The particles had a diameter of $13\mu m$ on average and a density of $1.6g/cm^3$. Two PowerView Plus 4MP cameras fitted with Nikon 105mm lenses photographed the illuminated area in each pulse of the laser. The camera and lasers were triggered by a TSI synchronizer box. The entire acquisition was controlled by a PC running Insight 3G software. One thousand image pairs were acquired at a time

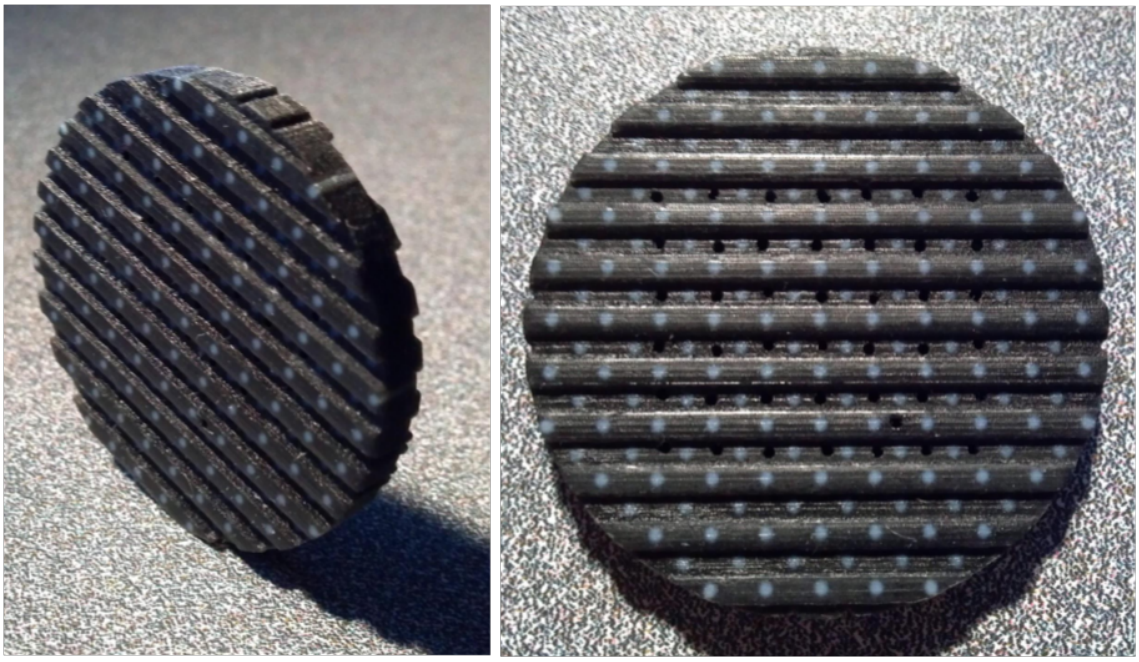

Figure 2.16: Photos of the 3D printed calibration plate

spacing between images, dt, of $0.5ms$. The spacing between the resulting vector fields, dT, was set at 2 seconds to ensure statistical independence between fields.

The downstream SPIV system to measure the flow inside puffs used a Photonics Industries DM-30 laser for illumination whose beam was focused using the same optics as in the upstream SPIV system. Two 1MP Photron Ultima APX cameras fitted with Nikon 105mm lenses were used to record images. The system was triggered by monitoring the voltage signal from the pressure transducer. The voltage from the transducer would spike when a puff entered the section monitored by the taps. The downstream SPIV was triggered from LabView by outputting a 5V signal from the BNC 2110 to the triggering input on a LaVision high-speed PIV controller. The trigger was set to begin recording two seconds ($z^* = 16.5$) after the voltage reached its peak. Image pairs were acquired with a time spacing, dt, of $500\mu s$ between images. For each puff record, 2048 image pairs were captured

for each camera, resulting in 1024 stereo vector fields. A total of 55 image sequences were captured. In 14 of the sequences, dT was $500\mu s$. As this value was found to be more than sufficient for reconstruction purposes, dT was increased to $3.33ms$ in the remaining 41 sequences to capture longer records. This was accomplished with more complex acquisition process that allowed dt to be a different value than dT.

For the case where $dt = dT$, the cameras and the laser operate at a steady frequency of $2000Hz$. For the case where $dT > dt$, the DM30 laser was set to 'dual pulse mode' with the time between dual pulses set as $500\mu s$. Because the frequency of the high-speed controller mandated that the laser repetition frequency and the frame rate of the cameras match, the controller was set to a frequency of dT^{-1}. However, this yielded the scenario shown in Figure 2.17a where the red timing pulse to the laser from the controller created a scenario such that images from frame 2 onward received two laser pulses. In order to remove the second set of laser pulses, the signal was interrupted between the high-speed controller and the laser using a BNC 500D frequency generator. The BNC 500D divided the signal so that only every other red pulse is allowed to pass through to the laser and trigger its dual pulses as shown in Figure2.17b. Once the output signal from the BNC 500D is passed to the laser, the desired timing is achieved as shown in Figure 2.17c, where each frame receives one laser pulse that is separated by the desired dt, and the desired value of dT separates the resulting vector fields.

SPIV data processing

The double-frame perspective particle images from each camera were processed into a single 2-dimensional 3-component vector field using DaVis 8.1. The images were preprocessed using an inversion filter and background subtraction. A pinhole calibration method was used to reconstruct the two 2D vector fields into a 3D stereo field. The final interroga-

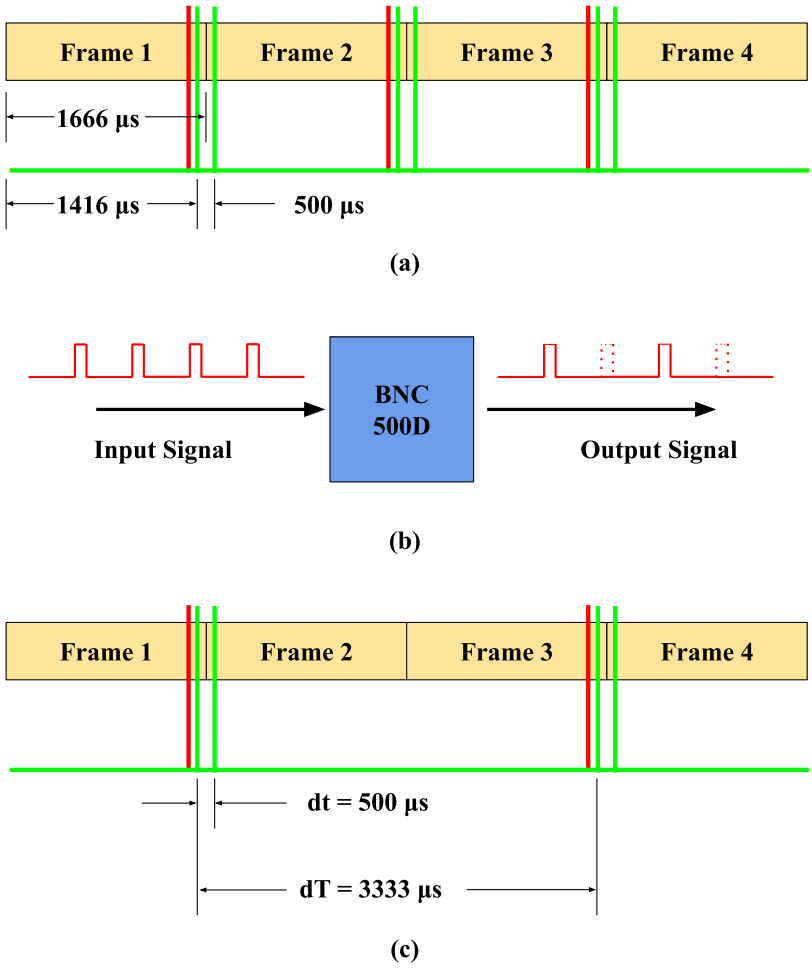

Figure 2.17: (a) The raw timing diagram for the puff measurements where $dt \neq dT$. The timing pulses (red) from the high-speed controller triggered dual laser pulses (green) that straddle image frames (yellow) (b) Using the 'Divide/N' frequency divider output on a BNC 500D frequency generator every other triggering pulse is removed (dashed) (c) With the modified triggering signal, each image frame contains only one laser pulse and the desired values of dt and dT are accomplished.

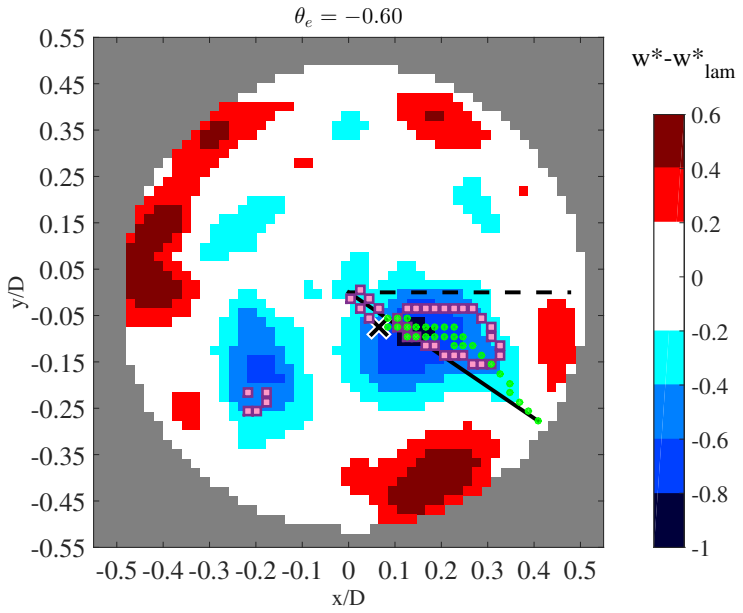

Figure 2.18: The trailing edge for puff number 9. The local minimum in $w^* - w^*_{lam}$ where $r^* < 0.1$ is located with the black 'X'. The green dots show the path from the local minimum to the wall. The ejection angle, θ_e is included between the solid black line and the dotted line at the x-axis. The region bounded by the purple squares indicates $u^*_r < -0.15$.

tion spot size was 32px x 32px with a 50% overlap. The resulting in-plane vector spacing was $0.009D$ in the case of the inlet. The in-plane vector spacing for the puff records was 0.022D and 0.021D for the high and low frequency data sets, respectively. A 3x3 median test was applied to remove spurious vectors, and in the case of the puff record data, replace them with an interpolated value (Westerweel and Scarano, 2005). Finally, a 3x3 denoising filter was applied in DaVis 8.1 to improve the quality of the gradient calculations. The average out-of-plane particle displacement in the processed vector fields was 5.1px in the case of the inlet data and 3.2px in the case of the puff data.

The upstream set of instantaneous vector fields was processed to obtain the mean and rms streamwise velocity, $\overline{w^*}(r^*, \theta)$ and $w^*_{rms}(r^*, \theta)$, where * denotes normalization by the bulk fluid velocity. The resulting values were binned into 20 rings of thickness, dr. The

values for dr were chosen such that the number of vectors in each bin was relatively constant. Finally, the average in each bin was computed to arrive at $\overline{w^*}(r^*)$ and $w^*_{rms}(r^*)$.

Registering puffs axially and azimuthally

In previous literature, various methods were employed to identify and track the z^* location of the trailing edge. These included using profiles of filtered velocity components at the centerline (Willis and Kerswell 2008, Wygnanski and Champagne 1973), the expected value of the distribution of q (Kuik 2011), and fitting a saw-tooth wave to w_{CL} (Shimizu and Kida 2009). None of these methods considered the azimuthal orientation of the data.

Here, we present a new method for ensemble averaging the recorded puff data that considers both the axial and azimuthal coordinates by attempting to locate a strong wall-normal fluid ejection associated with the sudden decrease in axial velocity that occurs at the trailing edge. Locating a strong ejection allows each puff trailing edge measurement to be assigned both an axial location and azimuthal orientation by which puff records can be aligned for averaging.

First the vector fields in each puff record were indexed with $n = 1 - 1024$ where $n = 1$ represents the earliest time in the sequence. A single cross-section that marks the upstream edge of the ejection structure is identified (via a method described later in Section 2.3.2) and designated as n_0. Next, using Taylor s hypothesis, each vector field index was converted into a normalized axial coordinate z^* for each record:

$$z^* = \frac{(n_0 - n)(w_b dT)}{D}. \tag{2.2}$$

In this form, the trailing edge, z^*_0 is located at $z^* = 0$.

In order to develop a method for determining z^*_0, ejections near the trailing edge were analyzed in some detail. Typically, they were associated with coherent wedge-shaped zones

of 25° with $u_r^* < -0.15$ extending from the wall to $r^* = 0.3$. The resulting ratio of the area of these wedges with the cross section, A_e, was approximately 0.026. Generally, A_e, increased rapidly downstream to a local maximum and began to show large oscillations relative to the maximum. For this reason, the most upstream location where $A_e = 0.026$ was selected as the z_0^* location. The z_0^* location was found to vary smoothly with changes in the choice of the threshold value of A_e, moving downstream monotonically with increasing A_e and moving upstream monotonically with decreasing A_e. The trailing edge was found to move by less than $0.25D$ with relative changes in A_e of +/- 20%. Similarly, decreasing the magnitude of the u_r^* threshold value shifted z_0^* upstream and increasing it moved z_0^* upstream on average. Relative changes in the u_r^* threshold of +/- 7% corresponded to an average change in z_0^* of less than 0.25D.

Once the z_0^* location was determined, the instantaneous w^* field at z_0^* was analyzed to determine an orientation angle corresponding with the ejection, θ_e. Figure 2.18, which will guide the discussion of how θ_e was calculated, shows a plot of $w^* - w_{lam}^*$ at z_0^*, where w_{lam}^* is the normalized laminar velocity field. First, the location of the local minimum in w^* within the range, $r^* < 0.1$, was found (black 'X'). A path (red circles) was traced from the local minimum to the wall by stepping recursively to the neighboring point with the minimum value of w whose r^* value is larger than the current point. A radial line (black solid) was fit from the center of the pipe to the location on the wall where the path terminated. Finally, θ_e, was calculated to be the angle between the fit line and the x-axis. The azimuthal coordinate for each vector field in that puff was transformed to θ^* coordinates according to,

$$\theta^* = \theta - \theta_e \tag{2.3}$$

Consequently, in the following results, x^* and y^* are defined such that the x^*-axis corresponds to the line at which $\theta^* = 0$. As in the example case, the line associated with θ_e

typically bisects a teardrop shaped slow moving region centered between two fast moving regions located closer to the wall in nearly all puff records.

Because the mean velocity was adjusted slightly to maintain a constant Reynolds number, and because 14 of the of puff records had a much smaller dT, all records were interpolated in z* to a common spacing of 0.029D to allow for ensemble averaging. Similarly, because the exact coordinates of vector locations in the 2D cross section do not match perfectly, the vector fields were interpolated onto a common (r^*, θ^*) plane with a spacing of 0.021D, which matched the in-plane spacing of the data sets to within $\pm$5%. An ensemble averaged puff record was calculated based on the (z^*, r^*, θ^*) coordinate system, resulting in reconstructed fields, $\langle w^* \rangle$, $\langle u_r^* \rangle$, $\langle u_\theta^* \rangle$.

To examine azimuthal variations within the puff records, the mode identification method used by Willis and Kerswell (2008) was followed. For a given puff record, at each z^*, w^* was extracted along a circle at $r^* = 0.4$, and plugged into an auto-correlation in θ^*:

$$C(\theta^*, z^*) = \left. \frac{2\{w'(\theta^* + \phi, z^*)w'(\phi, z^*)\}_\phi}{max[(\langle w' \rangle)^2]} \right|_{r^*=0.4} \tag{2.4}$$

where w' is

$$w' = w^* - \langle\langle w^* \rangle\rangle_{\theta^*},$$

and the double bracketed quantity is averaged over both the azimuthal angle and the ensemble. Additionally, $\{.\}_\phi$ denotes an average with respect to the shift angle, ϕ. Then, m-fold modal symmetry was identified by placing a threshold on the quantity,

$$C_m(z*) = 2\left\langle C(\theta^*, z^*)cos(m\theta^*) \right\rangle_\theta \tag{2.5}$$

that corresponded well with structures observed visually in cross-section plots of w'. The threshold of 0.1 chosen by Willis and Kerswell (2008), was also used in this study.

2.3.3 Single-phase planar PIV

The PPIV conducted on passing puffs used the same components as those used in the SPIV of puffs described in Section 2.3.2. In this configuration however, the cylindrical lens was rotated by 90° in order to illuminate the desired (z,r) plane, and the LOS of the single camera was placed perpendicular to the pipe axis and focused through one of the 90° facets on the viewing box. The dt used for the all of the PPIV measurements of puffs was $1.33ms$.

The large-FOV, was achieved by moving the camera farther from the pipe, and measured an area roughly $3Dx1D$ for a total of 28 puffs. In the large FOV images $1px < d_{PIV} < 3px$. The vector fields for the large-FOV were computed using a final interrogation spot size of $24pxx24px$ (3.8mm x 3.8mm) with a 75% overlap. On average, each interrogation spot had more than 10 particles. The largest displacements in the large FOV vector fields was approximately 7 pixels, while the average displacement was approximately 4 pixels. Finally, the average peak ratio, Q_{peak} was 2.85.

The small-FOV, measured an area roughly $1Dx1D$ for a total of 31 puffs. In the small-FOV images $2px < d_{PIV} < 4px$. The vector fields for the large-FOV were computed using a final interrogation spot size of $24pxx24px$ (1.3mm x 1.3mm) with a 75% overlap. On average, each interrogation spot had more than 10 particles. The largest displacements in the small-FOV vector fields was approximately 13 pixels, while the average displacement was approximately 9 pixels. The average value of Q_{peak} was 3.0.

2.3.4 Droplet-laden planar PIV

For 14 puffs, the FOV in the droplet-laden case captured an area roughly $1Dx1.5D$. The dT used in the droplet-laden case was $1.67ms$, while $2px < d_{PIV} < 4px$. The final interrogation spot size used for the data was $16pxx16px$ (0.9mm x 0.9mm) with a 50% overlap. On

average, each interrogation spot had more than 5-7 particles. The largest displacements in the large FOV vector fields was approximately 13 pixels, while the average displacement was approximately 9 pixels. The average value of Q was 2.75.

2.3.5 Data Collection Procedure

The data collection procedures for acquiring long voltage records that characterized puff frequency at a given Reynolds number and triggering the PIV measurements are described in detail in Appendix A.

2.4 PIV Uncertainty

The uncertainty in the PPIV measurements was dominated by the uncertainty in the peak fitting of the 2D cross-correlation algorithm. Following Westerweel et al. (1996), the uncertainty due to peak fitting in each of the 2D correlations, δ, was estimated to be $0.1px$. Projecting to the object plane dividing by dt, whose uncertainty was assumed to be negligible, the error in the single-phase flow PPIV fields were calculated to be $0.029w_b$ and $0.01w_b$ for the large and small FOV, respectively. The error in the droplet-laden PIV measurements was calculated to be $0.011w_b$.

In the case of the SPIV measurements, uncertainty in the instantaneous vector fields comes from a number of sources. First, as in the PPIV measurements, there was the uncertainty of the cross-correlation vector that comes from the 2D peak fitting. Then, there was the propagation of the 2D peak fitting uncertainty onto the generalized 3D space, and the uncertainty in the calibration equations that map the camera pixel space to real space. The SPIV measurements of passing puffs also included an uncertainty that resulted from the correction of a bias in the calibration that was revealed in the ensemble data. This cor-

rection was a parametric fit that corrects for a portion of the real w being calculated as u_r. The correction enforced the known physical impermeability of the pipe wall.

The uncertainty of the perspective images was propagated to the 2D3C field by considering a general 3D vector [DX,DY,DZ] in the lab system $[X, Y, Z]$ that was projected onto two perspective planes, each perpendicular to one camera's LOS, $[x_1, y_1]$ and $[x_2, y_2]$. This yielded a system of equations through which the two 2D uncertainties was propagated in order to estimate the uncertainty in the 3D vector.

Assuming a constant magnification throughout the field, the y-direction displacements projected directly onto the two perspective planes without a change in magnitude.

$$dy_1 = DY$$

$$dy_2 = DY$$

The x-direction and z-direction displacements projected according to the following equations:

$$dx_1 = DXcos(\alpha) - DZsin(\alpha)$$

$$dx_2 = DXcos(\alpha) + DZsin(\alpha),$$

where α, the angle between the pipe axis and the LOS of the given camera, was equal to $\pm\pi/6$, respectively. Rearranging to solve for the 3D vector components and assuming DY was the arithmetic mean of the two perspective displacements,

$$DX = \frac{dx_1 + dx_2}{2cos(\alpha)}$$

$$DZ = \frac{dx_2 - dx_1}{2sin(\alpha)}$$

$$DY = \frac{dy_1 + dy_2}{2}$$

Applying each of these equations to the general uncertainty equation and assuming $\delta x_1 = \delta x_2 = \delta y_1 = \sigma y_2 = 0.1px$ resulted in an expression for the instantaneous uncertainty due to peak fitting in the 3D displacement vector.

$$\delta_X = \sqrt{\frac{2}{3}}\delta_x$$

$$\delta_Z = \sqrt{2}\delta_x$$

$$\delta_Y = \frac{\sqrt{2}}{2}\delta_x$$

The resulting uncertainty in the velocity due to peak fitting are estimated to be 2.6%, 2.1%, and 4.4% of w_b in the x, y, and z directions, respectively.

The uncertainty associated with the calibration was inferred from the root mean squared error of the calibration fit, which was computed internally in the Davis software. This 2D error, δ_c, which was a similar value of 0.12px in both cameras was propagated through the same set of stereo equations as the peak fitting error to obtain an estimated instantaneous uncertainty due to the calibration of 3.1%, 2.7%, and 5.4% of w_b in the x, y, and z directions, respectively.

However, after a converged calibration, a clear positive bias existed in the radial velocity in the laminar flow upstream of the puffs. Further, since the magnitudes of u_θ were calculated to be very small in the laminar region, it was reasonable to conclude that this induced u_r was due to u_w being misregistered into the r-direction. The induced velocity was modeled using the following equation:

$$u^*_{r,bias}(r^*) = x^* w^* tan(\gamma_1) + y^* w^* tan(\gamma_2)$$

For small γ we approximated using $tan(\gamma) = \gamma$ resulting in a simplified expression that was used to fit γ_1 and γ_2 to minimize the root mean squared error between the calculated u^*_r field and $u^*_{r,bias}$. The result of this fit was $\gamma_1 = 0.044rad$ and $\gamma_2 = 0.018rad$.

The standard deviation of the residual error remaining in u_r^* after the correction was applied was 0.5% of w_b

The general error expression for the bias correction was,

$$\delta u_{r,bias}^{*\,2} = (\delta\gamma_1)^2 x^{*2} w^{*2} + (\delta w^*)^2 x^{*2} \gamma_1^2 + (\delta\gamma_2)^2 y^{*2} w^{*2} + (\delta w^*)^2 y^{*2} \gamma_2^2$$

and by using the variance of the fit error to estimate $\delta\gamma_1$, and $\delta\gamma_2$, the error estimate for the radial velocity bias was 0.26% of w_b.

Combining error sources using a root sum squared method results in total error estimates for the instantaneous velocity.

$$\delta_u = 0.040 w_b \;\; ; \;\; \delta_v = 0.035 w_b \;\; ; \;\; \delta_w = 0.070 w_b$$

The statistical uncertainty in $\overline{w}(r^*)$ is estimated as,

$$\delta_{w(r^*)} = 1.96 \frac{w'(r^*)}{\sqrt{m(r^*)N}}$$

where $m(r^*)$ is the number of vectors in a given bin and N is the number of statistically independent vector fields. The values for $m(r^*)$ vary over a small range from [262 to 267]. This causes the uncertainty in $\delta_{w(r^*)}$ to become primarily a function of the rms value. The maximum uncertainty in the mean flow profile, δ_w, is calculated to be .06% of w_b and occurs at $r^* = 0.4$ where $w'(r^*)$ reaches its maximum.

The error bounds in the axial rms velocity are estimated using a chi-squared distribution method as,

$$\sqrt{\frac{(mN-1)\sigma_w^2}{\chi^2_{(mN-1),\beta/2}}} \leq \sigma_w \leq \sqrt{\frac{(mN-1)\sigma_w^2}{\chi^2_{(mN-1),1-\beta/2}}}$$

where $(mN-1)$ is the number of degrees of freedom, and β is the confidence interval chosen to be 95%. The maximum uncertainty in σ_w was calculated to be 0.01% of W_b and occurs at $r^* = 0.4$.

The probability values calculated for modal structure observations were found to be converged to within 90% of the values shown in Section 3.2.1.

Chapter 3

Results

Parts of Section 3.1 and Section 3.2.1 are presented exactly as they appear in Winters, K. J., & Longmire, E. K. (2019). PIV-based characterization of puffs in transitional pipe flow. Experiments in Fluids, 60(4), 60.

Parts of Section 3.3 are presented exactly as they appear in Winters K.W., & Longmire, E.K. (September, 2015) Searching for transitional structures in droplet-laden pipe flow. Paper presented at the 11th International Symposium on Particle Image Velocimetry – PIV15, Santa Barbara California.

This chapter describes the results of the experimental investigations into the single-phase and droplet-laden cases. SPIV measurements of the flow immediately downstream of the disturbance generator were taken in partial fulfillment of Objective 1. Puff frequency measurements were made using the pressure transducer in order to fulfill Objectives 1, 2, and 4. SPIV and PPIV measurements were made in order to fulfill Objectives 3 and 4.

3.1 Inlet

In an effort to provide context for the disturbance generator in the present study, Figure 3.1 shows the mean and rms values of w^* plotted against radial location for the present study at $10D$ downstream of the disturbance generator and $Re = 2100$ compared to data reported by Wygnanski and Champagne (1973) at 15D downstream of their inlet disturbance and $Re = 2400$. Our choice of Reynolds number was based on the knowledge that at $Re = 2100$ puffs have extremely long lifetimes and therefore should not decay or split before they reach the measurement location. This was validated by the observation that we consistently observed isolated puffs which occurred often enough that wait times for triggering were around 48s on average, which corresponded with a streamwise trailing-edge spacing of 375D. The mean profile from the present study was similar to those of Wygnanski and Champagne (1973). It was relatively flat across the center region of the pipe before decreasing steeply near the wall. Near the center of the pipe, the profile of rms velocity most closely matched that measured by Wygnanski and Champagne (1973) downstream of the orifice obstruction. In both the present study and their orifice case, the rms velocity at the center of the pipe was close to 5% of the averaged centerline velocity, and increased to a maximum of 12% at $r^* = 0.39$. The peak magnitude was smaller in the present study. It is likely that the wake shed by the ring shaped disturbance was weaker than those shed by the orifice plate or the disc whose blockage ratios were much higher than in the present study.

Puffs triggered by the disturbance generator ring were sensed by the downstream pressure transducer. Figure 3.2 shows the voltage record associated with the pressure drop of a passing puff. The raw voltage was plotted against z^*, where for this plot, $z^* = 0$ was chosen to correspond to the peak voltage. The voltage increased over an equivalent distance of $64D$ which was equal to the tap spacing. Then the value decayed to the baseline voltage

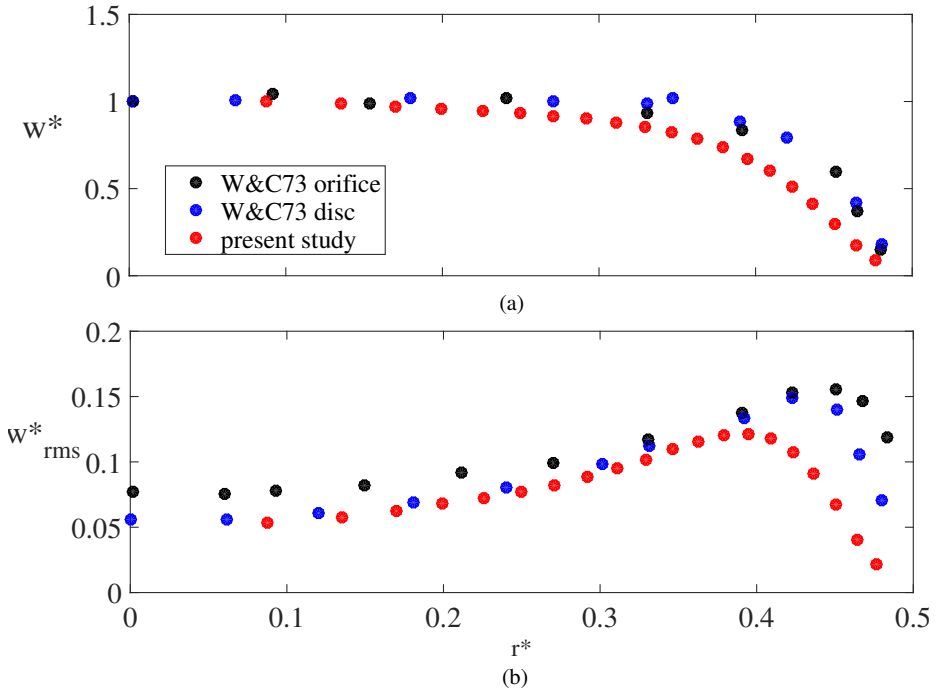

Figure 3.1: The (a) mean axial velocity and (b) the rms axial velocity for the present data(red) taken 10D from the disturbance ring at Re=2100 and compared against Wygnanski and Champagne (1973) disc(blue) and orifice(black) which was taken 15D from their disturbance at Re=2400.

over an additional equivalent distance of $175D$. Since the decay of the voltage signal was much longer than the known length of puffs, it is suspected that the voltage recorder was detecting a transient response in the pressure transducer. It was found that the decay time of the voltage signal decreased when the distance between the taps was shortened.

In order to determine the facility's response to a range of Reynolds numbers, the pressure signal was monitored over times corresponding to $z^* > 10^6$. The number of puffs identified in the voltage records was then tallied for each Reynolds number value. Figure 3.3 shows the frequency of puffs as a function of Reynolds number. The facility first started to register puffs at $Re = 1850$. At $Re = 2140$, the average spacing between puffs was 298D. Given

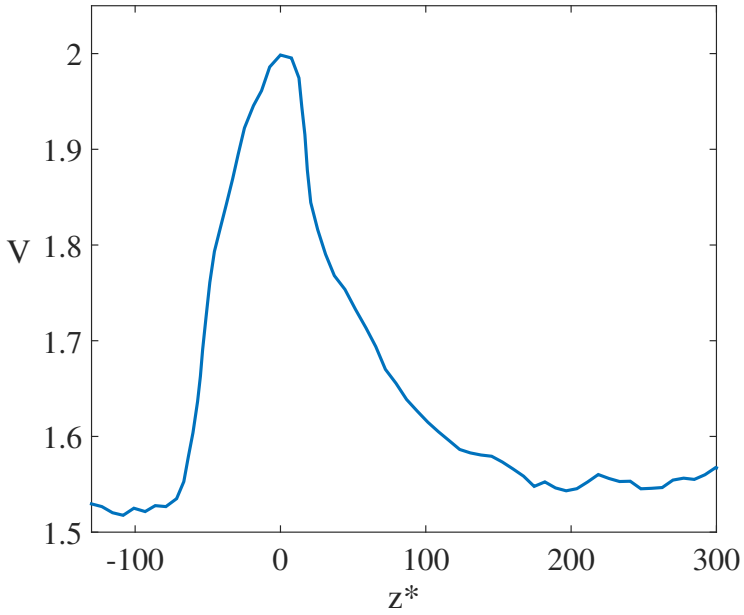

Figure 3.2: A typical voltage spike associated with a puff passing between the pressure taps in the facility as described in Section 2.1.

the length of the test section and the random spacing of puffs, frequently one or more puffs existed in the test section for $Re \geq 2140$.

3.2 Single-phase puff investigation

3.2.1 Stereo PIV

In total, 55 image sequences were obtained at a Reynolds number of 2100. In 48 of the sequences, the trailing edge was clearly present, and the record could be registered for ensemble averaging and plotting using the z^* coordinate. In the remaining seven sequences, the trailing edge fell outside the captured range. The 48 SPIV records with captured trailing edges are referred to using labels S-1 through S-48.

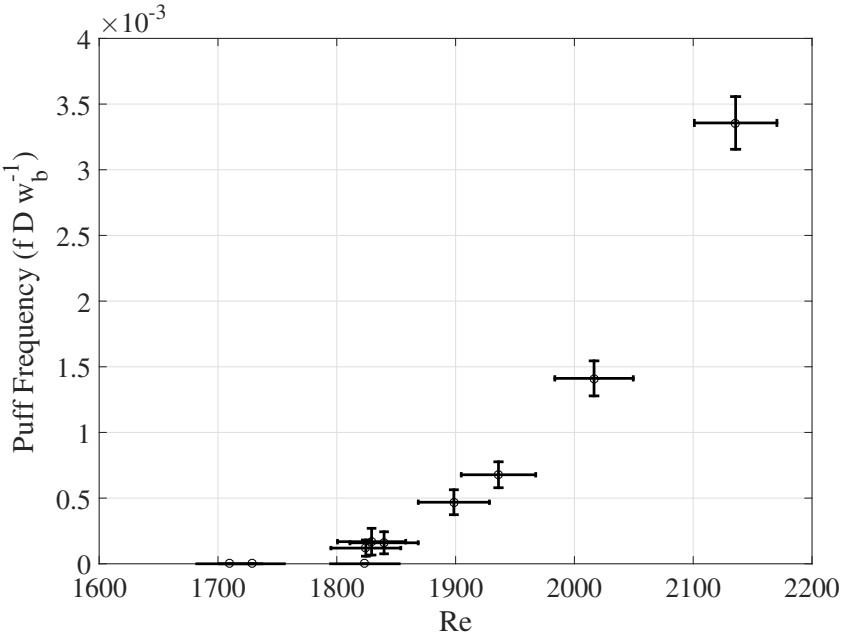

Figure 3.3: Normalized puff frequency. Error bars show the estimated uncertainty in Reynolds number and frequency for each point.

Figure 3.4(a-c) show composite plots of A_e, w^*_{CL} and q^* calculated for all puff observations, respectively. Each individual observation is represented by a gray line, except one highlighted in blue for further discussion which corresponds to puff record S-47. The ensemble average of all observations is shown in red. In 41 of 49 records shown in Figure 3.4a, a localized peak in A_e extends over an axial distance of $0.1D - 0.2D$ surrounding $z^* = 0$. Indeed, this can be seen in the example of puff S-47 and in the ensemble average. Downstream of the trailing edge, $z^* > 0.2$, the instantaneous A_e plots frequently show one to two localized peaks that cross the threshold before remaining elevated over an axial distance of 2-3 diameters. It is apparent from the collection of plots in Figure 3.4b that the localized peaks in A_e that define the trailing edge can sometimes, but not always, correspond to a significant disruption to the laminar value of w^*_{CL}. Puff S-47, for example, does not exhibit a significant disruption until $z^* = 2$. The averaged w^*_{CL} plot shows a steep drop that reaches

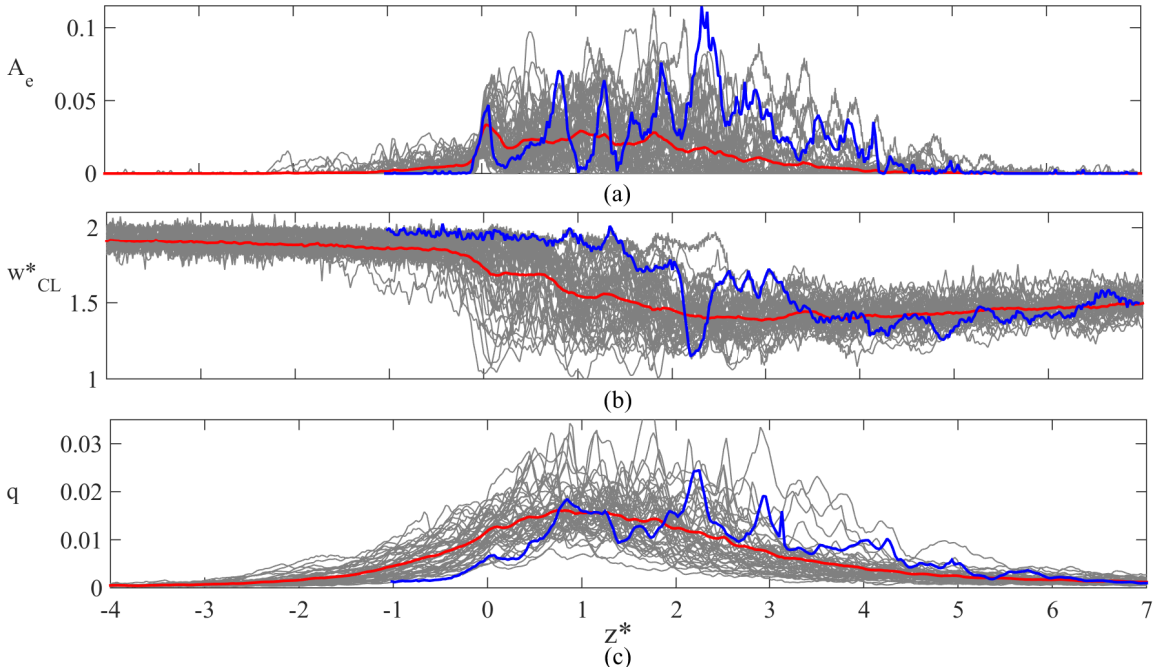

Figure 3.4: Composite plots of (a) A_e,(b) W_{CL}, and (c) q^*. Each gray plot corresponds to a single puff observation. The blue line in each plot highlights puff S-47 for comparison to the ensemble averages shown in red.

a local minimum at $z^* = 0.16$, eventually decreasing again until $z^* = 2.5$ where it begins to recover slowly toward the laminar value. Figure 3.4c reveals that q^*, from Equation 1.8, spans a wide range of values at the trailing edge. This is underscored by the relative standard deviation at the trailing edge which was 33%. In general, a small local peak exists in the plot of q^* at the trailing edge amid an overall increasing trend.

Coherent structures in single phase puffs

Figure 3.5 shows two views of isosurfaces of streamwise vorticity for which $|\omega_z^*| > 3$ from puff S-47 reconstructed from the SPIV data using Taylor's Hypothesis. The surfaces are colored by the sign of the vorticity where red is positive and blue is negative. Figure 3.5a shows an elevation view of the entire puff, while Figure 3.5b is a slice showing the region

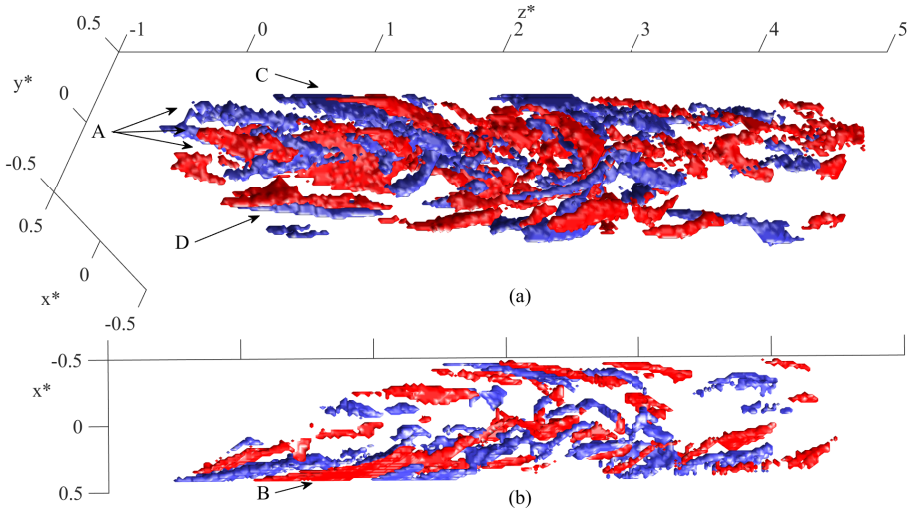

Figure 3.5: Isocontours at $\omega_z^* = 3$ (red) and $\omega_z^* = -3$ (blue) reconstructed from puff S-47 are shown for (a) the entire pipe cross section, (b) and a section including $-0.25 < y < 0.25$ centered along the ejection plane.

where $-0.25 < y^* < 0.25$. Upstream of the trailing edge, the isosurfaces of strong axial vorticity are confined to a small region near the y^*-axis. For $-0.5 < z^* < 0.5$, marked as A, two regions of negative vorticity extend upstream with a positive vorticity region centered between and above them. At $z^* = 0$, marked as B, another strong positive vorticity region appears between and below the two negative vorticity regions that have by then lifted away from the wall. By $z^* = 0.5$, axially oriented regions of strong vorticity appear near the wall in two other azimuthal locations, $\theta^* = +60°$ and $\theta^* = -70°$, marked by C and D respectively. By $z^* = 1.2$, these regions of strong vorticity extend towards the center of the pipe. Farther downstream, where $z^* > 3$, many smaller regions of strong vorticity exist, but they do not have long axially oriented portions that extend along the wall.

In order to visualize swirling structures the method used by Zhou et al. (1999) was followed whereby the eigenvalues of the velocity gradient tensor are computed. Then vortex identifier λ_{3D}^*, known as the three-dimensional swirling strength, represents the magnitude of the imaginary part of the the complex conjugate pair of eigenvalues. Figure 3.6 shows

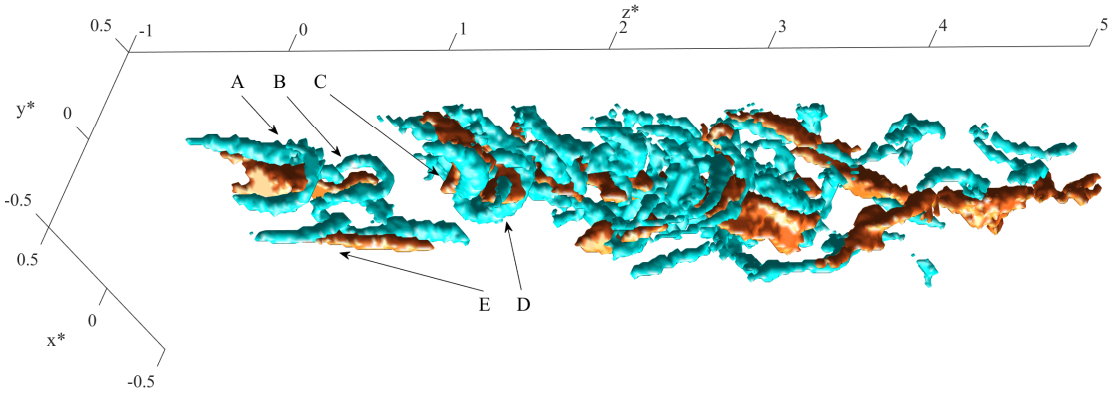

Figure 3.6: Isosurfaces of $\lambda^*_{3D} > 2.6$ (blue) and radial ejections where $u^*_r < -.12$ (orange) reconstructed from puff S-47 with key structures marked A-E.

isosurfaces in puff S-47 corresponding to three-dimensional swirling strength, $\lambda^*_{3D} > 2.6$ and inward radial velocity, $u^*_r < -0.12$ in the same orientation as Figure 3.5a. The strong ejection located at the trailing edge extends normal to the page, from the wall towards the center of the pipe. The ejection is wrapped by a hairpin shaped swirling region, marked by A, whose head is centered at $z^* = 0.18$. At $z^* = 0.57$ a second, smaller hairpin appears, marked by B, in line with the first. The ejection region associated with B is much smaller in volume than with hairpin A. A third hairpin, marked by C, is larger than the two upstream with its head centered at $z^* = 0.92$. It is shown in profile with its legs at the top of the field of view and head extending downward. A fourth hairpin at $z^* = 1.34$, marked D, is the largest and has a similar orientation to hairpin A. Other hairpins were isolated by examining small segments of the reconstructed domain at $z^* = 1.47$, 1.71, and 2.0. Among the hairpins, a long swirling region, marked E, remains close to the wall and extends through the range $0 < z^* < 1.1$.

Figure 3.7a shows an alternate orientation of puff S-47 (shown in Figure 3.6) with the

ejection velocity and swirl isocontours set to $u_r^* < -0.12$ and $\lambda_{3D}^* = 2.6$, respectively. This allows for a side by side comparison with Figure 3.7b, which shows plots of q^* along z^*. From the total q^* plot, apart from the hairpin located at the trailing edge, there is some correspondence between local peaks and the locations where hairpins were found. The connection becomes clearer however when the contribution to q^* from the ejection and swirl isocontours is summed along each cross section (green). Here, more prominent local peaks emerge at $z^* = 0.07, 0.44, 0.84, 1.30$ each of these peaks is just upstream of the hairpin heads noted in puff S-47. In the remaining three downstream hairpins in puff S-47, neither the green or the black curve correspond particularly well with the hairpin locations.

While the plot of q^* in Figure 3.7b shows a sharp local peak at the q_{max}^* location, no hairpin structure was observed in that region. The q_{max}^* location instead coincides with many irregularly-shaped swirling structures occurring throughout the cross section. The swirling structures found near the q_{max}^* location are discussed in detail later in this section.

Isosurfaces of λ_{3D}^* are plotted in a similar way to Figure 3.6 for each puff in Appendix C. For each record, the swirling regions are shown within $-2 < z^* < 4$, capturing the vast majority of the swirling structures inside the record, along with a subdomain covering the region near the trailing edge, $0 < x^* < 0.5$, $-.3 < y^* < .3$, $-1 < z^* < 0.75$. In order to capture the swirling structures that exist at the trailing edge, the threshold on λ_{3D}^* was set dynamically for each puff as 0.5 standard deviation above the mean value of λ_{3D}^* within $-0.07 < z^* < 0.07$. In a majority of records, full and half hairpin structures appear in the trailing edge subdomains, and are very frequently accompanied by additional axially aligned neighbors. In many records, S-17, S-19, S-29, S-37, additional hairpins are visible outside of the trailing edge subdomain in the full domain images. Many additional hairpins that are occluded or oriented in such a way that they cannot be recognized can be seen when the isosurfaces are viewed from other angles than the specific view chosen for the images

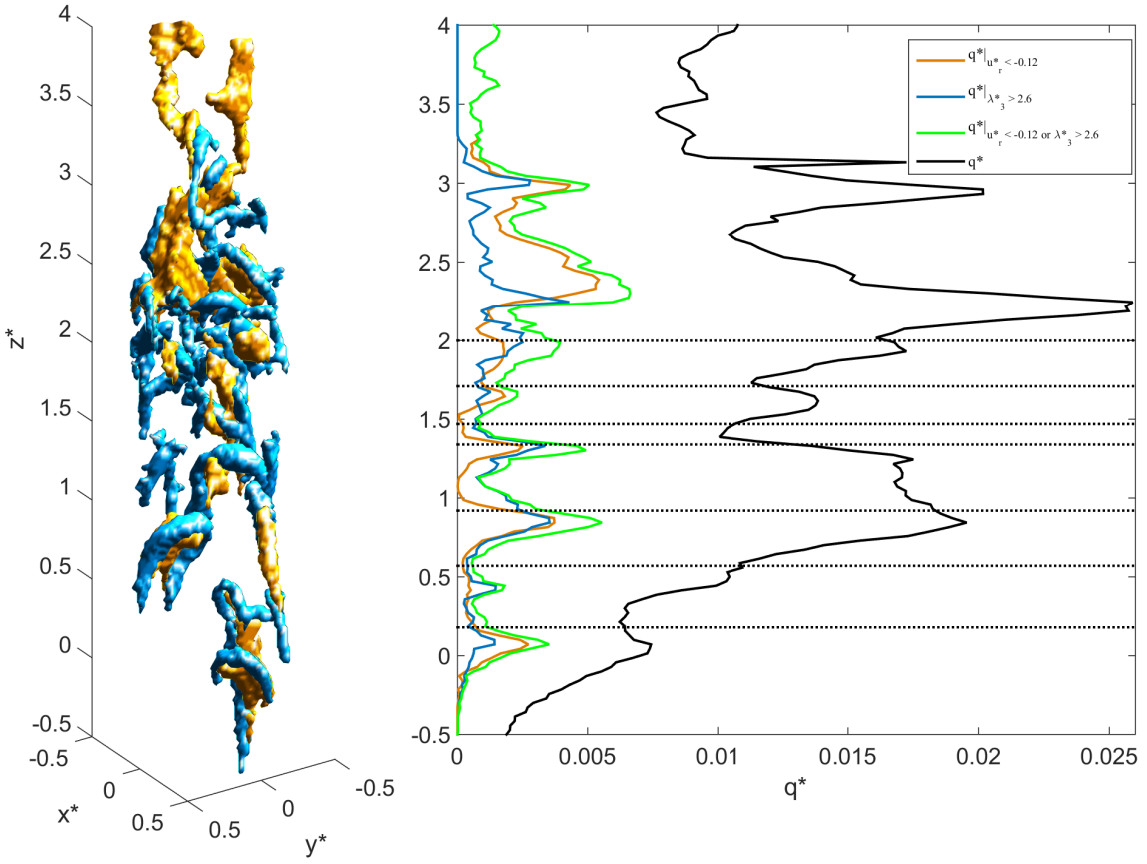

Figure 3.7: (a) Isosurfaces of $\lambda^*_{3D} > 2.6$ (blue) and radial ejections where $u^*_r < -.12$ (orange) reconstructed from puff S-47. (b) An examination of the total amount of q^* along the axial direction showing the total (black) along with that contained inside the isosurfaces of swirl (blue) and the ejection regions (orange). The green line represents the total q^* found in both the ejection and swirling regions. The horizontal dotted lines indicate the locations of hairpin heads noted by visual inspection in Figure 3.6. The green plot is not the sum of the yellow and blue plots because in some locations, the isosurfaces overlap.

in Appendix C.

From surveying the λ^*_{3D} isosurfaces in three records, fourteen hairpins were identified in the range $-1 < z^* < 2$ and accompanied by at least one additional hairpin aligned directly upstream or downstream with an average z^* spacing of $0.39D$ The hairpins identified were usually associated with small local peaks in q^*. For comparison, the distance between the hairpins noted near the trailing edge by van Doorne and Westerweel (2009) was $0.71D$. Also, the hairpins discussed by van Doorne and Westerweel, were not positioned at the same azimuthal location, but were displaced by an angle of 45°. van Doorne did however present a figure similar to Figure 3.5 including similar sequences of strong axial vorticity that might indicate an axially aligned hairpin sequence. In the records surveyed, local peaks in q^* beyond $z^* = 2$, did not correspond with hairpin structures, but rather with multiple disconnected structures of irregular shape.

Since the individual puffs studied by van Doorne and Westerweel (2009) and Kuik (2011), respectively, showed different shaped vortical structures associated with the peaks responsible for q^*_{max}, q^* for each record was examined and some records were selected for detailed examination. In the records from the present study, the global maximum in q^* was found within the range, $0.017 < q^*_{max} < 0.040$. On average, the q^*_{max} peaks occurred at $z^* = 1.18$, and rose to a value that was 0.01 greater than the nearest local minimum. The most downstream location of q^*_{max} was found at $z^* = 3.35$ in puff record S-42, while two puffs had q^*_{max} upstream of the trailing edge. These records were S-6($z^* = -0.30$), and S-4($z^* = -0.22$). In two records, S-34 and S-19, the trailing edge coincided with the location of q^*_{max}. No correlation was found between the location of q^*_{max} relative to the trailing edge and the magnitude of q^*_{max}.

Because the q^*_{max} location for S-19 was at the trailing edge, the record was investigated further along with S-26, and S-47. Figure 3.8 shows q^* for the three records. The mag-

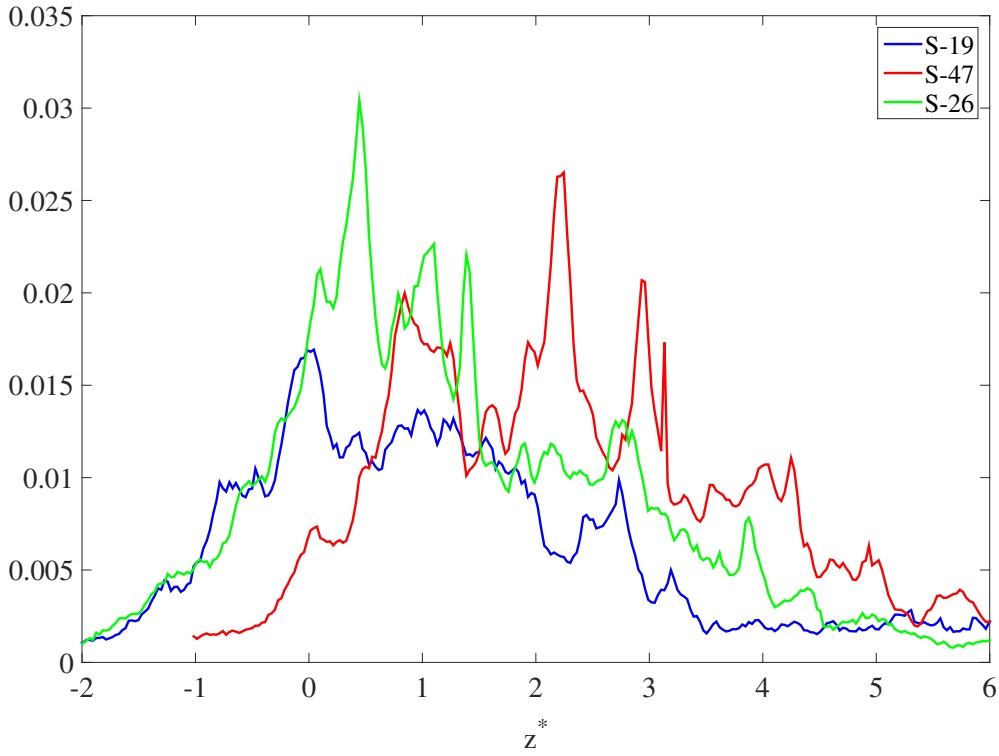

Figure 3.8: q* against axial location of the records, S-19(blue), S47(red), and S-26(green)

nitude of q^*_{max} for S-19, S-26, and S-47 was 0.017, 0.030, and 0.026 and was found at $z^* = 0, 0.44, 2.25$, respectively. It is interesting that in S-26, not only was q^*_{max} the weakest across all datasets, but the peak was unusually long in the axial direction.

Given the design of the trailing edge recognition method, it was suspected that the ejection at the trailing edge in S-19 would correspond to the center of a hairpin. Figure 3.9 shows isosurfaces of λ^*_{3D} in the neighborhood of the trailing edge. Much of a large hairpin structure can be seen, highlighted in magenta. A long hairpin leg stretched from $z^* = -1.25$ on the $y^* > 0$ side of the pipe to the trailing edge before arching across the center of the pipe and then back upstream. There was a slight discontinuity right at the trailing edge after which the shorter opposing leg stretched upstream to $z^* = -0.5$. Additionally, two hairpin

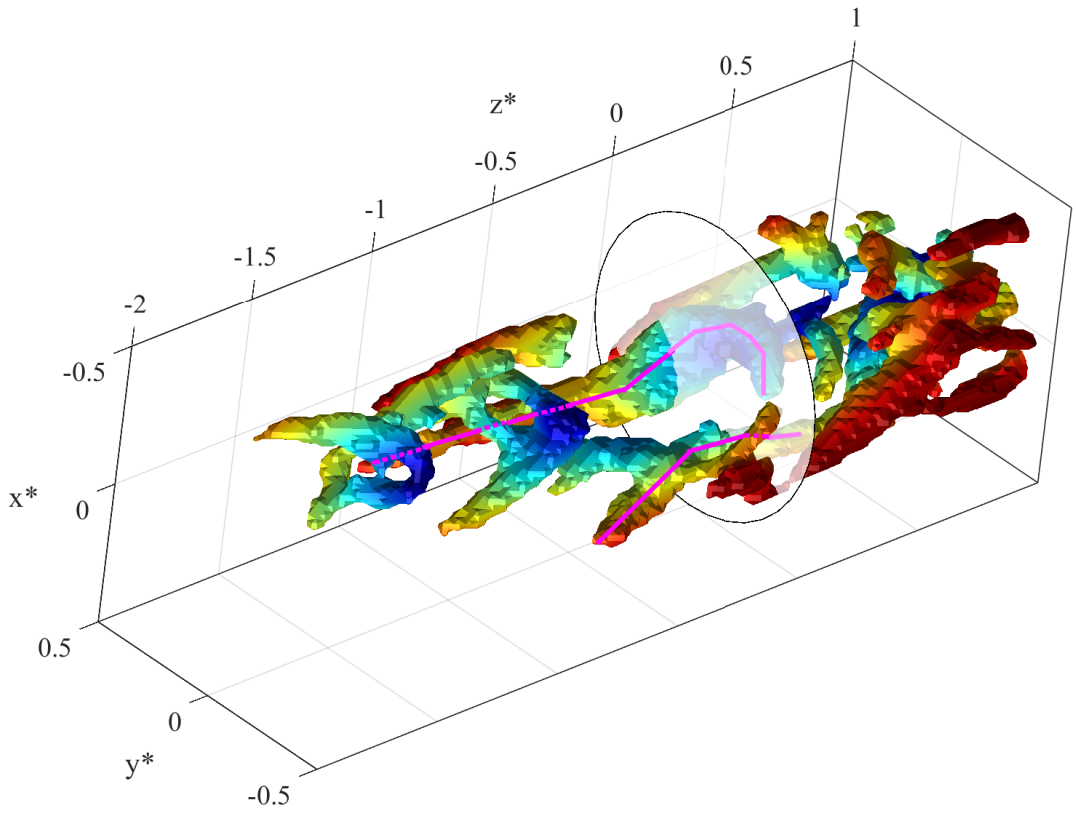

Figure 3.9: Isosurfaces of $\lambda^*_{3D} > 1.7$ are shown for puff record S-19. The surface color corresponds to increasing radial coordinate from the center or the pipe (blue) to the wall (red). A large hairpin structure is highlighted (magenta). The semi-transparent cross section shows the trailing edge/q^*_{max} location. The surfaces were smoothed using a 3x3x3 kernel for clarity.

structures were found upstream whose heads are located at $z^* = -1.14$ and $z^* = -0.54$. The presence of the three hairpins is hinted at by the three sharp increases found in the q^* plot in Figure 3.8 that level off just upstream of each hairpin head at z* = -1.3 and z* = -0.79.

To examine the location and direction of the motions responsible for q^*_{max} and investigate the connection to the swirling structures shown in Figure 3.9, the quantity k^*_{ip} was used to

define the local value of in-plane kinetic energy as,

$$k^*_{ip}(r^*, \theta^*) = {u^*_r}^2 + {u^*_\theta}^2 \tag{3.1}$$

.

Figure 3.10(a-f) show vector plots inside S-19 near the trailing edge/q^*_{max} location that display colored regions of vectors with strong k^*_{ip}, and shade regions with strong λ^*_{3D}. Figure 3.10g shows the individual contributions of each similarly colored region to the total q^* value near the peak.

Figure 3.10a is taken upstream of q^*_{max} and shows a high energy yellow region that coincides with a swirling region, and corresponds to the upstream portion of the shorter leg on the trailing edge hairpin in Figure 3.9. Orange and purple high-energy regions also appear on the inward and outward sides of a swirling region that slices the longer leg of the trailing edge hairpin, respectively.

In Figure 3.10b, all three high energy regions have grown in area and in the energy they contain. This coincides with a clearer swirl field where four well defined swirling cores dominate. The pair of cores that show the longer and shorter legs of the hairpin lie along $x* = 0.2$ at $y^* = 0.25$, and $y^* = -0.1$, respectively. The other two swirling cores in Figure 3.10b are associated with additional axially oriented swirling structures in Figure 3.9. The hairpin legs surround a coherent ejection region that is carrying fluid from the wall inward. Interestingly, it is not the fluid along the ejection axis that contains the highest values of k^*_{ip}. The highest values of k^*_{ip} occur where one of the axially oriented swirling structures outside the trailing edge hairpin acts in conjunction with the motion induced by the nearby counter rotating hairpin leg to accelerate fluid from the hairpin ejection back outward toward the wall.

The picture in Figure 3.10c is similar to that of Figure 3.10b except that orange vectors

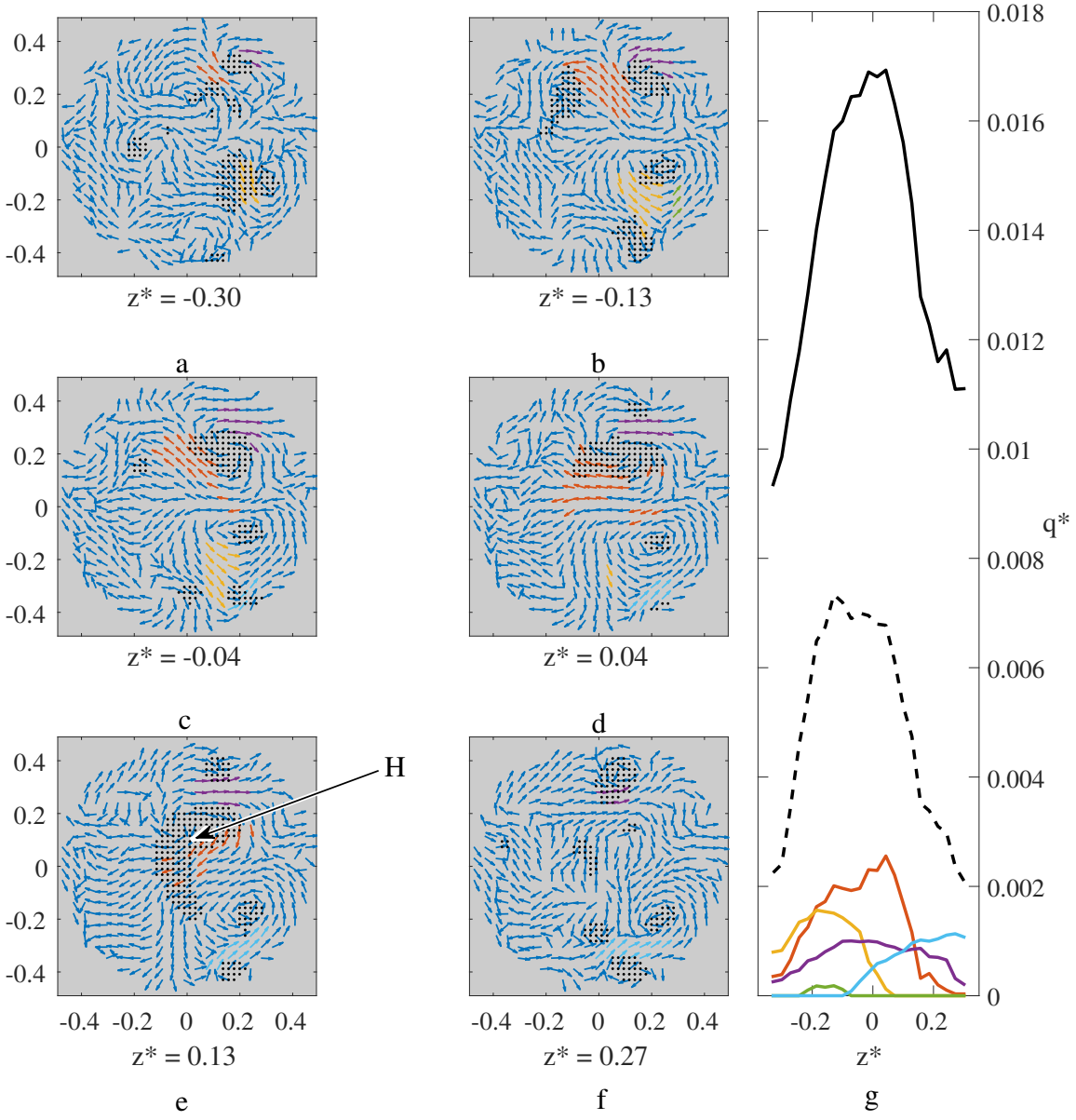

Figure 3.10: (a-f) The vectors of in-plane velocity for S-19 near the q^*_{max} location at the z^* values shown. In each vector plot, the horizontal axis corresponds to x^*. Blue vectors correspond to $k^*_{ip} < 0.07$, while each other color corresponds to a single contiguous region where the $k^*_{ip} > 0.07$. The black dotted regions represent areas where $\lambda^*_{3D} > 1.7$ (g) The colored curves represent the contribution to q^* from each contiguous region at each axial location between the cross sections (a) and (f). The solid black line shows the global peak in q^*, while the dashed black line represents the sum of the colored lines.

have begun to appear in the region bewteen the hairpin legs, and a small cyan region appears near the wall. By Figure 3.10d the contribution to q^* from the orange region reaches its peak and the shaded area representing the longer hairpin leg elongates inward as leg begins to arch inward to form the hairpin head.

The high k^*_{ip} values in Figure 3.10d are likely influenced by the hairpin legs, but also by the hairpin head in Figure 3.10e, labeled as (H), which extends across the centerline of the pipe. At this location, $z^* = 0.13$, the value of q^* has decreased sharply from its maximum. In Figure 3.10a-e, the four regions of high in-plane energy combine to create the peak responsible for q^*_{max}, and are each tied to the same swirling structure, the trailing edge hairpin. The orange region's most energetic parts, which contribute the most to the q^*_{max}, are directly tied to the hairpin ejection, while other high values of k^*_{ip} appear to come from the result of other swirling structures that are outside the hairpin rotating in such a way that they act with the hairpin legs to move fluid toward the pipe wall. This is seen most clearly in 3.10b where additional swirling regions outside of the hairpin leg coincides with the yellow region and upstream parts of the orange region. Figure 3.10f, downstream of the hairpin head, corresponds to a local minimum in q^* where the swirling regions are confined to small, mostly circular regions. The in-plane velocity vectors show fluid rotating around axes oriented parallel to the pipe axis.

To investigate whether hairpin structures accompanied q^*_{max} locations found farther downstream than in S-19, regions with high values of k^*_{ip}, and λ^*_{3D} were examined for puff record S-26. Figure 3.11 shows the in-plane energy and swirling isosurfaces inside S-26 near the q^*_{max} location (white circle) where $x^* > 0$, while Figure 3.12 shows similar regions in S-26 where $x^* < 0$.

In Figure 3.11, one axially oriented swirling structure upstream of the trailing edge was omitted from the image to better show the trailing edge structures. The location of q^*_{max} in

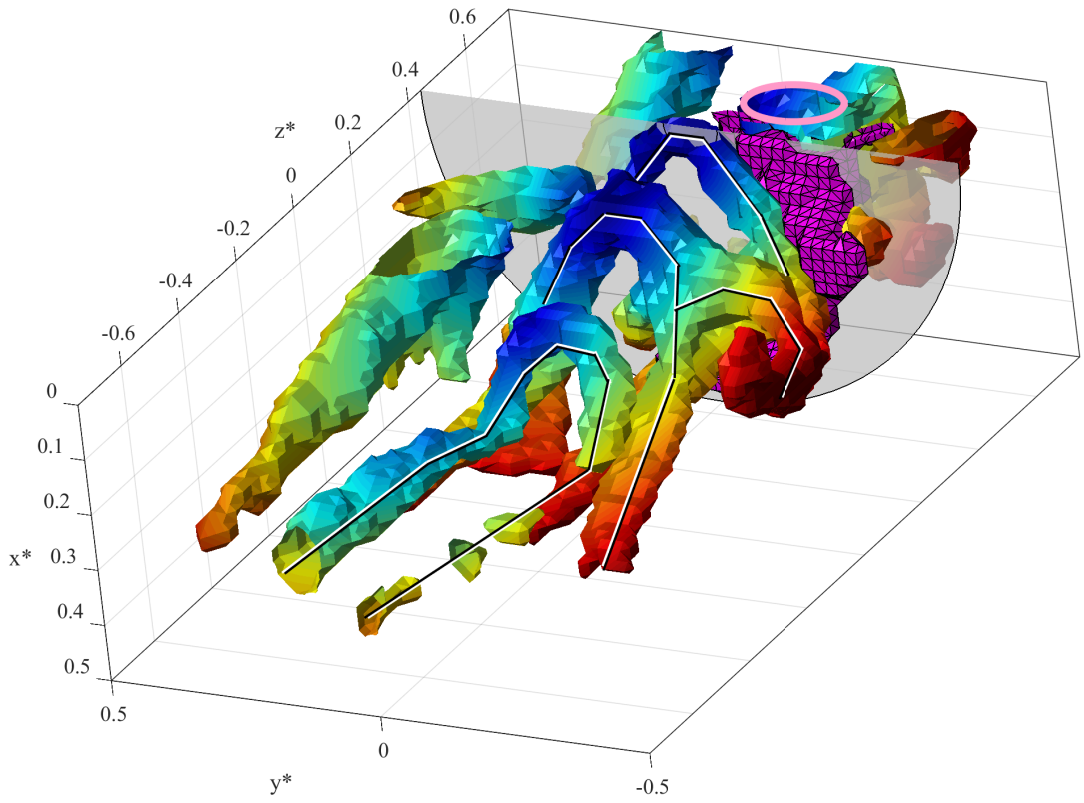

(b)

Figure 3.11: Isosurfaces inside S-26 where $x^* > 0$. $\lambda^*_{3D} > 2$ isosurfaces are colored corresponding to increasing radial coordinate from the center or the pipe (blue) to the wall (red). The lone isosurface where $k^*_{ip} > 0.09$ is shown as a magenta region with black edges. The semi-transparent cross section shows the q^*_{max} location. The pink oval shows the location where a large swirling structure crosses into the $x < 0$ domain. The surfaces were smoothed using a 3x3x3 kernel for clarity

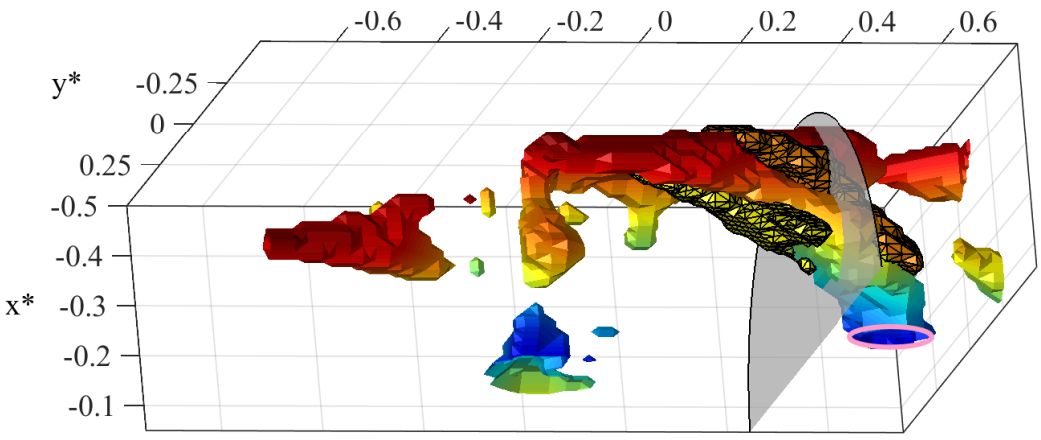

Figure 3.12: Isosurfaces inside S-26 where $x^* < 0$. The $\lambda^*_{3D} > 2$ isosurfaces are colored corresponding to increasing radial coordinate from the center or the pipe (blue) to the wall (red). The isosurfaces where $k^*_{ip} > 0.09$ are shown as yellow and orange regions with black edges. The semi-transparent cross section shows the q^*_{max} location. The pink oval shows the location where a large swirling structure crosses into the $x < 0$ domain. The surfaces were smoothed using a 3x3x3 kernel for clarity.

Figure 3.11 sits at the downstream end of a sequence of three axially aligned hairpins each of which is highlighted by a contrasting pair of black and white lines. The middle hairpin appears to be merging with another hairpin immediately to its right (also highlighted). The hairpin sequence is accompanied by additional axially oriented structures that turn away from the wall at their downstream ends. A region of elevated k^*_{ip} is sandwiched between the upstream hairpin and a large swirling region that extends from the wall inward towards the center of the pipe. This strong swirling region then crosses into the opposite half of the pipe (pink oval) depicted in Figure 3.12 where it extends to the wall and turns upstream.

Yellow and orange regions with high values of k^*_{ip} accompany the large swirling region in Figure 3.12 on its upstream and downstream sides, respectively. The yellow and orange regions are in turn flanked on their upstream and downstream ends by additional near-wall swirling structures, respectively. All together these regions create a [$\lambda^*_{3D} \rightarrow k^*_{ip} \rightarrow \lambda^*_{3D} \rightarrow$

$k^*_{ip} \rightarrow \lambda^*_{3D}$] sequence that spans just $0.5D$ in the axial direction.

Figure 3.13 shows vector plots of high λ^*_{3D} regions along with high k^*_{ip} regions and their contributions to q^*_{max}. The color scheme of the high k^*_{ip} regions is set to match that of Figures 3.12 and 3.11. From Figure 3.13g it is clear that the purple region is responsible for the peak in q^*. The vector sequence begins with a local minimum in q^*at $z^* = 0.30$. As in Figure 3.10, the local minimum is associated primarily with the axially oriented swirling regions shown in 3.12 located between the hairpin heads. The axially oriented regions show up in the vector plot as mostly circular shaded regions that create high values of k^*_{ip} close to the walls.

In Figure 3.13b, the most downstream hairpin head is visible as an arch shaped shaded region close to the center of the pipe. The downstream most portion of the hairpin head is shown in Figure 3.13c. Here, the purple region is stronger and coincides with the outward motion toward the wall that would be expected to be induced at the downstream side of a hairpin head. The contribution to q^* contained in the purple region peaks in Figure 3.13d, which is the part of the region sandwiched between the hairpin and the swirling region immediately downstream described in Figures 3.12 and 3.11 and visible as the large shaded region in Figure 3.13f.

Given the detailed analysis of puff record S-47 in earlier parts of Section 3.2.1, its q^*_{max} peak was also examined. Figure 3.14 follows the same layout as Figure 3.10 and Figure 3.13. Figure 3.14b-d, all correspond to q^*_{max}, while Figure 3.14a is upstream of q^*_{max}, and Figure 3.14f is downstream, at a local minimum of q^*. From Figure 3.14g, q^*_{max} in S-47 is due to the combination of two high energy structures, red and green. A third region, shown in purple decays before the peak.

The red region starting in Figure 3.14b remains in the $y^* > 0$ half of the pipe throughout its axial domain, and ends near Figure 3.14f. The red region consists of fluid moving mostly

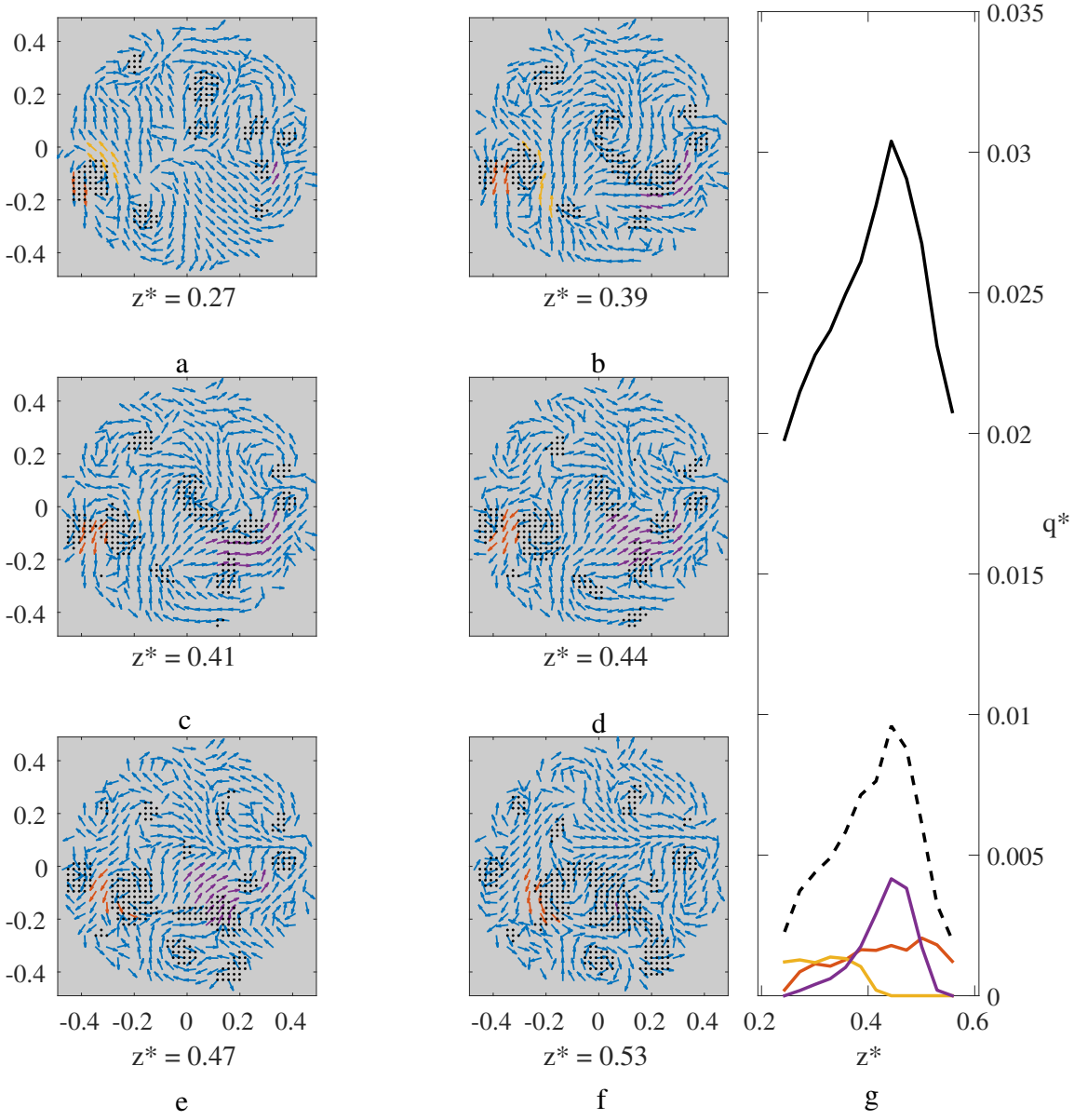

Figure 3.13: (a-f) The vectors of in-plane velocity near the q^*_{max} location for S-26 at the z^* values shown. In each vector plot, the horizontal axis corresponds to x^*. Blue vectors correspond to $k^*_{ip} < 0.09$, while each other color corresponds to a single contiguous region where the $k^*_{ip} > 0.09$. The black dotted regions represent areas where $\lambda^*_{3D} > 2$ (g) The colored curves represent the contribution to q^* from each contiguous region at each axial location between the cross sections (a) and (f). The solid black line shows the global peak in q^*, while the dashed black line represents the sum of the colored lines.

outward toward the wall. The red region has two lobes that extend downstream, from Figure 3.14b through Figure 3.14c,d before merging in Figure 3.14e. In Figure 3.14b-e, each lobe of the red region meanders through multiple small swirling regions. In Figure 3.14f, just downstream from where the lobes merge a large swirling region extends from the wall toward the center of the pipe. The purple region shown in Figure 3.14a-c consists of fluid that is already near the wall moving quickly toward it. It is bounded on either side by a pair of swirling regions.

The purple region is short in the axial direction, and peaks just upstream of the global peak in q^*.

The crescent-shaped green region moves radially outward from the center of the pipe. Its in-plane energy is focused into a short axial domain shown in Figure 3.14b-d. The vectors around the green region in Figure 3.14b,c closely resemble the strong cross flow observed near the q^* peak in the puff record of van Doorne (2004). Unlike van Doorne's record though, the green region does not correspond with a swirling structure that resembles a hairpin. The green region instead corresponds to the upstream side of a swirling region shown in Figure 3.14e that follows a similar crescent shape to the green region, but then extends to the wall at its downstream end. It is possible that the arch-shaped part of the swirling region could have once been a hairpin head whose shape has evolved through interaction with other structures.

As in S-19, and S-26, the regions in S-47 responsible for the global peak in q^* lie just upstream or dowstream of locations where there are large increases in the area of the shaded swirling regions. As these records show, an increase in the swirling area can correspond to the region where the legs of a hairpin arch inward and meet to form the head, or to regions where an irregular shaped swirling region extends perpendicular to the wall. While in all three records, some regions of high k_{ip}^* were caused by axially oriented swirling regions

pulling fluid from the inner part of the pipe outward toward the wall, the energy in these locations did not appear to be responsible for any of the q^* peaks.

The quantity, A_λ was defined for each puff record as the percentage of vectors in each cross section where $\lambda^*_{3D} > 2.0$ normalized by the maximum percentage area covered in that puff record. A_λ was defined in order to examine records for the large changes in the area covered by the shaded swirling regions in Figures 3.10, 3.13, and 3.14, and their possible connection to q^*_{max}. Figures 3.15a and 3.15b compare A_λ to q^*/q^*_{max} for the three puff records examined in this section, and each of the plots was aligned such that q^*_{max} occurs at $z^* = 1.18$, the average location of q^*_{max} across the SPIV dataset. In Figure 3.15b, the q^*/q^*_{max} was, by definition, 1 at $z^* = 1.18$. Figure 3.15a shows that each record had a sharp increase in A_λ that started just upstream of $z^* = 1.18$, and peaked at $z^* = 1.25$. Moving upstream in S-19, S-26 and S-47, the records had local minima at $z^* = 1.03, 1.14, 1.02$, respectively that followed local maxima at $z^* = 0.79, 1.00, 0.88$, respectively. For the case of S-19, the upstream local maximum in A_λ at $z^* = 0.79$ corresponds to the hairpin shaped structure near $z^* = -0.5$ in Figure 3.9. In each record, the location of the local maximum in A_λ that lies upstream of $z^* = 1.18$ corresponds with the location where q^*/q^*_{max} begins increasing rapidly towards its peak value. This suggests that regardless of the shape of the swirling region, the strong motions responsible for the q^*_{max} peak are tied to both local maxima in A_λ and that the local minimum between the two maxima creates the necessary space for the strong swirling motions on either side to generate a large, strong, coherent motion.

Two axial locations of interest have been discussed that exist for every SPIV record: the ejection structure that was identified as the trailing edge, and the location of q^*_{max}. By aligning q^*/q^*_{max} and A_λ from each of the 48 SPIV records on each of these two locations, two sets of ensemble averages were constructed. The relationship between q^*/q^*_{max} and A_λ

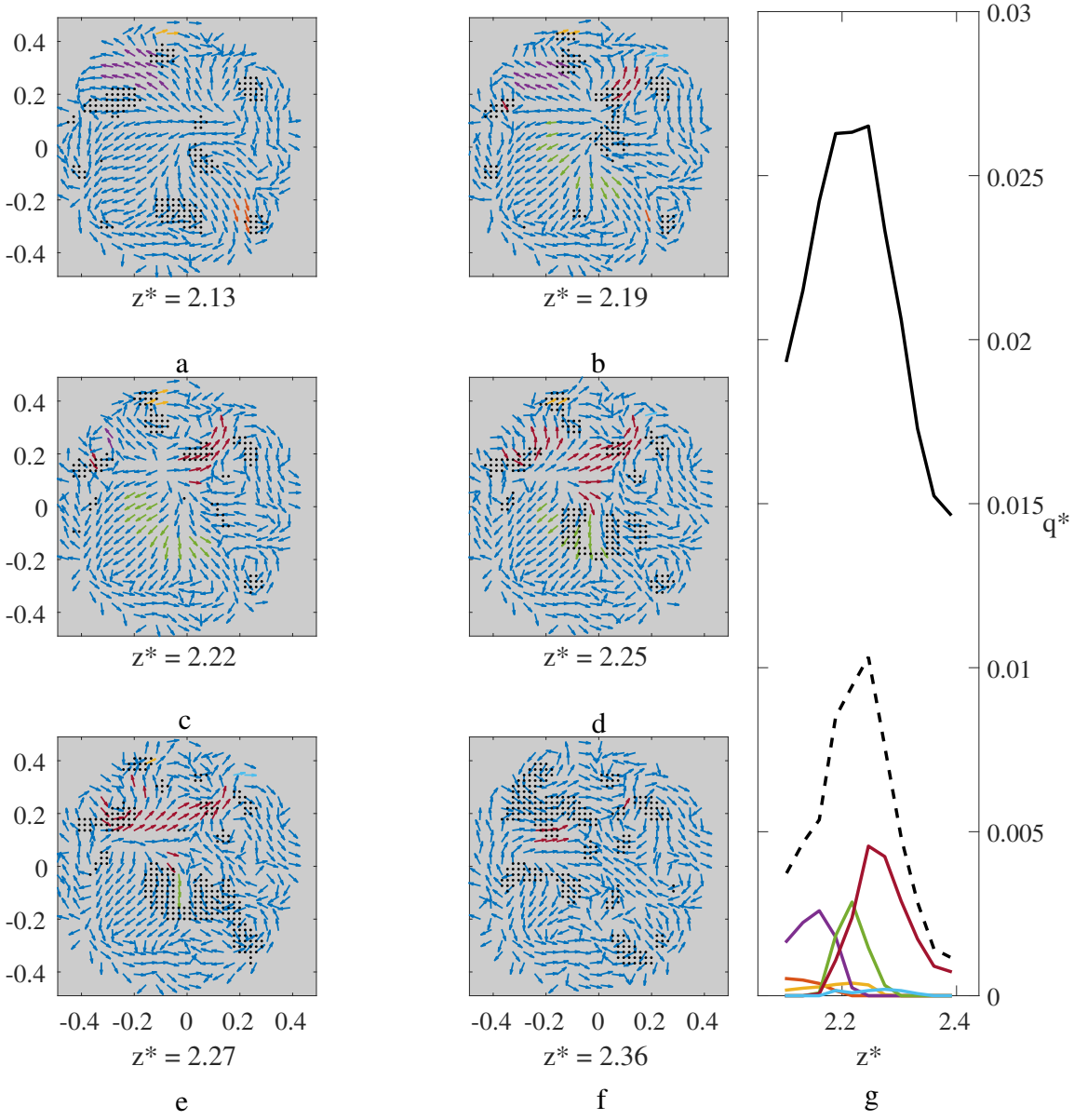

Figure 3.14: (a-f) The vectors of in-plane velocity near the q^*_{max} location for S-47 at the z^* values shown. In each vector plot, the horizontal axis corresponds to x^*. Blue vectors correspond to $k^*_{ip} < 0.07$, while each other color corresponds to a single contiguous region where the $k^*_{ip} > 0.07$. The black dotted(regions represent areas where $\lambda^*_{3D} > 2$ (g) The colored curves represent the contribution to q^* from each contiguous region at each axial location between the cross sections (a) and (f). The solid black line shows the global peak in q^*, while the dashed black line represents the sum of the colored lines.

was then examined for each alignment method. The averages were also used to examine potential connections between the structures responsible for the two locations of interest in each record. If the trailing edge hairpins often exist as part of a sequence that grows in strength with downstream distance in a well-defined way, culminating in an energetic event that creates the q^*_{max} peak, it might be expected that the ensembles would share some common features.

Figure 3.15c shows q^*/q^*_{max} and A_λ for each alignment method. The cyan plots show $< q^*/q^*_{max} >$, and the magenta plots show $< A_\lambda >$. The solid lines were computed by aligning the q^*_{max} location of each record to $z^* = 1.18$ as in Figure 3.15a,b. The dashed plots are computed by aligning the records on hairpins at $z^* = 0$ as in Section 2.3.2. In the ensembles representing the q^*_{max} registration method, there is a sharp discontinuity in the slope of $< q^*/q^*_{max} >$ at $z^* = 1.18$ upstream of which, $< q^*/q^*_{max} >$ shows a sharply increasing slope at $z^* = 1.1$. Over this axial length, of 0.08, q^*/q^*_{max} increases by 0.3 from ≈ 0.7 to 1. This sharp rise in $< q^*/q^*_{max} >$, corresponds to 30% of the global maximum and generally agrees with the proportion of q^*_{max} represented by the height of the peak in the dashed lines of Figures 3.10g, 3.13g, 3.14g. This suggests that the sharp localized peak responsible for q^*_{max} rises an amount that scales consistently with the value of q^*_{max}. $< A_\lambda >$ has a local minimum at $z^* = 1.18$, and two local maxima upstream and downstream at $z^* = 1.05$ and $z^* = 1.25$, respectively. The distance between the maxima in A_λ corresponds with the edges of the q^*/q^*_{max} peak, confirming the trend observed in the instantaneous records.

In the hairpin registered ensemble where $0 < z^* < 0.8$, there is a sequence of small local maxima in $< q^*/q^*_{max} >$, whose values are slightly greater than the magnitude of other $< q^*/q^*_{max} >$ fluctuations seen across the axial domain. There is a larger local maximum in A_λ that occurs just downstream of the trailing edge at $z^* = 0.19$, precisely the location

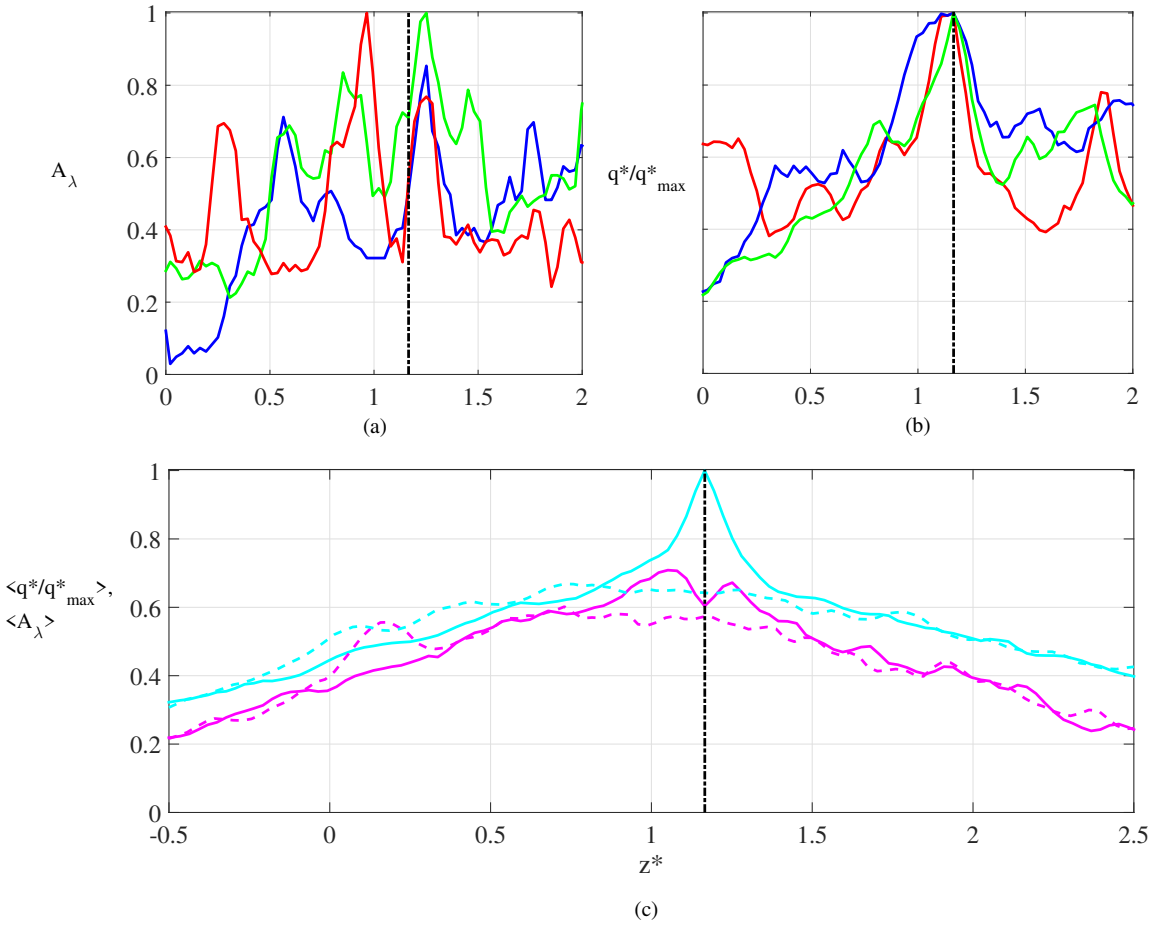

Figure 3.15: (a) A_λ for S-19(blue), S-26(red), and S-47(green) (b) q^*/q^*_{max} for S-19(blue), S-26(red), and S-47(green) (c) Comparison of $< A_\lambda >$(magenta) and $< q^*/q^*_{max} >$(cyan) ensembled by aligning all trailing edge ejections to $z^* = 0$(dashed) and by aligning all q^*_{max} locations to $z^* = 1.18$(solid).

where the head of a hairpin that generates the most upstream peak in $< q^*/q^*_{max} >$ would be expected.

While the trailing edge hairpin sequence was found to contribute to q^*_{max} in two (S-19 and S-26) of the three records examined, only in S-19 did a sequence of increasingly strong hairpins interact to form a strong ejection responsible for q^*_{max}. There were however some general commonalities between all three records examined. Instantaneous records along with the q^*_{max} aligned curves in Figure 3.15 suggest that q^*_{max} peaks correlate with

the axial regions bounded at either end by local maxima in A_λ and the location of q^*_{max} itself correlates with a local minimum in A_λ. Since large magnitude changes in A_λ are mostly associated with regions containing cross-stream oriented structure, the scenario most associated with the q^*_{max} peaks observed in the SPIV data set is the following:

Two highly localized strongly swirling structures (or parts thereof) are oriented in a non-streamwise direction and spaced closely together in the axial direction. The structures involved may be hairpins or other less regularly-shaped structures. The two structures rotate in such a way that together they create strong cross-stream motions in the short pipe segment between them when the fluid in that segment is free of strong wall-normal swirl.

As with S-19, and the results presented by van Doorne and Westerweel (2009) the two swirling regions in question can be hairpin heads that create a large ejection, but as with S-47 and Kuik (2011), the swirling regions can be much more irregular in shape. In light of this, it is expected that well developed hairpin sequences with sufficient strength often will create local a maximum in q^*, but not necessarily the global maximum.

The peak tracking results of Kuik (2011) show that the local peaks that eventually become q^*_{max} originate in the rising region of q^* near the trailing edge, the same region where the SPIV records in this work show frequent hairpins. In light of this, it was surprising that the two sets of curves for the different ensemble methods in Figure 3.15c did not show the key features of the other. This could suggest that on average, the structures associated with q^*_{max} that pass the measurement plane are not dynamically linked to the trailing edge hairpin that is commonly present upstream across the timespan over which each is interrogated. This is counter to what is suggested by the trailing edge hairpin sequences observed to be linked to q^*_{max} in S-19, and S-26. One explanation for this could be that rapid evolution of hairpin sequences, especially as they interact with swirling structures at other azimuthal

locations, creates a situation for records where the q^*_{max} location $1D$ or more downstream, where the hairpin sequence found upstream at the trailing edge has no relation to the process that spawned the q^*_{max} peak downstream. Alternatively, it could be that the distribution of length scales over which a hairpin vortex sequence evolves into a $q*_{max}$ peak is too wide to be captured in this way and smooths to a level that makes it indistinguishable in the ensembles.

Figure 3.16 examines the quantities, $\langle u_r \rangle$, $\langle w^* \rangle - w^*_{lam}$, and $\langle k^*_{ip} \rangle$ for the hairpin registered ensemble averaged puff. Figure 3.16(a,c,e) show the full (r^*,z^*) plane including $\theta = 0$. Figure 3.16(b,d,f) show the average of the two (r^*,z^*) half-planes located at $\theta = \pm 90°$. Figure 3.16a shows the average ejection structure located at the trailing edge centered at $z^* = 0.13$. A second weak ejection region appears downstream near the wall centered at $z^* = 0.62$. By contrast, in Figure 3.16b, the instantaneous radial velocity values in the perpendicular plane average toward zero with the exception of a small positive region near the center of the pipe that appears to be part of the main trailing edge structure. In Figure 3.16c, the strong streamwise velocity deficit at the trailing edge extends from $z^* = -1$ spreading toward the center of the pipe and intensifying as z^* increases. The flow near the trailing edge is slowest for $0 < z^* < 0.2$, the region associated with the strongest ejection velocities, and accelerates immediately downstream. The shapes of the contours in Figure 3.16c begin to match those in Figure 3.16d, beyond $z^* > 1.5$. This suggests that the flow trends toward an axisymmetric average in this region, and has lost its memory of the hairpin on which it was registered. The exception to this trend is a region of strongly accelerated flow near the wall in the lower half of the ejection plane for $1 < z^* < 3$.

Figure 3.16e, shows that the strong velocity deficit noted in Figure 3.16c extending upstream from the trailing edge corresponds closely to the regions where k^*_{ip} increases to its strongest values on average. These strongest values of k^*_{ip} start at the trailing edge and

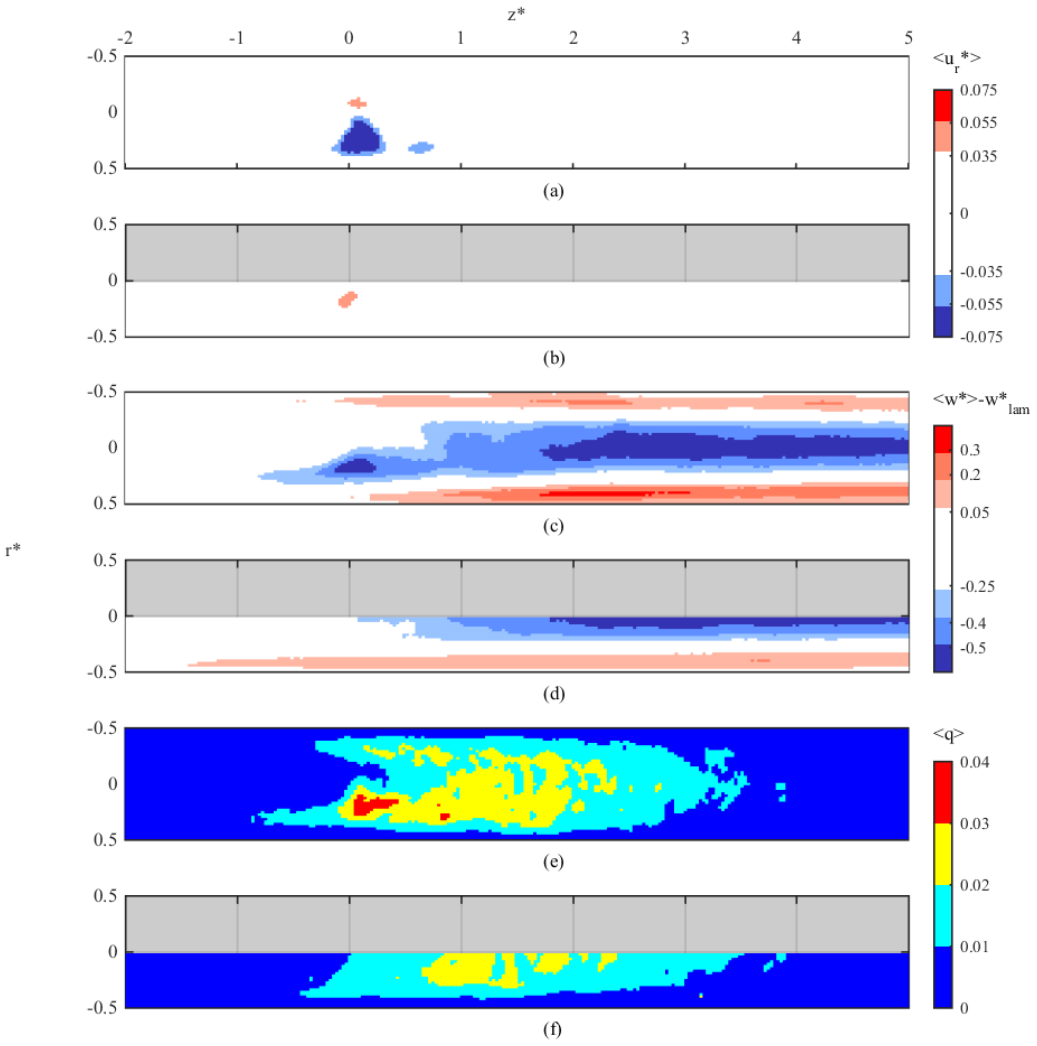

Figure 3.16: Ensemble averaged quantities, $\langle u_r^* \rangle$, $\langle w^* \rangle - w_{lam}^*$, $\langle k_{ip}^* \rangle$ shown for (a,c,e) the (r^*, z^*) plane including $\theta = 0$ and for (b,c,f) the averaged half plane including $\theta = \pm 90°$.

extend over a region that tapers to $z^* = 0.44, r^* = 0.14$. Figure 3.16c shows that the velocity increases through this region. A second small region of strong k_{ip}^* values is located at $z^* = 0.84, r^* = 0.28$. In Figure 3.16e, within $1 < z^* < 2$, the magnitude of k_{ip}^* near the wall directly behind the ejections is stronger than what is found directly opposite from the ejections on the opposing wall and what is found perpendicular to the ejections in Figure 3.16f. Beyond $z^* = 2$ the contours of k_{ip}^* in Figure 3.16e match closely those in Figure 3.16f, indicating an axisymmetric distribution of k_{ip}^* on average. Together, the ensemble contour plots in Figure 3.16 depict a strong ejection from the pipe wall whose effect on the streamwise velocity and in-plane kinetic energy spreads downstream until its interactions with other perturbations in the flow average toward axisymmetry.

Figure 3.17 shows the strongest values of λ_{3D}^* calculated from the ensemble averaged puff. A clear hairpin structure lifts away from the wall inducing an ejection in a similar way to what is shown in Figure 3.6. This average ejection creates a blockage that slows the axial flow locally, around which the rest of the fluid must accelerate, and causes the region of increased k_{ip}^* seen in Figure 3.16. The prominence of the structure reinforces how common it is among puff records. The second smaller average ejection region is also observable downstream of the trailing edge even though the spacing between structures varies within individual records. The streamwise spacing between the most inward radial points on the ejection isocontours is 0.45. This is similar to the average axial spacing of hairpins found in the instantaneous records examined.

Modal Dominance in Puffs

Figure 3.18a shows $C(\theta^*, z^*)$ from Equation 5 for a single puff record. The instantaneous magnitudes of C and C_m correspond well with the simulation data presented by Willis and Kerswell (2008). This is also true for the rest of the puff records in the present study.

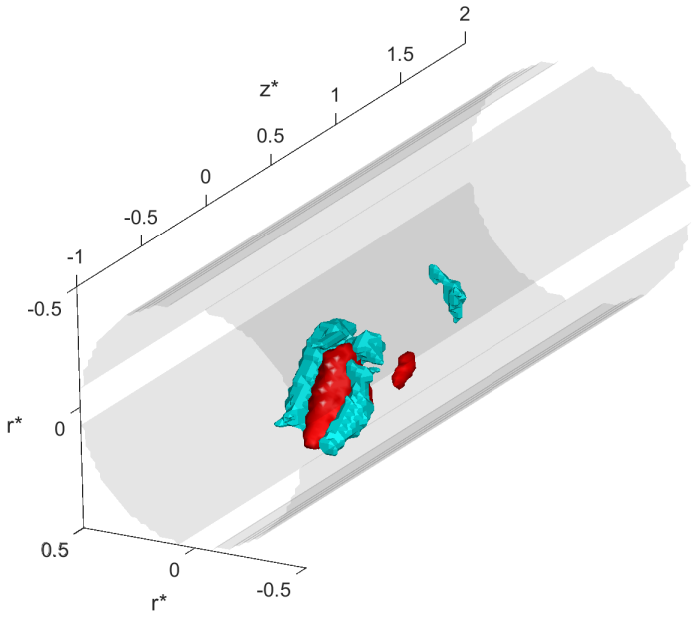

Figure 3.17: 3D isocontours of swirling strength, $\lambda^*_{3D} > 1$ (blue) and radial velocity, $\langle u^*_r \rangle < -0.05$ (red) found in the ensemble averaged puff.

Multiple alternating positive and negative streaks of $w^* - w^*_{lam}$ are clearly visible within $-3 < z^* < -1$. In the region $-1 < z^* < 0$, the length of the contoured areas in C become shorter and they begin to break up. For $0 < z^* < 2$, the pattern of alternating high and low speed regions has weakened significantly. A new streaked pattern appears for $2 < z^* < 6$ with larger azimuthal spacing and generally longer streaks. For $6 < z^* < 16$, a long pair of fast and slow moving regions extends downstream. The corresponding plots of C_m are shown in Figure 3.18b. The alternating streaks in Figure 3.18a within $-3 < z^* < -1$ correspond with large values in the plot of C_4. The elevated C_4 regions give way to C_5 where $-1 < z^* < 0$. Then at the trailing edge, C_5 drops off suddenly. In the region $0 < z^* < 2$, two brief peaks appear in C_4, after which C_3 begins to dominate. In the context of the ensemble average puff data presented in Figures 3.16 and 3.17, it could be expected that the large

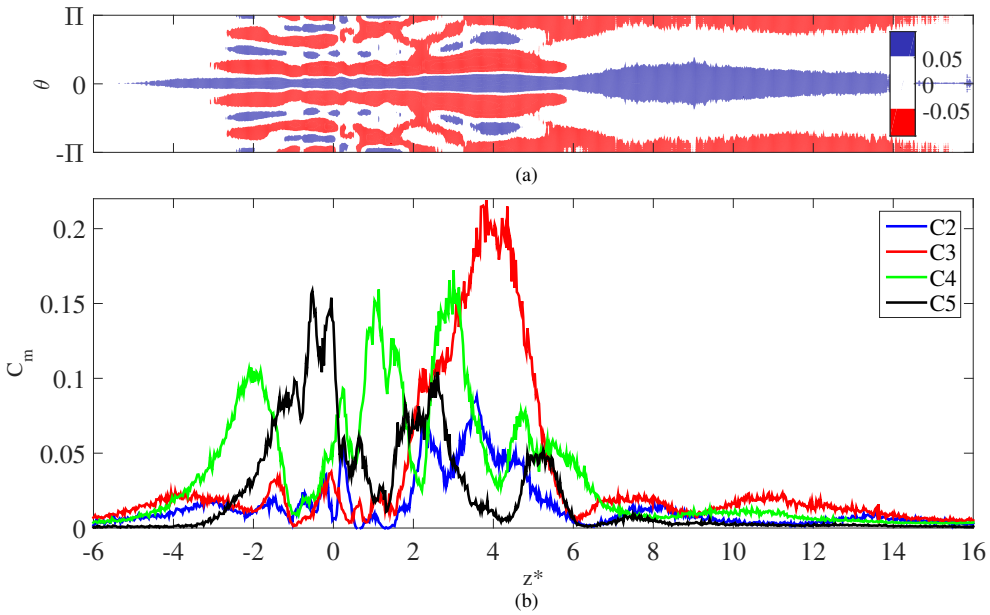

Figure 3.18: The modal analysis of puff S-18 showing (a) contours of $C(\theta^*, z^*)$ at -0.05 and 0.05 and (b) values of C_2-C_5. Dominant modes were defined as $C_m > 0.1$ in keeping with the definitions of Willis and Kerswell (2008).

and dominant hairpin structure would disrupt the m-fold symmetry for which $C(\theta^*, z^*)$ was examined.

For a small distance, $2.5 < z^* < 3.2$, both C_3 and C_4 are elevated above the dominance threshold of 0.1, although this was seldom seen in the overall data set. Typically, only one C_m value exceeded 0.1 at a given z^* location. Moreover, it was often the case that when one C_m value was greater than 0.1, the others were less than 0.05.

The plot in Figure 3.19, shows a gray horizontal line corresponding to each puff, overlaid with colored lines to show locations where a given C_m value exceeded the dominance threshold. In addition to depicting the streamwise evolution of the dominant modes in a given puff, Figure 3.19 allows for the examination of patterns across the data set. Figure 3.19 demonstrates that dominant $C_2 - C_5$ modes are infrequent within $0 < z^* < 1.5$ in

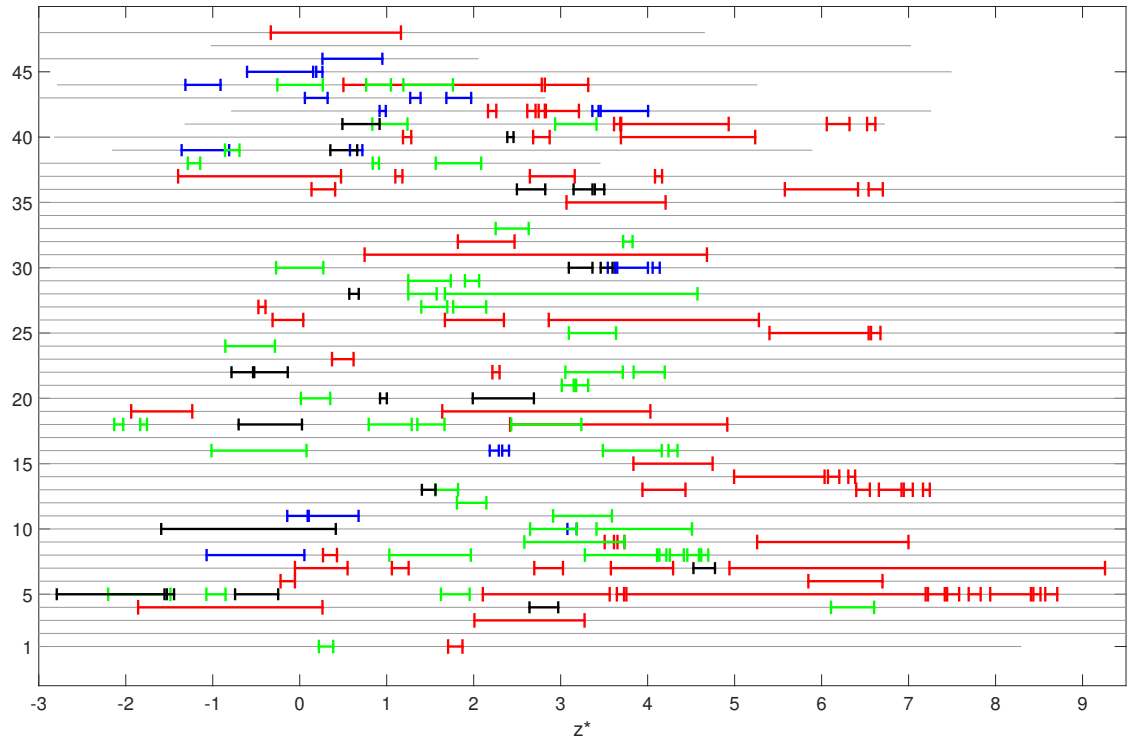

Figure 3.19: Location and length over which each puff exhibits a dominant C_m mode, m = 2(blue), m = 3(red), m = 4(green), and m = 5(black) with each puff numbered on the y-axis.

comparison to the rest of the puff domain. Further, any modal dominance observed within $0 < z^* < 1.5$ is often very short. Only one region centered within $0 < z^* < 1.5$ is longer than 0.7D, while a total of 36 regions centered outside of $0 < z^* < 1.5$ are longer than 0.7D. This shows that the disruption of modes $C_2 - C_5$ by the hairpin structure is a dominant behavior across the dataset.

Overall, we find that 44 of the 48 puffs contain at least one region where some value of C_m dominates. Of these 44, 21 contain dominance upstream of the trailing edge, and 43 have dominance downstream of the trailing edge. Of the 141 regions identified, there were only seven instances where two values of C_m exceeded the dominance threshold in the same location. These overlapping regions revealed no preference in m number as dominant

regions of each number were found to overlap with any of the others. Downstream of the trailing edge in 10 puffs, at least three repeated regions of dominance occurred for the same mode number. Of these, 8 were $m = 3$ and two were $m = 4$. In general, $m = 3$ dominance occurred most frequently, 61 times in total, followed by $m = 4$. In 22 of the 48 puffs, the most downstream region with modal dominance corresponded with m = 3. The data set was examined to determine whether certain upstream mode values or patterns could be linked to the modes observed downstream, and no obvious link or trend was found. Of the 16 puffs that exhibited modal dominance on both sides of the trailing edge, no mode was more likely to persist on either side of the trailing edge than any other. Similarly, the presence of a certain mode upstream did not predict the presence of another downstream.

Figure 3.20 shows the $C(\theta^*, r^*)$ and C_m plots for two additional puffs. These records help illustrate general trends that are common to the overall data set. In both records, there is a long smooth increase in one or more C_m values from as early as $z^* = -6$ up to $z^* = -1$. Then, near the trailing edge, all C_m values fluctuate rapidly, frequently decreasing nearly to zero. These rapid fluctuations occur in Figure 3.18 as well as in Figure 3.20a-b. The steep gradients in C_m create a region of sharp local peaks until $z^* \approx 2$, suggesting a complicated and rapidly evolving organization. Across the data set, in locations where $z^* > 2$, there are many long regions of elevated C_m values that include localized peaks. The end result of this behavior can be seen in Figure 3.19, which shows long regions of modal dominance where $z^* < 0$, short regions of dominance within $0 < z^* < 2$, and long regions where $z^* > 2$. The local peaks amid a generally elevated C_m value explain the intermittent dominance of a single C_m value when $z^* > 2$. No obvious correlation was found between the C_m plots and the features observed in corresponding plots of q^*.

Figure 3.21 shows the probability for the occurrence of each mode at a given value of z^* for the present study along with the corresponding results from Willis and Kerswell

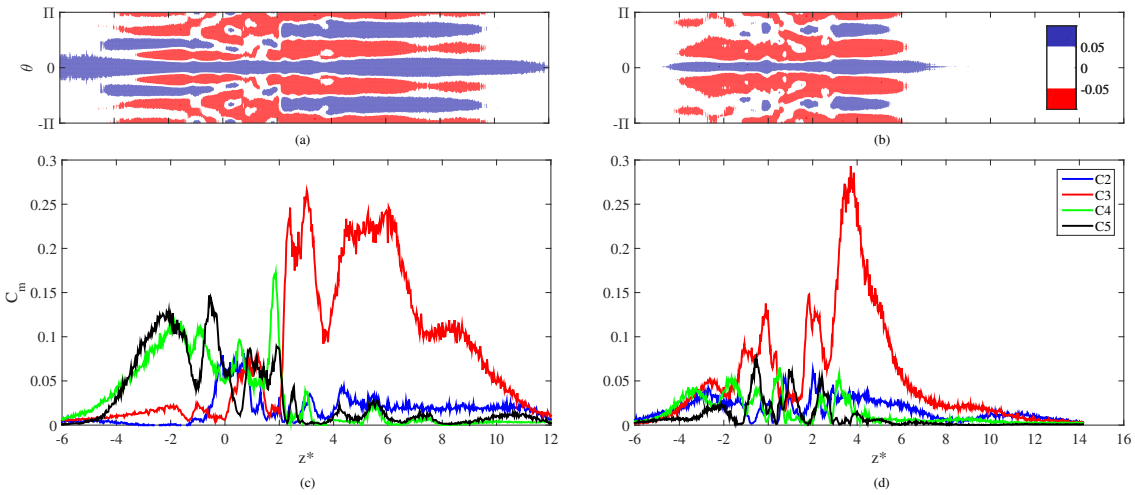

Figure 3.20: The modal analysis for puffs (left) S-5 and (right) S-26, showing (a,b) $C(\theta^*, z^*)$, and (c,d) $C_2 - C_5$.

(2008). The general trends and values in the probabilities from the present study agree well with the findings of Willis and Kerswell (2008). Both studies show that $m = 3$ is the most probable followed by $m = 4$. The plots also reveal a few differences. Figure 3.21a, which corresponds to $m = 2$, indicates that the mode 2 dominance is confined mostly to the region, $-2 < z^* < 2$, with a peak of 0.06 at $z^* = 0.5$. A second peak centered at $z^* = 4$ rises to a probability value of 0.04. For $m = 3$, in Figure 3.21b, a local peak exists at $z^* = 0$ that decreases to a local minimum at $z^* = 1.5$ followed by a wider global peak centered at $z^* = 3.5$. The features are similar to those found in Willis and Kerswell (2008) until $z^* = 5$. Beyond this location, the Willis and Kerswell (2008) curve decreases monotonically, but in the present study, the curve rises to an additional peak at $z^* = 6.2$. In Figure 3.21c(m=4), the two curves are comparable except for two notable features. In the experimental data, the probability decreases immediately after $z^* = 0$ before increasing again, and the strongest peaks are shifted downstream relative to those from the numerical simulation. Figure 3.21d representing C_5 shows strong local peaks at $z^* = 0.2$ and $z^* = 2.9$ along with a local

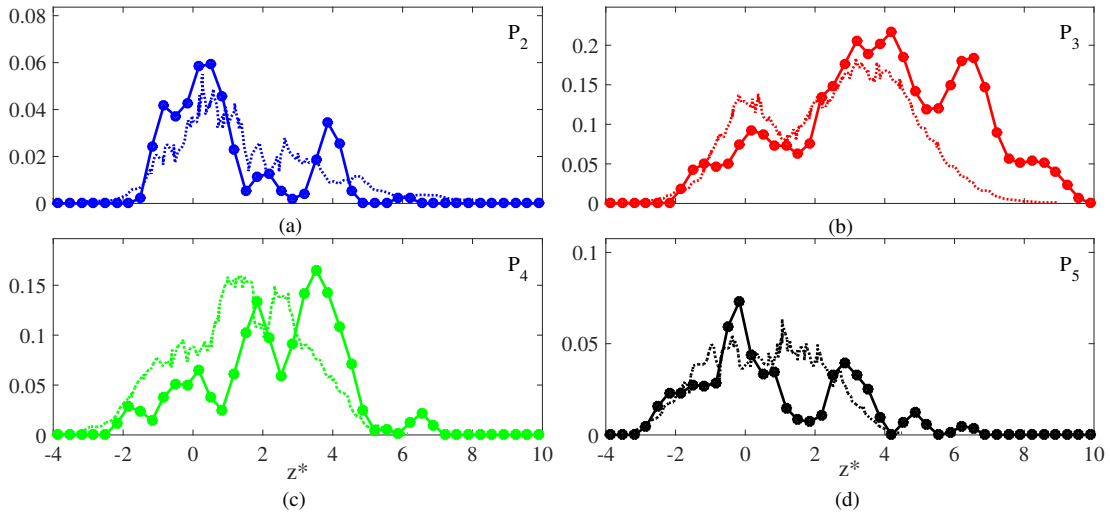

Figure 3.21: The probability that w' at a given z^* location (with bin size in z^* for is 0.33) will contain a dominant azimuthal mode, $m = (a)2$, (b) 3, (c) 4 or (d) 5 at $r^* = 0.4$ for the present study (—). Corresponding plots reproduced from Willis and Kerswell (2008) (- - -) are shown for comparison.

minimum at $z^* = 1.8$. The corresponding results from Willis and Kerswell (2008) instead showed a relatively flat distribution of $P_5 \approx 0.04$ for $-1.5 < z^* < 2.2$.

Figure 3.22 shows the sum of the probabilities for dominant modes with $m = 2 - 5$ from the present study and that of Willis and Kerswell. In both cases, the probability of a dominant mode increases rapidly from $z^* = -2$ up to the trailing edge. In the data from the present study, we note a local minimum at $z^* = 0.8$ which represents the cumulative effect of the decreasing trends downstream of the trailing edge from each mode plotted in Figure 3.21. The overall lower probability of modal dominance at $z^* = 0.8$ along with the higher probability at $z^* = 3$ are prominent differences between the present study and the results from Willis and Kerswell (2008) which show a relatively flat total probability of 0.3 for $0 < z^* < 3$. The local minimum near $z^* = 0.8$ is also consistent with the instantaneous C_m plots for individual puffs like the ones in Figure 3.18 and Figure 3.20, where many C_m values just behind the trailing edge fall below the 0.1 threshold. Downstream of $z^* = 5$,

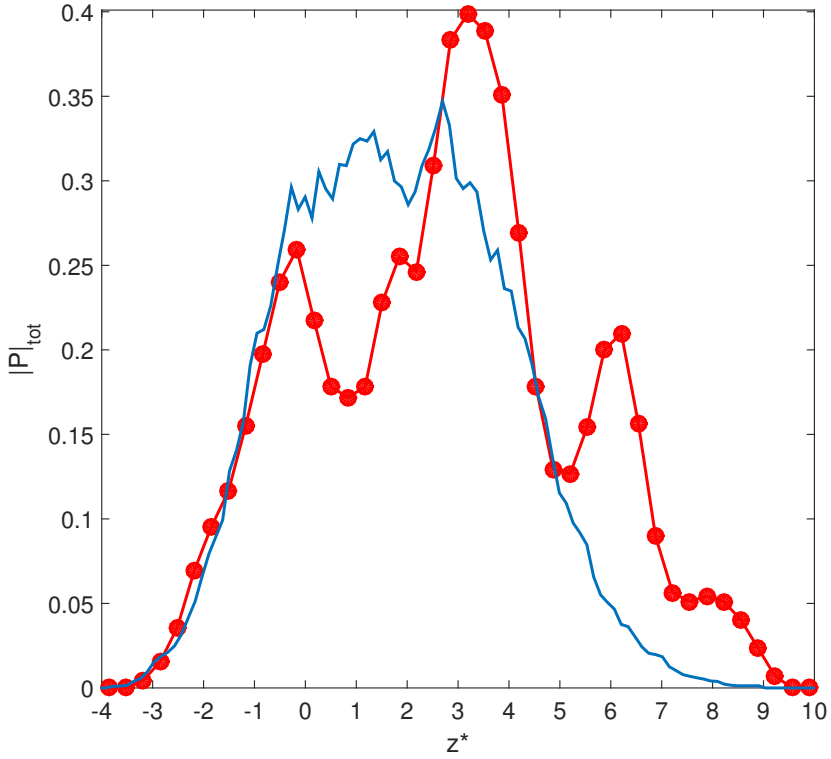

Figure 3.22: The sum of the $m = 2-5$ modal dominance probabilities vs z^* for the present study (red) and that of Willis and Kerswell (2008) (blue).

the present study shows higher probabilities than those found in Willis and Kerswell (2008) including the local peak at $z^* = 6.2$ that comes predominantly from $m = 3$.

To understand the differences in the results, we consider differences in how they were obtained in the two studies. First, the trailing edge location was determined differently. Willis and Kerswell (2008) smoothed w_{CL} over a range of $+/-1D$ near the trailing edge, then identified $z^* = 0$ based on a threshold value. When this method is applied to the present data, the trailing edge shifts downstream by 0.6D on average. This average shift was unexpected given the agreement between the total probability curves between the present study and Willis and Kerswell (2008) within $-4 < z^* < -1$. The shape of the total probability

curve from the present study is also altered. The first two peaks are smoothed somewhat, although the first local minimum remains distinct and occurs at a similar location, In addition, the third peak is largely smoothed out, leaving elevated probability values for $4 < z^* < 10$ compared with the curve of Willis and Kerswell (2008).

Qualitatively, we find that the nature of the streamwise velocity variations upstream of the trailing edge differs from that downstream. Figure 3.23 shows cross-sections of $w^* - w^*_{lam}$ in two puffs where $m = 5$ is found to be dominant. In Figure 3.23a the cross section is upstream of the trailing edge, while in Figure 3.23b it is downstream. The strengths of the w' values responsible for the m=5 mode patterns in both cross sections are similar in magnitude. Despite this similarity, q^*, and streamwise vorticity magnitude averaged over the cross section in Figure 3.23b are 25 and 3.8 times higher than in Figure 3.23a, respectively. In the upstream field, the strongest values of streamwise vorticity are located near the center of the pipe. There is no obvious correspondence with the $m = 5$ streamwise velocity variations close to the wall. On the other hand, the downstream field includes alternating regions of positive and negative vorticity surrounding each location of slow moving fluid.

Differences also exist in the streamwise velocity patterns themselves. The upstream field shows regions of fast moving fluid near the pipe wall alternating with coherent slow moving regions. This pattern was noted also in Willis and Kerswell (2008) and associated with traveling waves. By contrast, the downstream field shows stronger fast-moving regions near the wall with a strongly decelerated central region that only infrequently extends towards the wall between the fast-moving regions. Willis and Kerswell (2008) noted a similar pattern of a slow central region with radial extensions towards the wall and an absence of defined slow moving zones near the wall within $-2 < z^* < 4$. They noted that this flow pattern was similar to those found in slug flows at higher Reynolds numbers, where energy characteristics differ from those in known traveling wave solutions.

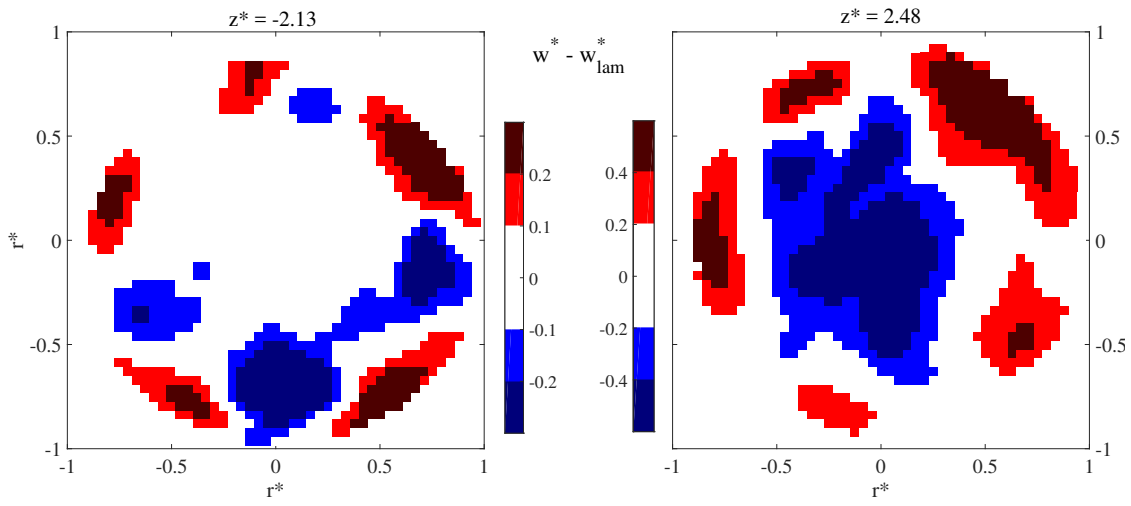

Figure 3.23: Two different m=5 dominant cross sections of $w^* - w^*_{lam}$ are shown, (a) upstream of the trailing edge in puff S-5, and (b) downstream of the trailing edge in puff S-20.

3.2.2 Planar PIV

Important considerations of the quasi-3D reconstructions built from the SPIV data motivated the employment of the PPIV setup. Since the reconstruction employs Taylor's Hypothesis, local differences in propagation velocity of coherent structures are neglected. This could lead to uncertainties that are substantial. Flow structures inside the puff could be propagated at an incorrect velocity that results in improper spacing between structures. Radial differences in propagation velocity, as suggested by Shimizu and Kida (2009), could result in distorted reconstructions of structures that span an appreciable radial domain. Finally, the timescales over which hairpins evolve and interact with other structures were unknown, and therefore, so too were the axial distances over which structures could be assumed 'frozen'.

To investigate these considerations, PPIV measurements were taken in two configurations, wide-field and narrow field. A total of 35 narrow-field PPIV puff records were recorded. Because the bulk displacement of the fluid was in the plane of the light sheet,

a larger dt was allowable than in the SPIV case. Thus, the PPIV records, despite being obtained prior to the development of the timing system that allowed $dt \neq dT$, captured a span of $z^* \approx 21$. For some of these records the PIV trigger was deliberately set in order to capture regions of the puff away from the trailing edge for further investigation. As a result 19 narrow field puffs contained trailing edges. These puff records are labeled as PN-1 through PN-19.

A total of 28 wide-field PPIV puff records were recorded, and because the trailing edge was the specific target for capture, 27 of the records contained trailing edges. The one record without the trailing edge captured most of the puff but did not contain enough laminar flow upstream to include it. The wide-field puff records are labeled PW-1 through PW-27.

Using the propagation velocities of axial fluctuations reported in Shimizu and Kida (2009) (see Section 1.2.2), it would be expected that radially localized features such as hairpin heads near the trailing edge located at $r^* < 0.37$ would propagate faster than w_b, and therefore be spaced closer together in the SPIV reconstructions than they exist in reality. Results from Shimizu and Kida (2009) would also suggest that the ensemble averaged ejection and hairpin structures at the trailing edge shown in Figure 3.17 which extend over a radial domain $0.15 < r^* < 0.31$ would experience a mismatch in axial propagation velocity of $\approx 0.53 w_b$ between the outward and inward most locations. Over the length of the structure, $0.28D$, this velocity mismatch would act to overestimate the propagation of the outward parts of the structure and underestimate that of the inward parts. The difference in propagation distance at the downstream end of the structure developed by this velocity mismatch would be $0.15D$, roughly half the axial length of the structure. For a sequence of hairpins that span a larger axial and radial domain, the fidelity of the reconstruction could be affected even more.

The predictions using the data from Shimizu and Kida (2009) are problematic, however,

due to a number of factors:

- The method for constructing the time average was based on aligning snapshots using the average propagation velocity of the puff and not by aligning the trailing edge location in each time step. As a result the trailing edge location in the average has been smoothed significantly.

- The propagation velocities were calculated as an average over the azimuthal coordinate. As noted in the SPIV results, large asymmetries exist on average in w^*, k_{ip}^*, and u_r^* near the trailing edge.

- The propagation velocities were calculated using a large time difference that corresponds to $t^* = 1.57$. This time difference would correspond to four times the average spacing found between hairpins in the SPIV data.

- The axial spacing of grid points in the simulation was such that the minimum resolvable wavelength is $0.098D$, which may be insufficient to capture significant energy peaks in the flow (see Kuik (2011)).

As a result, the accuracy of applying the estimated propagation velocities to structures like hairpins and hairpin sequences was unknown. While a direct comparison between simultaneously measured instantaneous structures (a la Dennis and Nickels (2008)) was not possible with the present data, comparisons were still possible across the SPIV and PPIV datasets.

Since SPIV reconstructions suggest that hairpins in puffs could be at any azimuthal location when they pass the PPIV measurement plane, it was expected that only a limited number of the records would contain hairpin sequences whose legs straddle the PPIV measurement plane. By inspecting the wide-field PPIV data, three such records were identified.

This section explores these three records along with two others to explore both the evolution of the hairpin sequences and the possible implications on the fidelity of the SPIV reconstructions.

For clarity, in the discussion of the instantaneous PPIV records, the terms 'core', 'ejection' , and 'injection' are used to describe regions in the field with, large magnitude λ^*_{2D}, large mangitude velocity components inward, away from the wall, and large magnitude velocity components outward, toward the wall, respectively.

Figure 3.24a-h shows eight instantaneous u^* fields from one wide-field planar puff record, PW-23. The cores, with large values of λ^*_{2D}, and all with clockwise rotation, are marked and their corresponding velocities throughout the sequence are shown below the sequence in Figure 3.24i. The swirling cores shown lie upstream of the largest fluctuations in u^* for PW-23 and downstream of nearly all strong fluctuations in u^*. This suggests that the swirling cores are near the location that would have been registered as the trailing edge in the SPIV setup. In Figure 3.24a, a single core swirls strongly, unaccompanied by strong cross-stream velocity fluctuations. Strong cross-stream fluctuations begin to develop by 3.24b where an ejection appears upstream of the core and an injection appears downstream. In Figure 3.24c an inclined ejection develops upstream, extends away from the wall, and terminates at the now stronger core. The shape of the core along with the upstream ejection and downstream injection is remarkably similar to hairpins noted in the SPIV data, and likely indicates the head of a hairpin. From Figure 3.24(a-c), the core grows and the ejection associated with it grows and intensifies. By Figure 3.24d, a second core appears 0.41D upstream from the first. This spacing agrees with the spacing of hairpins reconstructed from SPIV records. Additionally, the ejection upstream of the original core intensifies and extends away from the wall toward the center of the pipe. The ejection associated with the downstream swirling region extends upstream outside of a much stronger

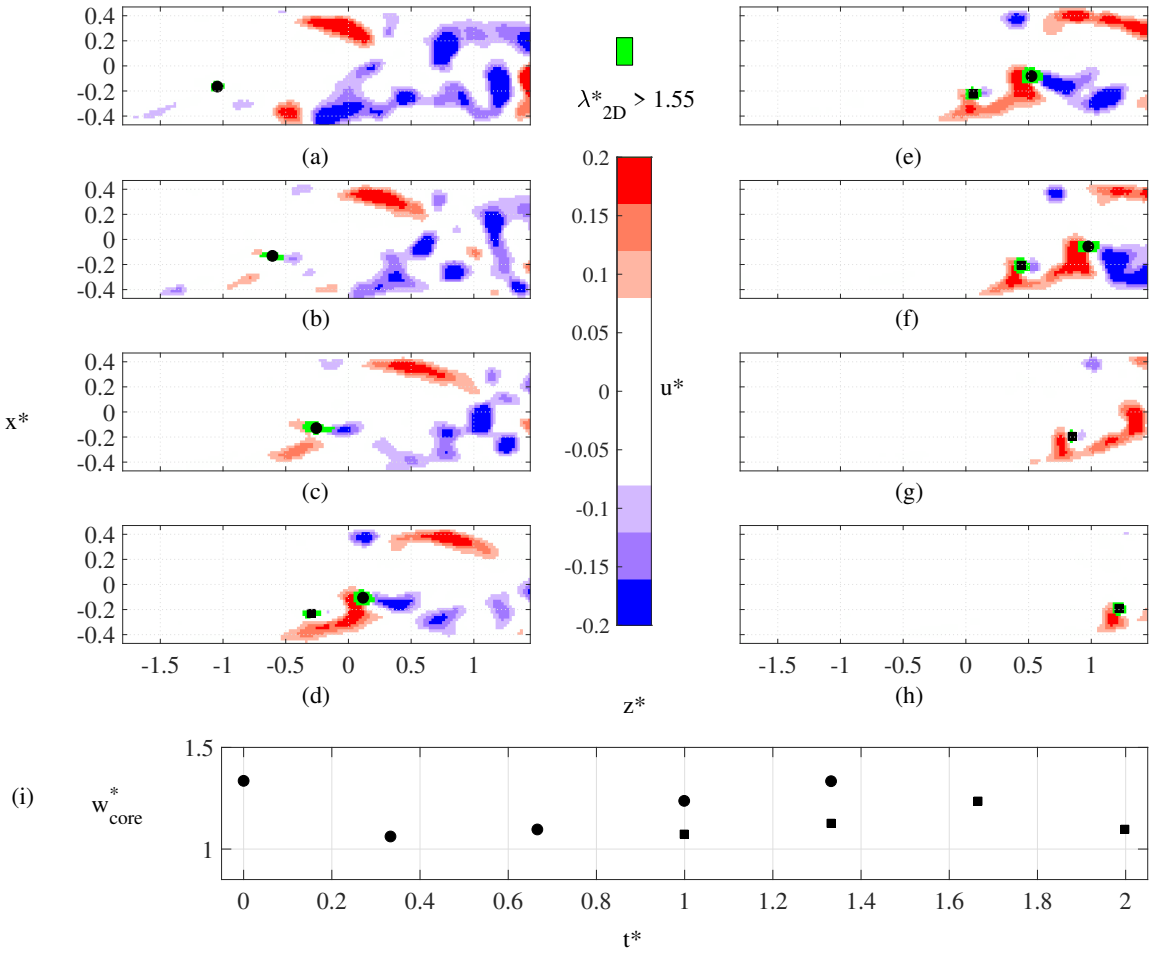

Figure 3.24: (a-h) PPIV sequence showing the development of a hairpin sequence in record PW-23. The dimensionless time spacing between images is $0.33D/w_b$. The vertical axis in each sub-figure shows the x^* coordinate defined from the center of the pipe, while the horizontal axis shows the z^* coordinate defined from the coordinates used in the PIV calibration image. Seven equally spaced contours range from blue to red show $-0.2 < u^* < 0.2$, while green areas show selected regions where $\lambda^*_{2D} > 1.55$. and $\omega^*_y < 0$. The centriods of the swirling regions are each marked with a different shape and were used to calculate the velocities shown in (i).

injection. In Figure 3.24e, the injection accompanying the upstream core becomes strong enough to visualize, and the ejections upstream of both cores strengthen.

In Figure 3.24f a strong streamwise gradient in u^* develops at the downstream side of the core located at $x^* = -0.06$ and extends almost all the way out to the wall. Because the

downstream core leaves the frame in Figure 3.24g, its velocity was not calculated in Figure 3.24i. In Figure 3.24g, the intensity of both the ejection and injection associated with the upstream core diminishes. Additionally, the downstream ejection lifts further from the wall and stretches downstream significantly. The remaining upstream core is associated with zones of cross-stream velocity that continue to weaken by the time it reaches Figure 3.24h. As they move downstream through the sequence, both the downstream and upstream cores move inward steadily, covering a distance in x^* of 0.11 and 0.04, respectively.

Figure 3.24i shows that the swirling cores move faster than w_b throughout the sequence. The average uncertainty in the core velocity is estimated to be $0.05w_b$ for all of the swirling cores discussed in this section. The original swirling core decelerates from $1.34w_b$ to $1.06w_b$ between Figure 3.24b and Figure 3.24c. It then accelerates to $1.24w_b$, by the time the upstream core is formed. Both the downstream and upstream cores continue to accelerate throughout the sequence to Figure 3.24f and Figure 3.24g where they reach velocities $1.33w_b$ and $1.24w_b$, respectively. In Figure 3.24h, the upstream region decelerates to $1.1w_b$.

Figure 3.25 shows contours of $w^* - 1$ for the same sequence shown in Figure 3.24. Throughout the sequence the flow both opposite to and upstream of the swirling cores is laminar-like, with velocity above $1.8w_b$ near the center of the pipe, and velocity close to w_b near $x^* = \pm 0.3$. This is further evidence that the swirling cores are located near the trailing edge as it was defined in the SPIV records. At the beginning of the sequence, the initial core is accompanied by a slow moving region that extends outward from the wall starting more than $0.5D$ upstream of the swirling core despite the lack of a strong ejection region in Figure 3.24a. The lone core is roughly $1D$ upstream of the location where the laminar flow across the center region of the pipe is disrupted. This distance is larger than what was observed on average in the SPIV data shown in Figure 3.16, where the upstream hairpin structure has its head roughly $0.6D$ upstream of the point where the centerline velocity is similarly disrupted.

However, the distance noted between the core and centerline disruption in Figure 3.24a is within the range of distances between similar events observed in the quasi-instantaneous SPIV reconstructions. By Figure 3.25c, the slow moving region has elongated significantly and the slow moving fluid just upstream of the core has concentrated into a local minimum at ($z^* = -0.7, x^* = -0.3$). The local minimum location corresponds with the strengthening of the ejection region in Figure 3.24c. As the new upstream core develops in Figure 3.25d, the fluid between the two cores has accelerated nearly to w_b. This is likely due to the upstream core pulling fast moving fluid outward on its downstream side, against the inward motion induced at the upstream side of the downstream core. When the ejections in Figure 3.24 are compared to the axial velocity plots in Figure3.25, the axial velocity component varies less than $0.1w_b - 0.2w_b$ over the area of the ejection. The axial velocity of the ejection regions also does not vary more than one contour level from frame to frame suggesting their propagation velocity varies over time within a similar range as the swirling cores.

Interestingly, the angle made by the pair of cores with the wall is 17° when they first appear in Figure 3.25d and later in Figure 3.25f is 16°, the same values made by inclined hairpin packet structures observed by Christensen and Adrian (2001) in instantaneous fields inside a turbulent boundary layer experiment at $Re_\tau = 547$ and 1734, respectively. Christensen and Adrian (2001) found the mean structure to be inclined at an angle of $12° - 13°$. The angle of the cores in Figure 3.25 remained consistent over time despite the increasing velocity and inward motion of both cores.

Figure 3.26 shows a similar sequence to Figure 3.24, but measured in puff record PW-9. In this case, coherent cores in the top half of the subplots rotate counterclockwise. This results in inverted colors that represent ejections vs. injections compared to Figure 3.24. In Figure 3.26a two cores are present. The most upstream core has a stronger ejection while the downstream core has a stronger injection. In Figure 3.26b, the cores are accom-

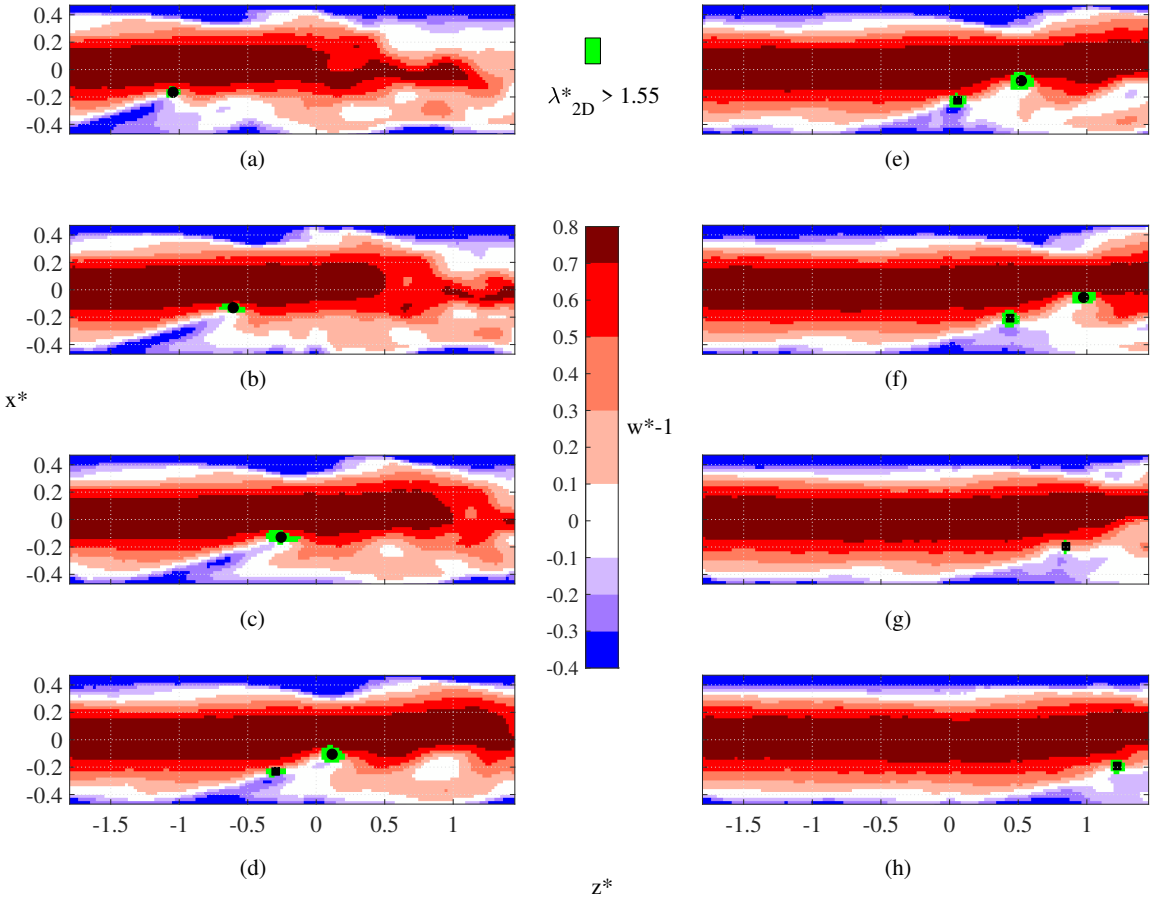

Figure 3.25: PPIV sequence showing $w^* - 1$, the difference in the axial velocity from w_b for PW-23. The dimensionless time spacing between images is $0.33D/w_b$. The vertical axis in each sub-figure shows the x^* coordinate defined from the center of the pipe, while the horizontal axis shows the z^* coordinate defined from the coordinates used in the PIV calibration image. Green areas show selected regions where $\lambda^*_{2D} > 1.55$. and $\omega^*_y < 0$ The centriods of the swirling regions are each marked with a different shape.

panied by stronger cross-stream velocity regions. The contours of u^* near the downstream core,marked by a circle, show a strong streamwise gradient in Figure 3.26c that appears similar to the one found in Figure 3.24f near a swirling core coincidentally also marked by a circle. Meanwhile, a new upstream core develops. As the record progresses to Figure 3.26d, the most downstream core from Figure 3.26c reorients or leaves the measurement plane. The sharp gradient however, remains. From Figure 3.26e, the cycle repeats again, where the most downstream core disappears, and a new fast-moving core develops upstream. This time however, the cores begin to move radially inward in Figure 3.26f, and the strong streamwise gradient in u^* is no longer visible in the field. The most upstream core in Figure 3.26f develops a stronger ejection upstream in Figures 3.26(g-h), while the most downstream swirling region in Figure 3.26f develops a strong injection in Figure 3.26g. The ejection associated with the downstream core appears to weaken in Figure 3.26h. Throughout the sequence, none of the cores in Figure 3.26 develop the elongated ejection region observed in Figure 3.26. Apart from the two initial cores in Figure 3.26i, the swirling cores move significantly faster than w_b.

As with the cores from PW-23 in Figure 3.25, Figure 3.27 shows that the cores in PW-9 begin roughly $1D$ upstream from the centerline velocity disruption. However, unlike the fields from PW-23, neither of the two initial cores in Figure 3.27a-b are accompanied by an inclined region of relatively slow moving fluid. Instead the slow moving fluid extends further inward everywhere upstream. However, an inclined slow moving region does appear in association with the developing triangle core in Figure 3.27c-d. By Figure 3.27d, the relatively slow moving cores are now more than $1.5D$ upstream from the center region velocity disruption. A new inclined slow moving region develops to accompany the star region in Figure 3.27e-g. The angle made the by triangle and star cores with the wall in Figure 3.27g is 7°, much lower than that of PW-23. By Figure 3.25h, the sequence of cores that was once

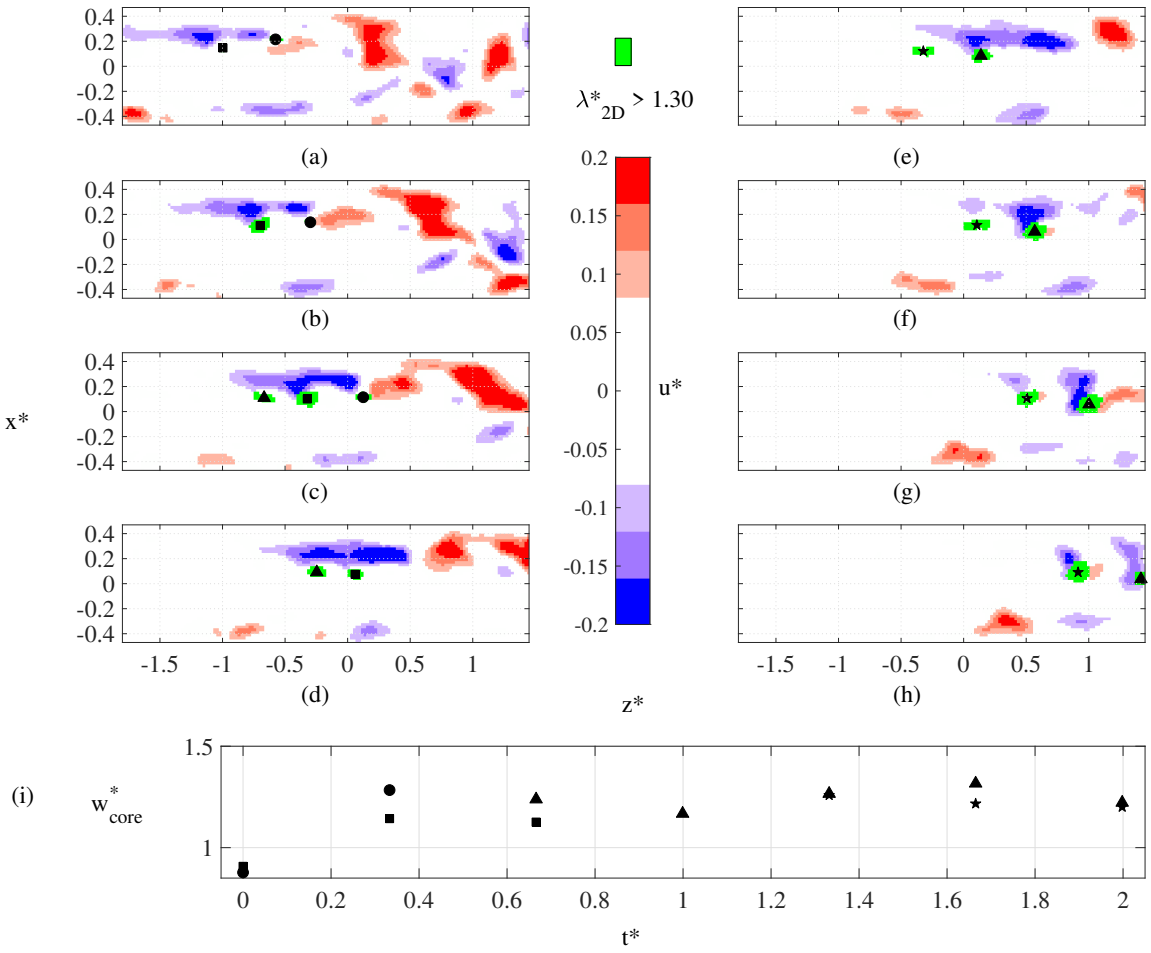

Figure 3.26: (a-h) PPIV sequence showing the development of a hairpin sequence in record PW-9. The dimensionless time spacing between images is $0.33D/w_b$. The vertical axis in each sub-figure shows the x^* coordinate defined from the center of the pipe, while the horizontal axis shows the z^* coordinate defined from the coordinates used in the PIV calibration image. Seven equally spaced contours range from blue to red show $-0.2 < u^* < 0.2$, while green areas show selected regions where $\lambda^*_{2D} > 1.3$. and $\omega^*_y > 0$. The centriods of the swirling regions are each marked with a different shape and were used to calculate the velocities shown in (i).

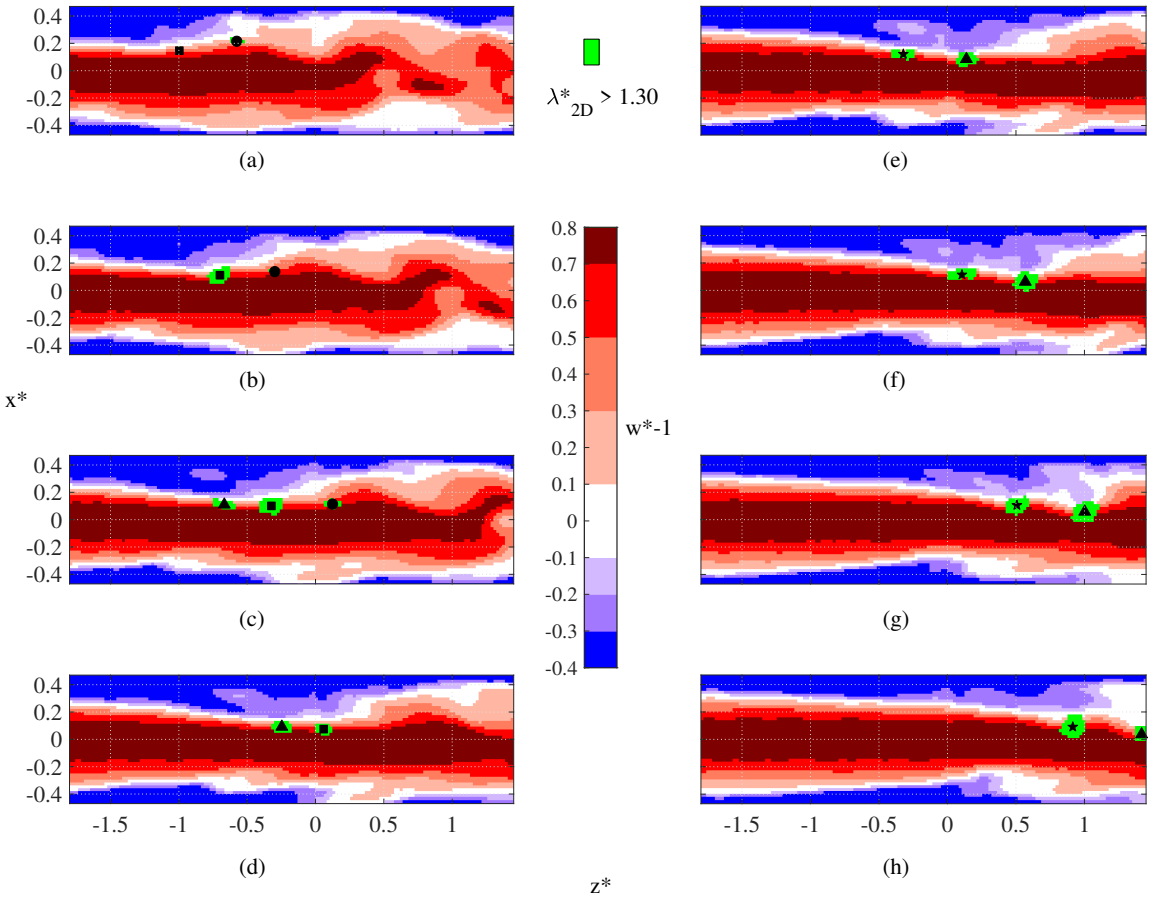

Figure 3.27: PPIV sequence showing $w^* - 1$, the difference in the axial velocity from w_b for PW-9. The dimensionless time spacing between images is $0.33D/w_b$. The vertical axis in each sub-figure shows the x^* coordinate defined from the center of the pipe, while the horizontal axis shows the z^* coordinate defined from the coordinates used in the PIV calibration image. Green areas show selected regions where $\lambda^*_{2D} > 1.3$ and $\omega^*_y > 0$ The centriods of the swirling regions are each marked with a different shape.

slowing relative to the velocity disruption at the center of the pipe, now contributes to it. The variation in the axial velocity over the area of the ejections and with time throughout PW-9 is similar to that found in PW-23.

Figure 3.28 shows a well developed core in PW-20 and its associated ejection that by Figure 3.28c, extends $1D$ upstream from the core location with an inflection point that is about $0.4D$ upstream. Meanwhile, a sharp streamwise gradient in u^* develops at $z^* = -0.5$

that extends from $x^* = 0.2$ through the swirling core near the centerline and outward to $x^* = 0.3$. In Figure 3.28d, a new core and an associated ejection pinches off $0.61D$ upstream from the first. The circles in Figure 3.28i show that the initial core in Figure 3.28a-d is moving rapidly downstream at velocities near $1.4w_b$. In Figure 3.28e the initial core is no longer visible and has likely reoriented and distorted through interactions with other swirling motions outside the measurement plane. In a similar way to Figure 3.25, the secondary core that develops in Figure 3.28d continues downstream throughout the rest of the sequence moving slightly inward with an axial velocity that remains close to $1.1w_b$. In Figure 3.28(e-h), on the opposite side of the pipe, a counterclockwise swirling core develops (triangle) and shows a strong upstream ejection region in blue. By Figure 3.28h, its ejection region has inclined significantly leaning inward over its downstream length and the injection downstream of the core is stronger in agreement with the increased strength of the core. By the end of the sequence, the triangle core has decelerated from its originally high propagation velocity of $1.33w_b$ to $1.13w_b$.

Figure 3.29 further highlights the striking similarities to the process that was observed in PW-23 (Figures 3.24 and 3.25), including the $1D$ distance between the initial core and the center region velocity disruption, and the 17° angle created by the swirling cores and the wall. The slower moving region associated with the downstream core in Figure 3.29d is still present in Figure 3.29e despite the loss of the core. This is similar to the centerline velocity disruption in Figure 3.29b, and similar to the scenario in S-26, shown in Figures 3.12 and 3.11, where the most downstream in a sequence of hairpins has its head at the centerline and is interacting with other strong swirling structures that extend to the center from other azimuthal locations. Consistent with what has been observed for PW-23 and PW-9, the ejection regions on the outward and upstream side of all three cores show large areas of near-uniform axial velocity with small accelerations over time.

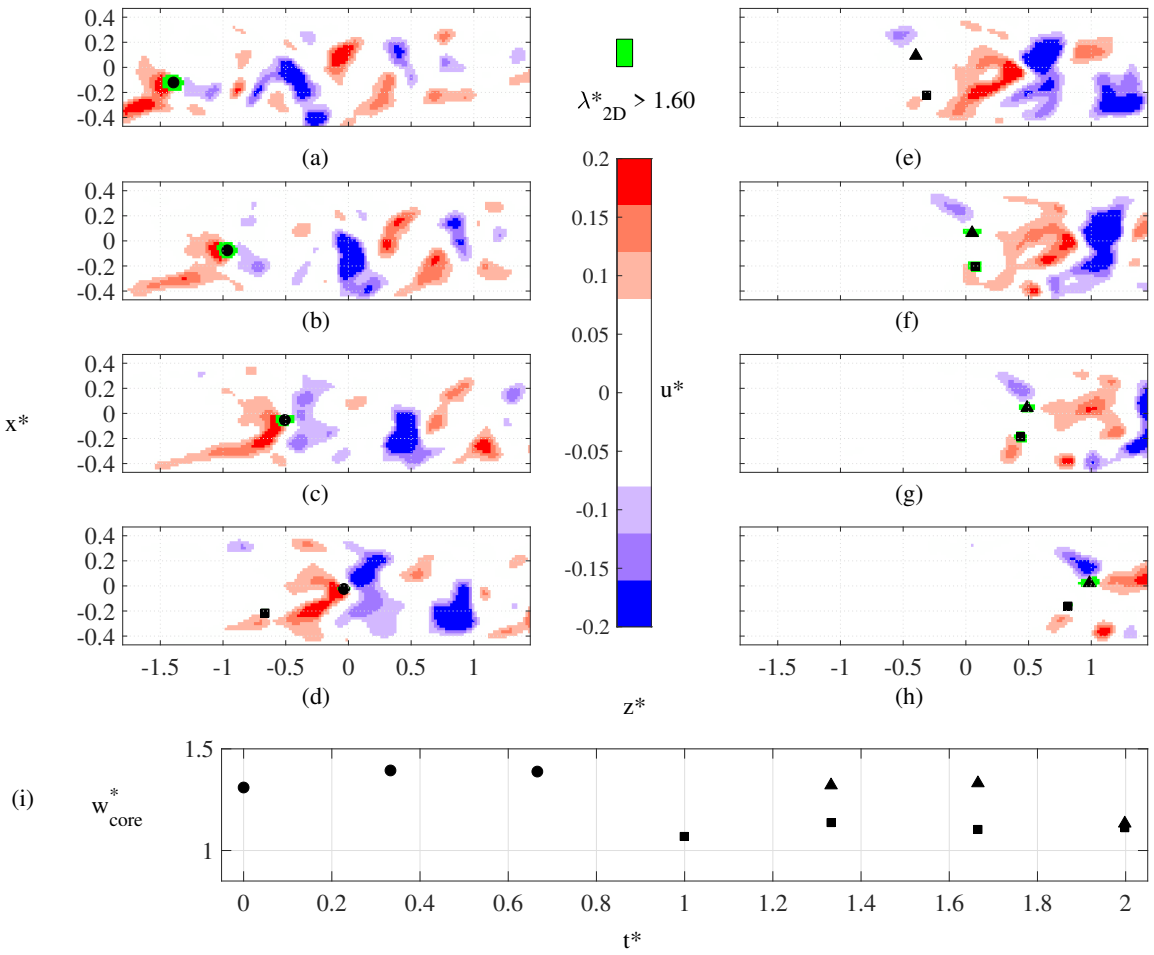

Figure 3.28: (a-h) PPIV sequence showing the development of a hairpin sequence in record PW-20. The dimensionless time spacing between images is $0.33D/w_b$. The vertical axis in each sub-figure shows the x^* coordinate defined from the center of the pipe, while the horizontal axis shows the z^* coordinate defined from the coordinates used in the PIV calibration image. Seven equally spaced contours range from blue to red show $-0.2 < v^* < 0.2$, while green areas show selected regions where $\lambda^*_{2D} > 1.6$. and $x^* > 0$. The centriods of the swirling regions are each marked with a different shape and were used to calculate the velocities shown in (i).

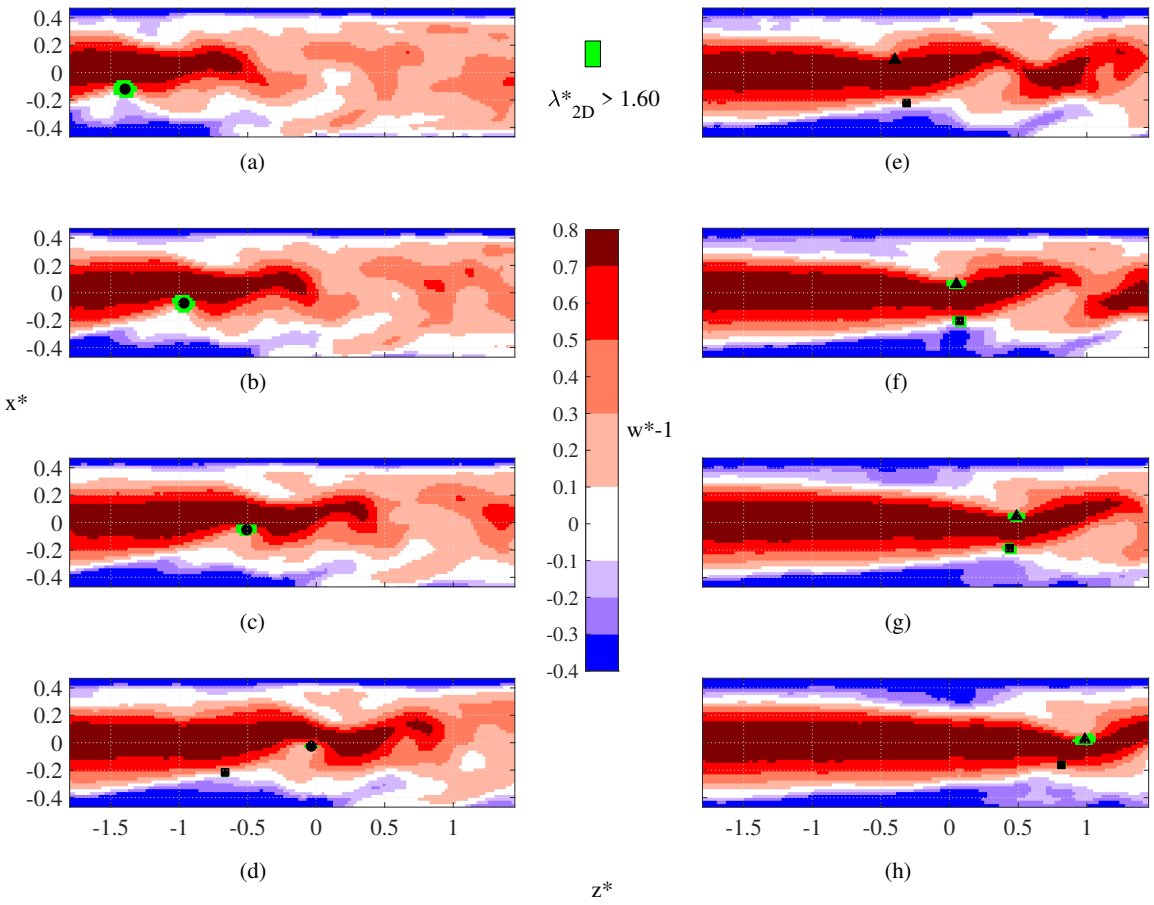

Figure 3.29: PPIV sequence showing $w^* - 1$, the difference in the axial velocity from w_b for PW-20. The dimensionless time spacing between images is $0.33D/w_b$. The vertical axis in each sub-figure shows the x^* coordinate defined from the center of the pipe, while the horizontal axis shows the z^* coordinate defined from the coordinates used in the PIV calibration image. Green areas show selected regions where $\lambda^*_{2D} > 1.6$ and $\omega^*_y > 0$ The centriods of the swirling regions are each marked with a different shape.

It is worth noting that the hairpin sequence development observed in Figures 3.24-3.28 parallels closely that which was tracked in a turbulent boundary layer by Jodai and Elsinga (2016), specifically Figure 10c-f of that publication. Additionally, the formation of a strong streamwise gradient in the u^* velocity component occurred in Figures 3.24-3.28 when an injection region found at the most downstream end of a hairpin sequence strengthened and created a wall normal interface with a similarly strong ejection region. The development of this gradient seemed to signal the reorganization of the fluid in the downstream hairpin and also correlated with the generation of a new hairpin upstream.

In PW-19, PW-23, and PW-47, the average propagation velocity of swirling cores that appeared to be hairpin heads was $1.19w_b$ and increased with wall normal distance. This trend is shown in Figure 3.30. Apart from the two slow moving cores found at the beginning of the PW-9 sequence in Figure 3.26, the propagation velocities found in the PPIV data showed relatively good agreement with those calculated by Shimizu and Kida (2009) and Duguet et al. (2010) near the trailing edge. The velocity cores from the present data were all found to move slower than those calculated by Shimizu and Kida (2009) $1D$ upstream from the average trailing edge location. The trailing edge definition used by Shimizu and Kida (2009) searches for the steep drop off in centerline velocity and likely located the trailing edge approximately $0.5D - 1D$ downstream, on average, from the method used to identify the trailing edge ejections in the SPIV records. The vortices tracked by Duguet et al. (2010) were defined as local maxima in azimuthal vorticity and were found in locations that represent a boundary between regions upstream with very little azimuthal vorticity and regions downstream with high values of azimuthal vorticity. These vortices are expected to lie in a similar axial location to the trailing edges calculated for the SPIV data.

The spacing between the neighboring vortex cores shown in the PPIV data over time is displayed in Figure 3.31. In general, the vortex sequences observed show a trend of

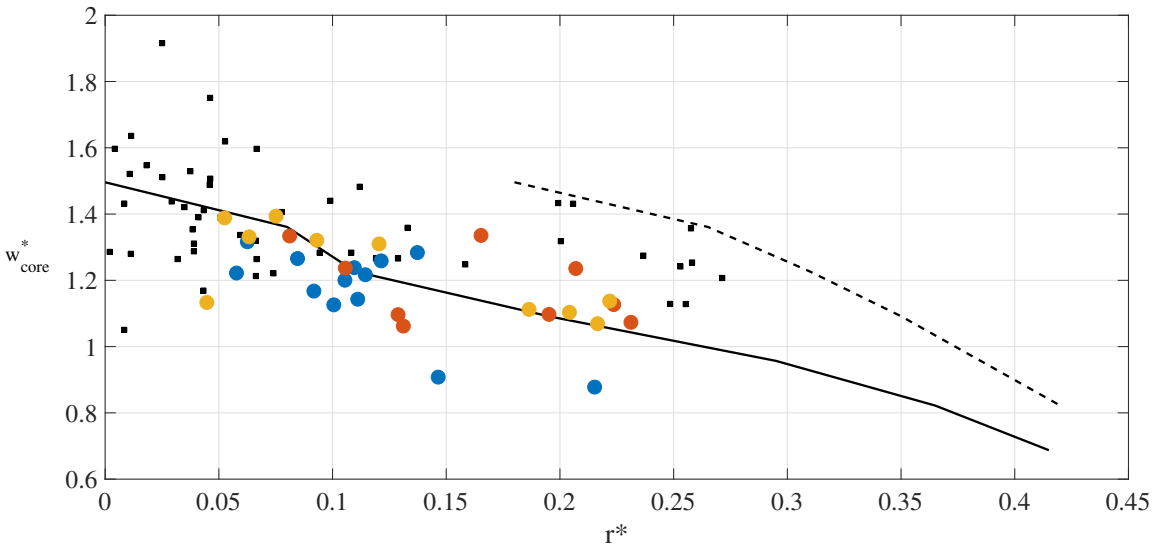

Figure 3.30: The propagation velocities of swirling cores against radial location in found in the PPIV data set in PW-9(blue circles), PW-23(orange circles), and PW-13(red circles) is shown along with the data extracted from Shimizu and Kida (2009) at the trailing edge (—) and 1D upstream (- - -), and individual velocities of vortices at the trailing edge of a puff in Duguet et al. (2010) (■).

increasing spacing with time as the older hairpin moves away from the wall and is accelerated by the oncoming undisturbed flow. The average spacing between hairpin heads in the PPIV records was 0.45D, which is larger than the 0.39D found by sampling hairpins in the SPIV reconstructions. This is in-line with the observation that hairpin heads found in the PPIV nearly always propagated at velocities higher than w_b, the propagation velocity used in SPIV reconstructions. Further, it was common in the PPIV records that the downstream hairpin head was moving faster than the upstream hairpin head, resulting in the trend of increasing spacing in Figure 3.31. On average the spacing between hairpin heads grew at $0.03w_b$. Assuming the average propagation velocity from PPIV, and accounting for the average growth rate of hairpin spacing, it could be predicted that the apparent axial spacing between hairpin heads in the stereo reconstruction should be 0.37D, within one grid step of the actual value found in the SPIV reconstructions. However, with such a small sample

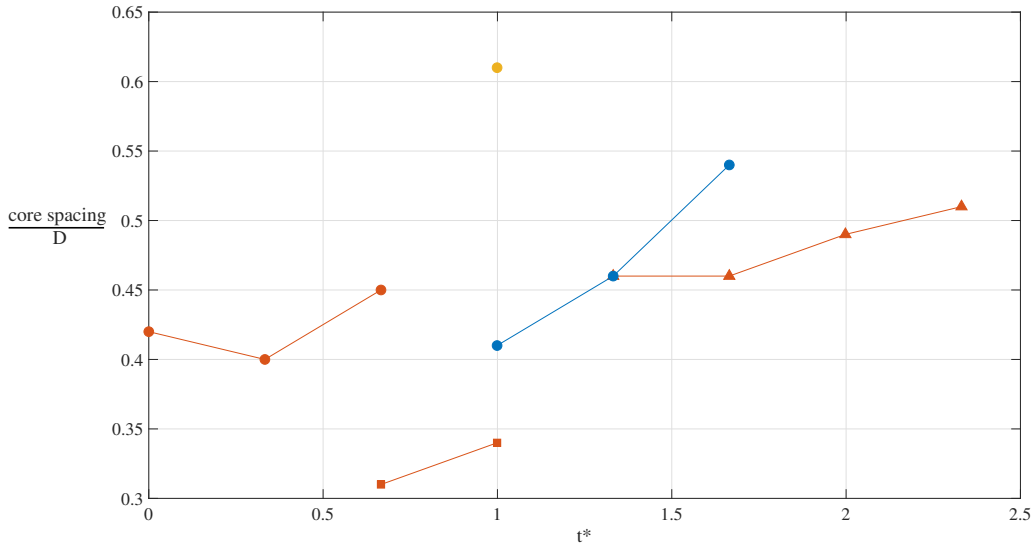

Figure 3.31: The normalized axial spacing of vortex cores over time extracted from PW-23 (blue), PW-9 (red), and PW-20 (yellow).

size, it is hard to know if the numbers have converged. Since there was a relatively small magnitude variation in axial velocity over the ejection regions, and the small variation was steady in time, the data suggest that while Taylor's Hypothesis may result in appreciable shear deformation of the actual structures that span a large radial domain, the deformation would be far less than what was predicted from Shimizu and Kida (2009). The results from the SPIV reconstructions suggest that the axial spacing between the hairpin heads is likely under-predicted by $\approx$ 15%. The uniformity of the axial velocity across ejection regions in each of the thee PPIV sequences examined suggests that these structures are not likely to be significantly deformed over their length as a result of the SPIV reconstruction. These results say nothing of the hairpin legs, especially the inclined portions, whose angles with respect to the wall could be less faithfully represented in the SPIV reconstructions than the ejections and hairpin heads. The hairpin heads observed in Figures 3.24-3.28 developed and disappeared over timescales ranging from $t^* = 1 - 1.5$.

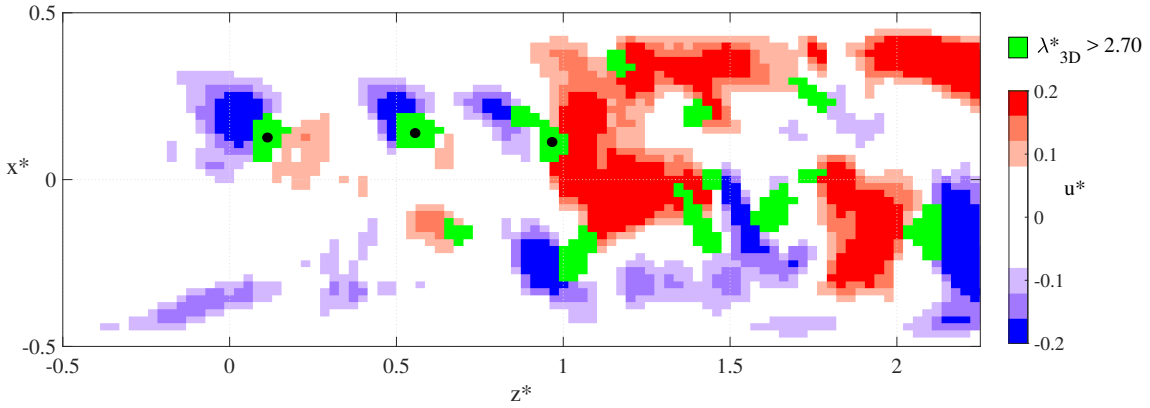

Figure 3.32: An (x^*, z^*) plane taken from puff record S-4 at $y^* = 0$ showing u^* from red to blue corresponding to $(-0.2 < u^* < 0.2)$. The green regions show where $\lambda^*_{3D} > 2.70$, and the black dots are centered in regions that correspond to hairpin heads. A detailed view of the 3D swirling regions inside this record is shown in Figure C.8

Figure 3.32 shows a slice taken from the reconstructed SPIV volume for puff record S-4 which shows similar velocity contours to the PPIV sequences in Figures 3.24-3.28. The green swirling regions are colored using λ^*_{3D}. Three counterclockwise swirling regions marked with black dots spaced at distances of $0.44D$ and $0.4D$ were located in a line along $x^* \approx 0.13$, and corresponded to hairpin heads in the reconstructed volume. The slice exhibits a strong resemblance to Figure 3.26h with three strongly swirling regions each spaced $0.4D$ from their neighbor, and where the most downstream swirling region exhibits the previously noted sharp streamwise gradient in u^* that extends from the core outward to the upper wall.

Most often, the vectors in the measurement plane in the PPIV records do not show obvious hairpin sequences. Some records show structures that appear similar to single hairpins, while many show more complicated swirling interactions that do not appear to cut any hairpins along their plane of symmetry. Figure 3.33 shows puff record PW-13, a record where no obvious hairpin sequence develops in the measurement plane. The quiet flow upstream

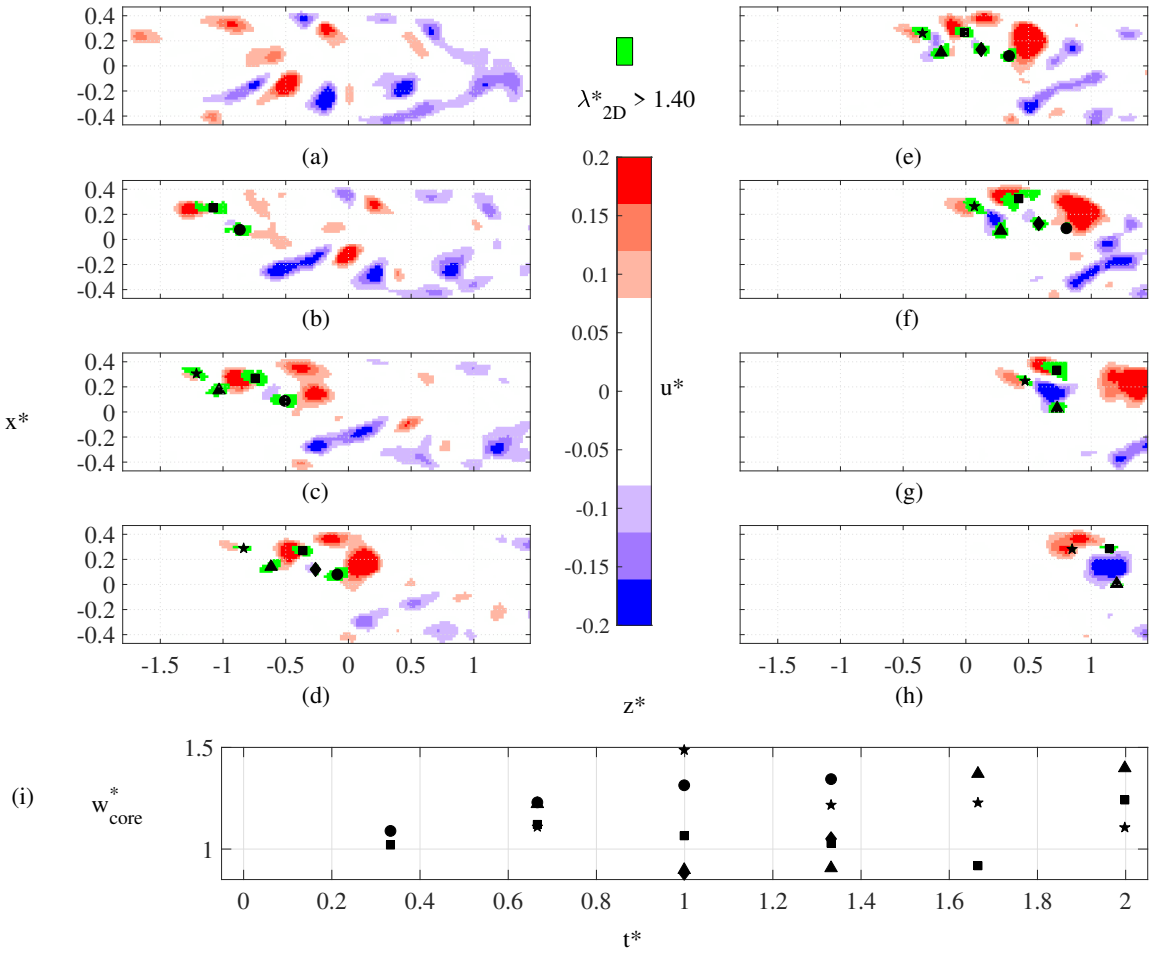

Figure 3.33: (a-h) PPIV sequence showing the development of a hairpin sequence in record PW-13. The dimensionless time spacing between images is $0.33D/w_b$. The vertical axis in each sub-figure shows the x^* coordinate defined from the center of the pipe, while the horizontal axis shows the z^* coordinate defined from the coordinates used in the PIV calibration image. Seven equally spaced contours range from blue to red show $-0.2 < u^* < 0.2$, while green areas show selected regions where $\lambda^*_{2D} > 1.4$.. The centriods of the swirling regions are each marked with a different shape and were used to calculate the velocities shown in (i).

of the appearance of strong cross-stream motions that move downstream throughout the sequence suggest that the sequence coincides with the transit of the puff's trailing edge.

The cross-stream motions at the trailing edge region of the record are accompanied by strong swirling cores as in the records with hairpins, but they appear more suddenly and are

associated with strong injection regions near the top wall with some ejection regions developing later in the sequence farther inward. In Figure 3.33e there are four well developed injections near the wall, that look similar to the injections found in Figure 3.32 near the upper wall within $1 < z^* < 2$. The cores in Figure 3.33, have rotations that are both clockwise (square and star symbols), and counterclockwise (triangle, diamond, and circle symbols). The core velocities are shown in Figure 3.33i, and sometimes vary wildly and show no obvious trend with time. One explanation for this behavior is that the measurement plane cuts through hairpin or other swirling structures that are interacting with other structures that lie at a nearby azimuthal location. This interaction could result in the complicated and swiftly evolving structures noted in PW-13. Examples of this can be found throughout Appendix C, where axially aligned swirling structures near the trailing edge interweave and interact as they turn inward from the wall. A good example of this can be found in Figure C.70 where a subdomain of the reconstruction of puff record S-35 shows a well-defined half-hairpin that turns inward on the $y^* < 0$ side of the pipe and arches over to the $y^* > 0$ side. In Figure C.69, which shows the whole domain, multiple axially aligned swirling structures lift inward from the wall at various axial and azimuthal locations upstream of the trailing edge.

Up to now, the ejection and injection structures examined in the PPIV records have been aligned parallel to the measurement plane. To investigate ejections that could be perpendicular to the measurement plane, a hypothesis was formulated. Strong ejections near the trailing edge with motions perpendicular to the measurement plane could be visible in the w^* component as slow moving regions located at the center of the pipe surrounded by otherwise laminar-like flow. It was expected that few records would satisfy the above conditions because not only was the ejection required to be oriented perpendicular to the measurement plane, but it also needed to be sufficiently strong to cross that plane and isolated from other

strong motions. As suggested from the SPIV results, isolated trailing edge ejections are not always of sufficient strength to be visible in this way. Further, the fluid motions that are associated with the disruption of the centerline flow are often accompanied by strong motions at other azimuthal locations. Searching for such regions in the PPIV data yielded two records, PW-10 and PW-26. Figures 3.34 and 3.35 show sequences of $w^* - 1$ and u^* for PW-10, respectively.

Figure 3.34a shows a centerline velocity disruption entering the field at its upstream end. Based on the SPIV data, this disruption likely occurs $0.5D - 1D$ downstream of the trailing edge hairpin. Downstream of the disruption, the contours of w^* are turbulent-like with large coherent regions. The velocity of the centerline disruption is tracked through Figure 3.34d, and found to propagate at $1.24w_b^*$. By Figure 3.34d, laminar-like fluid with some large-scale deviations near the wall has entered the field upstream of $z^* = -0.25$. In Figure 3.34e, a localized island of slow moving fluid appears near $z^* = -1$ Moving into Figure 3.34f, the centerline disruption continues at a similar velocity, while the slow moving island cuts off the fast moving fluid downstream of it as it propagates downstream at $z^* = 1.35$. Figure 3.34f also shows a tiny slow moving region upstream at $z^* = -1.5$ This region, like the original one downstream of it grows into an island of slow moving fluid in Figure 3.34g. Meanwhile, the original island has now become the centerline disruption. In Figure 3.34h, the newer island strengthens.

The u^* contours on the regions corresponding to the structures described in Figure 3.34 are also interesting. Figure 3.35a shows that along with the centerline disruption, there is an accompanying region of outward flow that appears as a pair of regions, one red and one blue located near $z^* = -1.5$. The outward moving regions continue downstream to Figure 3.35d remaining in the same axial location as the centerline velocity disruption, suggesting they are all parts of the same structure and that the white region between them is likely

moving outward toward the wall as well, but normal to the page. Also in Figure 3.35d, a second weaker pair of outward moving regions appears roughly $1.25D$ upstream from the first. By Figure 3.35e, the first pair of outward moving regions is no longer visible, while the second pair travels downstream in a similar way to the first, strengthening, and remaining axially aligned with one another and with the first island of slow moving fluid in Figure 3.34. The second island, appearing in Figure 3.34 does not show a corresponding pair of outward moving regions in Figure 3.35. The outward moving regions associated with the second island do not become visible in the PPIV data until $0.9D/w_b$ after Figure 3.34h. The motions of the regions described in PW-10 are similar to the large centerline disrupting ejection described by van Doorne and Westerweel (2009) as (13) and (16) in Figure 6 of that publication, that extends across the pipe and fans outward to the wall.

In record PW-26 (not shown), another sequence of two strong ejections normal to the measurement plane unfolds in a similar way as in PW-10. The first ejection moves downstream at $1.34w_b$, while the second ejection that appears $1.0D$ upstream moves downstream at $1.47w_b$.

The propagation velocities of the out-of-plane ejections observed in PW-10 and PW-26 agree with the velocities found for hairpin heads in PW-23, PW-9, and PW-13, and with the propagation velocities of the axial perturbations tracked by Shimizu and Kida (2009), and by the vorticity maxima tracked by Duguet et al. (2010). Figures 3.34 and 3.35 showing PW-10 together with the description of PW-26 suggest that these two puffs exhibit repeated strong ejections that are aligned in regions at or upstream of the centerline velocity disruption. The ejections themselves appear similar to the one noted by van Doorne and Westerweel (2009), and are likely due to particularly isolated hairpin sequences that develop ejection motions strong enough to overwhelm the otherwise laminar-like fluid at other azimuthal locations.

While the SPIV data show that hairpin vortices are a dominant feature of the trailing edge

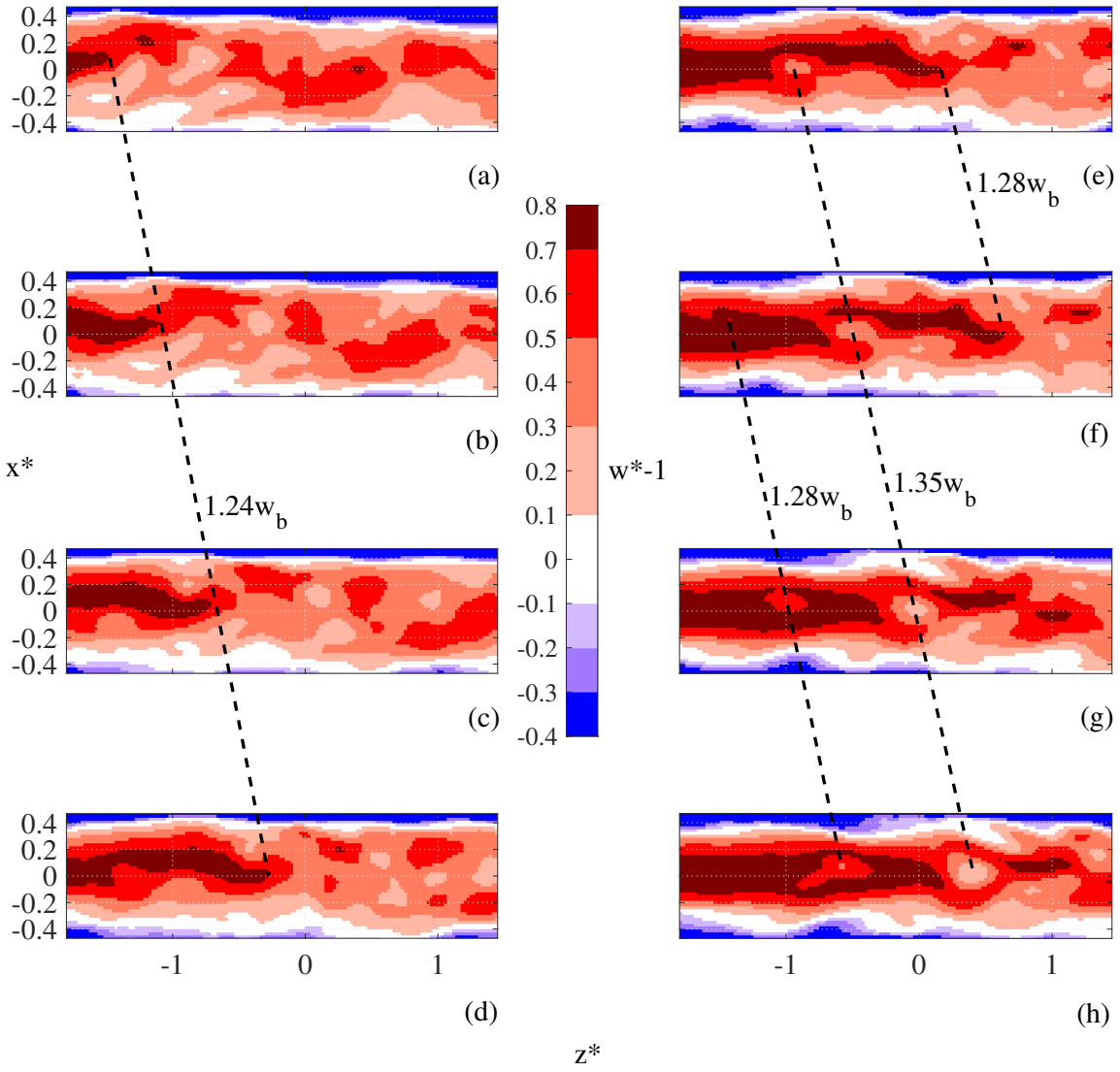

Figure 3.34: PPIV sequence showing $w^* - 1$, the difference in the axial velocity from w_b for PW-9. The dimensionless time spacing between images is $0.33D/w_b$. The vertical axis in each sub-figure shows the x^* coordinate defined from the center of the pipe, while the horizontal axis shows the z^* coordinate defined from the coordinates used in the PIV calibration image. The locations of key features in the sequence are tracked with dashed lines and labeled with their corresponding propagation velocity.

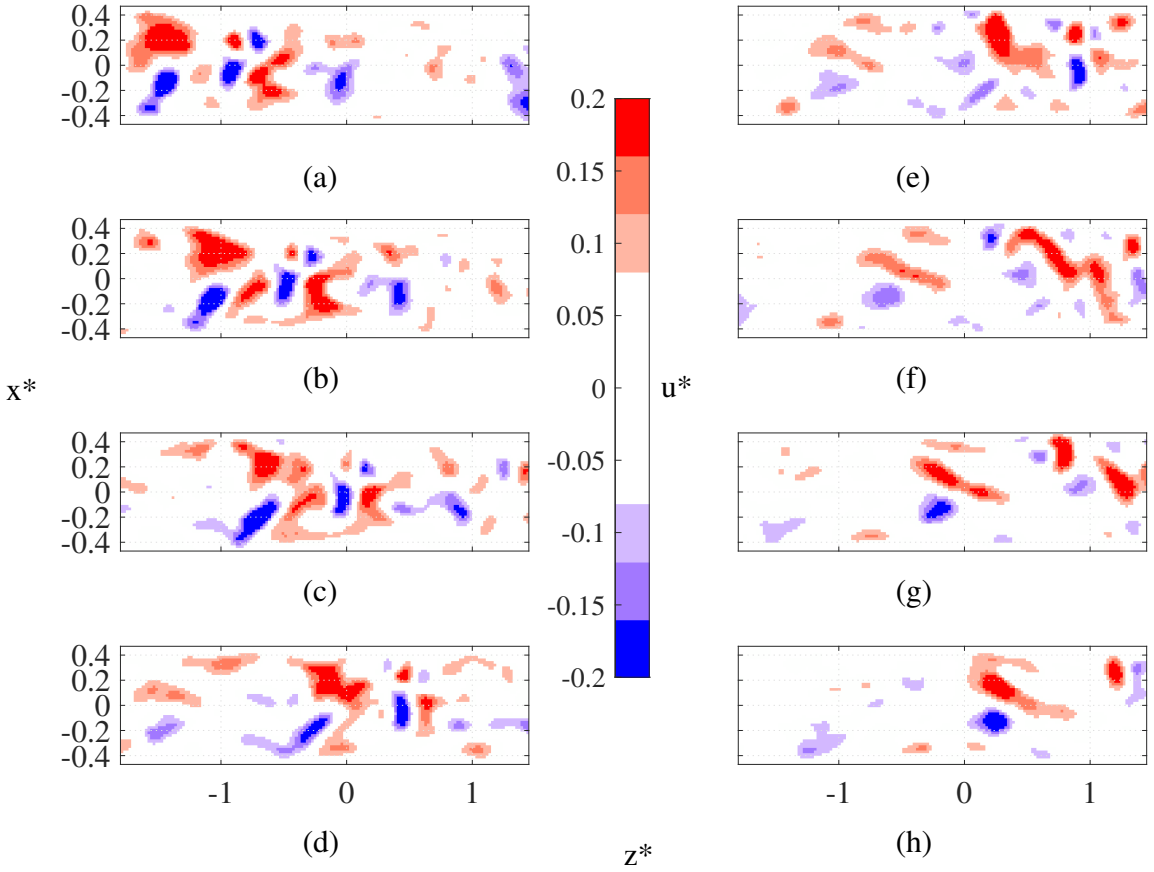

Figure 3.35: PPIV sequence showing the development of a hairpin sequence in record PW-10. The dimensionless time spacing between images is $0.33D/w_b$. The vertical axis in each sub-figure shows the x^* coordinate defined from the center of the pipe, while the horizontal axis shows the z^* coordinate defined from the coordinates used in the PIV calibration image. Seven equally spaced contours range from blue to red show $-0.2 < u^* < 0.2$.

in puffs, the evolution and propagation of the structures observed in the PPIV data partially support that a clear-cut scenario can take place like that outlined by van Doorne and Westerweel (2009). Namely, a scenario whereby perturbations near the wall roll-up into hairpin vortices near the trailing edge. The hairpins extract energy from the fast moving laminar-like fluid as they grow, spawn new hairpins and create q^*_{max} before finally propagating into the more turbulent-like parts of the puff, and sustain it against viscous decay. Indeed, this is just the scenario that appears to be underway in S-19. The structures observed in the SPIV

and PPIV data, however, indicate that the process is often more complicated. Sometimes the hairpin structures grow slowly with time, and reorient before growing sufficiently to create a centerline disrupting ejection as in PW-9. Still other times, as with PW-13, and many other SPIV reconstructions in Appendix C, additional hairpins or inclined swirling structures appear at other azimuthal locations near the trailing edge hairpin. These swirling structures can interact before a well developed hairpin sequence can form and instead, the interacting swirling motions grow and propagate into the puff.

3.3 Droplet-laden flow investigation

The investigation into droplet-laden flow was conducted in the facility configured as described in Section 2.3.4. During this investigation, both single-phase and droplet-laden PPIV data were acquired. The key difference in the facility configuration was that for these records, a disturbance generator was not included downstream of the flow conditioning. This altered the value of Re where transition occurred. For both the droplet-laden and single-phase cases, puffs were first observed at $Re = 2000$. PPIV time series were analyzed for the 3.8% oil volume fraction with 10 micron droplets for 7 puffs each found at $Re = 2150$ (labeled as DA-1 through DA-7) and 2250 (labeled as DB-1 through DB-7). Similar data was taken in 20 puffs with no droplets at $Re = 2250$ and are labeled R-1 through R-20. The values of $Re = 2150$ and $Re = 2250$ were selected because they represented, in both the single-phase and droplet-laden cases, the location where puffs were observed at an average interval near $1000D/w_b$ and $500D/w_b$, respectively. For the droplet-laden case, the pressure transducer recorded transitional structure signatures identical to those found in the single-phase flow. Based on the results from Matas et al. (2003b), it was expected that any change in transition Reynolds number due to the droplets would be less than 200 for the

volume fraction and particle diameter ratio in the present study.

Figure 3.36 shows a reconstruction of a single puff found in the dispersion flow at Re = 2150, record DA-1. Two separate contour image sequences are given showing w^*, and $u*$. The reconstruction is generated by concatenating PIV fields using Taylor's hypothesis to determine each subsequent field in the reconstruction. The specific location of z_0^* is found, in this case, by locating where the velocity in the center of the pipe falls below 75% of the laminar center line velocity. This was chosen in order to compare our findings with those of van Doorne and Westerweel (2009).

From the reconstruction in Figure 3.36, both the overall length and shape as well as classic structure features can be compared to puffs known to occur in single-phase flows. From left to right, in Figure 3.36a the laminar profile is slightly perturbed near the wall and remains undisturbed in the center. At the trailing edge, there is a strong deceleration near the bottom wall. Then, downstream near $z^* > 1.5$ the laminar velocity profile is fully disrupted from wall to wall with the axial velocity across the entire pipe dropping below $1.5w_b$. Downstream of $z^* > 1.5$ strong local variations in axial velocity dominate up to $z^* = 5$. By $z^* = 5$, the local variations in w^* have decayed significantly and the laminar velocity profile is recovering. In Figure 3.36b, the trailing edge, despite being defined using a centerline velocity, shows two strong ejection regions similar to those shown to occur in conjunction with hairpin vortices in single-phase puffs. For $0 < z^* < 5$, strong wall-normal fluctuations occur with the strongest occurring where $1 < z^* < 3$. This shows good agreement with the single-phase data analyzed from both the SPIV and PPIV presented in Section 3.2.1 and Section 3.2.2.

Figures 3.37 and 3.38 show time sequences of the w^* and u^* velocity components around $z^* = 0$ in DA-2, respectively, along with strong swirling cores where λ_{2D}^* is large. Figure 3.37i also shows the velocity of the swirling cores. There is an initial core in Figure 3.37a

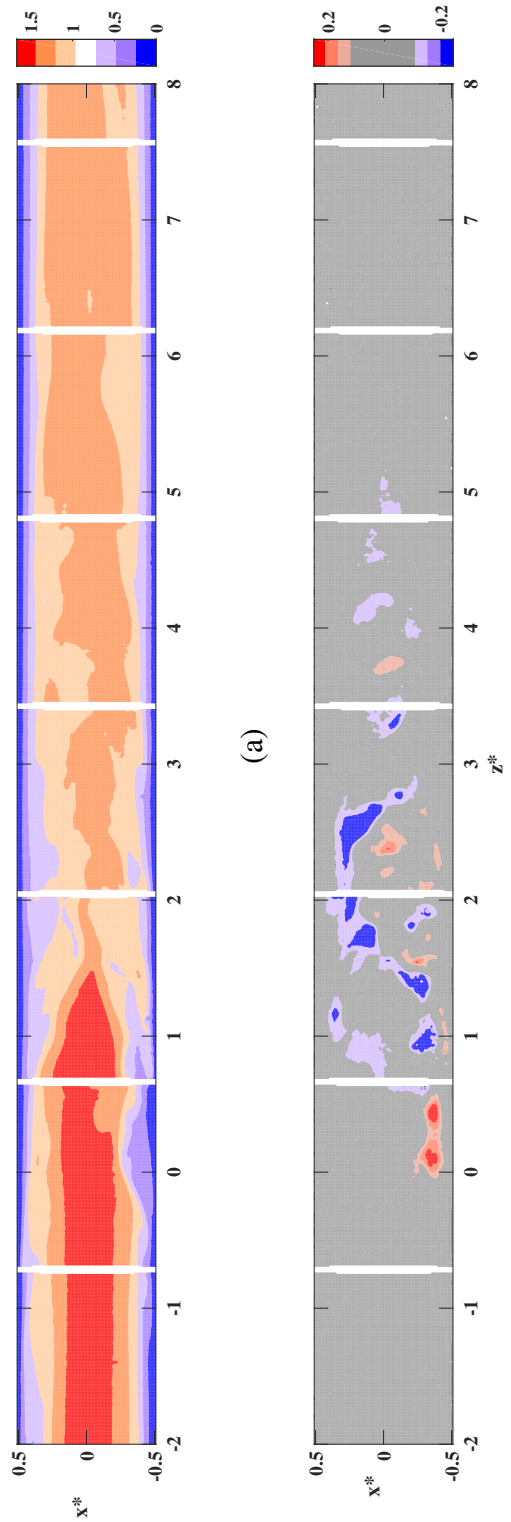

Figure 3.36: Isocontours of (a) w^* and (b) u^* inside DA-1 for the droplet-laden flow at $Re = 2150$ reconstructed to show the spatial aspects of the puff and its interior swirling structures.

that is accompanied by a strong injection of fluid toward the wall. An accompanying ejection develops in Figure 3.37b that remains very close to the wall along with other strong injections that develop upstream near $z^* = -0.5$. The original core decelerates from $1.3w_b$ to below w_b and moves outward as it progresses through Figure 3.37c and Figure 3.37d. In Figure 3.37d, the original core has elongated in the axial direction, and two new cores have developed upstream. The two new cores strengthen and develop strong ejections as they accelerate through the rest of the sequence to Figure 3.37g which corresponds to the frame that $z^* = 0$ in Figure 3.36. The velocities shown in Figure 3.37i are in agreement with those found in the single phase PPIV, and there is a qualitative similarity in the development of the hairpin sequence.

The puff features can be further analyzed by examining axial velocity profiles in the single-phase and droplet-laden case and comparing to existing single-phase data from the literature. In Figure 3.39, velocity profiles for increasing z^* are plotted for three puffs. Two are from single-phase and droplet-laden flows at $Re = 2250$ in the current study, labeled R-5 and DA-7, respectively. The third represents data extracted from the only puff for which axial velocity contours are available from van Doorne (2004) at $Re_b = 2000$. The exact values of z^* were chosen to match those used by van Doorne (2004). The data from van Doorne (2004) was extracted from cross-section oriented SPIV contour plots using a Matlab script. The angle of the profile extracted from van Doorne's cross section was chosen to capture the most upstream perturbation to the laminar profile, which occurred at $z^* = -3.4$. Far upstream of the trailing edge, at $z^* = -3.4$, each profile is nearly laminar with small deviations. These deviations increase in magnitude for each of the profiles as $z^* \rightarrow 0$. It should be noted here that the velocity profiles of puffs found in single-phase flow have a strong azimuthal dependence upstream of the trailing edge as this area contains meandering vortices at random azimuthal locations. As a result, the velocity profiles are not expected to

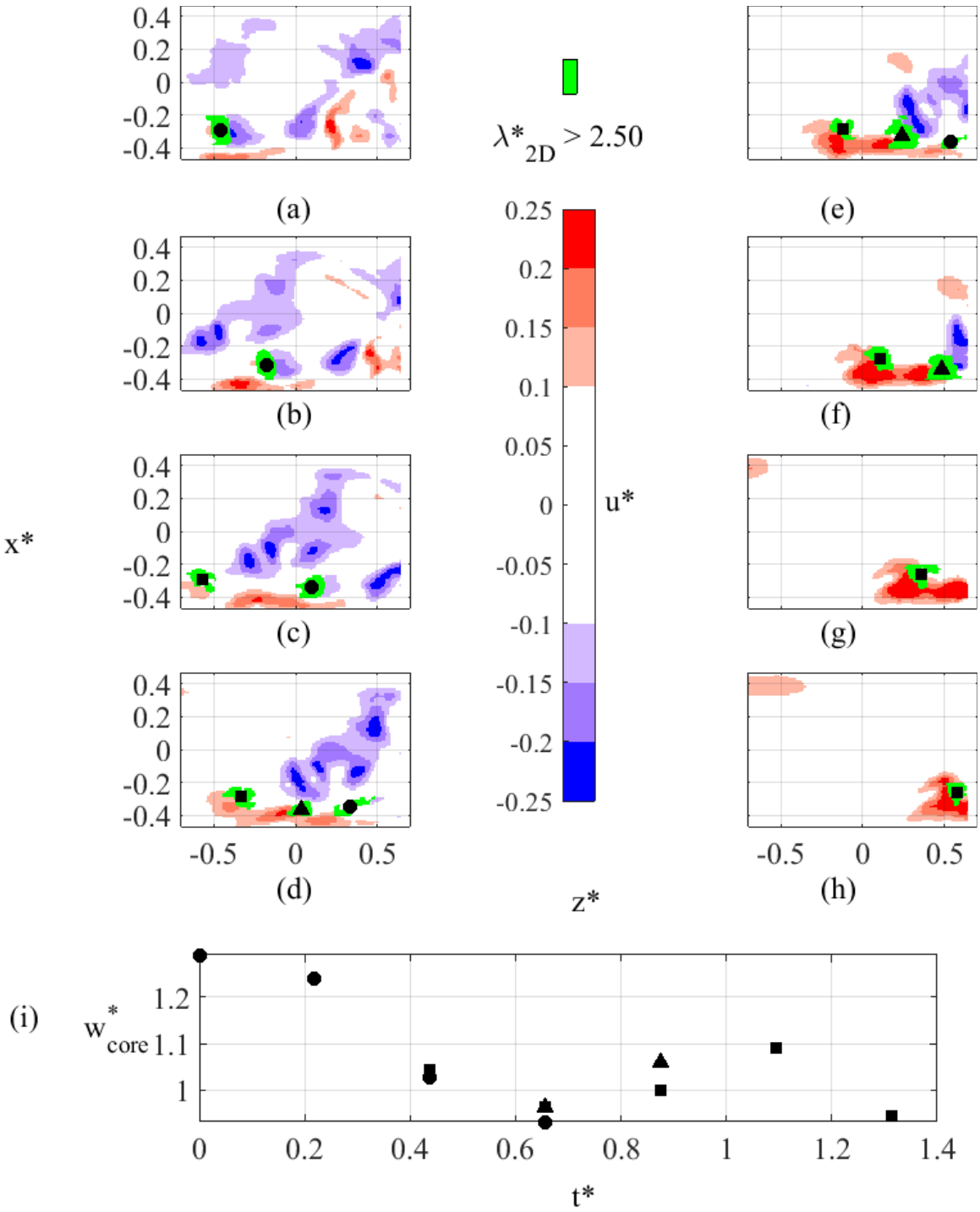

Figure 3.37: PPIV sequence showing the development of a hairpin sequence in record DA-1. The dimensionless time spacing between images is $0.22D/w_b$. The vertical axis in each sub-figure shows the x^* coordinate defined from the center of the pipe, while the horizontal axis shows the z^* coordinate defined from the coordinates used in the PIV calibration image. Seven equally spaced contours range from blue to red show $-0.2 < u^* < 0.2$.

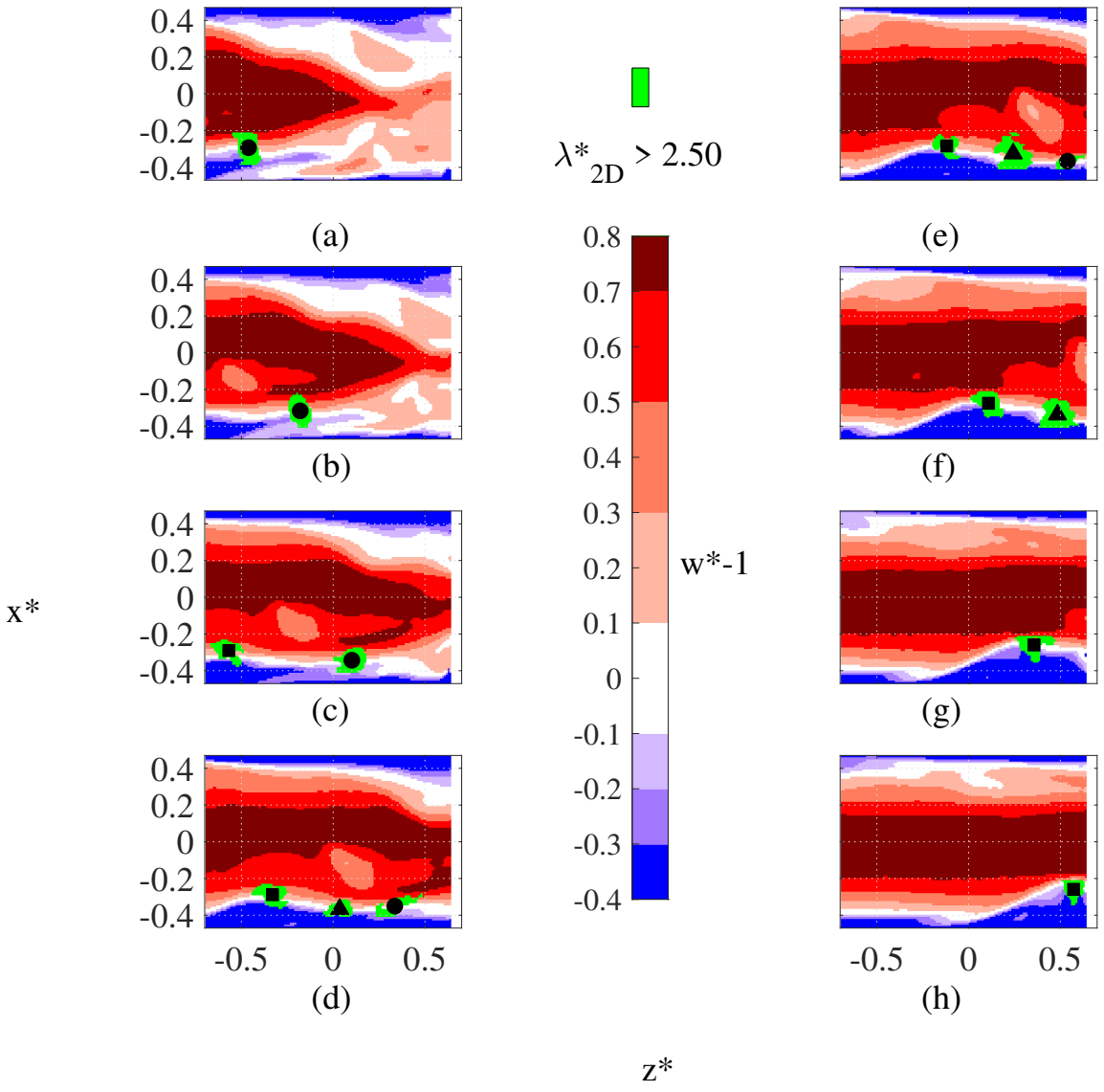

Figure 3.38: PPIV sequence showing the development of a hairpin sequence in record DA-1. The dimensionless time spacing between images is $0.22D/w_b$. The vertical axis in each sub-figure shows the x^* coordinate defined from the center of the pipe, while the horizontal axis shows the z^* coordinate defined from the coordinates used in the PIV calibration image. Seven equally spaced contours range from blue to red show $-0.2 < u^* < 0.2$.

have the same perturbation locations for a given z^*, only similar perturbation magnitudes. Near the trailing edge, i.e. $z^* = 0.038$, a strong deviation from the laminar centerline velocity can be seen across all three profiles. Within $0 < z^* < 3$, the velocity profiles in all three puffs begin to flatten, and sharper gradients near the wall develop as compared to the ideal laminar flow. In each case, the modulations in the velocity profiles begin to smooth out by $z^* = 3.9$, and the centerline velocity has begun to increase towards the ideal laminar value by $z^* = 6.3$.

Figure 3.40 shows data in a similar way to Figure 3.39, but includes profiles of all puffs captured for this experiment in single-phase and droplet-laden case, respectively. Additionally, the profiles across two perpendicular diameters of the ensemble averaged SPIV data are shown for comparison. At $z^* = -3.4$, we see similar behavior in all puffs regardless of whether they contain droplets. The laminar velocity profile is weakly perturbed in locations near the wall. The effect of any weak perturbations that persist in the SPIV data is not visible in either diameter profile from the ensemble. By $z^* = -1.1$, however, effect can be seen in both ensemble profiles where low speed regions appear between inflection points near $r^* = 0.2$ and $r^* = 0.3$. In the instantaneous profiles, the weak deviations from laminar move inward at a similar rate across all puffs until they create the puff's trailing edge near $z^* = 0.038$. At this location, the magenta curve, which is centered on the trailing edge ejection, shows a larger low speed region on the right side. The variations in the instantaneous profiles, both single-phase and droplet-laden show similar magnitudes as the low speed region associated with the trailing edge ejection. Immediately downstream of the trailing edge, where $0 < z^* < 1$, all instantaneous puffs have a wildly varying profile, with most containing 3-4 oscillations with magnitudes about $0.5w_b - 1w_b$. These low frequency spatial variations are consistent with the large-scale structures known to occur near the puff's trailing edge. These are the structures, hairpin sequences and others, that are ob-

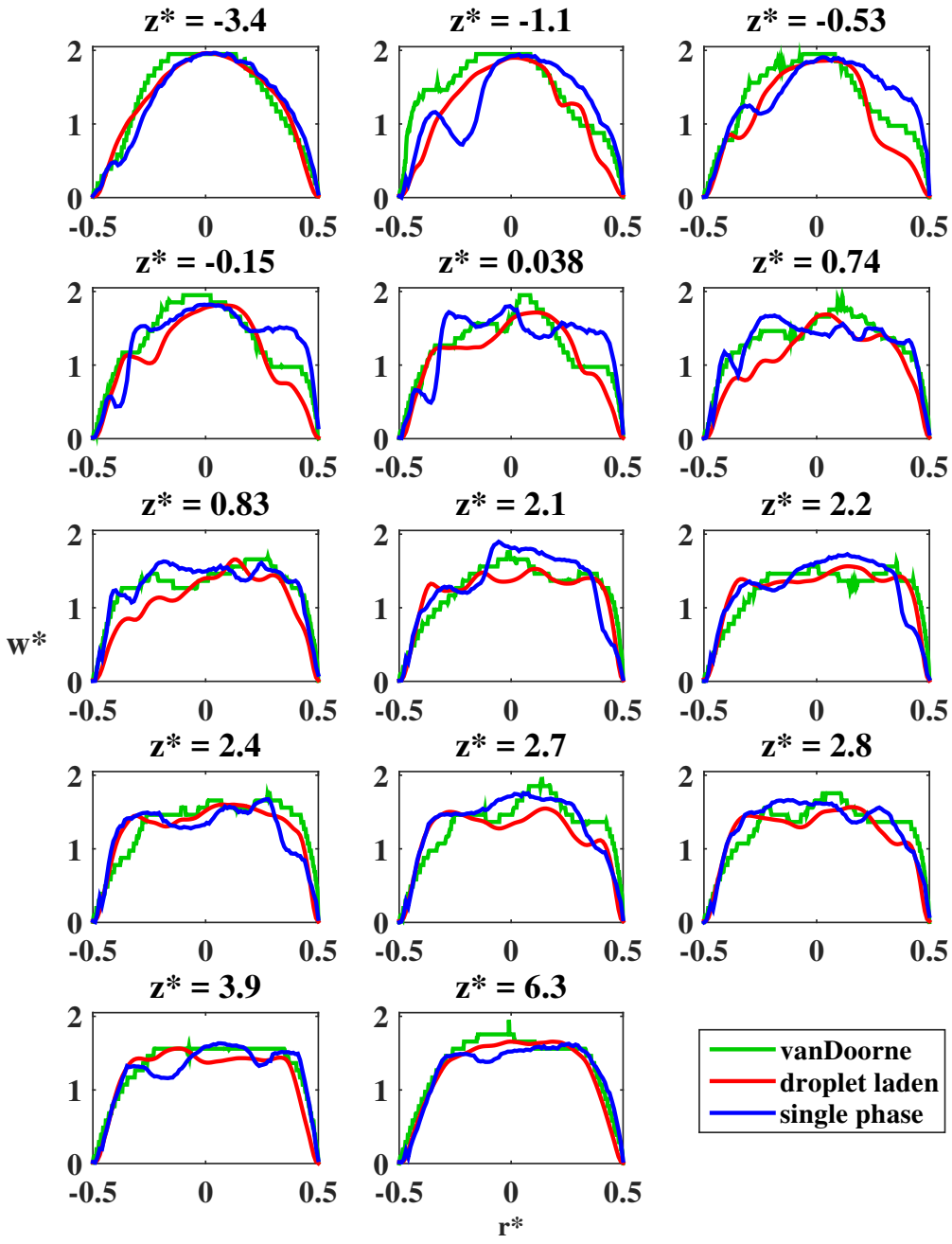

Figure 3.39: Fourteen plot comparing profiles of w^* at various z^* locations for puff DA-7, R-5, and data extracted along a diameter from van Doorne (2004).

served to create high q^* values. The range spanned by these oscillations is bisected by both the green and magenta curves with show increasingly close agreement with one another for all plots where $z^* >= 0.74$. The velocity profiles across all puffs, including those from the ensemble, begin to converge farther downstream of the trailing edge where $z^* > 2$. This is consistent with the current view of the dynamics observed in single-phase puffs in this investigation and previous works, where large-scale structures initiated at the trailing edge interact with one another to form smaller, higher frequency velocity variations, that begin to decay as they travel far downstream without being re-energized by more strong ejections from the wall. By $z^* = 6.3$, the velocity profiles in both the droplet-laden and single-phase cases have begun to collapse tightly around the ensemble profiles. The large-scale, low frequency variations have mostly decayed, and the low frequency variations remain concentrated mostly near the center of the pipe.

The flow that was laden with $10\mu m$ droplets at $\phi = .038$ contains puffs that are dynamically similar to those that are found in single phase data, and does not exhibit signs that the constantly fluctuating base flow found at higher volume fractions for larger particle diameters.

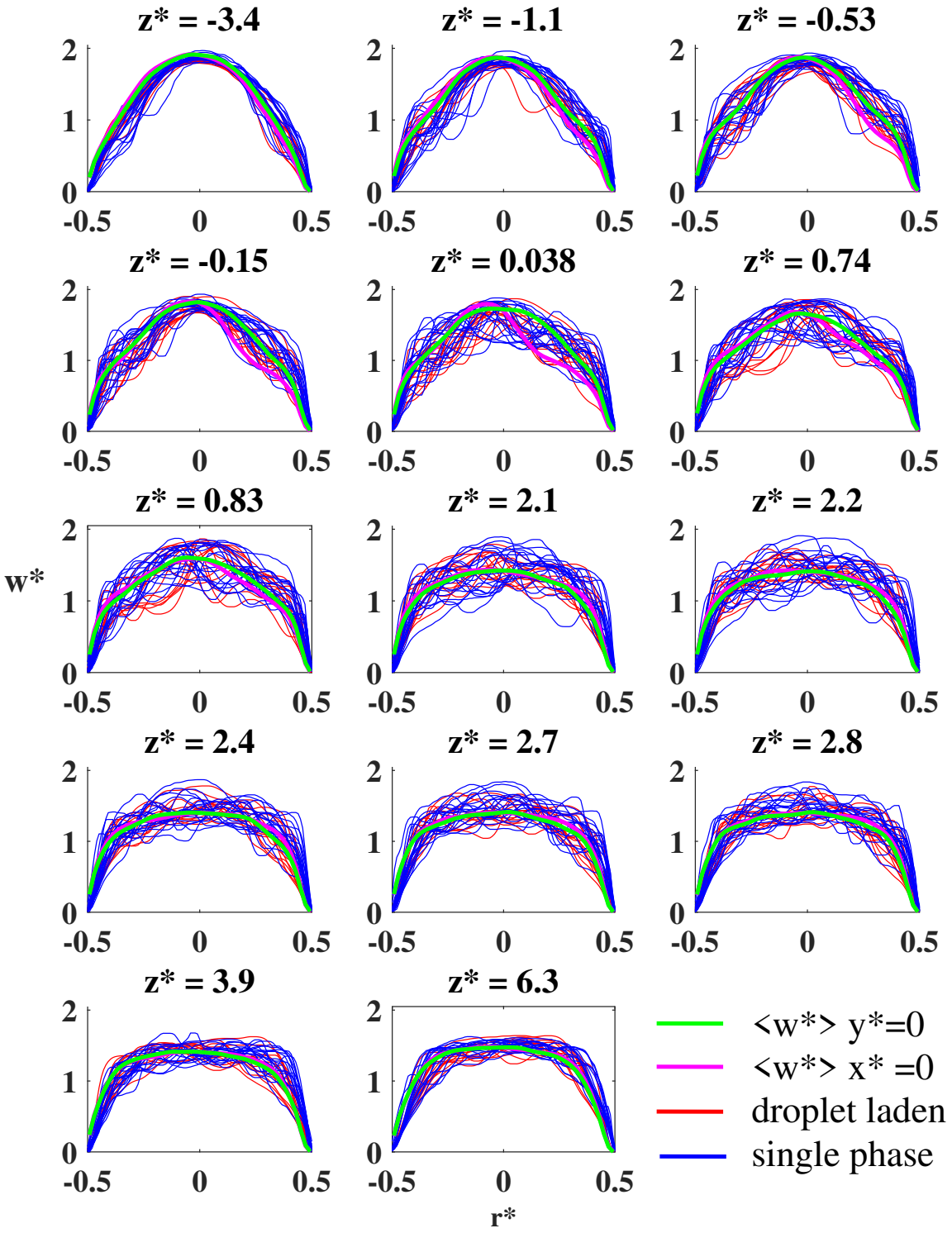

Figure 3.40: Fourteen composite plots showing profiles of w^* at various z^* locations for each of the droplet-laden (red), and single-phase reference (blue) puffs. The green and magenta profiles in each plot correspond to the ensemble averaged SPIV data at each z^* location examined by van Doorne (2004).

Chapter 4

Conclusions

This chapter summarizes the progress made in completing the objectives laid out in Section 1.4. Then, the conclusions that arise from analysis of the data collected Chapter 3 are presented. Finally, the open questions that remain and the potential for future work are identified.

The objectives of this work were four-fold; design and construct a facility capable of investigating transitional structures in both single-phase and droplet-laden flow; characterize the facility's response to varying Re and ϕ; characterize the coherent structures within single-phase puffs; and present the progress of the investigations into droplet-laden flows.

Through careful component selection, custom fabrication, and testing, the facility produces high-quality repeatable flow with fine control over Re. The pressure sensor it employs is capable of sensing puffs and triggering the PIV systems that were developed to interrogate the puffs. A large set of high-resolution data was captured in single-phase puffs using both the SPIV and PPIV setups. Droplet-laden flow was realized in the facility and index matched PPIV data was obtained that allowed for comparison between the droplet-laden and single-phase flows.

The facility's response to increasing *Re* has been characterized for single-phase flow with the disturbance ring installed, and for both single-phase and droplet-laden flow where $\phi = 0.038$ without the disturbance ring.

Certain coherent motions inside single-phase puffs were reconstructed, examined, and averaged in the SPIV analysis, then tracked in the PPIV analysis. The fidelity of the SPIV reconstructions was investigated using insights from the PPIV results. A detailed summary of the single-phase puff and droplet-laden results and the conclusions they led to are included in Section 4.1 and 4.2, respectively.

4.1 Single-phase flow investigation

This section presents a summary of the results, and outlines the conclusions that can be drawn regarding the dynamics of single-phase puffs presented in Chapter 3.

4.1.1 SPIV in single-phase flow

A new method for defining both the trailing edge location and azimuthal orientation of a puff was developed based on observations of the velocity fields in multiple puff structures. The method first identified the most upstream ejection to determine the axial location of the trailing edge. Then the azimuthal orientation of the puff was determined based on a radial line corresponding to the strongly decelerated flow accompanying the ejection. The method was able to register a puff reliably in all image sequences that included the trailing edge region.

The ejection at the trailing edge location was typically associated with a hairpin vortex. In general, hairpin vortices were a common structure found within $-1 < z^* < 2$. In this region, the strong ejections that accompany hairpins were responsible for local peaks in

q^*. By contrast, the local peaks in q^* further downstream were associated with irregularly shaped swirling structures. Typically, individual hairpin vortices in a puff were aligned axially with additional hairpin vortices. This vortex alignment was also seen in the ensemble averaged puff, confirming the 'quasi-periodic' regeneration process suggested by Bandyopadhyay (1986) and solidified by van Doorne and Westerweel (2009). The average axial spacing between streamwise aligned hairpins was 0.45D based on the ejections found in the ensemble average, and 0.39D based on the hairpin sequences examined in the SPIV data.

The peaks that rise to the q^*_{max} value noted by van Doorne (2004) and examined in detail by Kuik (2011) left open questions about the structures involved in their formation. Analysis of the SPIV data in this work suggest that hairpin sequences can indeed generate cross-stream motions in the space between hairpin heads sufficient to create the q^*_{max} value. However, based on the records examined in detail and axial location of q^*_{max} in most records, the general scenario is that two cross-stream-oriented swirling structures bookend a short pipe segment without strong cross-stream-oriented swirl and create powerful cross-stream motions localized to relatively small portions of the cross-section. It could be that local peaks in q^* created by hairpin sequences are amplified as the sequence interacts with other swirling structures that have grown from other azimuthal locations and the SPIV reconstructions show peaks that are in various stages of that process. A dynamic link could not be established between the trailing edge hairpins and q^*_{max} using ensemble averages. This may be a limitation of the reconstruction, or due to a wide range of characteristic length scale involved in the evolution of q^*_{max}.

The regions found in the ensembles with strong asymmetry suggests that there was most often a dominant coherent structure that sat upstream of the otherwise most energetic parts of the puff. The present study defined the average region of influence of the strong initial ejections and the hairpin sequences found to accompany them. This region started near the

wall at $z^* = -1$, and grew to reach the center of the pipe at the trailing edge. In the region, $0 < z^* < 1$ the flow induced by the ejections maintained a strong asymmetry throughout the range of r^*. By $z^* = 1.5$ the averaged flow near the center of the pipe was nearly axisymmetric, but the flow near the wall remained asymmetric until at least $z^* = 3$.

Based on the experiments performed, modal dominance was a robust feature of puffs in a pipe flow with non-idealized in-flow conditions, and in relatively young puffs that originated individually from broadband disturbances. As with Willis and Kerswell (2008), modes 3 and 4 were twice as probable as modes 2 and 5 in the present study. The lack of slow streaks in regions of modal dominance downstream of the trailing edge was also a similarly robust feature of these flows. This evidence supports the assertion by Willis and Kerswell (2008) that the dynamics in more turbulent regions of the flow are disconnected from those at play in traveling waves.

Despite the similarities, we noted significant differences between the present study and that of Willis and Kerswell (2008), particularly among modal probability distributions. Based on uncertainty estimates in both the present data and that of Willis and Kerswell (2008), these differences are greater than the level of statistical uncertainty. While the total probabilities derived from Willis and Kerswell (2008) created a smoothly varying distribution over $-3 < z^* < 8$, the data from the present study included three distinct peaks covering a larger axial distance. These peaks were due, at least in part, to the registration method developed in the present study. The most upstream peak in the present data occurs at the trailing edge, and the second occurs at $z^* = 3$. This region corresponds closely to the region of asymmetry in the ensemble showing memory of the trailing edge hairpin.

The hairpin related dynamics in the region, $0 < z^* < 1.5$ decreased the probability for modes 2-5 in general, rapidly disrupting any upstream modes that were present. Specifically, the initial ejection and accompanying hairpin sequence did not conform with any of

the modes 2-5 as they were defined. Further downstream, mode 3 was not only the most common mode, but it also dominated for long regions in a significant number of individual puffs. These long lasting structures were largely responsible for elevated total probabilities within $4 < z^* < 10$ as compared to Willis and Kerswell (2008), and for the third peak in the experimental pdf.

4.1.2 PPIV in single-phase flow

In the PPIV measurements of puffs in single-phase flow, three records containing well defined hairpin sequences that straddled the measurement plane were examined. The sequences presented appeared similar to an axial-radial plane from an SPIV reconstruction that sliced through a known hairpin sequence. In the three PPIV records, nine hairpin heads were identified and tracked through the measurement plane.

The hairpin heads and the motions associated with them were found to evolve substantially as they propagated through the measurement plane. Often, the hairpins developed in an area of the flow free from large disturbances into strong hairpins that disrupted major areas of the laminar flow in a time corresponding to $t^* = 1-1.5$. Additionally, well-developed hairpins that entered the measurement plane from upstream became unrecognizable as they reoriented and interacted with other swirling structures over a similar time span. The number of hairpin sequences identified and the limited axial domain covered by the measurement plane did not allow for a stronger characterization of the timescales involved in hairpin sequence evolution.

In most cases, as time increased, the initial hairpin heads moved inward, their associated cross-stream motions grew in strength, and spawned a new hairpin upstream. Each hairpin head was tracked across multiple frames and their velocities and axial spacings were cal-

culated. The hairpin heads were found to propagate with velocities above w_b in nearly all instances, at an average speed of $1.19w_b$.

On average, the spacing between the hairpin heads observed in the PPIV was $0.45D$, and was found to grow at a rate of $0.03w_b$. The spacing between heads in the PPIV measurements was larger than what was found in the SPIV data. This difference could be accounted for by correcting for two factors mentioned above: 1) the propagation velocity, w_b, assumed in the SPIV was slower than the average calculated in the PPIV, 2) downstream hairpins appear to travel slightly faster than their upstream neighbors.

Additional trailing edge swirling structures were observed in many of the other records that did not appear to be hairpin sequences straddling the measurement plane. These structures were tracked in a single record and found to vary wildly as the structures evolved more quickly than the hairpin heads. Finally, one of two records in the data set was presented where a strong ejection sequence was oriented normal to the measurement plane. The ejection sequence was isolated upstream from the most turbulent fluctuations in the puff and each ejection was found to grow substantially throughout the sequence until it disrupted the the laminar-like flow across the entire pipe diameter in a way that appears similar to what was observed by van Doorne and Westerweel (2009).

The propagation velocities of the hairpin heads and other swirling structures, along with those of the slow moving fluid associated with the out-of-plane ejections showed good agreement with Shimizu and Kida (2009) and Duguet et al. (2010). Further, the hairpin head propagation velocity showed a similar dependence on radial location as was found in Shimizu and Kida (2009) and Duguet et al. (2010).

Analysis of the axial velocity contours in the areas of the hairpin ejections and heads coupled with observations of the evolution timescales of hairpins suggested that the ejections and head spacing are likely distorted in the SPIV reconstructions by the assumptions

of frozen turbulence and choice of propagation velocity. In reality, the inward parts of the ejections are moving faster than the outward parts. This would mean that the ejections identified in the SPIV reconstructions should lean farther downstream. This would also presumably apply to the hairpin legs. The degree of distortion, however, is such that real hairpin shapes would likely be qualitatively similar to the SPIV reconstructions and their distortion would be less than what would be predicted by simply using the average radial trend in propagation velocity.

4.2 Droplet-laden flow investigation

The facility used to identify and measure transitional structures in droplet-laden pipe flow was shown to work effectively. Detecting puffs and triggering their measurement in real time allowed for the measurement of puffs as they arise naturally due to background perturbations.

In the context of the previous works by Matas et al. (2003b) and Pouplin (2009), and given that the droplets introduced to the flow were at such a low volume fraction, $\phi = 3.8\%$, and had a large diameter ratio, $D/d = 4400$, it was expected that any change in critical Reynolds number would be very small. As such, it is not surprising that the lower threshold for puff creation in the facility remained unchanged from that of the single-phase flow, $Re = 2150$.

The dynamics inside the droplet-laden puffs were found to be consistent with single-phase puffs found in both the present study and from the literature. Signs of hairpin vortices and their associated ejections were found to develop in a similar way to those found the single-phase puffs in Section 3.2.2. In other words, the addition of droplets at the size and concentration investigated caused no obvious effects to the puffs in the flow or the

conditions under which they initiated. Features of the w^* profiles in droplet-laden puff were examined and found to be similar to those found in single-phase flows. Further, similar relative magnitudes and growth rates of the perturbations in w^* that lead to the eventual vigorous swirling motion inside a puff were matched between the droplet-laden and single-phase flows.

4.3 Future Work

For the single-phase flow, there is a potential to investigate PPIV for insights into the evolution of q^*_{max}. There is also potential to separate the modal dominance results into two groups, with and without low-speed streaks to yield potential insights into the change in dynamics that could be associated with the triple peak distribution of modal dominance. Additionally, for the droplet-laden flow, there is much potential for future work. First, characterizing the response of the droplet-laden flow at the concentration and droplet size investigated in this dissertation to the facility with the disturbance ring, and obtaining SPIV measurements for the resulting puffs could allow for more detailed comparisons to the single-phase condition. Additionally, varying both the droplet size and concentration could allow for comparisons to the results of Hogendoorn and Poelma (2018) and Agrawal et al. (2019) to examine if the so-called mixed and particle-induced regions occur for the given droplet size and at concentrations.

Bibliography

Agrawal N, Choueiri GH, Hof B (2019) Transition to turbulence in particle laden flows. Physical Review Letters 122(11):114502

Avila K, Moxey D, de Lozar A, Avila M, Barkley D, Hof B (2011) The onset of turbulence in pipe flow. Science 333(6039):192–196, DOI 10.1126/science.1203223

Balachandar S, Eaton J (2009) Turbulent dispersed and multiphase flow. Annual Review of Fluid Mechanics 42:111–133

Bandyopadhyay PR (1986) Aspects of the equilibrium puff in transitional pipe flow. Journal of Fluid Mechanics 163:439–458

Barkley D (2016) Theoretical perspective on the route to turbulence in a pipe. J Fluid Mech 803:1

Brown G (2002) The history of the darcy-weisbach equation for pipe flow resistance. In: Rogers J, AJ F (eds) Environmental and Water Resources History, American Society of Civil Engineers, DOI 10.1061/9780784406502

Cheng NS (2008) Formula for the viscosity of a glycerol−water mixture. Industrial & Engineering Chemistry Research 47(9):3285–3288, DOI 10.1021/ie071349z

Christensen K, Adrian RJ (2001) Statistical evidence of hairpin vortex packets in wall turbulence. Journal of Fluid Mechanics 431:433–443

Corcos GM, Sellars JR (1958) On the stability of fully developed flow in a pipe. Journal of Fluid Mechanics 5:47

Darbyshire AG, Mullin T (1995) Transition to turbulence in constant-mass-flux pipe flow. Journal of Fluid Mechanics 289:83–114, DOI 10.1017/S0022112095001248

Darcy H (1857) Recherches Expérimentales Relatives Au Mouvement De L'eau Dans Les Tuyaux. Texte. Mallet-Bachelier, Paris

Davey A, Drazin P (1969) The stability of poiseuille and flow in a pipe. J Fluid Mech 36:209–218

Dennis DJC, Nickels TB (2008) On the limitations of taylor's hypothesis in constructing long structures in a turbulent boundary layer. Journal of Fluid Mechanics 614:197, DOI 10.1017/S0022112008003352

Duguet Y, Pringle CCT, Kerswell RR (2008a) Relative periodic orbits in transitional pipe flow. Physics of Fluids 20(11):114102, DOI 10.1063/1.3009874

Duguet Y, Willis AP, Kerswell RR (2008b) Transition in pipe flow: the saddle structure on the boundary of turbulence. Journal of Fluid Mechanics 613:255–274, DOI 10.1017/S0022112008003248

Duguet Y, Willis AP, Kerswell RR (2010) Slug genesis in cylindrical pipe flow. Journal of Fluid Mechanics 663:180–208, DOI 10.1017/S0022112010003435

Eilers (1941) Die viskositat von emulsionen hochviskoser stoffe als funktion der konzentration. KOLLOID-ZEITSCHRIFT 3:313

Faisst H, Eckhardt B (2003) Travelling waves in pipe flow. Physical Review Letters 91:224502–1, DOI 10.1103/PhysRevLett.91.224502

Faisst H, Eckhardt B (2004) Sensitive dependence on initial conditions in transition to turbulence in pipe flow. Journal of Fluid Mechanics 504:343–352

Garg VK, Rouleau WT (1972) Linear spatial stability of pipe poiseuille flow. Journal of Fluid Mechanics 54:113–127

Gill A (1965) On the behaviour of small disturbances to poiseuille flow in a circular pipe. Journal of Fluid Mechanics 21:145–172

Hamilton, Kim J, Waleffe F (1995) Regeneration mechanisms of near-wall and turbulence structures. Journal of Fluid Mechanics 287:317–348

Hof B, Juel A, Mullin T (2003) Scaling of the turbulence transition threshold in a pipe. Physical Review Letters 91(24):244502, DOI 10.1103/PhysRevLett.91.244502

Hof B, van Doorne CWH, Westerweel J, Nieuwstadt FTM, Faisst H, Eckhardt B, Wedin H, Kerswell RR, Waleffe F (2004) Experimental observation of nonlinear traveling waves in turbulent pipe flow. Science 305(5690):1594–1598, DOI 10.1126/science.1100393

Hof B, van Doorne CW, Westerweel J, Nieuwstadt F (2005) Turbulence regeneration in pipe flow at moderate reynolds numbers. Physical Review Letters 95:214502

Hogendoorn W, Poelma C (2018) Particle-laden pipe flows at high volume fractions show transition without puffs. Physical review letters 121(19):194501

Holzner M, Song B, Avila M, Hof B (2013) Lagrangian approach to laminar-turbulent iinterface in transitional pipe flow. J Fluid Mech 723:140–162

Hoyt LF (1934) New table of the refractive index of pure glycerol at 20°c. Industrial & Engineering Chemistry 26(3):329–332, DOI 10.1021/ie50291a023

Jeong J, Hussain F (1995) On the identification of a vortex. Journal of fluid mechanics 285:69–94

Jodai Y, Elsinga GE (2016) Experimental observation of hairpin auto-generation events in a turbulent boundary layer. Journal of Fluid Mechanics 795:611–633, DOI 10.1017/jfm.2016.153

Kerswell R, Tutty O (2007) Recurrence of travelling waves in transitional pipe flow. Journal of Fluid Mechanics 584:69–102

Koohyar F, Rostami A, Chaichi M, Kiani F (2012) Study on thermodynamic properties for binary systems of water. Journal of Chemistry 2013

Krieger IM, Dougherty TJ (1959) A mechanism for non-newtonian flow in suspensions of rigid spheres. Journal of Rheology 3(1):137, DOI 10.1122/1.548848

Kuik D (2011) Localized turbulence in pipe flow. PhD thesis, TU Delft

Kuik D, Poelma C, Westerweel J (2010) Quantitative measurement of the lifetime of localized turbulence in pipe flow. Journal of Fluid Mechanics 645:529–539, DOI 10.1017/

Lessen M (1968) Stability of pipe poiseuille flow. Physics of Fluids 11(7):1404, DOI 10.1063/1.1692122

Lessen M, Fox JA, Bhat WV, Liu TY (1964) Stability of hagen-poiseuille flow. Physics of Fluids 7(8):1384, DOI 10.1063/1.1711385

Matas JP, Morris JF, Guazzelli E (2003a) Influence of particles on the transition to turbulence in pipe flow. Philosophical Transactions of the Royal Society A: Mathematical, Physical and Engineering Sciences 361(1806):911–919, DOI 10.1098/rsta.2003.1173

Matas JP, Morris JF, Guazzelli E (2003b) Transition to turbulence in particulate pipe flow. Physical Review Letters 90:014501

Meseguer A, Trefethen LN (2003) Linearized pipe flow to reynolds number 10^7. Journal of Computational Physics 186:178–197

Moody LF (1944) Friction factors for pipe flow. Trans ASME 66:671–684

Mukund V, Hof B (2018) The critical point of the transition to turbulence in pipe flow. Journal of Fluid Mechanics 839:76–94

Nishi M, Unsal B, Durst F, Biswas G (2008) Laminar-to-turbulent transition of pipe flows through puffs and slugs. J Fluid Mech 614:425–446, DOI 10.1017/S0022112008003315

Pal R (1993) Pipeline flow of unstable and surfactant-stabilized emulsions. AIChE Journal 39(11):1754–1764, DOI 10.1002/aic.690391103

Peixinho J, Mullin T (2007) Finite-amplitude thresholds for transition in pipe flow. Journal of Fluid Mechanics 582:169, DOI 10.1017/S0022112007006398

Pekeris C (1948) Stability of the laminar flow through a straight pipe of circular cross-section to infinitesimal disturbances which are symmetrical about the axis of the pipe. Proceedings of the National Academy of Sciences of the United States of America 34:285–195

Pouplin A (2009) Ecoulments liquide-liquide disperses homogenes en conduite horizontale: approche locale en milieu concentre. PhD thesis, Universite de Toulouse

Pouplin A, Masbernat O, Decarre S, Line A (2011) Wall friction and effective viscosity and of a homogeneous dispersed and liquid–liquid flow in a horizontal pipe. Fluid Mechanics and Transport Phenomena AIChE 57:1119–1131, DOI 10.1002/aic.12334

Pringle CC, Willis AP, Kerswell RR (2012) Minimal seeds for shear flow turbulence: using nonlinear transient growth to touch the edge of chaos. Journal of Fluid Mechanics 702:415–443, DOI 10.1017/jfm.2012.192

Pringle CCT, Kerswell R (2010) Using nonlinear transient growth to construct the minimal seed for shear flow turbulence. Phys Rev Let 105:154502

Pringle CCT, Willis AP, Kerswell RR (2015) Fully localised nonlinear energy growth optimals in pipe flow. Physics of Fluids 27(6):064102, DOI 10.1063/1.4922183

Reddy SC, Trefethen LN (1990) Lax-stability of fully discrete spectral methods via stability regions and pseudo-eigenvalues. Computer Methods in Applied Mechanics and Engineering 80(1-3):147–164

Reddy SC, Schmid PJ, Henningson DS (1993) Pseudospectra of the orr–sommerfeld operator. SIAM Journal on Applied Mathematics 53(1):15–47

Reynolds O (1883) An experimental investigation of the circumstances which determine whether the motion of water shall be direct or sinuous, and of the law of resistance in parallel channels. Philosophical Transactions of the Royal Society of London 17:935–982

Samanta D, de Lozar A, Hof B (2011) Experimental investigation of laminar turbulent intermittency in pipe flow. Journal of Fluid Mechanics 681:193–204

Schensted I (1960) Contributions to the linear theory of hydrodynamic stability. PhD thesis, University of Michigan

Schmid PJ, Henningson DS (1994) Optimal energy density growth in hagen–poiseuille flow. Journal of Fluid Mechanics 277:197–225, DOI 10.1017/S0022112094002739

Sexl T (1927) Zur stabilitatsfrage der poiseuilleschen und couetteschen stromung. Annalender Physik 83:835

Shimizu M, Kida S (2009) A driving mechanism of a turbulent puff in a pipe flow. Fluid Dyn Res 41:045501

Toms BA (1948) Some observations on the flow of linear polymer solutions through straight tubes at large reynolds numbers. Proc of In Cong On Rheology, 1948 135

Trefethen LN, Trefethen A, Reddy S, Driscoll T (1993) Hydrodynamic stability without eigenvalues. Science 261:578

van Doorne CW, Westerweel J (2009) The flow structure of a puff. Philosophical Transactions of the Royal Society A: Mathematical, Physical and Engineering Sciences 367(1888):489–507, DOI 10.1098/rsta.2008.0227

van Doorne CWH (2004) Stereoscopic piv on transition in pipe flow. PhD thesis, TU Delft

Waleffe F (1997) On a self-sustaining process in shear flows. Physics of Fluids 9(4):883, DOI 10.1063/1.869185

Waleffe F (1998) Three-dimensional coherent states in shear plane flows. Phys Rev Let 81:4140

Waleffe F (2001) Exact coherent structures in channel flow. Journal of Fluid Mechanics 435:93–102

Waleffe F (2003) Homotopy of exact coherent structures in plane shear flows. Physics of Fluids 15(6):1517, DOI 10.1063/1.1566753

Wedin H (2004) Nonlinear solutions to pipe. PhD thesis, University of Bristol

Weisbach JL (1845) Lehrbuch der Ingenieur-und Maschinen-Mechanik: Theoretische Mechanik, vol 1. Druck und Verlag von Friedrich Vieweg und Sohn

Westerweel J, Scarano F (2005) Universal outlier detection for piv data. Experiments in Fluids 39(6):1096–1100, DOI 10.1007/s00348-005-0016-6

Westerweel J, Draad AA, van der Hoeven J G Th, van Oord J (1996) Measurement of fully-developed turbulent pipe flow with digital particle and image velocimetry. Experiments in Fluids 20:165–177

Willis AP, Kerswell R (2008) Coherent structures in localized and global pipe turbulence. Phys Rev Let 100:124501

Wygnanski I, Champagne FH (1973) On transition in a pipe. part 1. the orgin of puffs and slugs and the flow in a turbulent slug. Journal of Fluid Mechanics 59:281–335, DOI 10.1017/S0022112073001576

Wygnanski I, Sokolov M, Friedman D (1975) On transition in a pipe. and part 2. the and equilibrium puff. Journal of Fluid Mechanics 69:283–304

Zhou J, Adrian RJ, Balachandar S, Kendall TM (1999) Mechanisms for generating coherent and packets of hairpin vortices in channel flow. Journal of Fluid Mechanics 387:353–396

Appendix A

Data Collection Procedures

A.1 The procedure for the puff frequency records

1. Use either Visual Monitoring VI, or manual input from the inverter to run the pump at a moderate speed. (approximately 1V from the VI or 7Hz on the inverter) for approximately five minutes. This ensures that the liquid in the facility is well mixed.
2. Once mixed, use a small pipet to sample fluid from the discharge tank to measure the index of refraction, and read the temperature.
3. Use the temperature, index of refraction, and desired voltage as inputs into CalcRe() to determine the density, viscosity, volume/mass fraction, and Reynolds number of the fluid. Adjust if necessary leaving a few minutes between adjustments to allow for complete mixing.
4. Run "Visual Monitoring Station Long Records w control and vision.vi"
5. Enter the "number of files to generate" by entering the number of independent Reynolds numbers that are going to be tested.
6. Enter the "number of samples per file" and the "sampling frequency" required for each file.
7. Click "OK"
8. Slowly increase the "Inverter Voltage Control" to the desired voltage according to the result from ReCalc() using the "Inverter Voltage Control".
9. Click "Done Setting Voltage"
10. At the end of each run, save the voltage records from the pressure transducer and the RTD.

11. Check that the RTD voltage did not drift during the course of the record.
12. Repeat steps 8-11 until the last file has been generated and saved.

A.2 The procedure for the PIV records

1. Steps 1-3 from above.
2. Once mixed, use a small pipet to sample fluid from the discharge tank to measure the index of refraction, and read the temperature.
3. Use the temperature, index of refraction, and desired voltage as inputs into CalcRe() to determine the density, viscosity, volume/mass fraction, and Reynolds number of the fluid. Adjust if necessary leaving a few minutes between adjustments to allow for complete mixing.
4. Open "Visual Monitoring Station Triggering w control.vi".
5. Set dt [s] to the desired voltage sampling time step. (default 0.001s).
6. Set the filter number as the number of samples with which to median filter the raw voltage signal (default 5).
7. Set the "Samples per update" to the number of raw voltage samples to be taken before the VI plots and checks the triggering criteria (default 10).
8. Run "Visual Monitoring Station Triggering w control.vi".
9. Slowly increase the "Inverter Voltage Control" to the desired voltage.
10. Click "Done Setting Voltage"
11. Observe the system for some time to ensure that puffs are occurring at a rate that is desired.
12. Set the "Threshold" to a value that corresponds to roughly 3/4 of the peak voltage generated by a passing puff.
13. Set the "Trigger Delay [s]" to the number of seconds the VI will wait after the voltage peak before it sends the triggering signal to the Lavision High Speed Controller in the PIV system.
14. Click the red "Armed" button to "On" to allow the system to trigger the PIV system the next time the triggering conditions are met.

Appendix B

PIV Cabling

Figure B.1 shows the cabling between the PCs, laser, cameras, and other hardware.

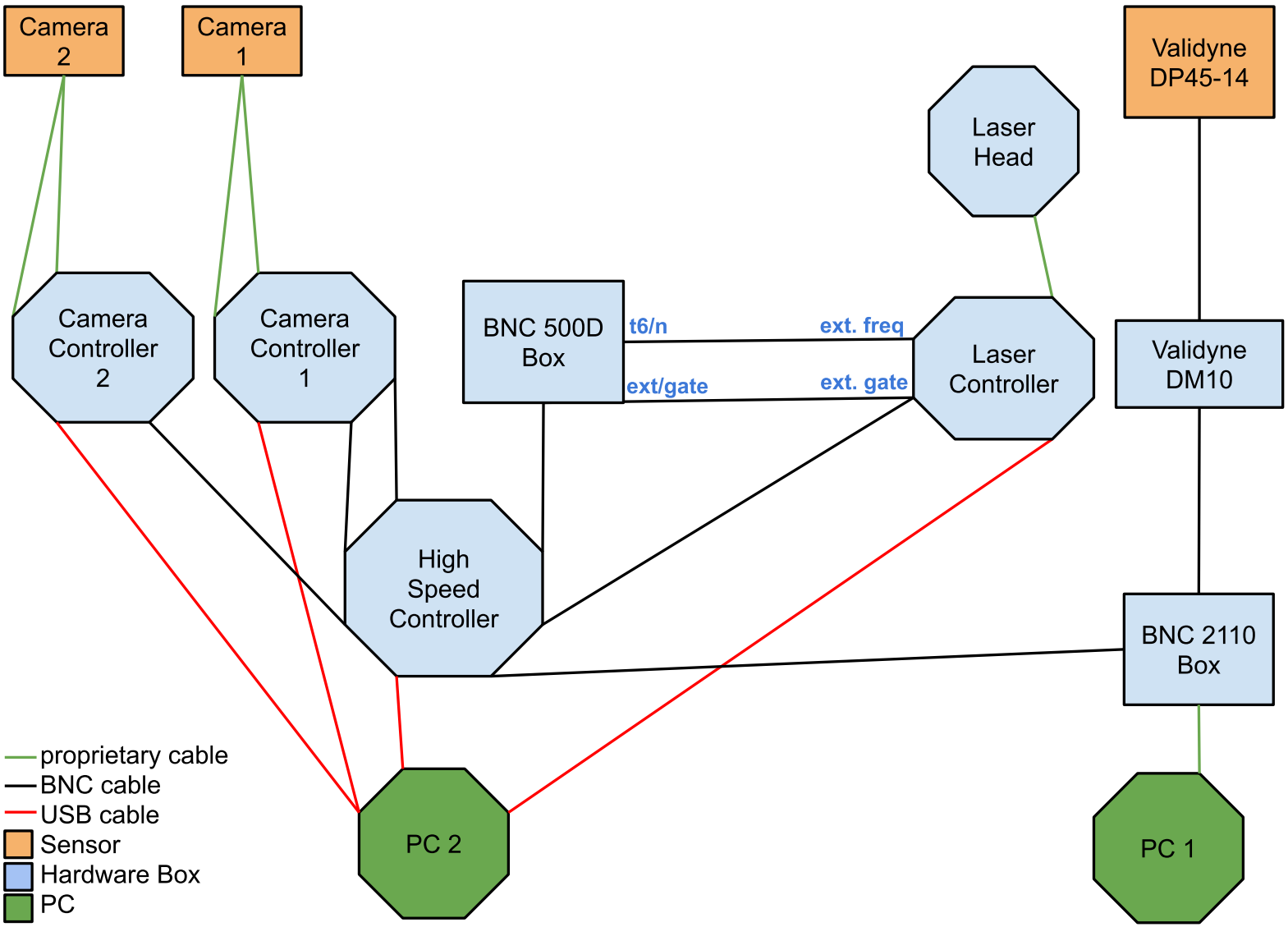
Camera 2
Camera 1
Validyne DP45-14
Laser Head
Camera Controller 2
Camera Controller 1
BNC 500D Box
t6/n
ext. freq
ext/gate
ext. gate
Laser Controller
Validyne DM10
High Speed Controller
BNC 2110 Box
proprietary cable
BNC cable
USB cable
Sensor
Hardware Box
PC
PC 2
PC 1

Figure B.1

Appendix C

Swirl Plots of SPIV Puffs

Appendix C is a gallery of images showing isosurfaces of strongly swirling regions in each record. Each page shows two domains, a large one that depicts the entirety of such regions for the given puff record, and a smaller sub-domain located at the trailing edge. The isosurfaces are found by calculating a threshold at 0.5 standard deviation above the mean of λ_{3D}^{i} within $-0.07 < z^{*} < 0.07$. Thus, the threshold on λ_{3D}^{*} is specific to each record, and is likely to capture the dominant swirling structure at the trailing edge.

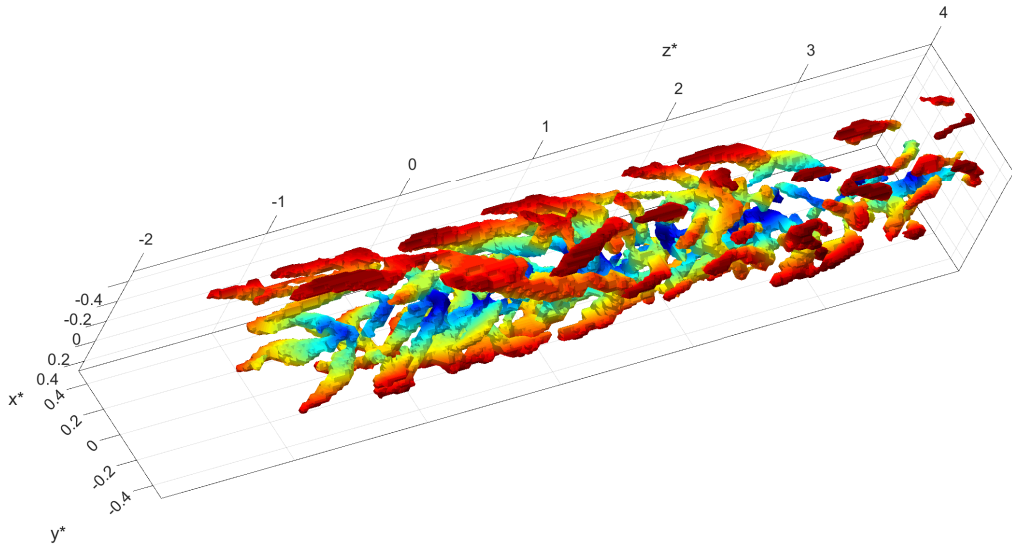

Figure C.1: Isosurfaces of swirl corresponding to $\lambda_{3D}^{*,i} > 1.7979$ inside Puff S-1. Colors move from red to blue with increasing wall distance.

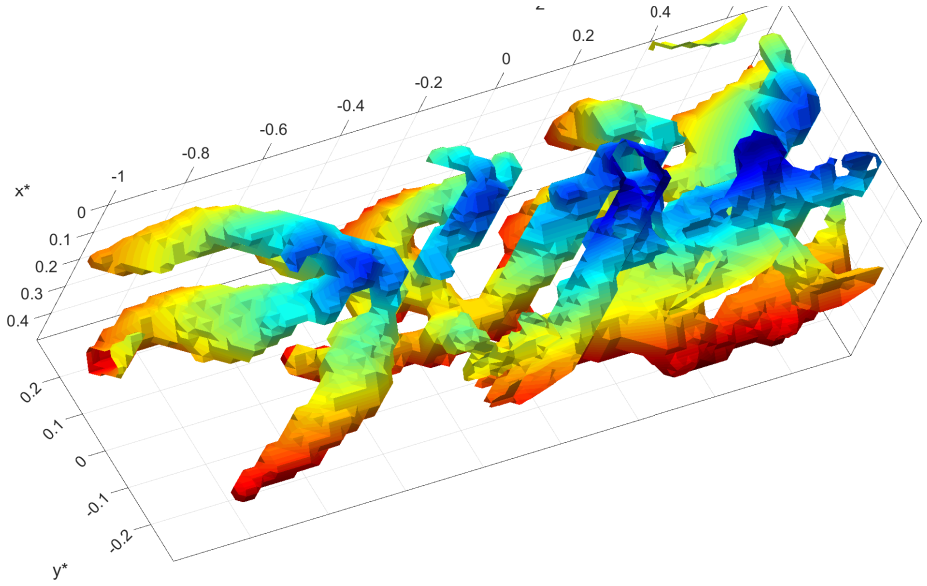

Figure C.2: Isosurfaces of swirl corresponding to $\lambda_{3D}^{*,i} > 1.7979$ within $-0.07 < z^* < 0.07$ inside Puff S-1. Colors move from red to blue with increasing wall distance.

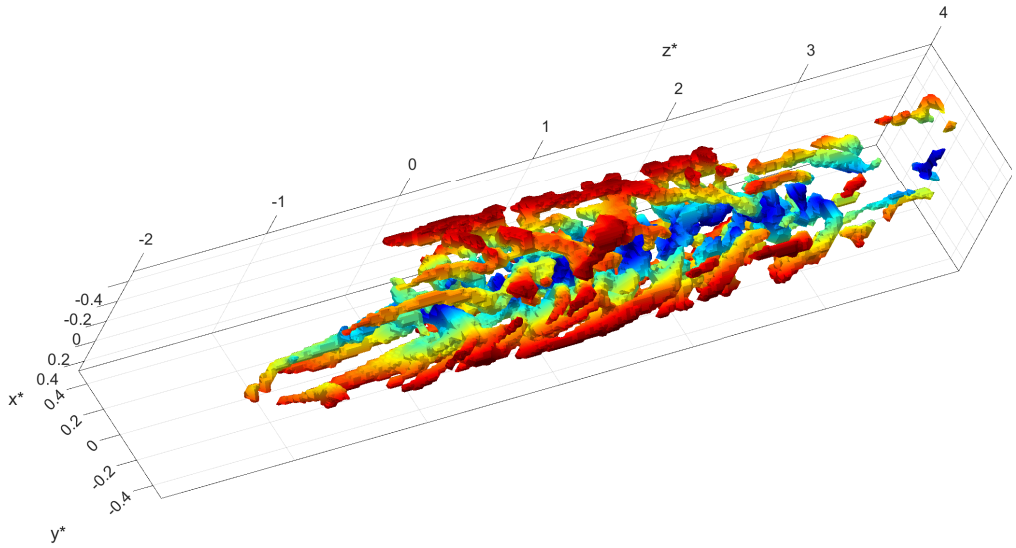

Figure C.3: Isosurfaces of swirl corresponding to $\lambda_{3D}^{*,i} > 1.5062$ inside Puff S-2. Colors move from red to blue with increasing wall distance.

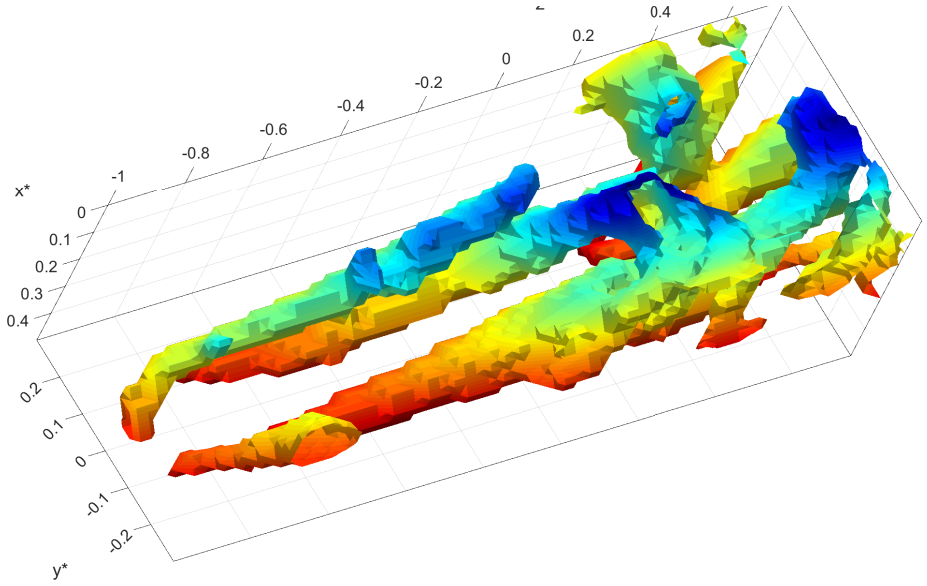

Figure C.4: Isosurfaces of swirl corresponding to $\lambda_{3D}^{*,i} > 1.5062$ within $-0.07 < z^* < 0.07$ inside Puff S-2. Colors move from red to blue with increasing wall distance.

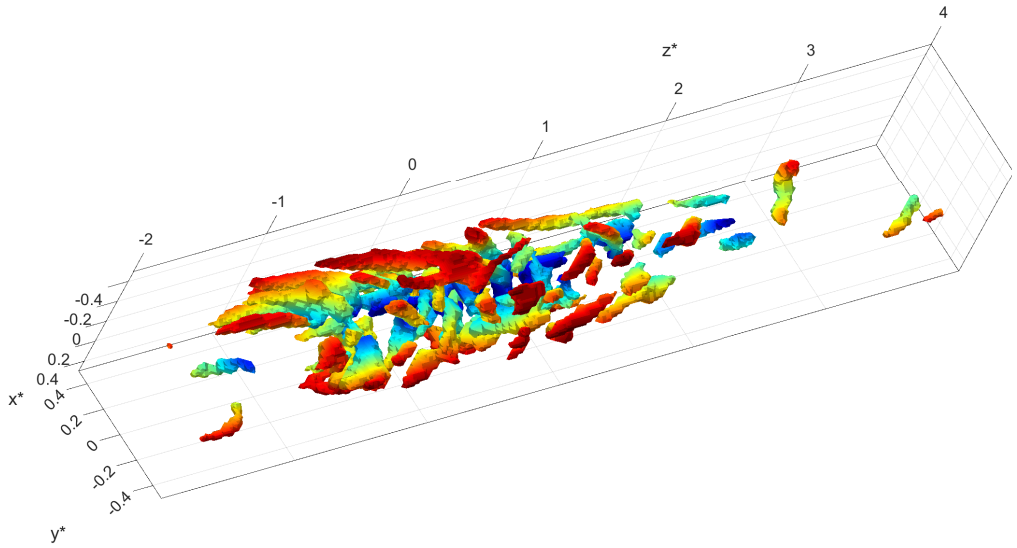

Figure C.5: Isosurfaces of swirl corresponding to $\lambda_{3D}^{*,i} > 1.776$ inside Puff S-3. Colors move from red to blue with increasing wall distance.

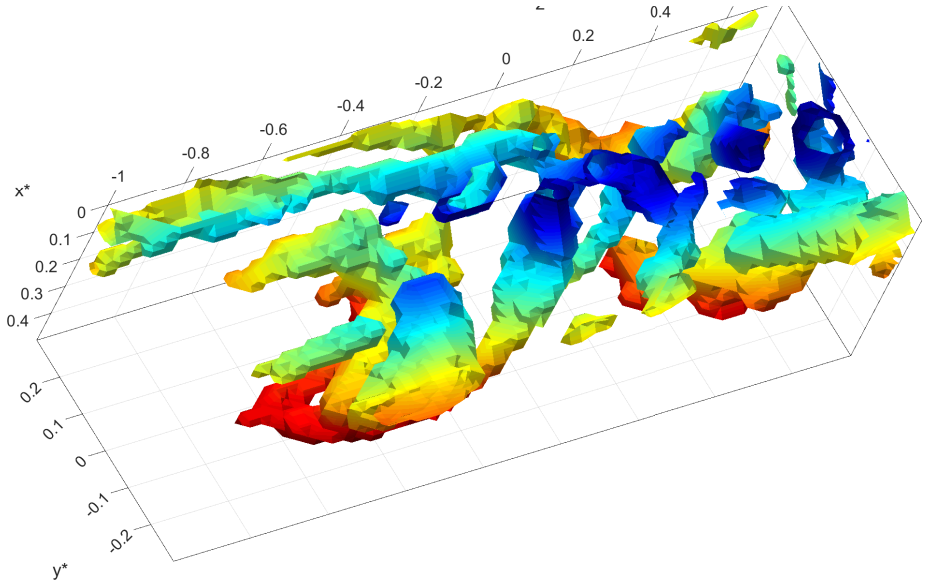

Figure C.6: Isosurfaces of swirl corresponding to $\lambda_{3D}^{*,i} > 1.776$ within $-0.07 < z^* < 0.07$ inside Puff S-3. Colors move from red to blue with increasing wall distance.

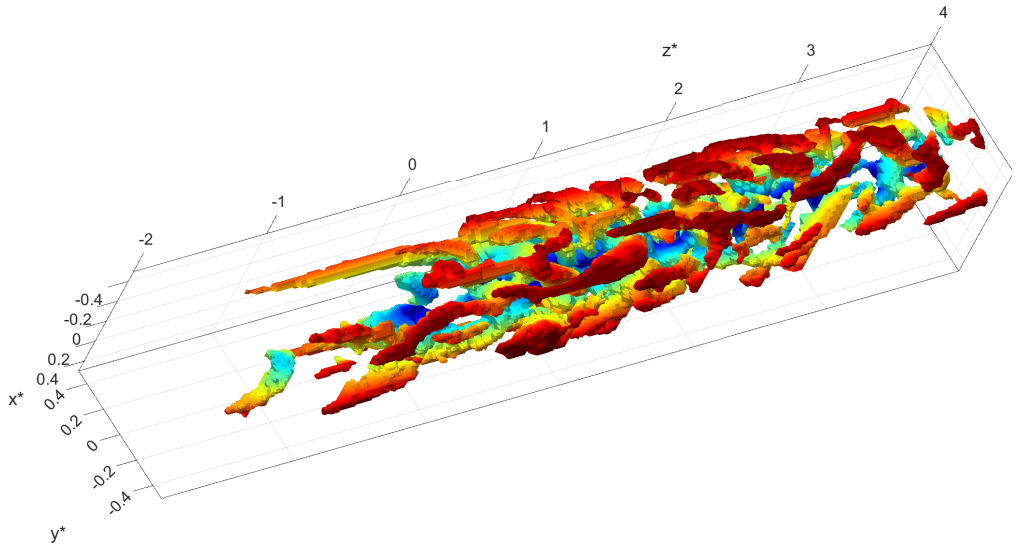

Figure C.7: Isosurfaces of swirl corresponding to $\lambda_{3D}^{*,i} > 1.4179$ inside Puff S-4. Colors move from red to blue with increasing wall distance.

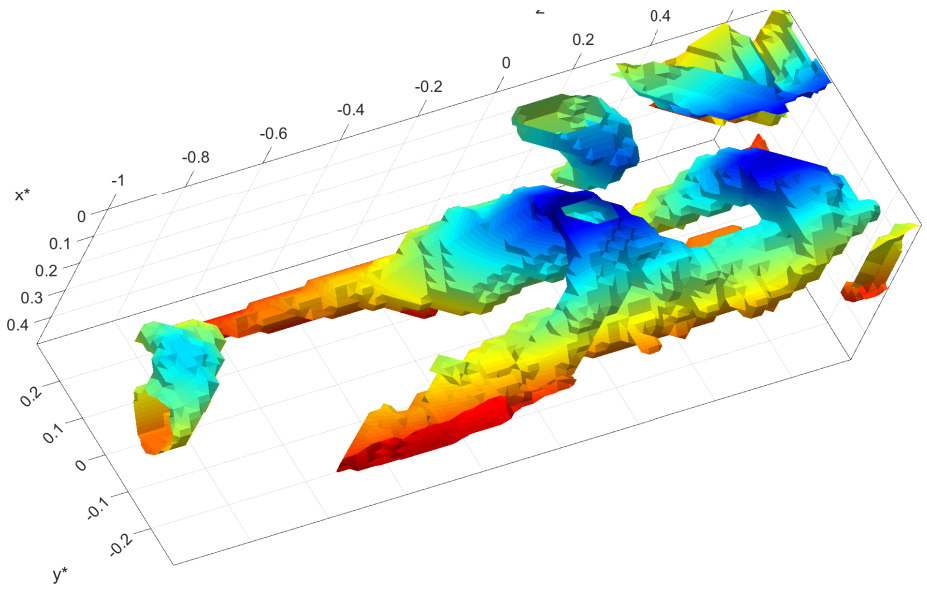

Figure C.8: Isosurfaces of swirl corresponding to $\lambda_{3D}^{*,i} > 1.4179$ within $-0.07 < z^* < 0.07$ inside Puff S-4. Colors move from red to blue with increasing wall distance.

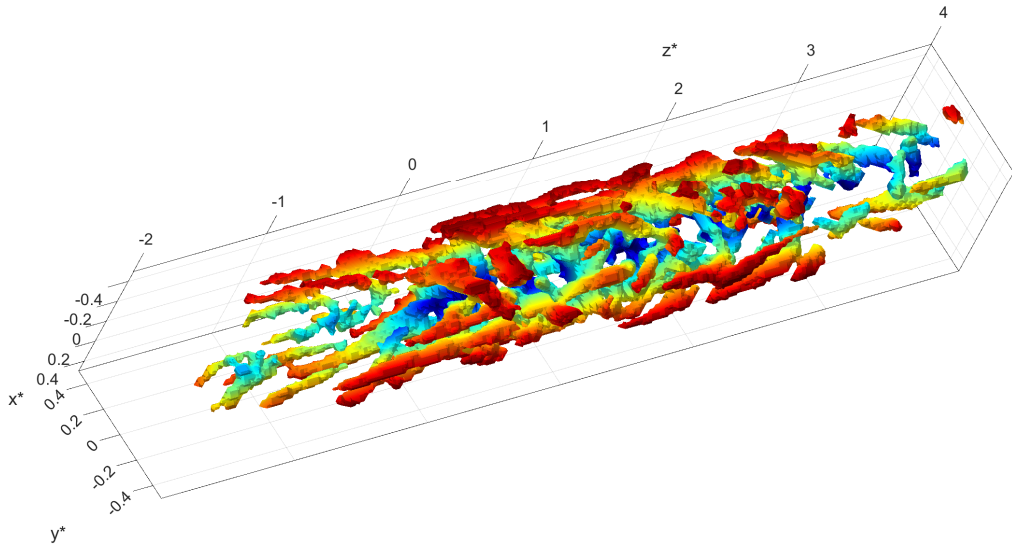

Figure C.9: Isosurfaces of swirl corresponding to $\lambda_{3D}^{*,i} > 1.3642$ inside Puff S-5. Colors move from red to blue with increasing wall distance.

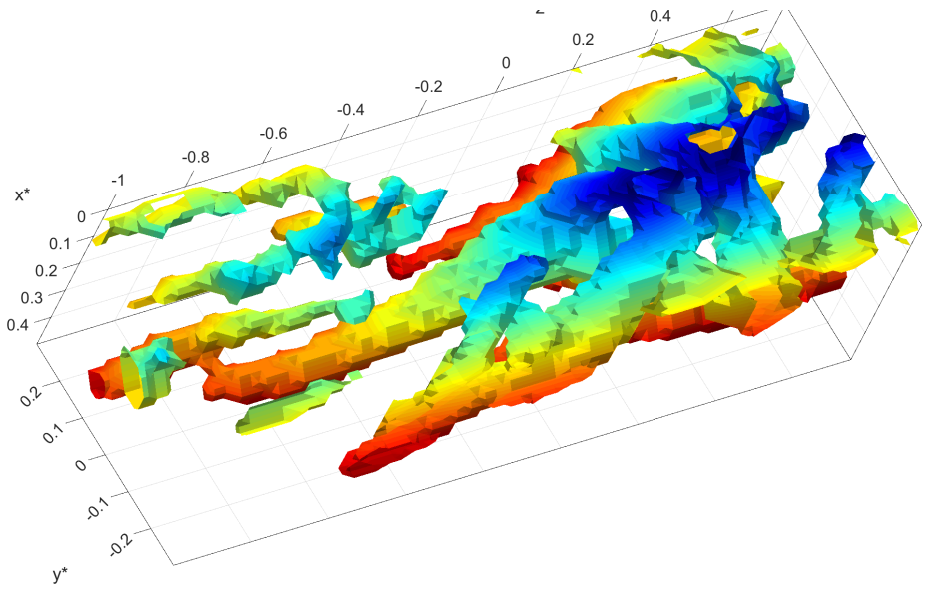

Figure C.10: Isosurfaces of swirl corresponding to $\lambda_{3D}^{*,i} > 1.3642$ within $-0.07 < z^* < 0.07$ inside Puff S-5. Colors move from red to blue with increasing wall distance.

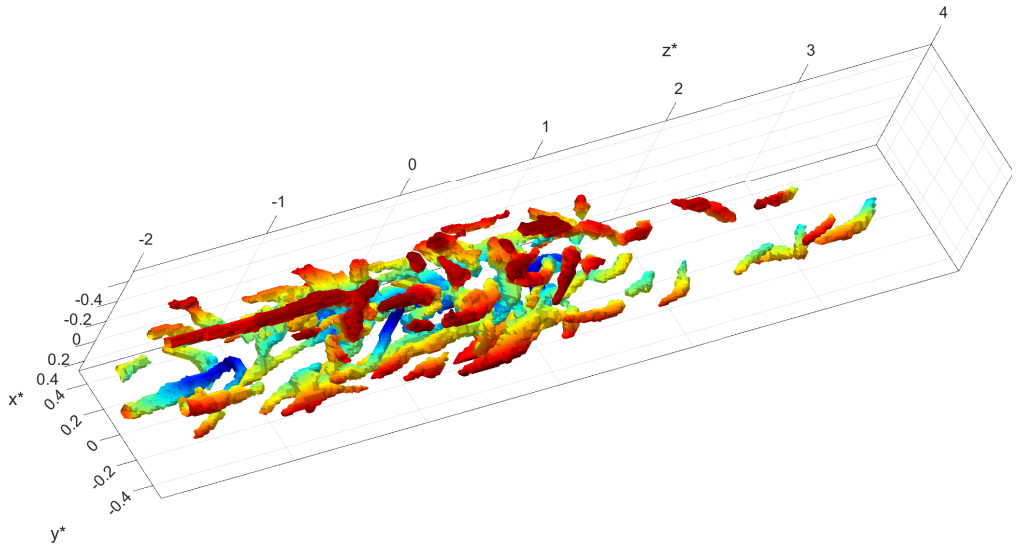

Figure C.11: Isosurfaces of swirl corresponding to $\lambda_{3D}^{*,i} > 1.67$ inside Puff S-6. Colors move from red to blue with increasing wall distance.

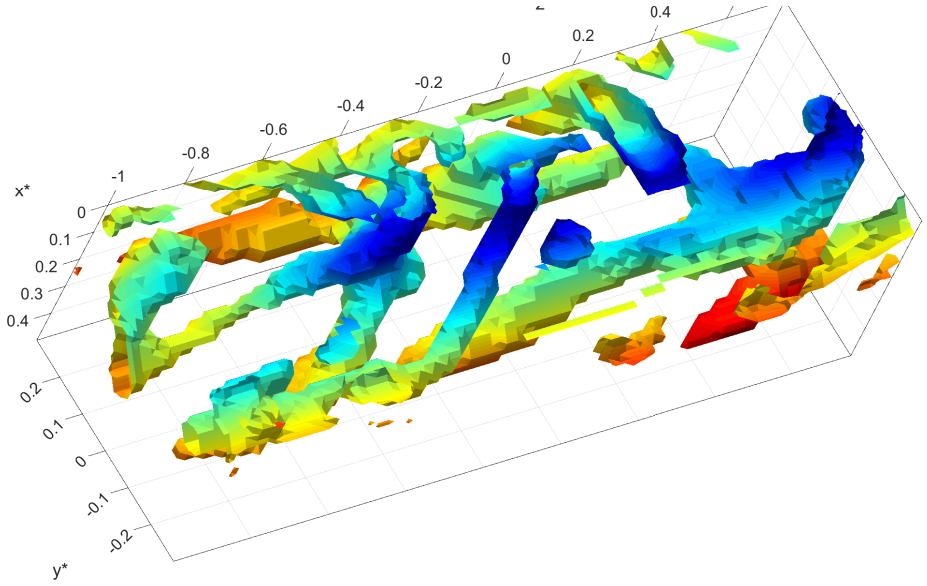

Figure C.12: Isosurfaces of swirl corresponding to $\lambda_{3D}^{*,i} > 1.67$ within $-0.07 < z^* < 0.07$ inside Puff S-6. Colors move from red to blue with increasing wall distance.

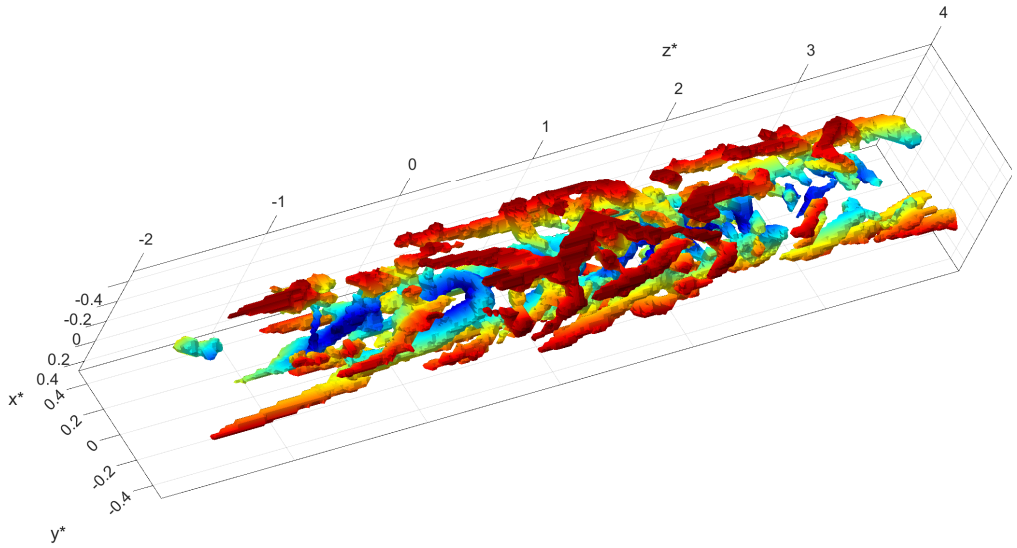

Figure C.13: Isosurfaces of swirl corresponding to $\lambda_{3D}^{*,i} > 1.5018$ inside Puff S-7. Colors move from red to blue with increasing wall distance.

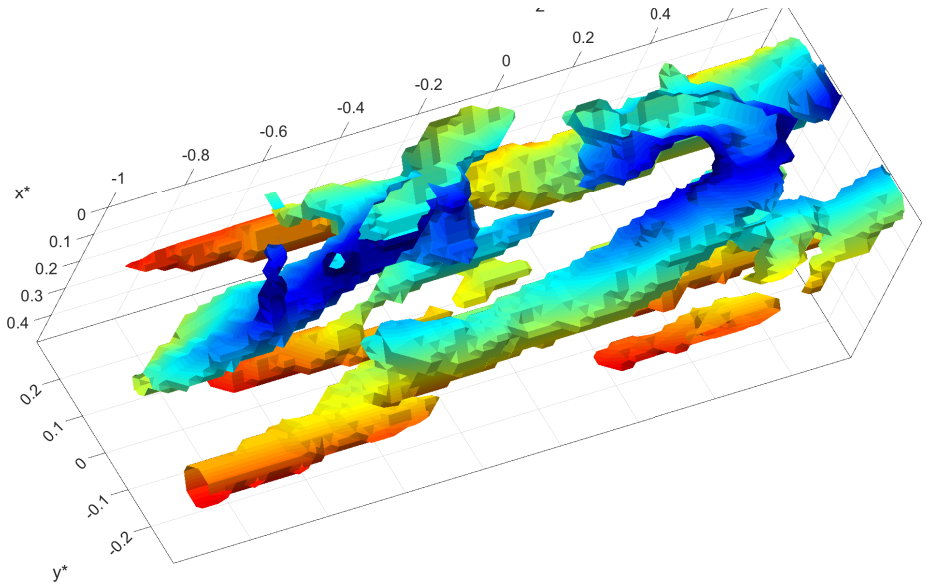

Figure C.14: Isosurfaces of swirl corresponding to $\lambda_{3D}^{*,i} > 1.5018$ within $-0.07 < z^* < 0.07$ inside Puff S-7. Colors move from red to blue with increasing wall distance.

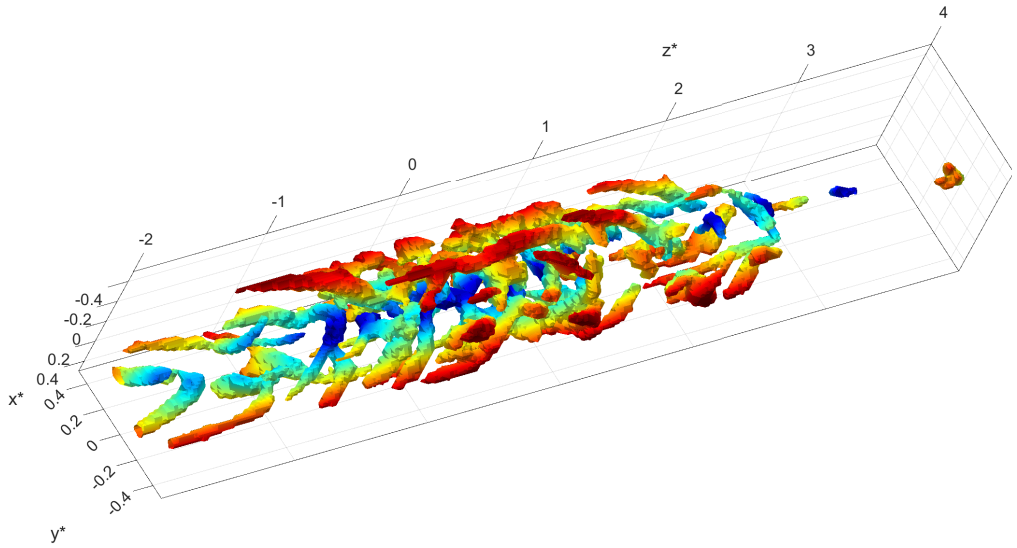

Figure C.15: Isosurfaces of swirl corresponding to $\lambda_{3D}^{*,i} > 1.7415$ inside Puff S-8. Colors move from red to blue with increasing wall distance.

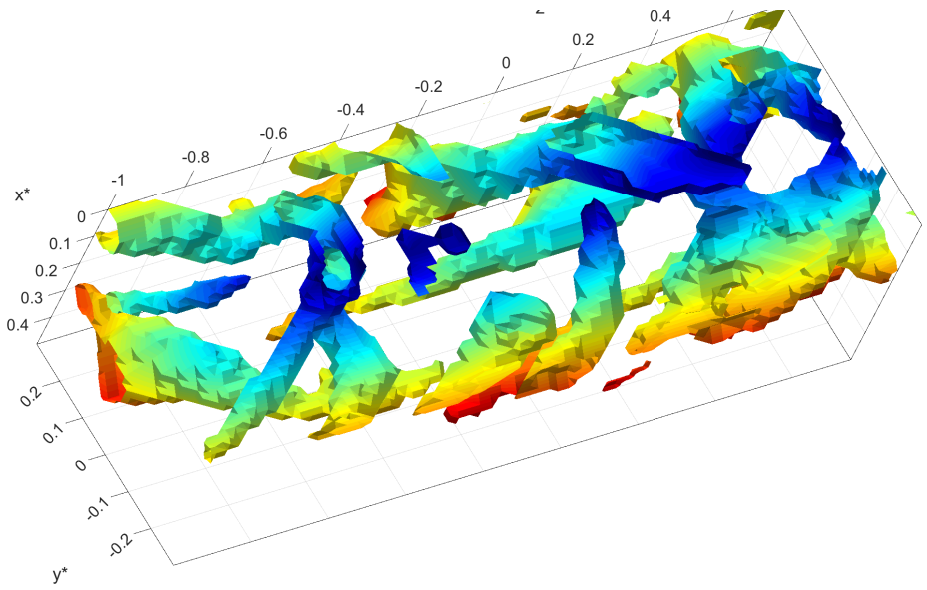

Figure C.16: Isosurfaces of swirl corresponding to $\lambda_{3D}^{*,i} > 1.7415$ within $-0.07 < z^* < 0.07$ inside Puff S-8. Colors move from red to blue with increasing wall distance.

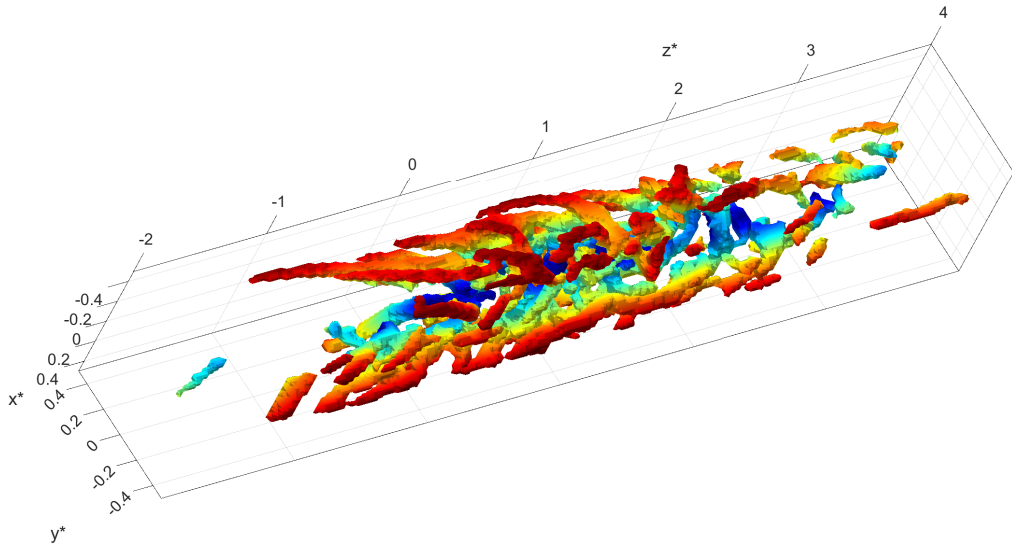

Figure C.17: Isosurfaces of swirl corresponding to $\lambda_{3D}^{*,i} > 1.6767$ inside Puff S-9. Colors move from red to blue with increasing wall distance.

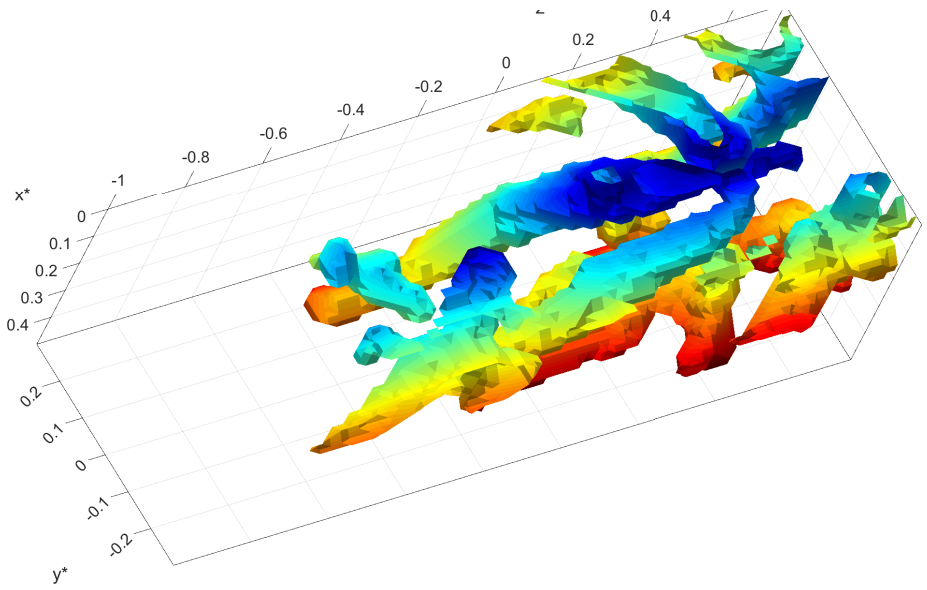

Figure C.18: Isosurfaces of swirl corresponding to $\lambda_{3D}^{*,i} > 1.6767$ within $-0.07 < z^* < 0.07$ inside Puff S-9. Colors move from red to blue with increasing wall distance.

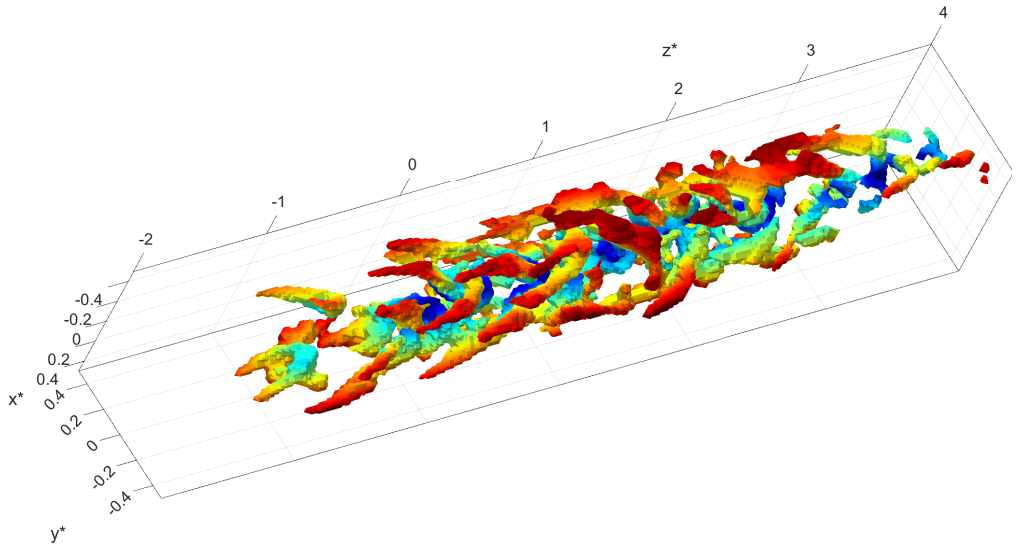

Figure C.19: Isosurfaces of swirl corresponding to $\lambda_{3D}^{*,i} > 1.6961$ inside Puff S-10. Colors move from red to blue with increasing wall distance.

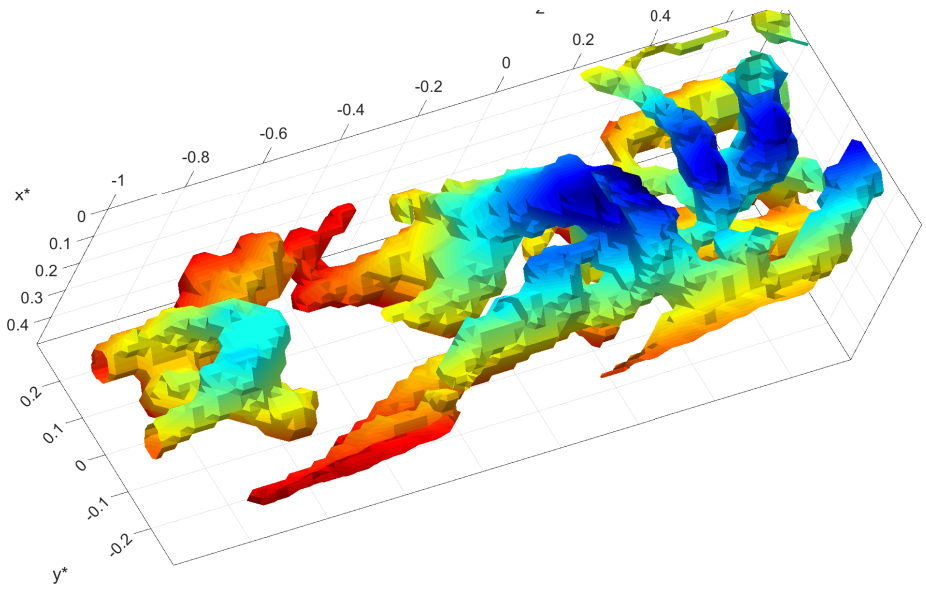

Figure C.20: Isosurfaces of swirl corresponding to $\lambda_{3D}^{*,i} > 1.6961$ within $-0.07 < z^* < 0.07$ inside Puff S-10. Colors move from red to blue with increasing wall distance.

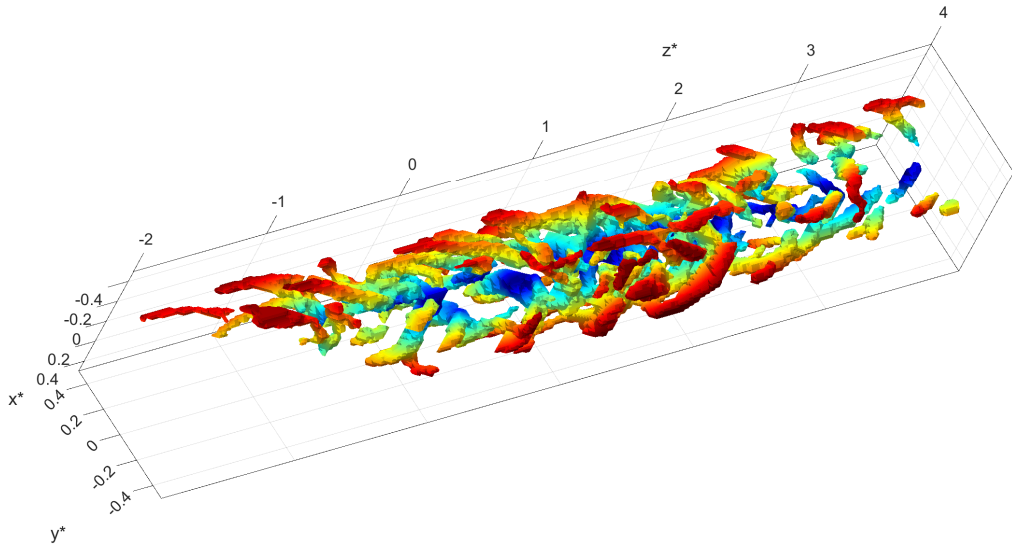

Figure C.21: Isosurfaces of swirl corresponding to $\lambda_{3D}^{*,i} > 1.657$ inside Puff S-11. Colors move from red to blue with increasing wall distance.

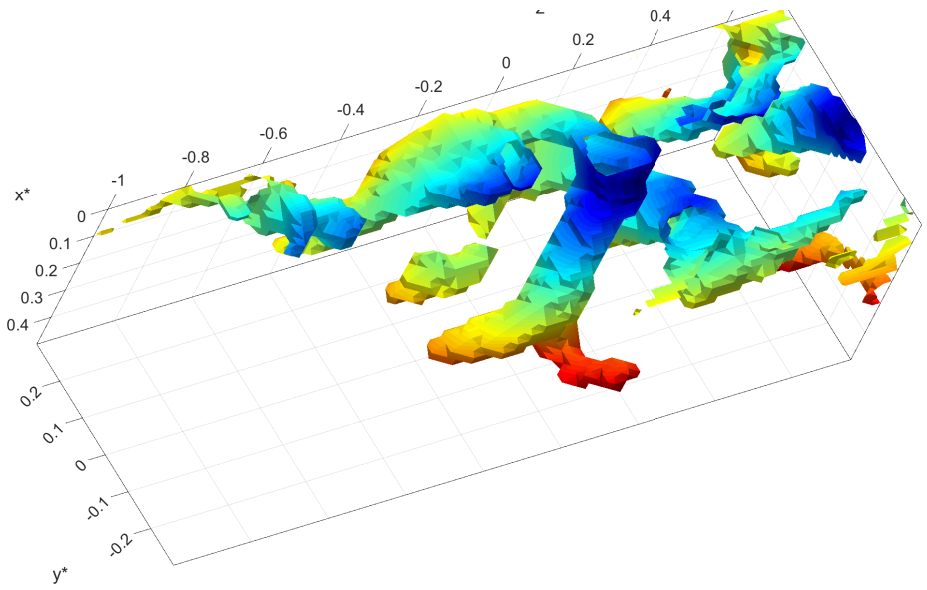

Figure C.22: Isosurfaces of swirl corresponding to $\lambda_{3D}^{*,i} > 1.657$ within $-0.07 < z^* < 0.07$ inside Puff S-11. Colors move from red to blue with increasing wall distance.

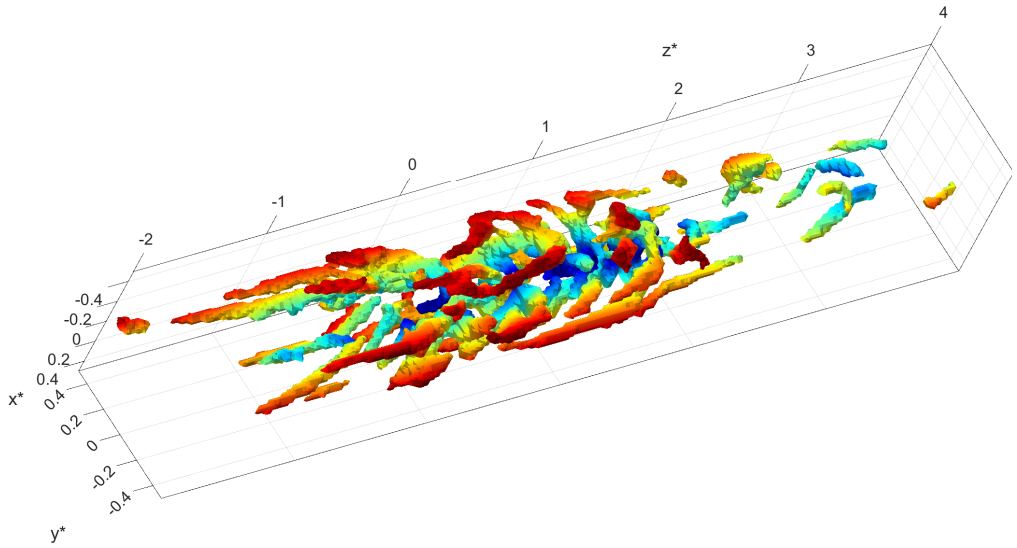

Figure C.23: Isosurfaces of swirl corresponding to $\lambda_{3D}^{*,i} > 1.7062$ inside Puff S-12. Colors move from red to blue with increasing wall distance.

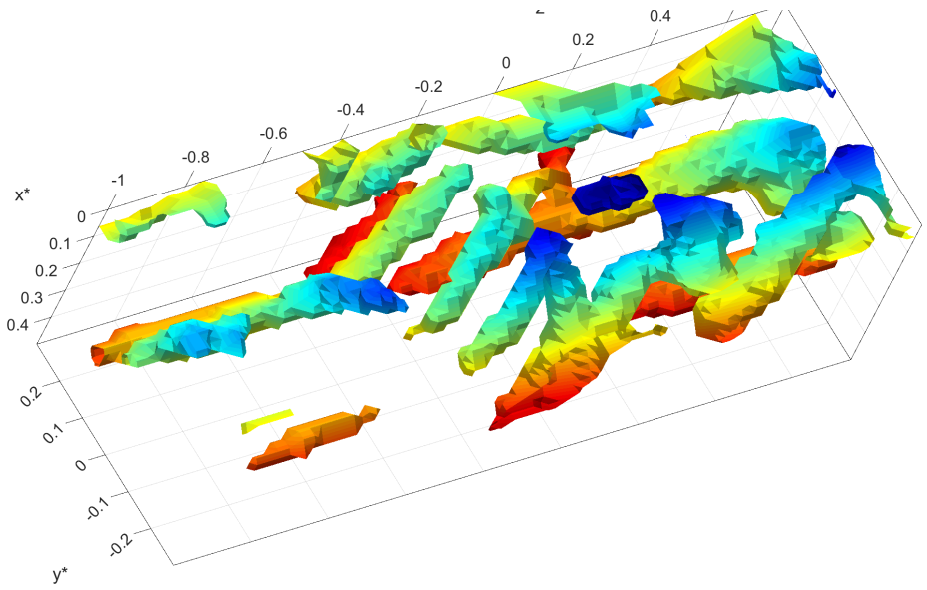

Figure C.24: Isosurfaces of swirl corresponding to $\lambda_{3D}^{*,i} > 1.7062$ within $-0.07 < z^* < 0.07$ inside Puff S-12. Colors move from red to blue with increasing wall distance.

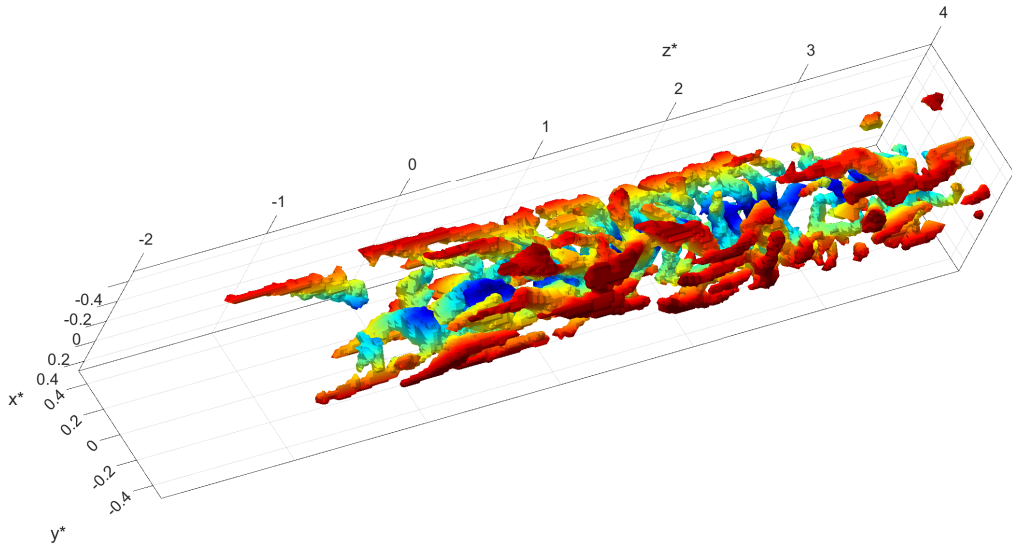

Figure C.25: Isosurfaces of swirl corresponding to $\lambda_{3D}^{*,i} > 1.4969$ inside Puff S-13. Colors move from red to blue with increasing wall distance.

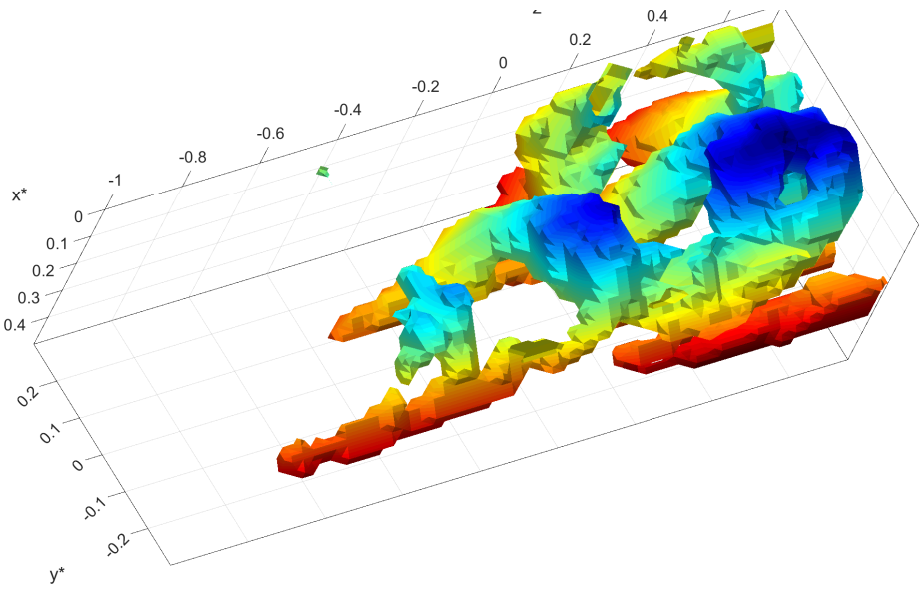

Figure C.26: Isosurfaces of swirl corresponding to $\lambda_{3D}^{*,i} > 1.4969$ within $-0.07 < z^* < 0.07$ inside Puff S-13. Colors move from red to blue with increasing wall distance.

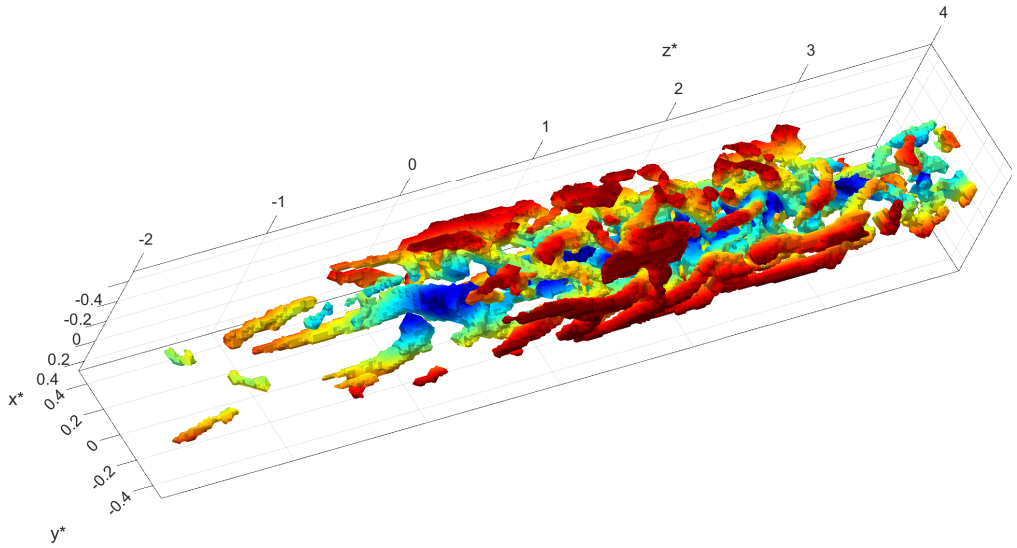

Figure C.27: Isosurfaces of swirl corresponding to $\lambda_{3D}^{*,i} > 1.3963$ inside Puff S-14. Colors move from red to blue with increasing wall distance.

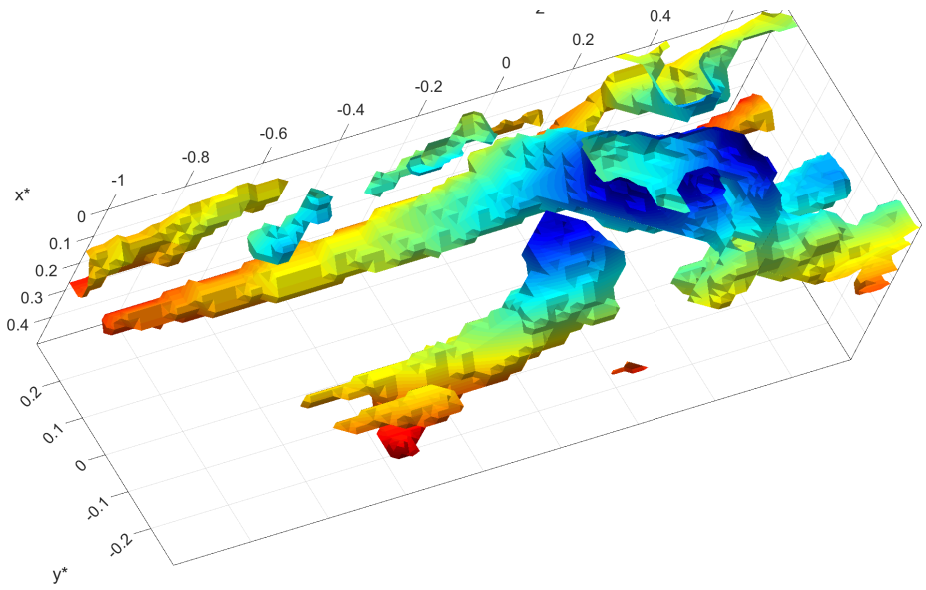

Figure C.28: Isosurfaces of swirl corresponding to $\lambda_{3D}^{*,i} > 1.3963$ within $-0.07 < z^* < 0.07$ inside Puff S-14. Colors move from red to blue with increasing wall distance.

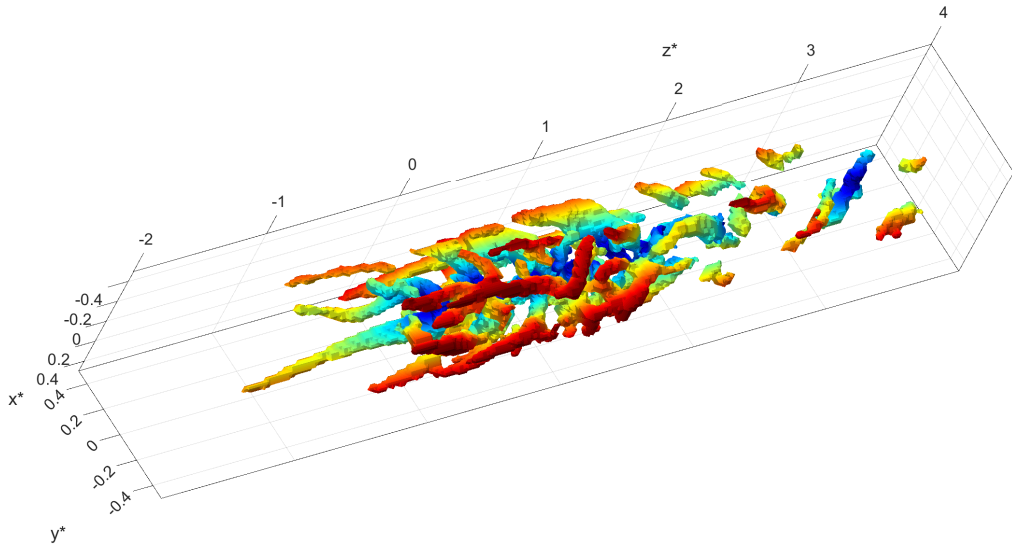

Figure C.29: Isosurfaces of swirl corresponding to $\lambda_{3D}^{*,i} > 1.6842$ inside Puff S-15. Colors move from red to blue with increasing wall distance.

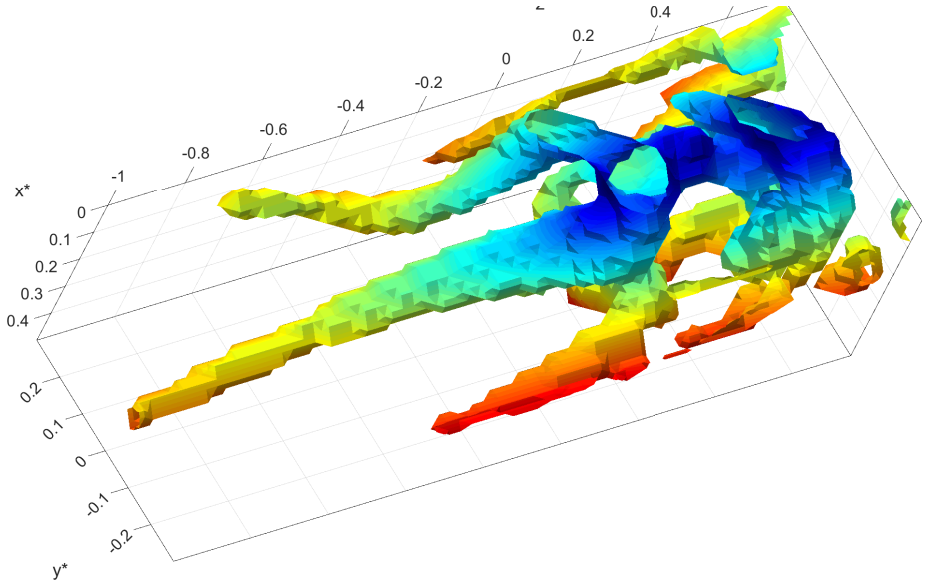

Figure C.30: Isosurfaces of swirl corresponding to $\lambda_{3D}^{*,i} > 1.6842$ within $-0.07 < z^* < 0.07$ inside Puff S-15. Colors move from red to blue with increasing wall distance.

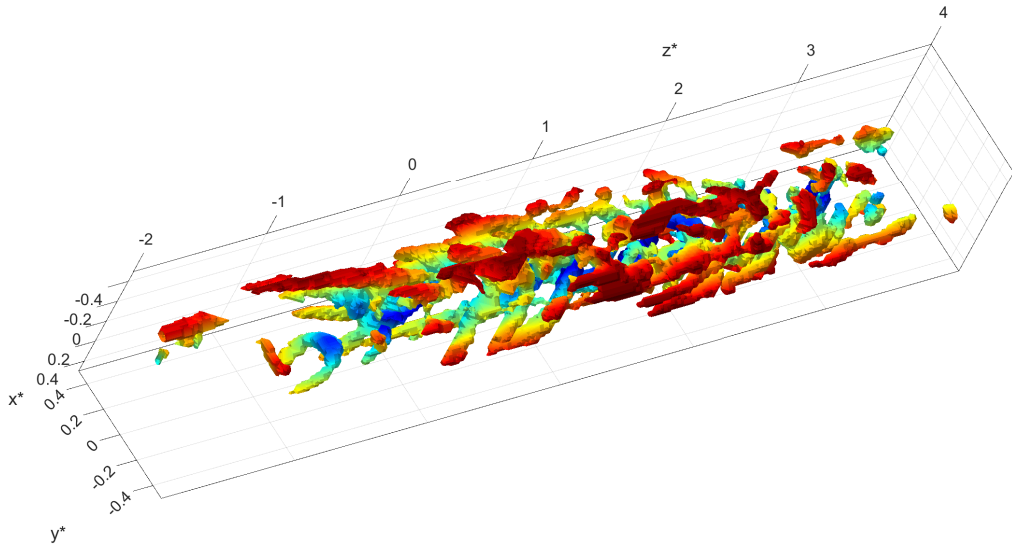

Figure C.31: Isosurfaces of swirl corresponding to $\lambda_{3D}^{*,i} > 1.4241$ inside Puff S-16. Colors move from red to blue with increasing wall distance.

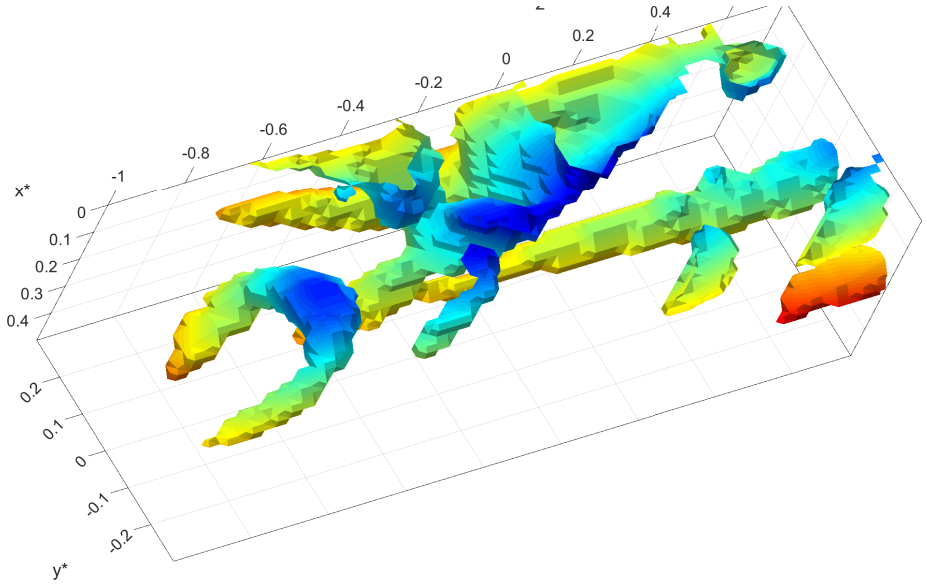

Figure C.32: Isosurfaces of swirl corresponding to $\lambda_{3D}^{*,i} > 1.4241$ within $-0.07 < z^* < 0.07$ inside Puff S-16. Colors move from red to blue with increasing wall distance.

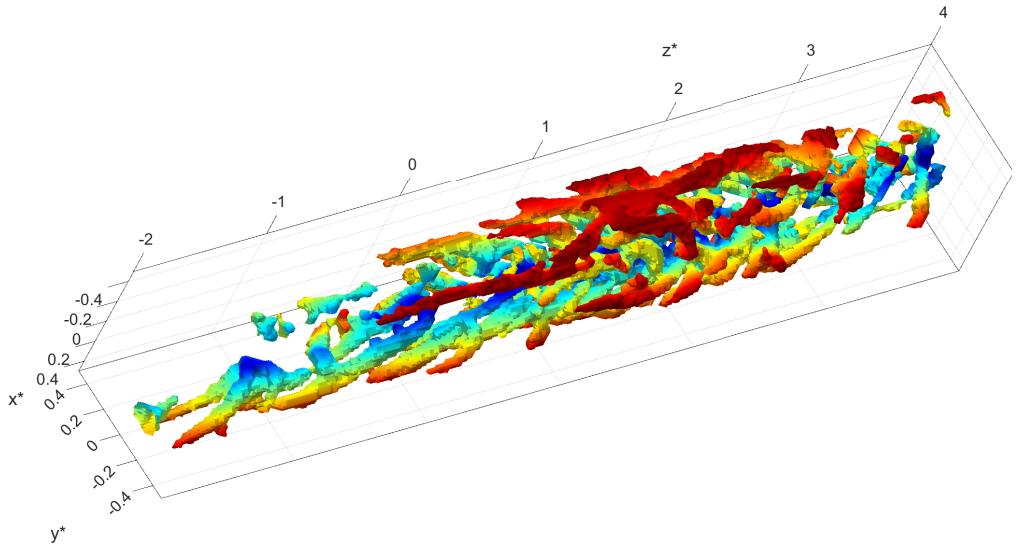

Figure C.33: Isosurfaces of swirl corresponding to $\lambda_{3D}^{*,i} > 1.3923$ inside Puff S-17. Colors move from red to blue with increasing wall distance.

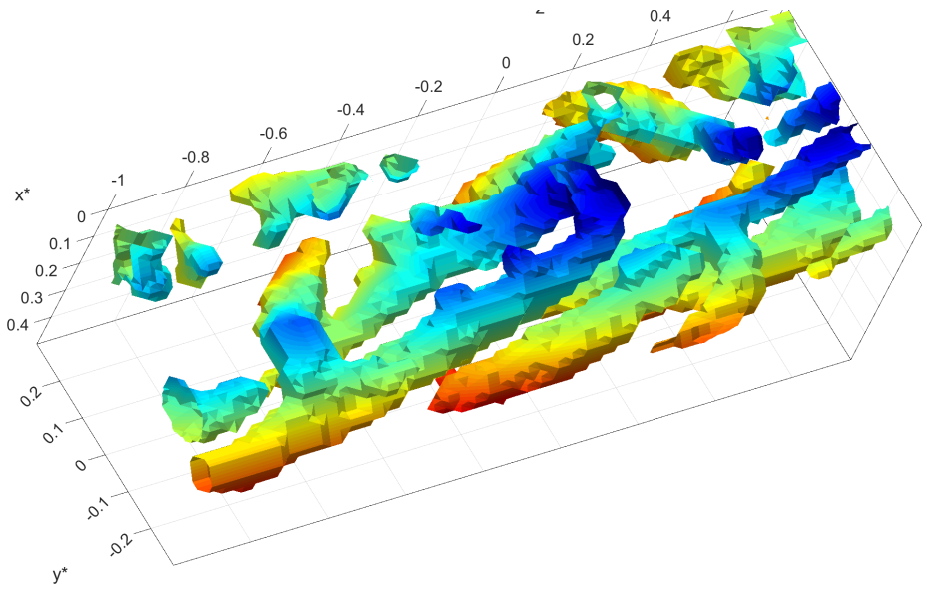

Figure C.34: Isosurfaces of swirl corresponding to $\lambda_{3D}^{*,i} > 1.3923$ within $-0.07 < z^* < 0.07$ inside Puff S-17. Colors move from red to blue with increasing wall distance.

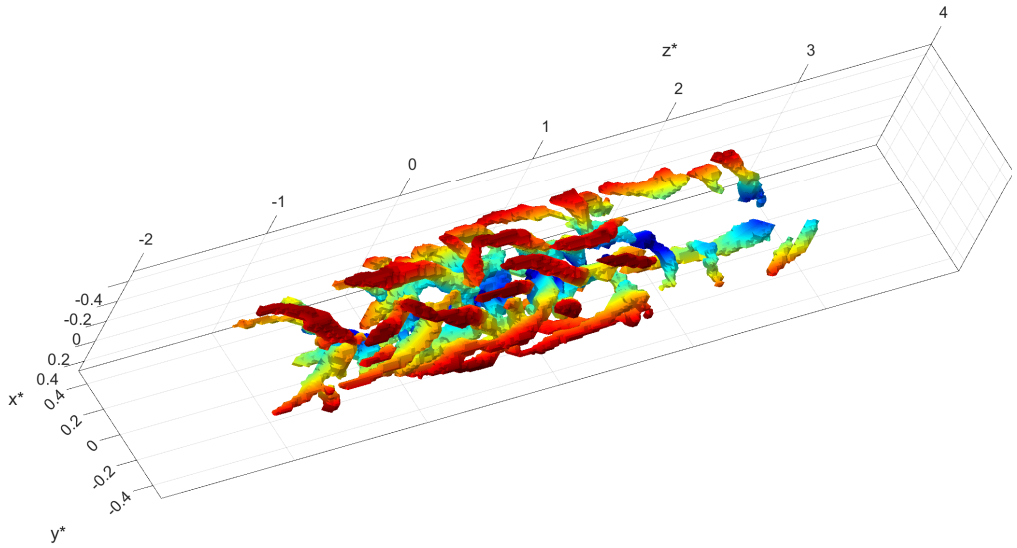

Figure C.35: Isosurfaces of swirl corresponding to $\lambda_{3D}^{*,i} > 1.8865$ inside Puff S-18. Colors move from red to blue with increasing wall distance.

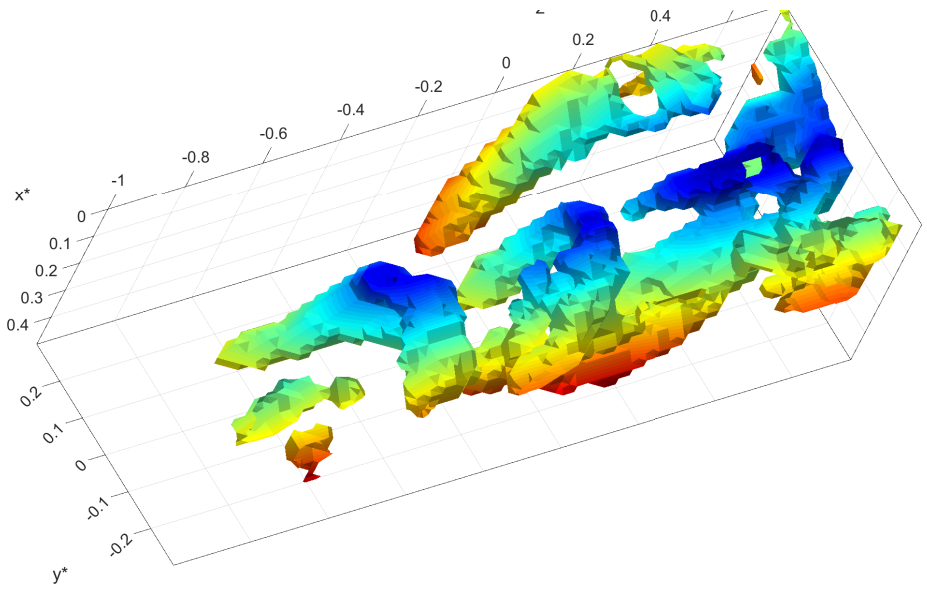

Figure C.36: Isosurfaces of swirl corresponding to $\lambda_{3D}^{*,i} > 1.8865$ within $-0.07 < z^* < 0.07$ inside Puff S-18. Colors move from red to blue with increasing wall distance.

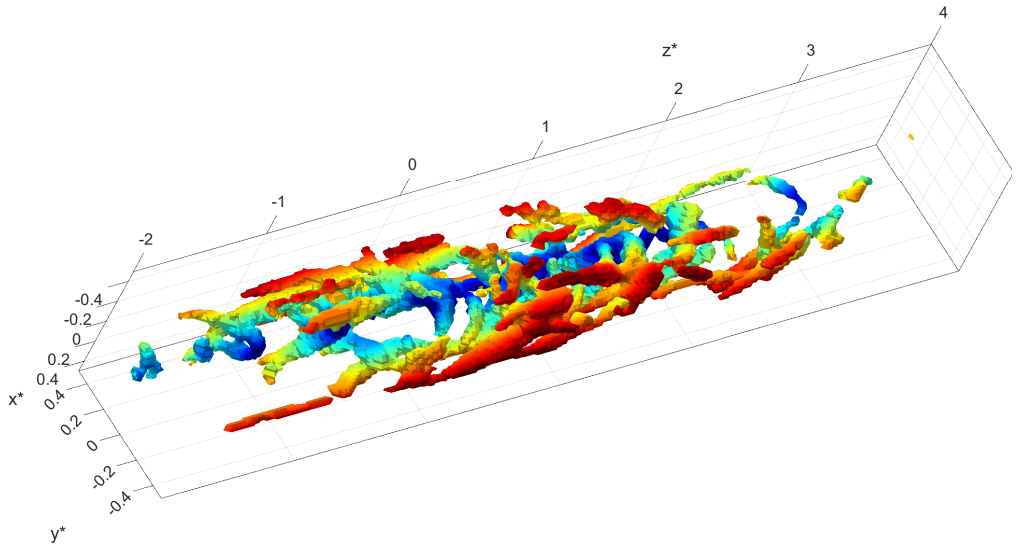

Figure C.37: Isosurfaces of swirl corresponding to $\lambda_{3D}^{*,i} > 1.5214$ inside Puff S-19. Colors move from red to blue with increasing wall distance.

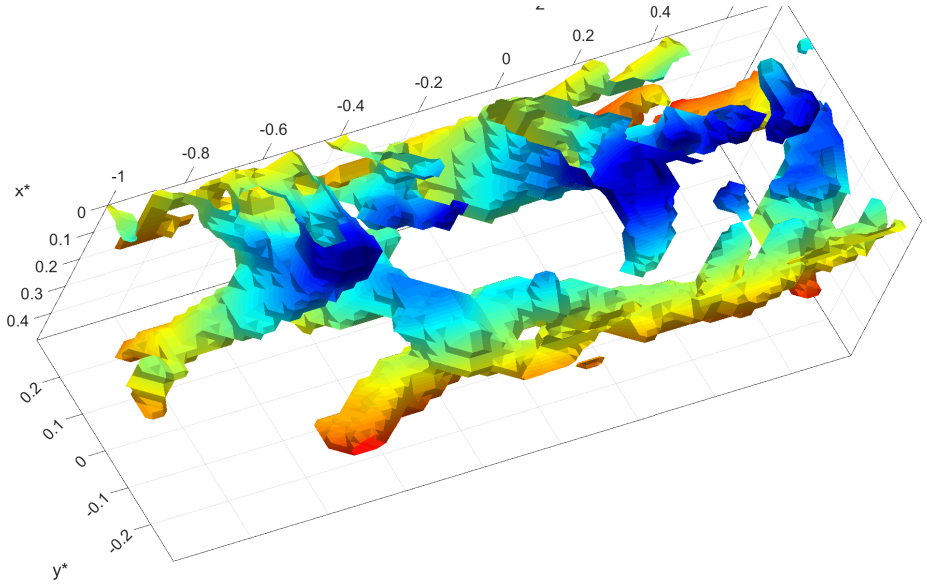

Figure C.38: Isosurfaces of swirl corresponding to $\lambda_{3D}^{*,i} > 1.5214$ within $-0.07 < z^* < 0.07$ inside Puff S-19. Colors move from red to blue with increasing wall distance.

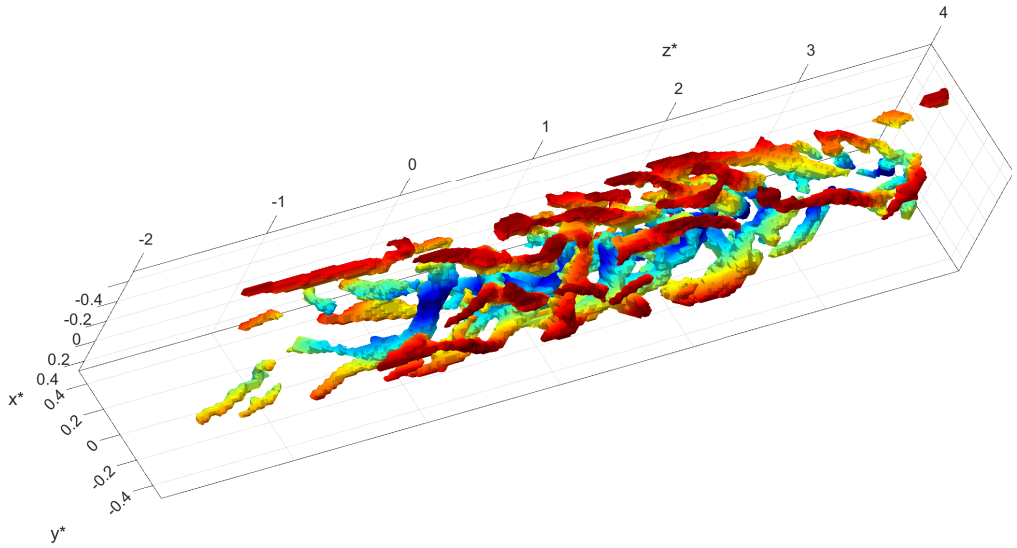

Figure C.39: Isosurfaces of swirl corresponding to $\lambda_{3D}^{*,i} > 1.6317$ inside Puff S-20. Colors move from red to blue with increasing wall distance.

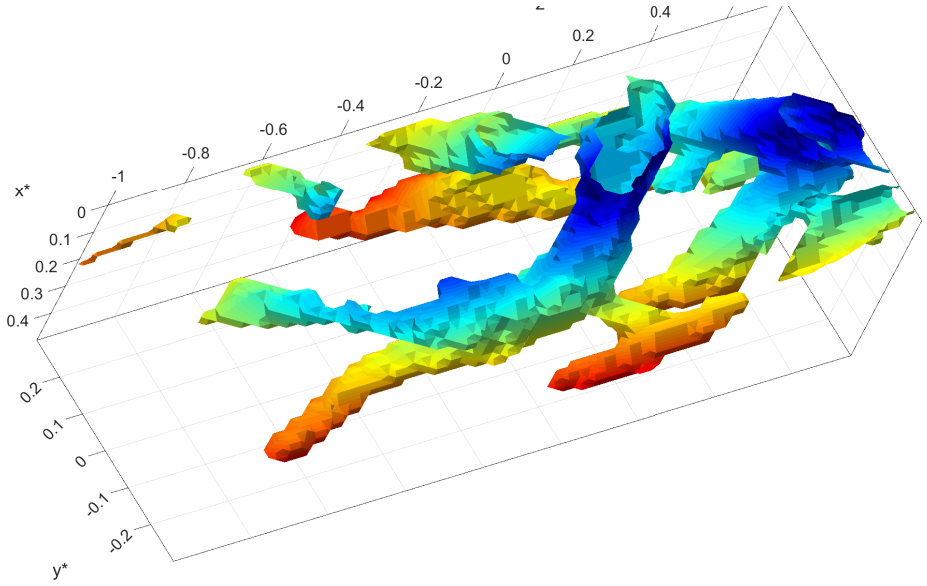

Figure C.40: Isosurfaces of swirl corresponding to $\lambda_{3D}^{*,i} > 1.6317$ within $-0.07 < z^* < 0.07$ inside Puff S-20. Colors move from red to blue with increasing wall distance.

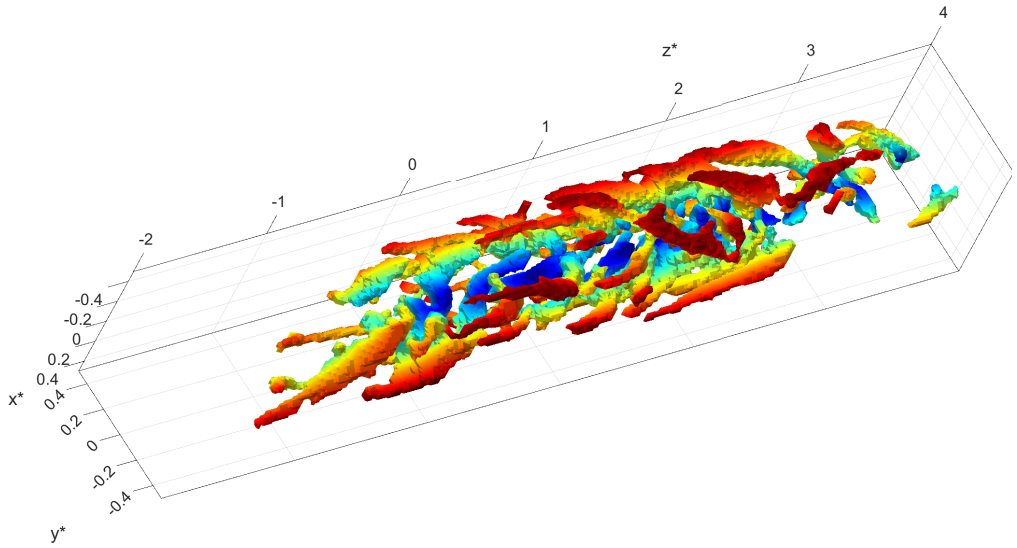

Figure C.41: Isosurfaces of swirl corresponding to $\lambda_{3D}^{*,i} > 1.7704$ inside Puff S-21. Colors move from red to blue with increasing wall distance.

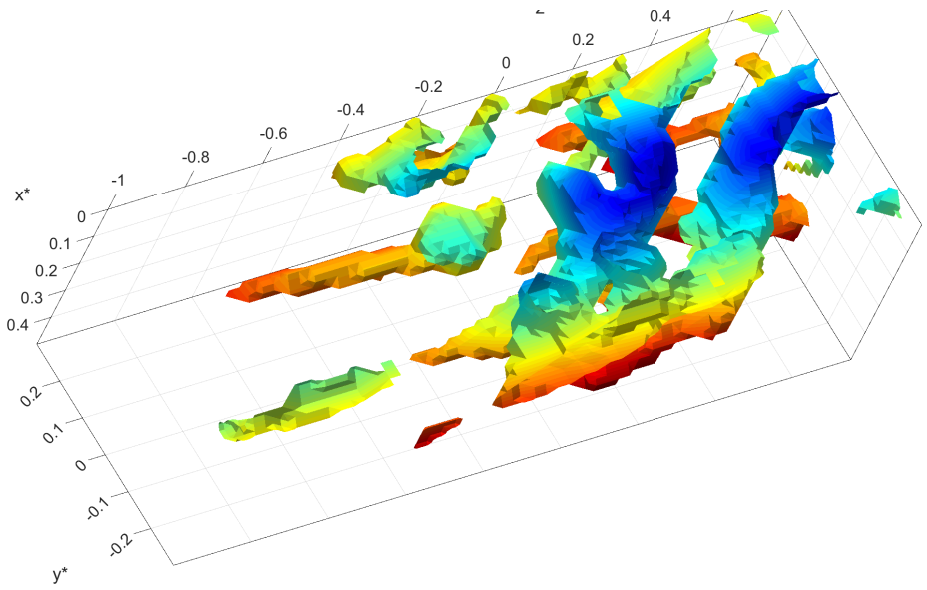

Figure C.42: Isosurfaces of swirl corresponding to $\lambda_{3D}^{*,i} > 1.7704$ within $-0.07 < z^* < 0.07$ inside Puff S-21. Colors move from red to blue with increasing wall distance.

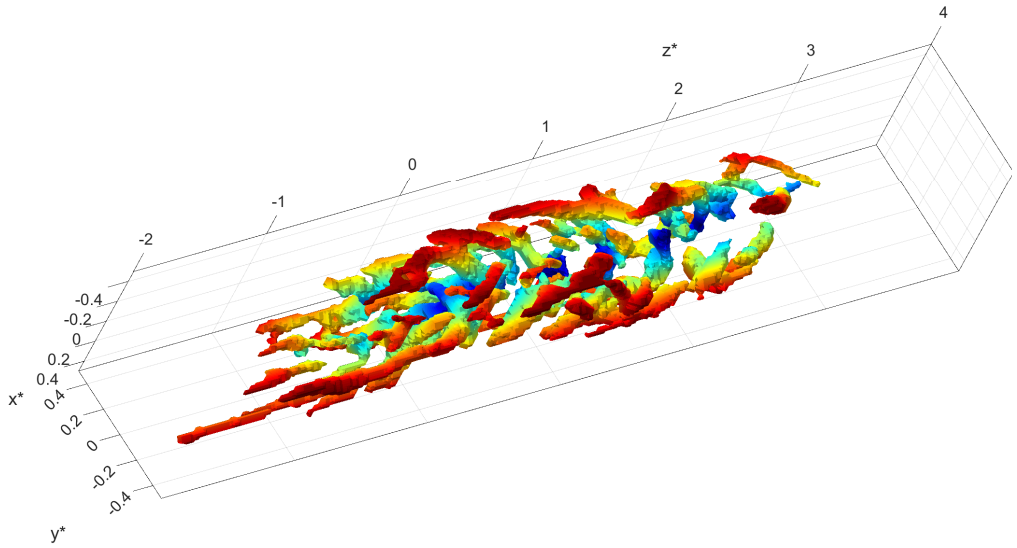

Figure C.43: Isosurfaces of swirl corresponding to $\lambda_{3D}^{*,i} > 1.8621$ inside Puff S-22. Colors move from red to blue with increasing wall distance.

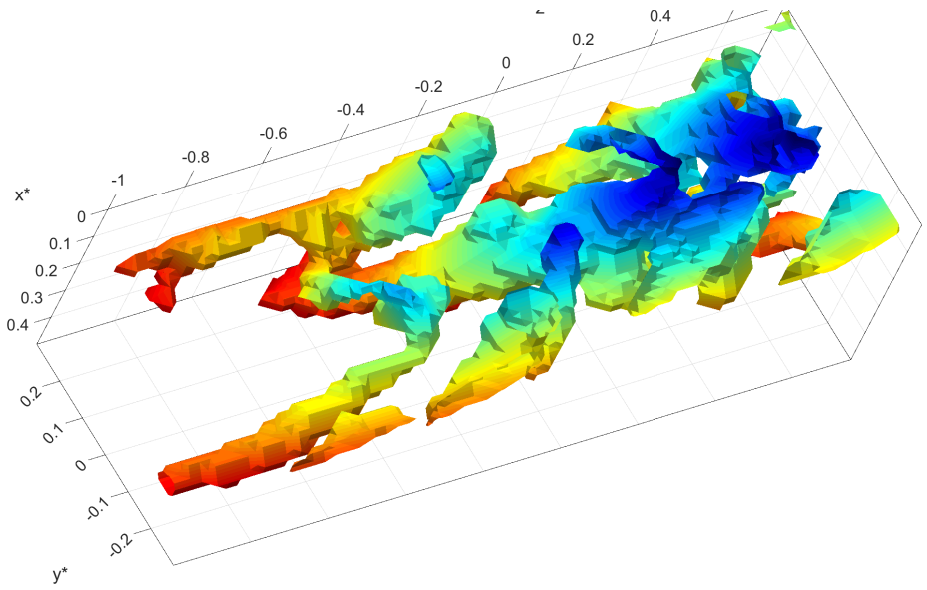

Figure C.44: Isosurfaces of swirl corresponding to $\lambda_{3D}^{*,i} > 1.8621$ within $-0.07 < z^* < 0.07$ inside Puff S-22. Colors move from red to blue with increasing wall distance.

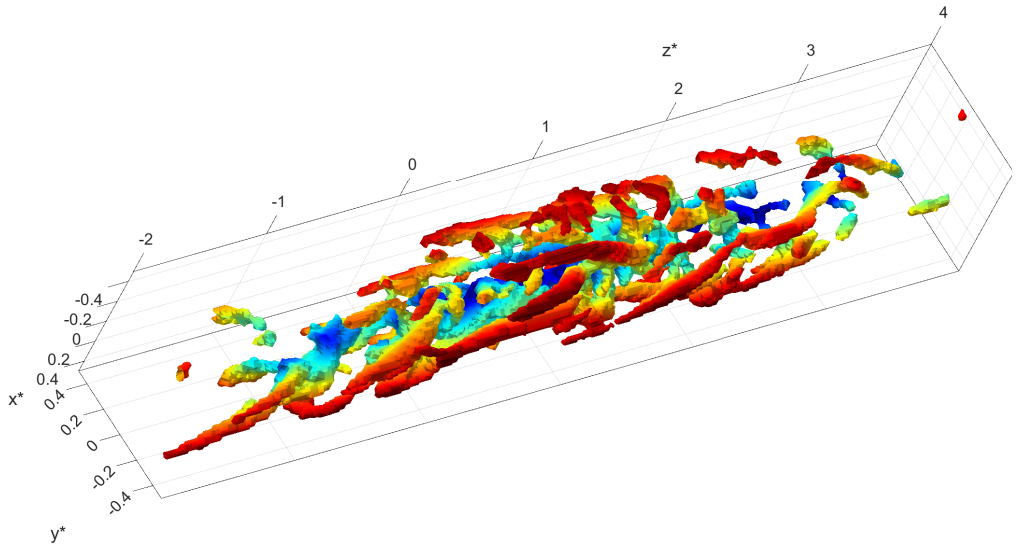

Figure C.45: Isosurfaces of swirl corresponding to $\lambda_{3D}^{*,i} > 1.5456$ inside Puff S-23. Colors move from red to blue with increasing wall distance.

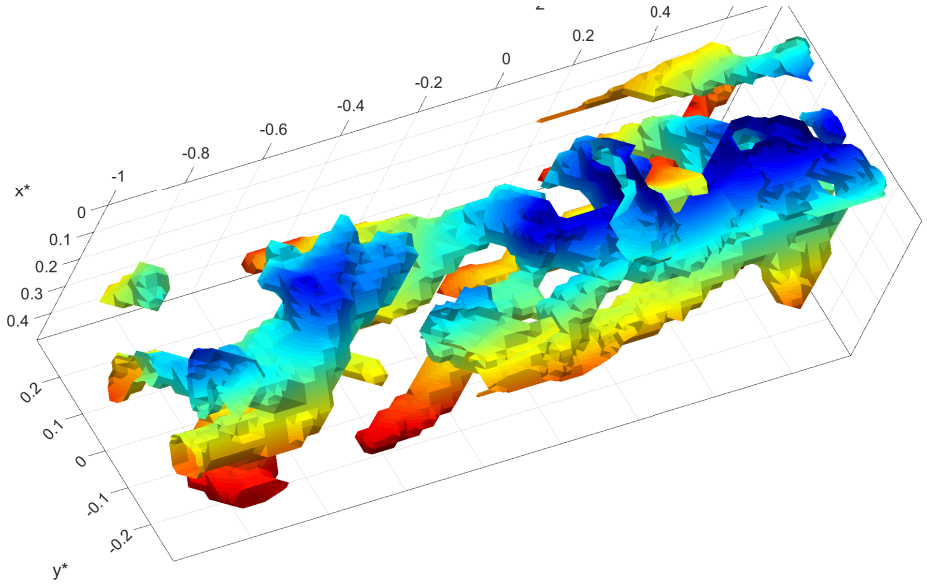

Figure C.46: Isosurfaces of swirl corresponding to $\lambda_{3D}^{*,i} > 1.5456$ within $-0.07 < z^* < 0.07$ inside Puff S-23. Colors move from red to blue with increasing wall distance.

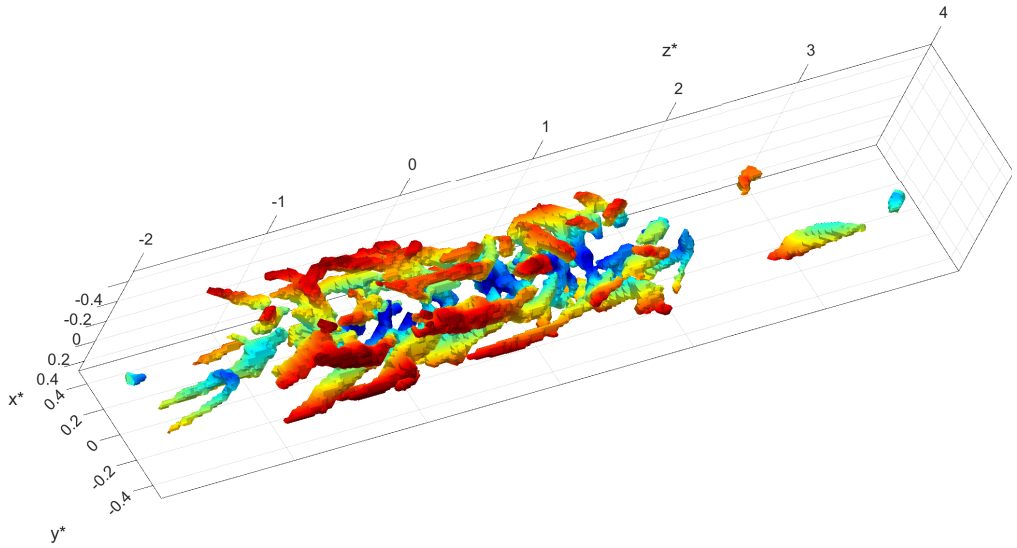

Figure C.47: Isosurfaces of swirl corresponding to $\lambda_{3D}^{*,i} > 1.7182$ inside Puff S-24. Colors move from red to blue with increasing wall distance.

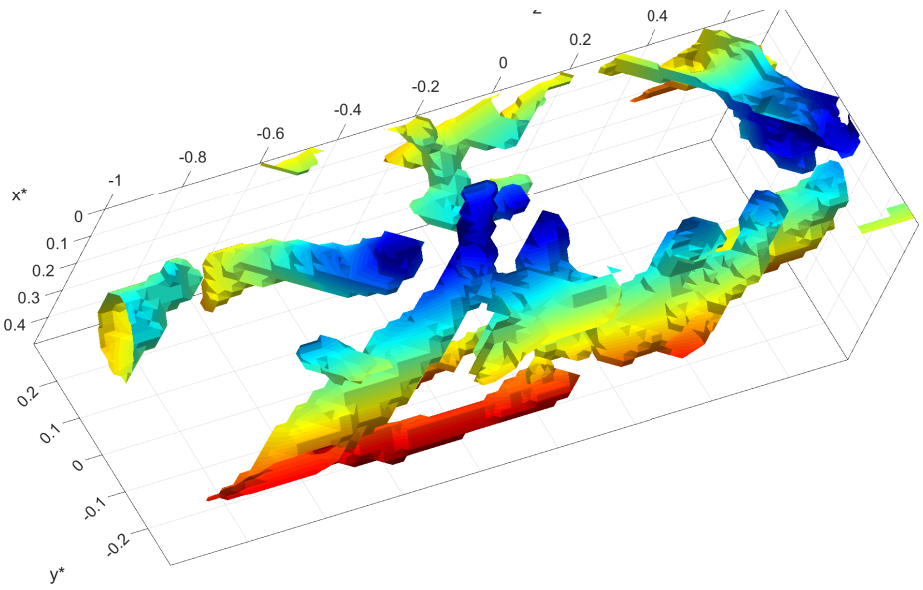

Figure C.48: Isosurfaces of swirl corresponding to $\lambda_{3D}^{*,i} > 1.7182$ within $-0.07 < z^* < 0.07$ inside Puff S-24. Colors move from red to blue with increasing wall distance.

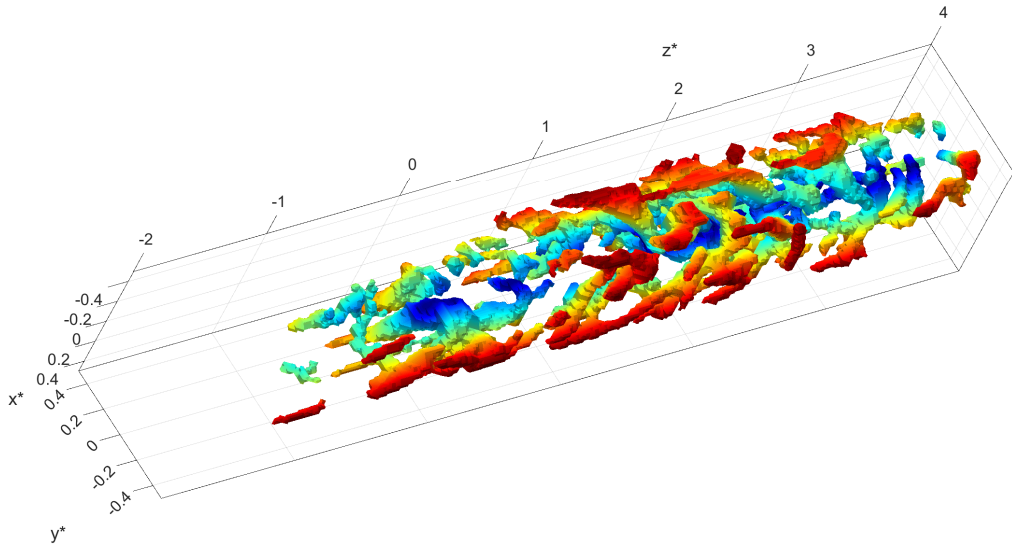

Figure C.49: Isosurfaces of swirl corresponding to $\lambda_{3D}^{*,i} > 1.5306$ inside Puff S-25. Colors move from red to blue with increasing wall distance.

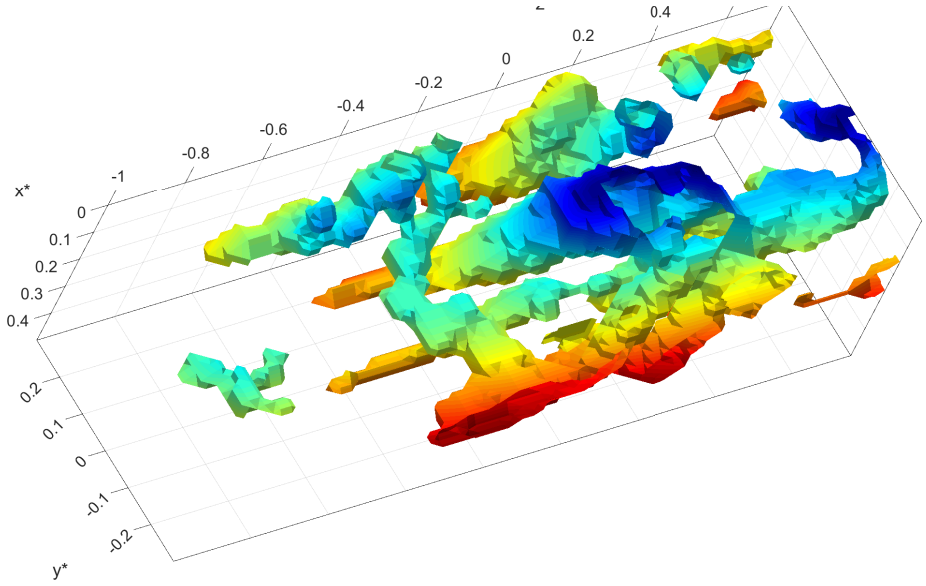

Figure C.50: Isosurfaces of swirl corresponding to $\lambda_{3D}^{*,i} > 1.5306$ within $-0.07 < z^* < 0.07$ inside Puff S-25. Colors move from red to blue with increasing wall distance.

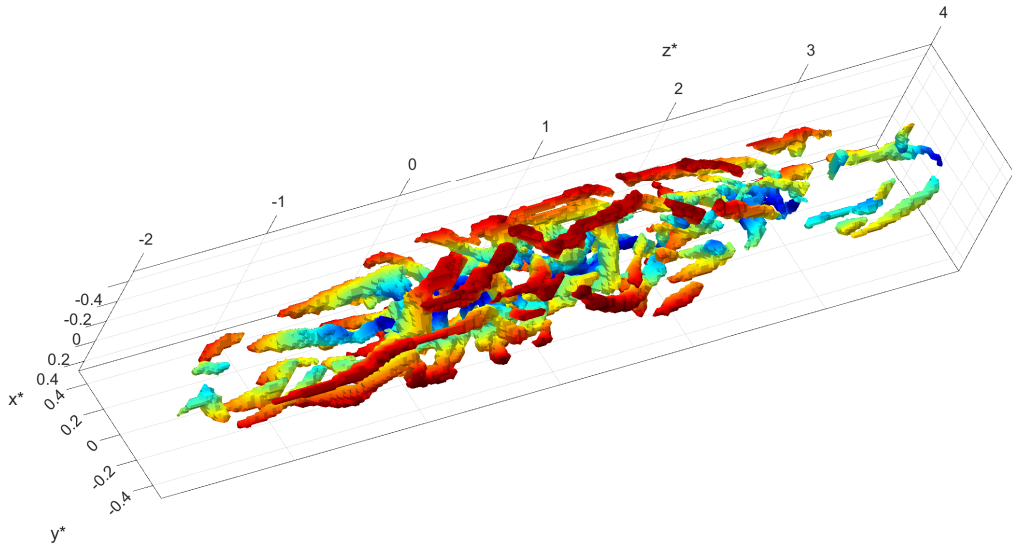

Figure C.51: Isosurfaces of swirl corresponding to $\lambda_{3D}^{*,i} > 1.8435$ inside Puff S-26. Colors move from red to blue with increasing wall distance.

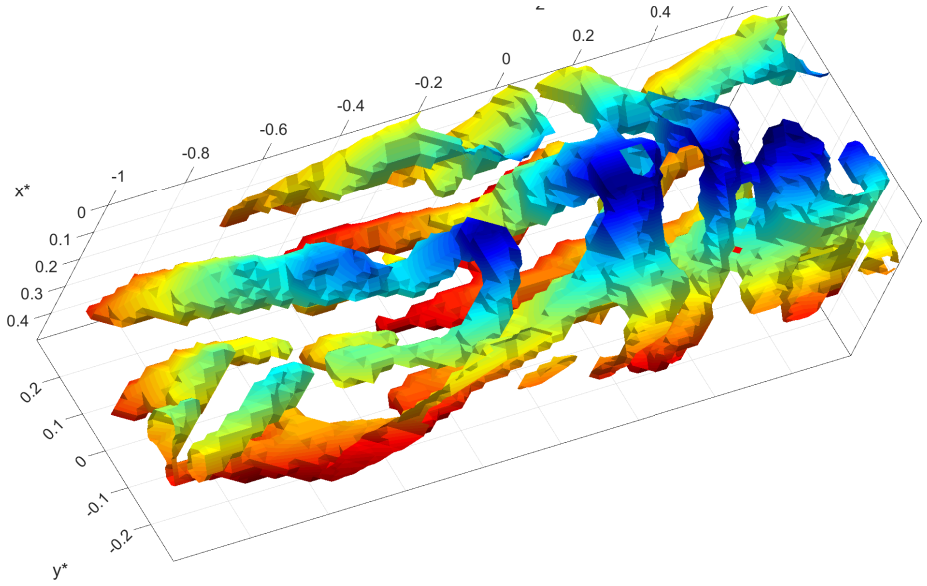

Figure C.52: Isosurfaces of swirl corresponding to $\lambda_{3D}^{*,i} > 1.8435$ within $-0.07 < z^* < 0.07$ inside Puff S-26. Colors move from red to blue with increasing wall distance.

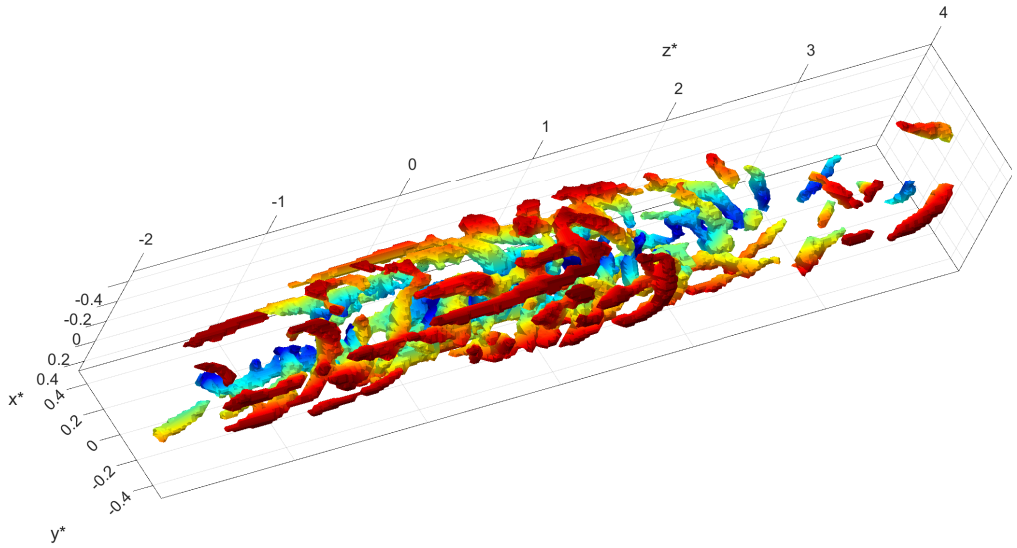

Figure C.53: Isosurfaces of swirl corresponding to $\lambda_{3D}^{*,i} > 1.6252$ inside Puff S-27. Colors move from red to blue with increasing wall distance.

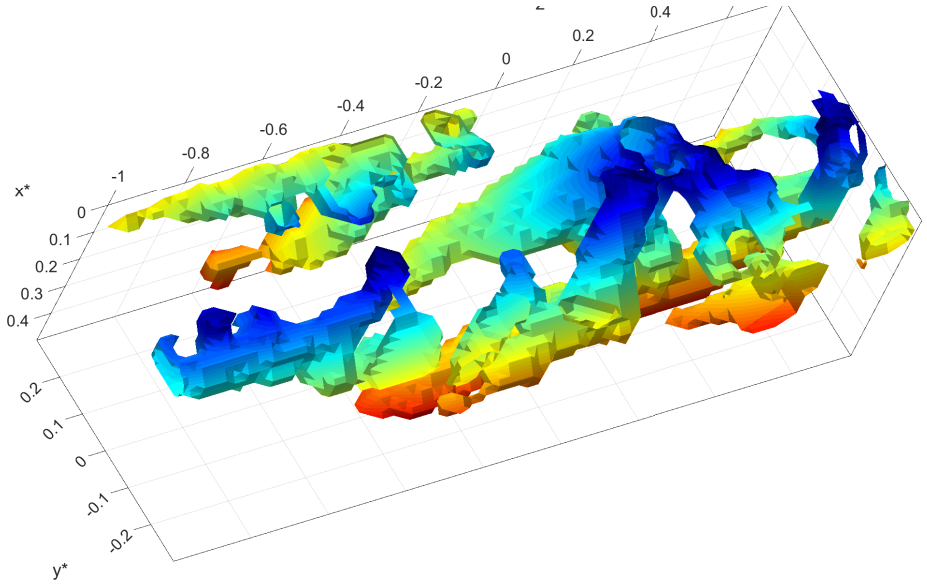

Figure C.54: Isosurfaces of swirl corresponding to $\lambda_{3D}^{*,i} > 1.6252$ within $-0.07 < z^* < 0.07$ inside Puff S-27. Colors move from red to blue with increasing wall distance.

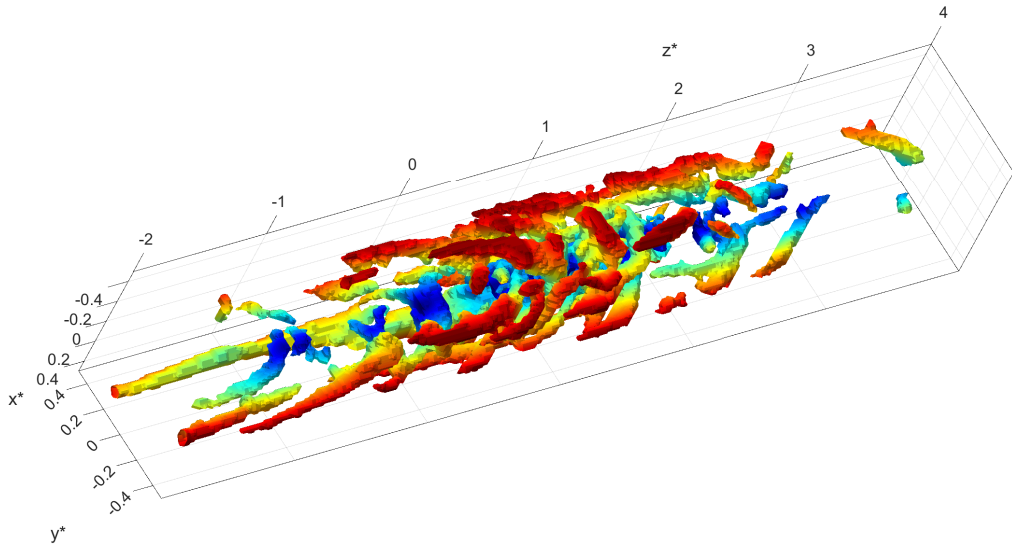

Figure C.55: Isosurfaces of swirl corresponding to $\lambda_{3D}^{*,i} > 1.6107$ inside Puff S-28. Colors move from red to blue with increasing wall distance.

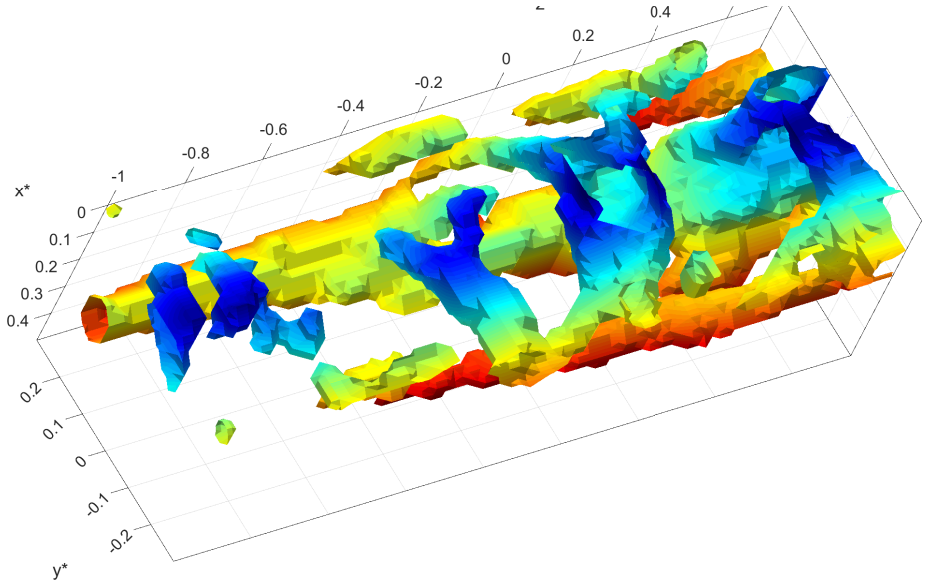

Figure C.56: Isosurfaces of swirl corresponding to $\lambda_{3D}^{*,i} > 1.6107$ within $-0.07 < z^* < 0.07$ inside Puff S-28. Colors move from red to blue with increasing wall distance.

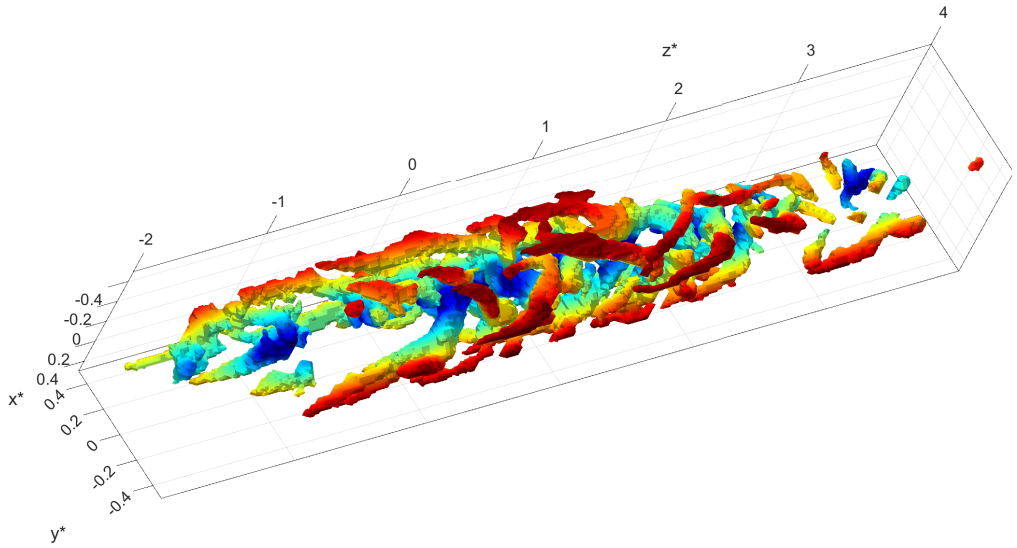

Figure C.57: Isosurfaces of swirl corresponding to $\lambda_{3D}^{*,i} > 1.6376$ inside Puff S-29. Colors move from red to blue with increasing wall distance.

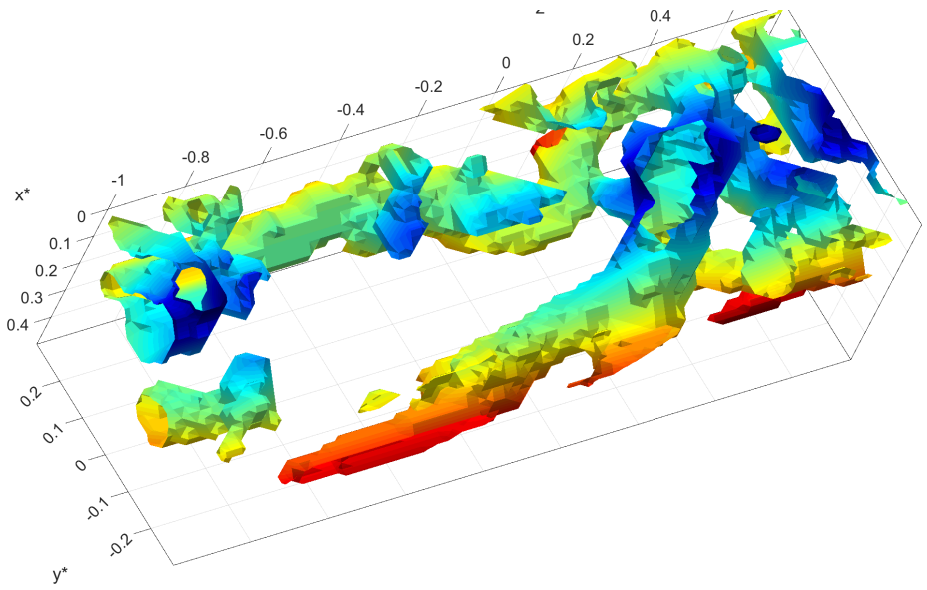

Figure C.58: Isosurfaces of swirl corresponding to $\lambda_{3D}^{*,i} > 1.6376$ within $-0.07 < z^* < 0.07$ inside Puff S-29. Colors move from red to blue with increasing wall distance.

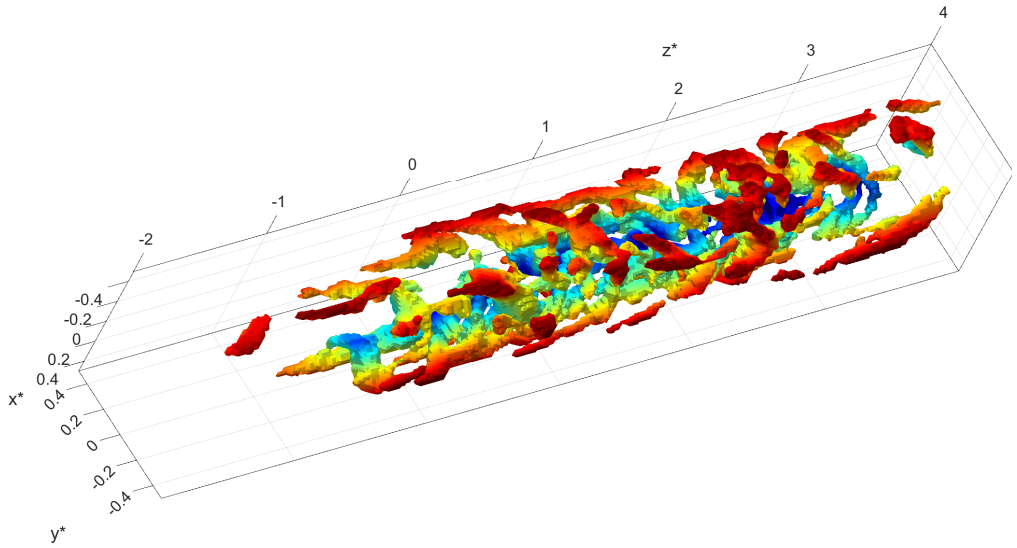

Figure C.59: Isosurfaces of swirl corresponding to $\lambda_{3D}^{*,i} > 1.6973$ inside Puff S-30. Colors move from red to blue with increasing wall distance.

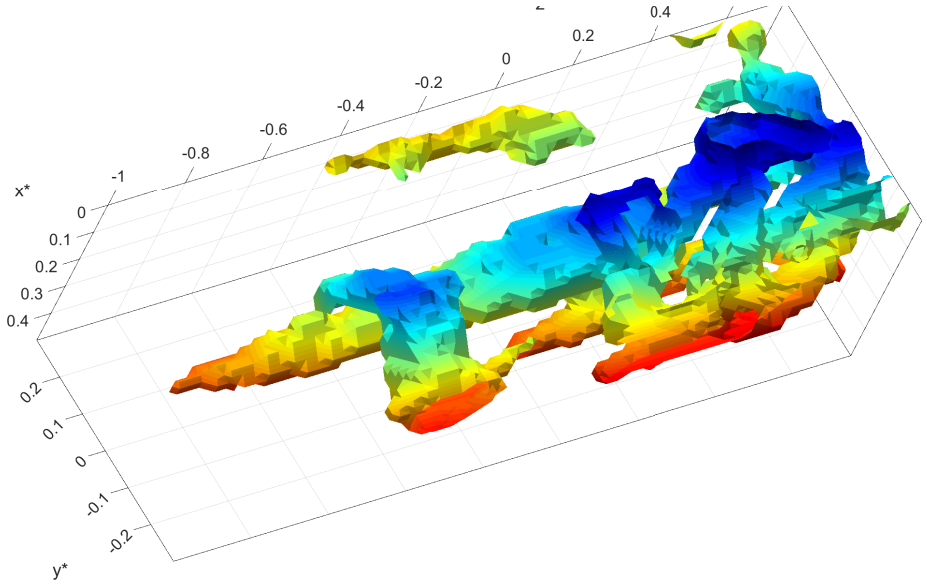

Figure C.60: Isosurfaces of swirl corresponding to $\lambda_{3D}^{*,i} > 1.6973$ within $-0.07 < z^* < 0.07$ inside Puff S-30. Colors move from red to blue with increasing wall distance.

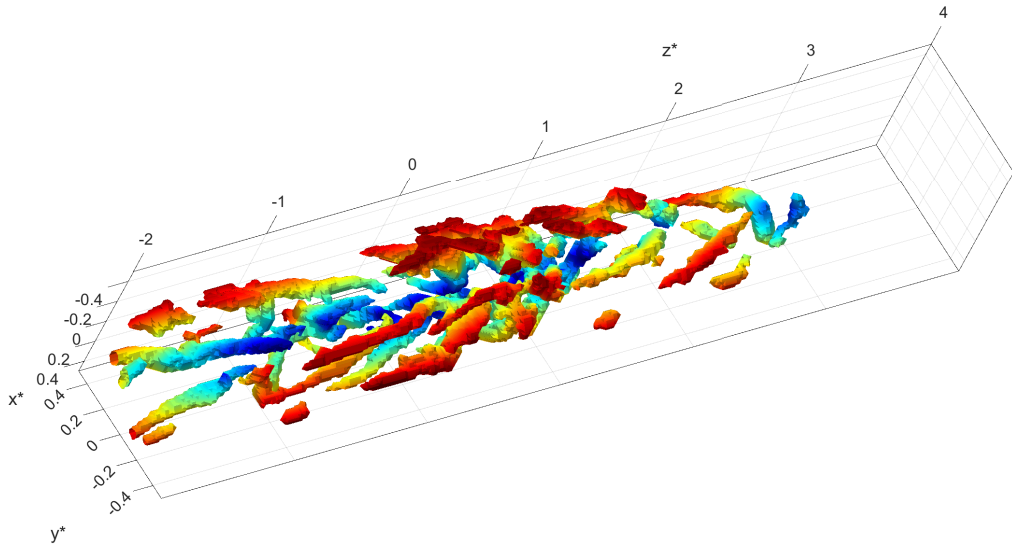

Figure C.61: Isosurfaces of swirl corresponding to $\lambda_{3D}^{*,i} > 1.77$ inside Puff S-31. Colors move from red to blue with increasing wall distance.

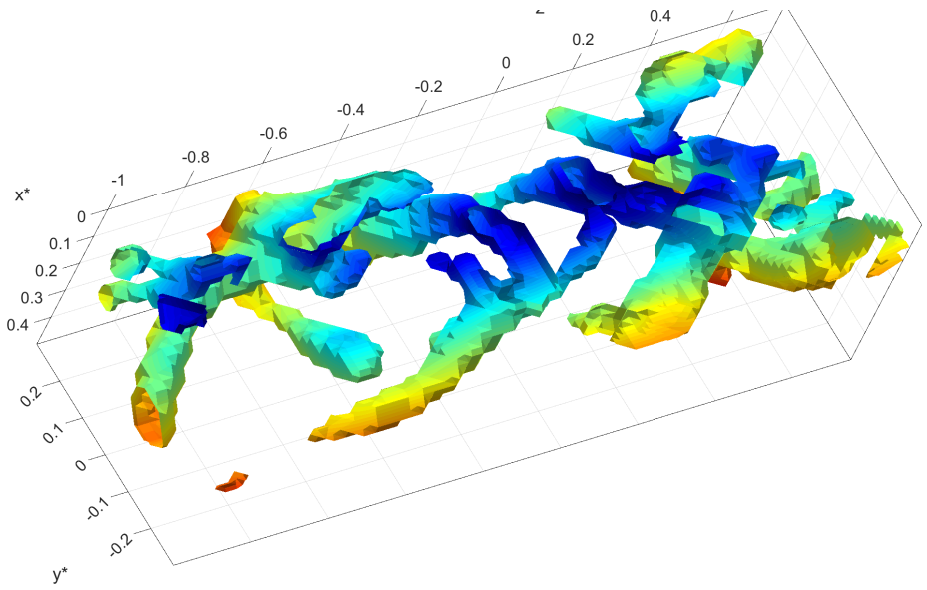

Figure C.62: Isosurfaces of swirl corresponding to $\lambda_{3D}^{*,i} > 1.77$ within $-0.07 < z^* < 0.07$ inside Puff S-31. Colors move from red to blue with increasing wall distance.

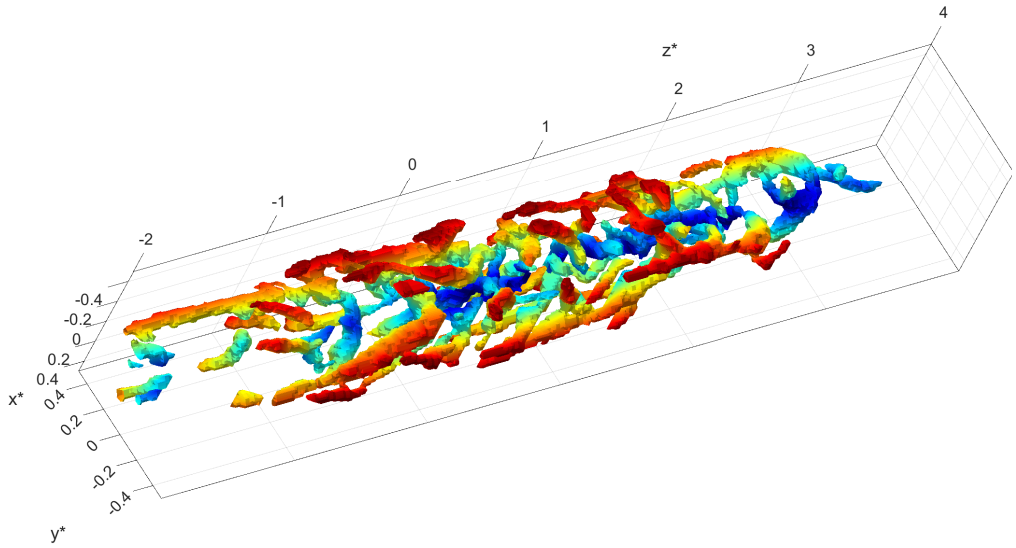

Figure C.63: Isosurfaces of swirl corresponding to $\lambda_{3D}^{*,i} > 1.838$ inside Puff S-32. Colors move from red to blue with increasing wall distance.

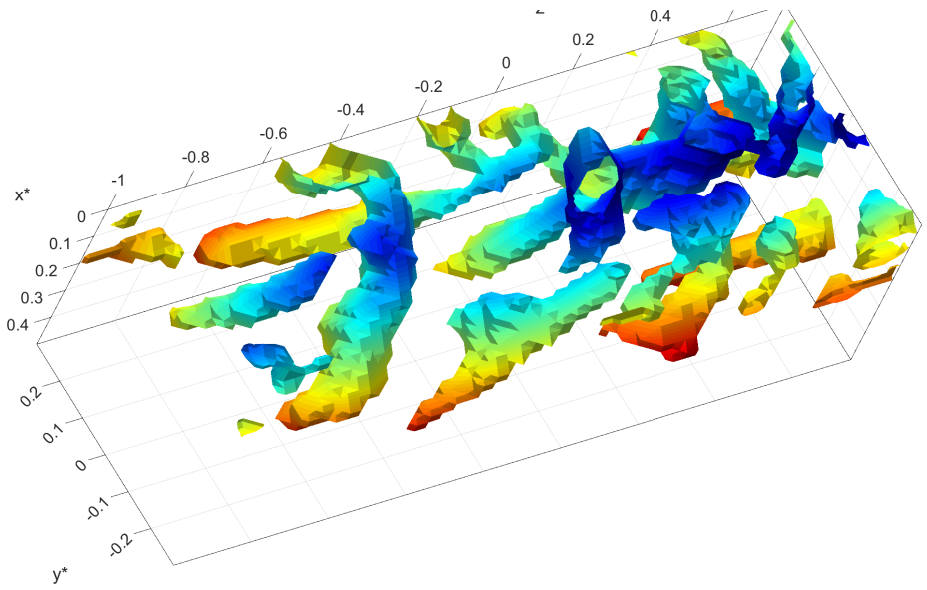

Figure C.64: Isosurfaces of swirl corresponding to $\lambda_{3D}^{*,i} > 1.838$ within $-0.07 < z^* < 0.07$ inside Puff S-32. Colors move from red to blue with increasing wall distance.

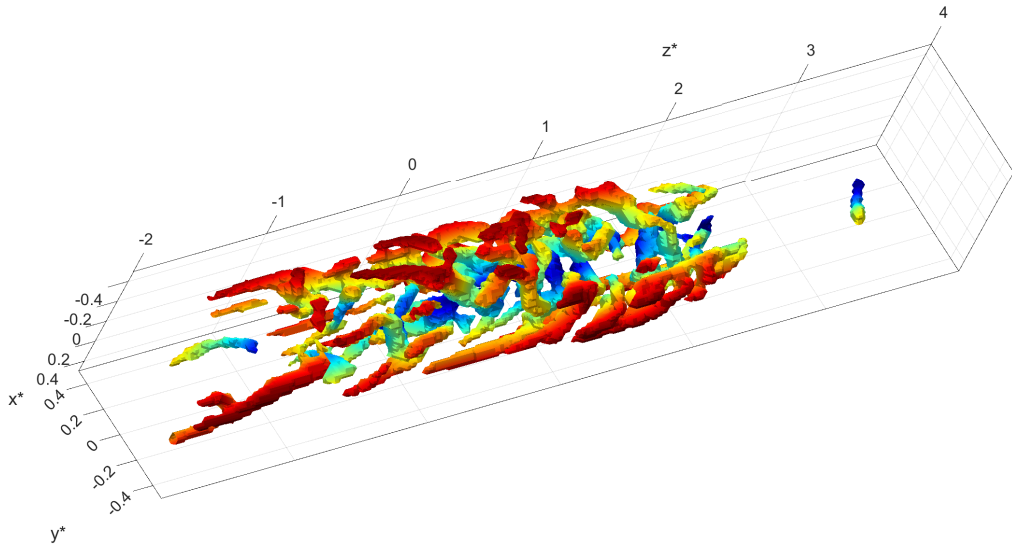

Figure C.65: Isosurfaces of swirl corresponding to $\lambda_{3D}^{*,i} > 1.8511$ inside Puff S-33. Colors move from red to blue with increasing wall distance.

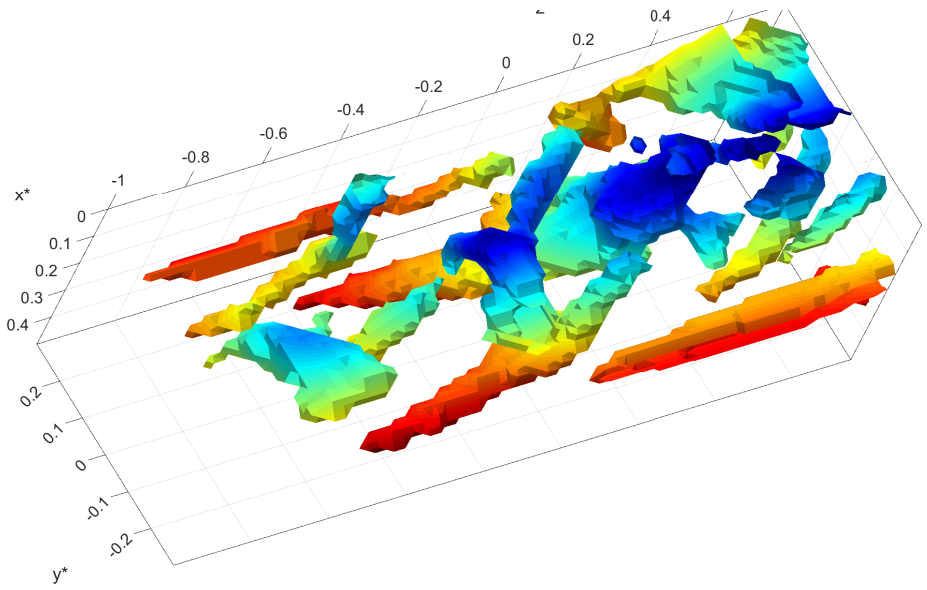

Figure C.66: Isosurfaces of swirl corresponding to $\lambda_{3D}^{*,i} > 1.8511$ within $-0.07 < z^* < 0.07$ inside Puff S-33. Colors move from red to blue with increasing wall distance.

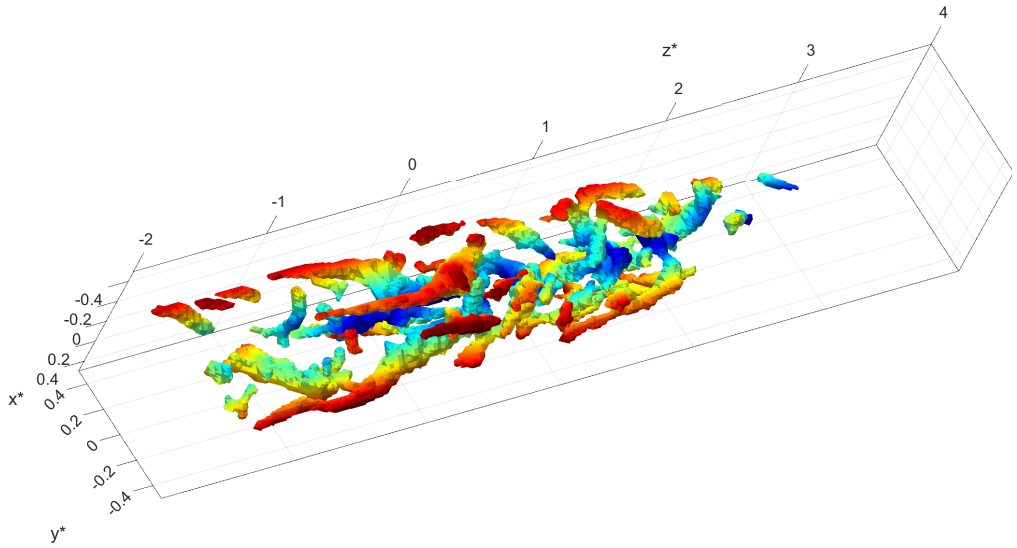

Figure C.67: Isosurfaces of swirl corresponding to $\lambda_{3D}^{*,i} > 1.706$ inside Puff S-34. Colors move from red to blue with increasing wall distance.

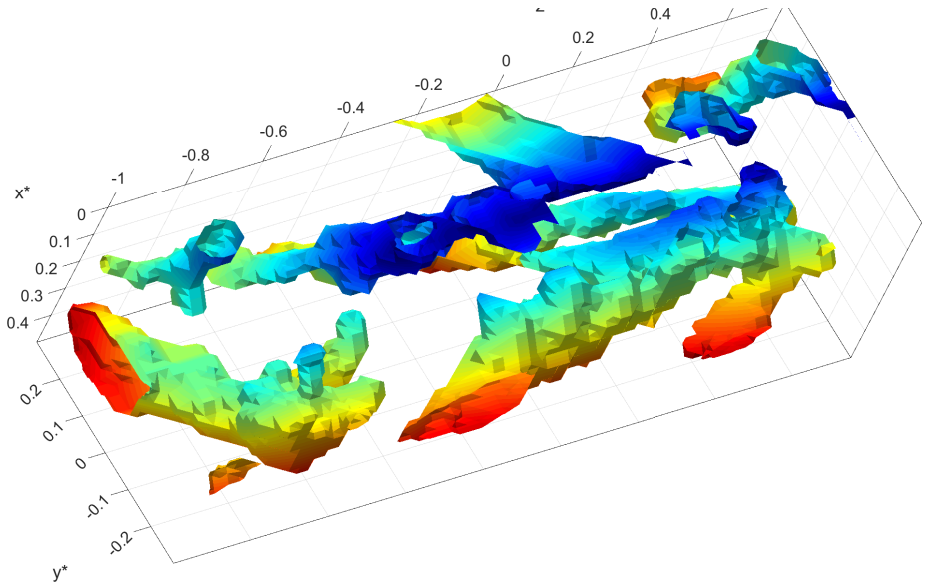

Figure C.68: Isosurfaces of swirl corresponding to $\lambda_{3D}^{*,i} > 1.706$ within $-0.07 < z^* < 0.07$ inside Puff S-34. Colors move from red to blue with increasing wall distance.

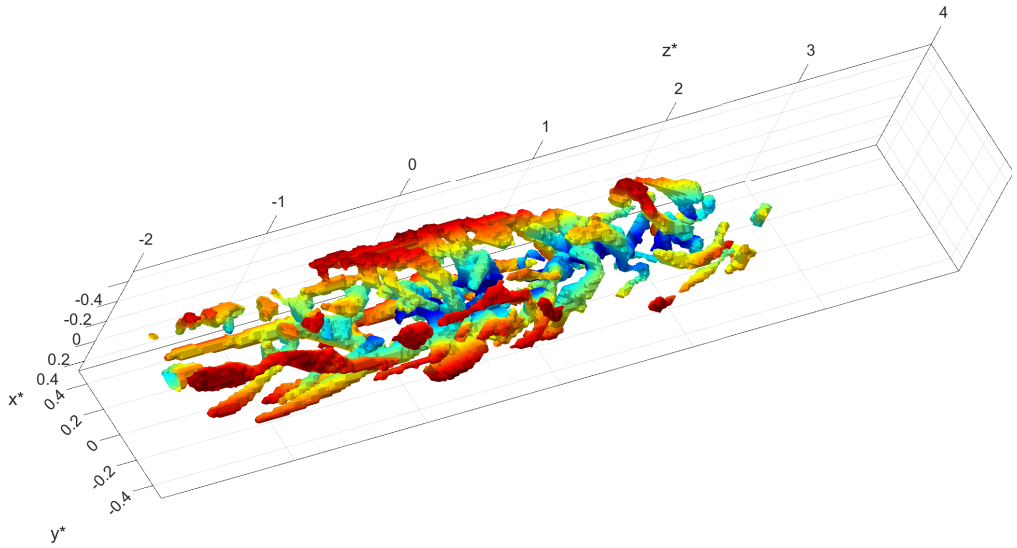

Figure C.69: Isosurfaces of swirl corresponding to $\lambda_{3D}^{*,i} > 1.6421$ inside Puff S-35. Colors move from red to blue with increasing wall distance.

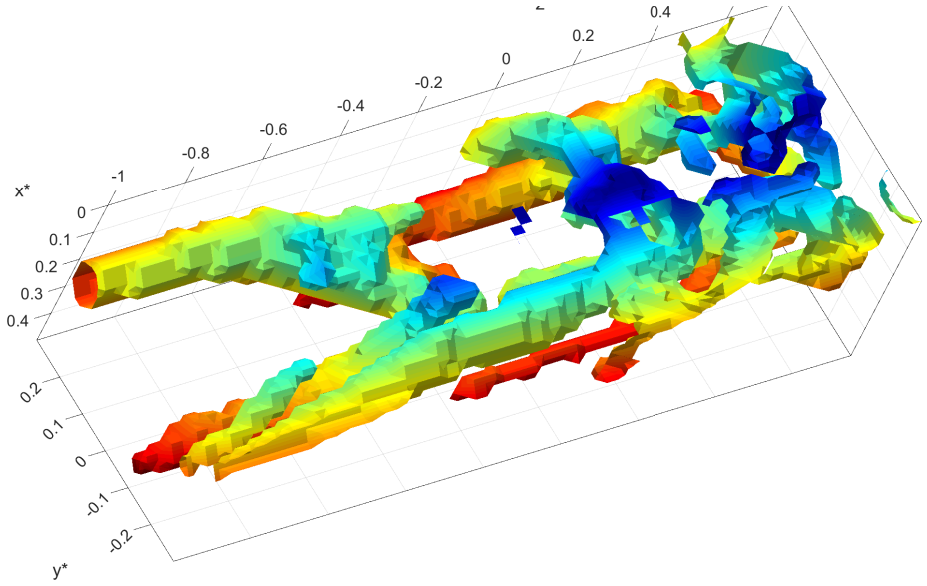

Figure C.70: Isosurfaces of swirl corresponding to $\lambda_{3D}^{*,i} > 1.6421$ within $-0.07 < z^* < 0.07$ inside Puff S-35. Colors move from red to blue with increasing wall distance.

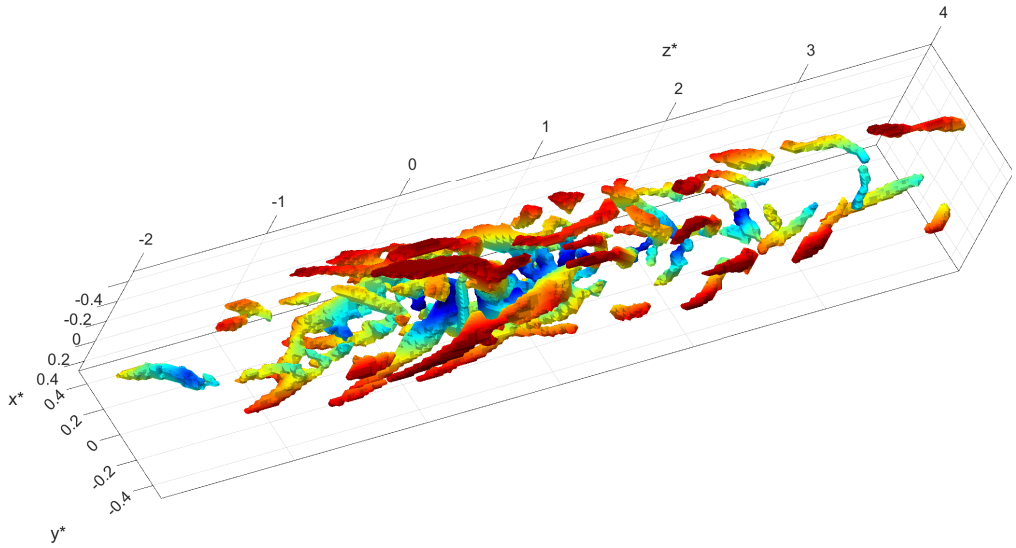

Figure C.71: Isosurfaces of swirl corresponding to $\lambda_{3D}^{*,i} > 2.0556$ inside Puff S-36. Colors move from red to blue with increasing wall distance.

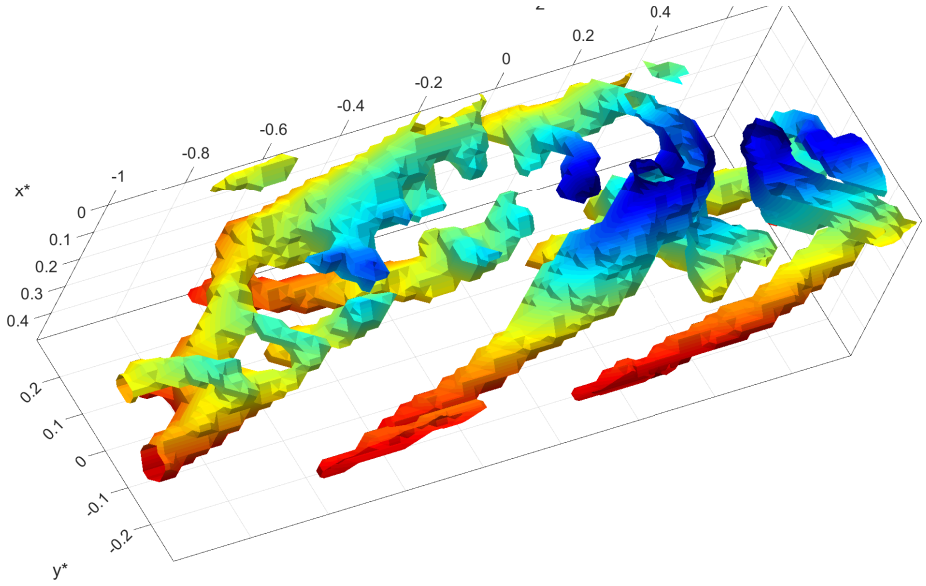

Figure C.72: Isosurfaces of swirl corresponding to $\lambda_{3D}^{*,i} > 2.0556$ within $-0.07 < z^* < 0.07$ inside Puff S-36. Colors move from red to blue with increasing wall distance.

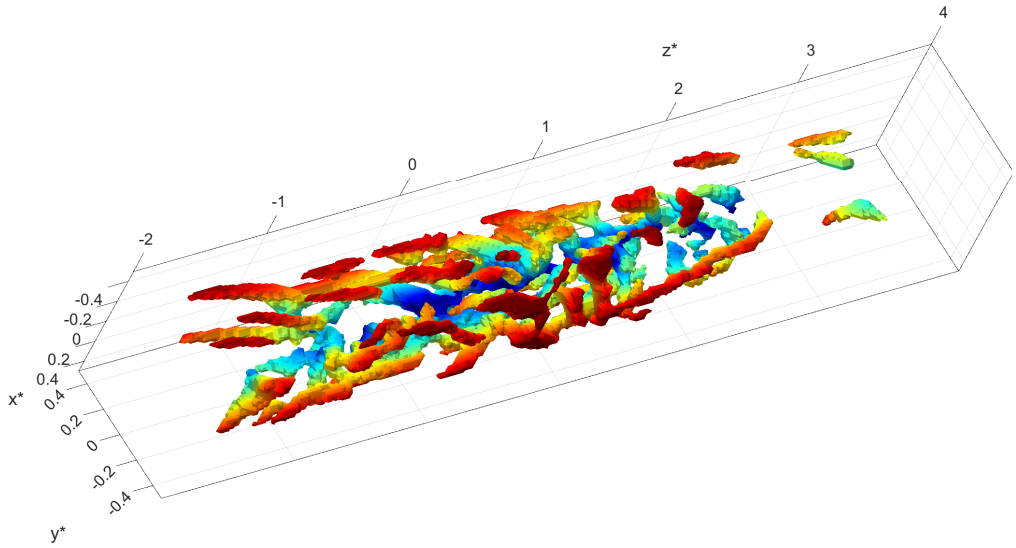

Figure C.73: Isosurfaces of swirl corresponding to $\lambda_{3D}^{*,i} > 1.7304$ inside Puff S-37. Colors move from red to blue with increasing wall distance.

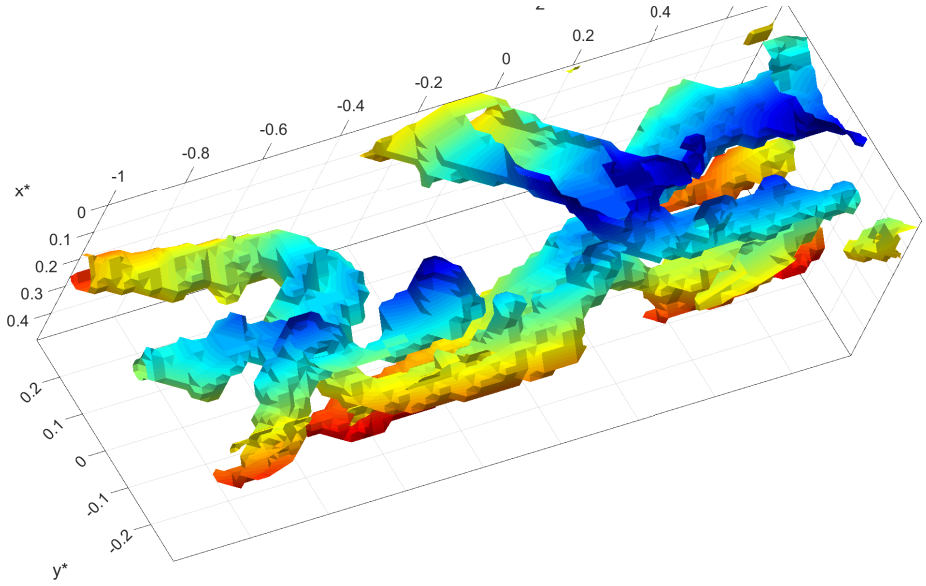

Figure C.74: Isosurfaces of swirl corresponding to $\lambda_{3D}^{*,i} > 1.7304$ within $-0.07 < z^* < 0.07$ inside Puff S-37. Colors move from red to blue with increasing wall distance.

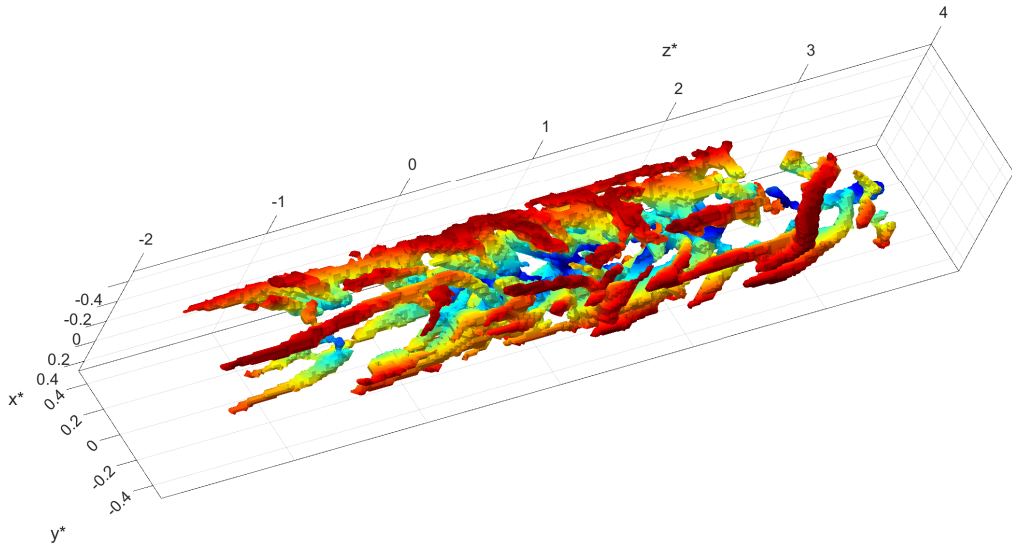

Figure C.75: Isosurfaces of swirl corresponding to $\lambda_{3D}^{*,i} > 1.446$ inside Puff S-38. Colors move from red to blue with increasing wall distance.

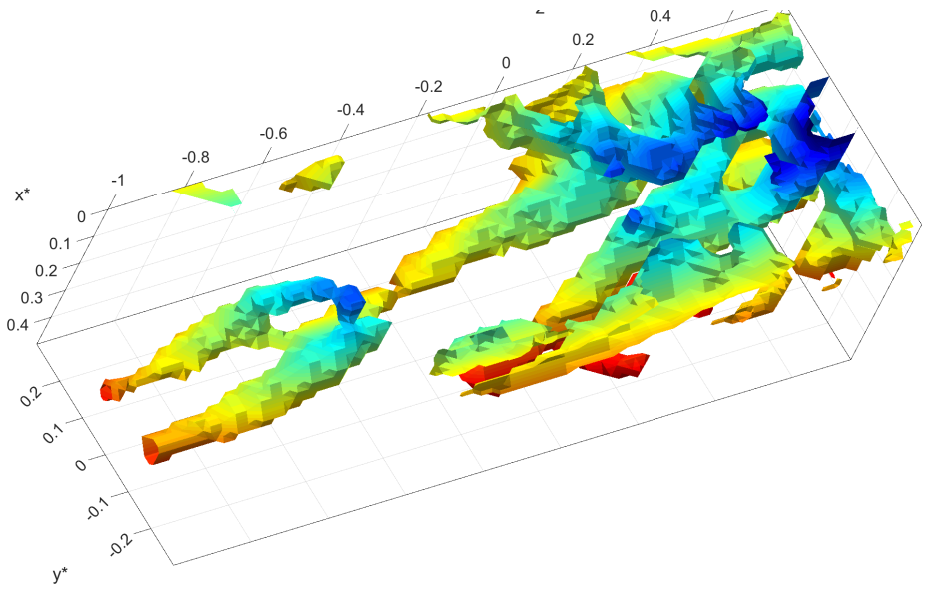

Figure C.76: Isosurfaces of swirl corresponding to $\lambda_{3D}^{*,i} > 1.446$ within $-0.07 < z^* < 0.07$ inside Puff S-38. Colors move from red to blue with increasing wall distance.

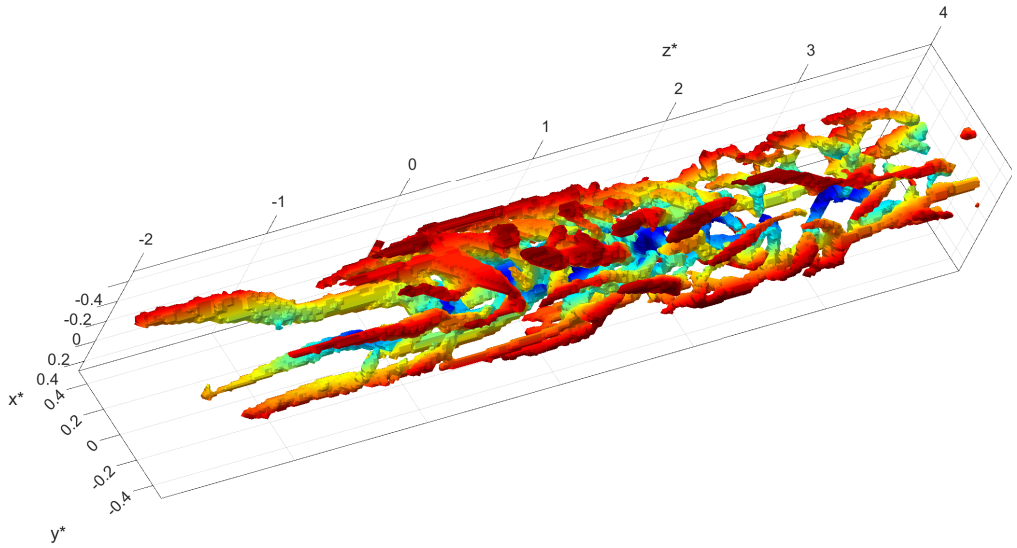

Figure C.77: Isosurfaces of swirl corresponding to $\lambda_{3D}^{*,i} > 1.6005$ inside Puff S-39. Colors move from red to blue with increasing wall distance.

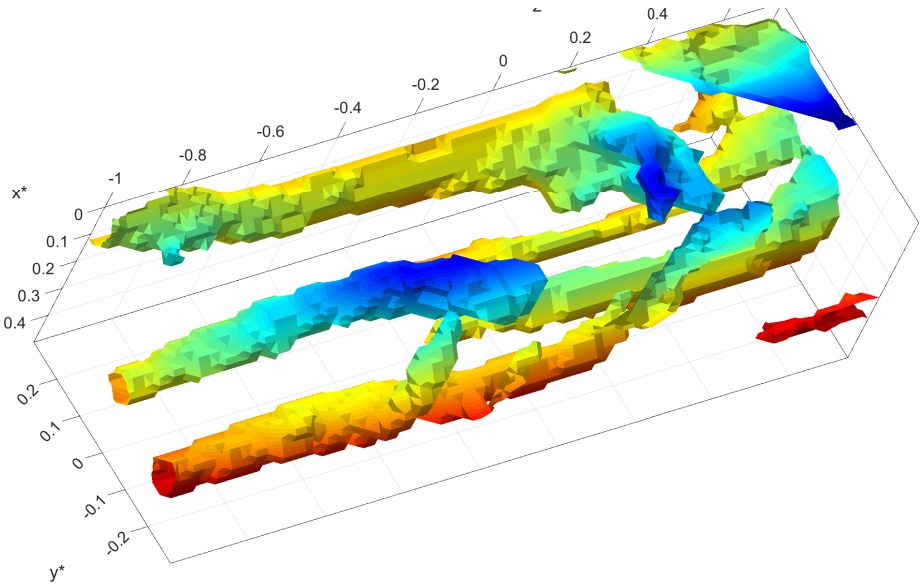

Figure C.78: Isosurfaces of swirl corresponding to $\lambda_{3D}^{*,i} > 1.6005$ within $-0.07 < z^* < 0.07$ inside Puff S-39. Colors move from red to blue with increasing wall distance.

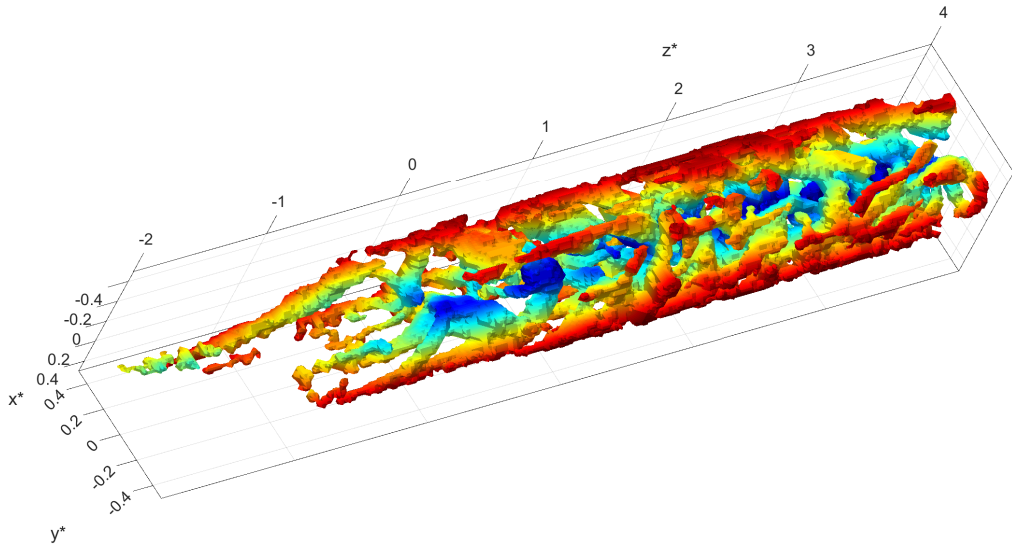

Figure C.79: Isosurfaces of swirl corresponding to $\lambda_{3D}^{*,i} > 1.2456$ inside Puff S-40. Colors move from red to blue with increasing wall distance.

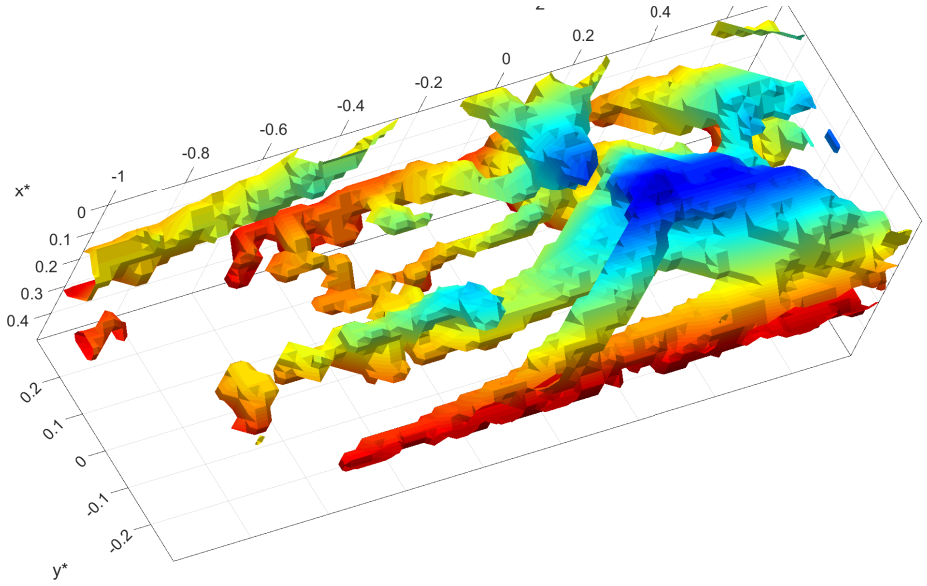

Figure C.80: Isosurfaces of swirl corresponding to $\lambda_{3D}^{*,i} > 1.2456$ within $-0.07 < z^* < 0.07$ inside Puff S-40. Colors move from red to blue with increasing wall distance.

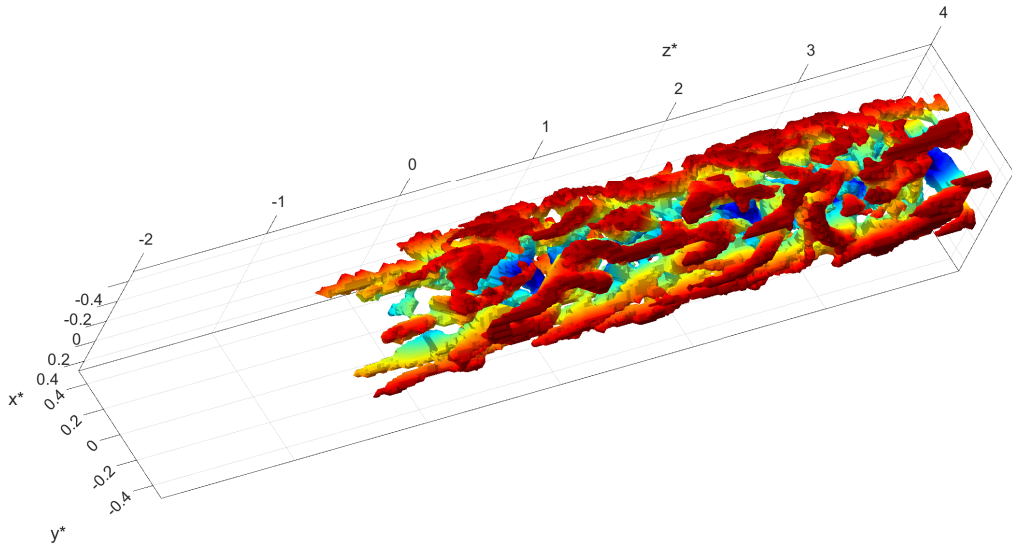

Figure C.81: Isosurfaces of swirl corresponding to $\lambda_{3D}^{*,i} > 1.2836$ inside Puff S-41. Colors move from red to blue with increasing wall distance.

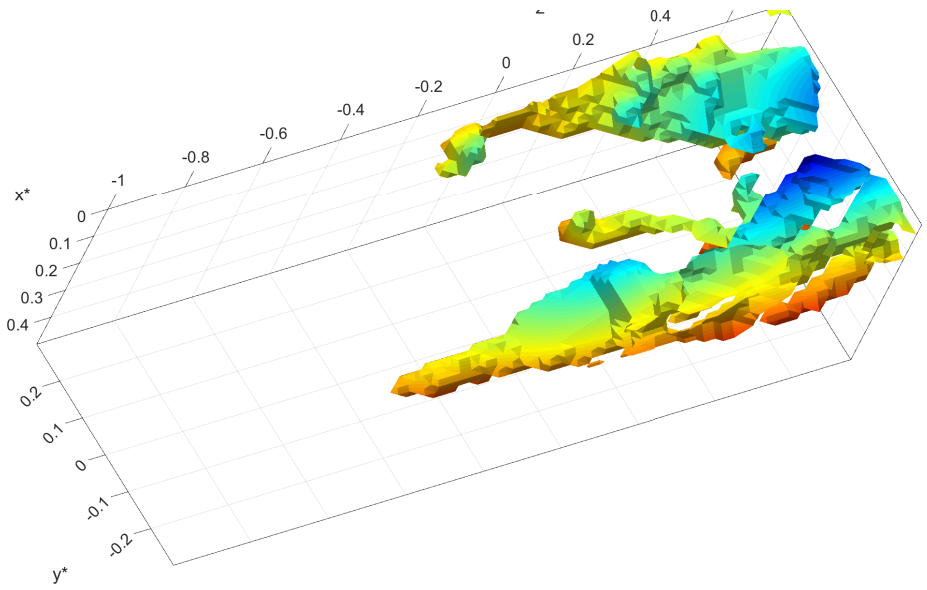

Figure C.82: Isosurfaces of swirl corresponding to $\lambda_{3D}^{*,i} > 1.2836$ within $-0.07 < z^* < 0.07$ inside Puff S-41. Colors move from red to blue with increasing wall distance.

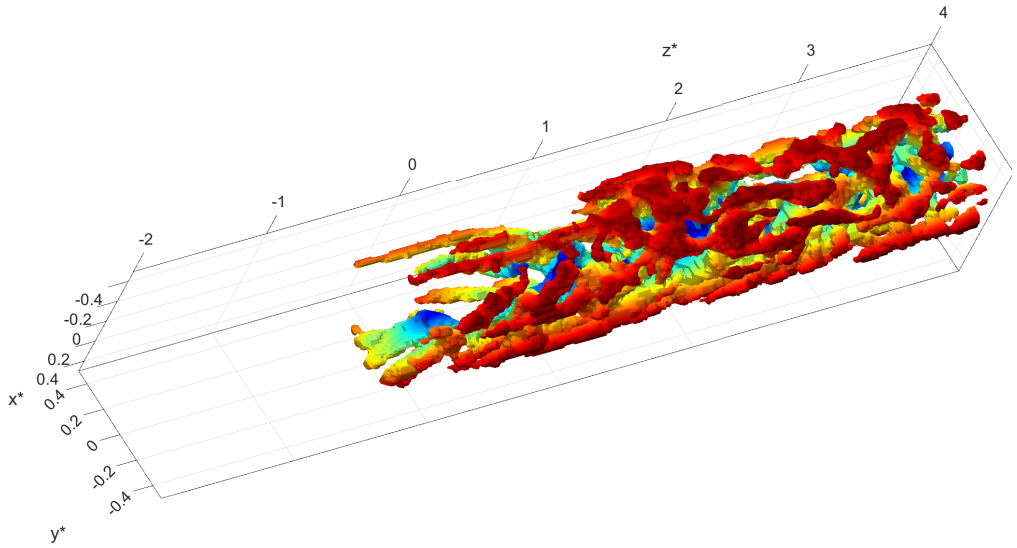

Figure C.83: Isosurfaces of swirl corresponding to $\lambda_{3D}^{*,i} > 1.2989$ inside Puff S-42. Colors move from red to blue with increasing wall distance.

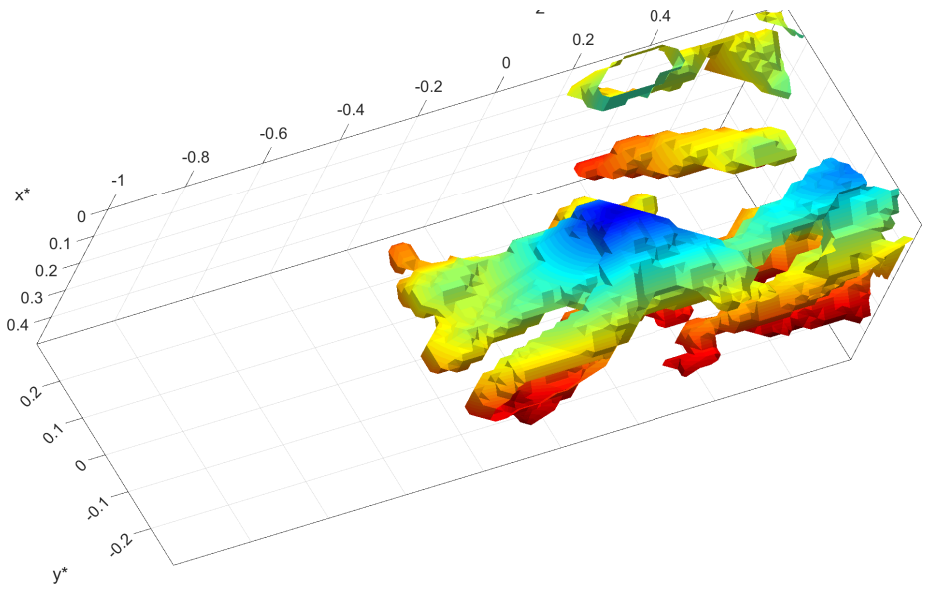

Figure C.84: Isosurfaces of swirl corresponding to $\lambda_{3D}^{*,i} > 1.2989$ within $-0.07 < z^* < 0.07$ inside Puff S-42. Colors move from red to blue with increasing wall distance.

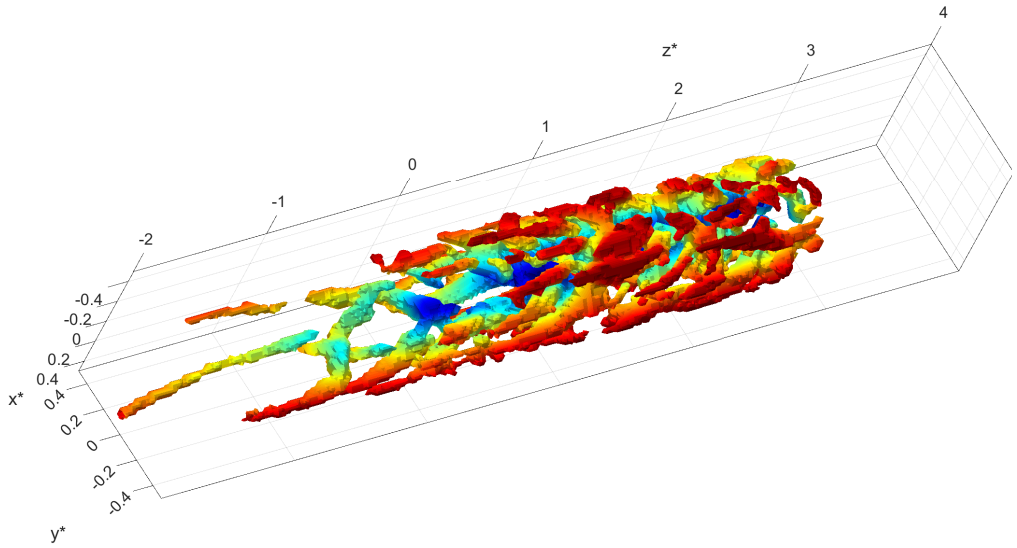

Figure C.85: Isosurfaces of swirl corresponding to $\lambda_{3D}^{*,i} > 1.5227$ inside Puff S-43. Colors move from red to blue with increasing wall distance.

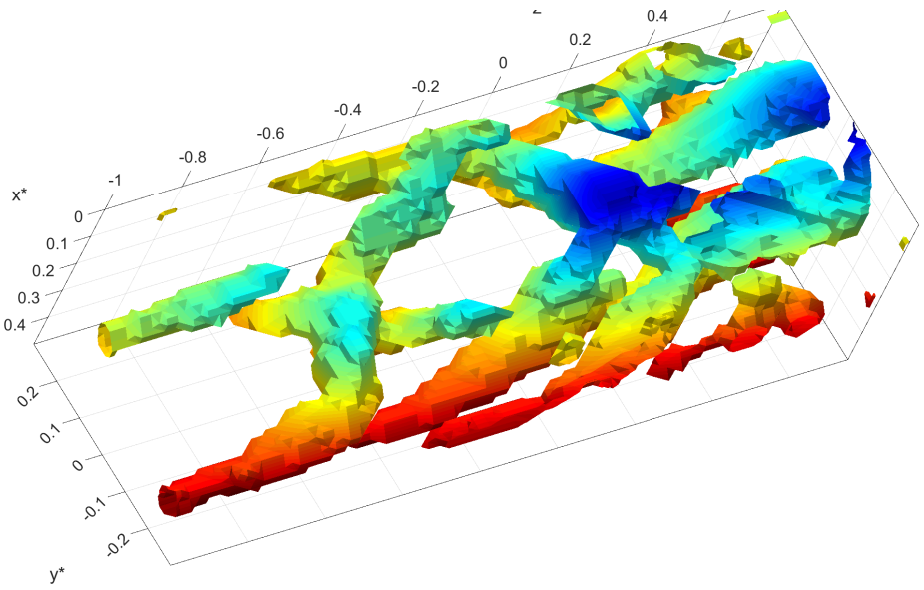

Figure C.86: Isosurfaces of swirl corresponding to $\lambda_{3D}^{*,i} > 1.5227$ within $-0.07 < z^* < 0.07$ inside Puff S-43. Colors move from red to blue with increasing wall distance.

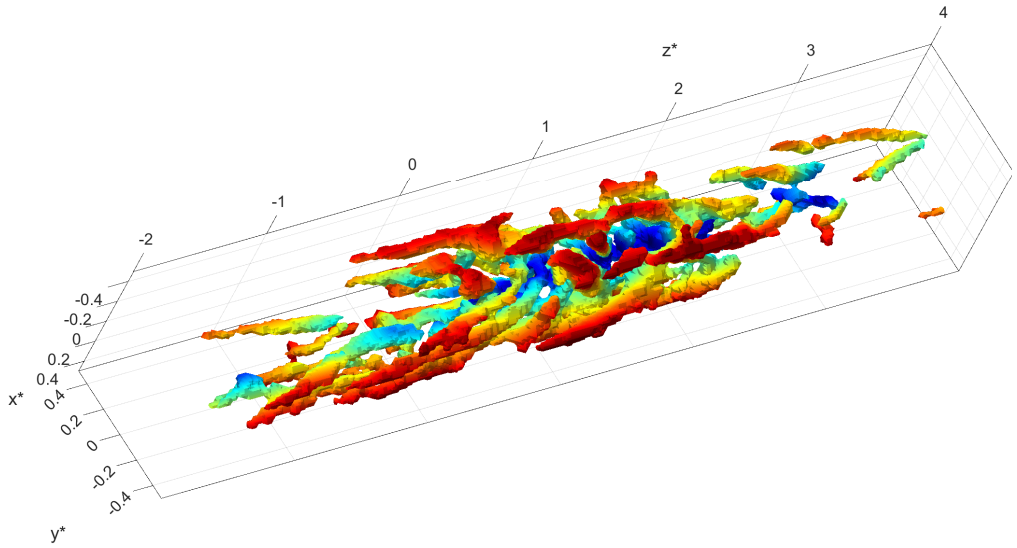

Figure C.87: Isosurfaces of swirl corresponding to $\lambda_{3D}^{*,i} > 1.5787$ inside Puff S-44. Colors move from red to blue with increasing wall distance.

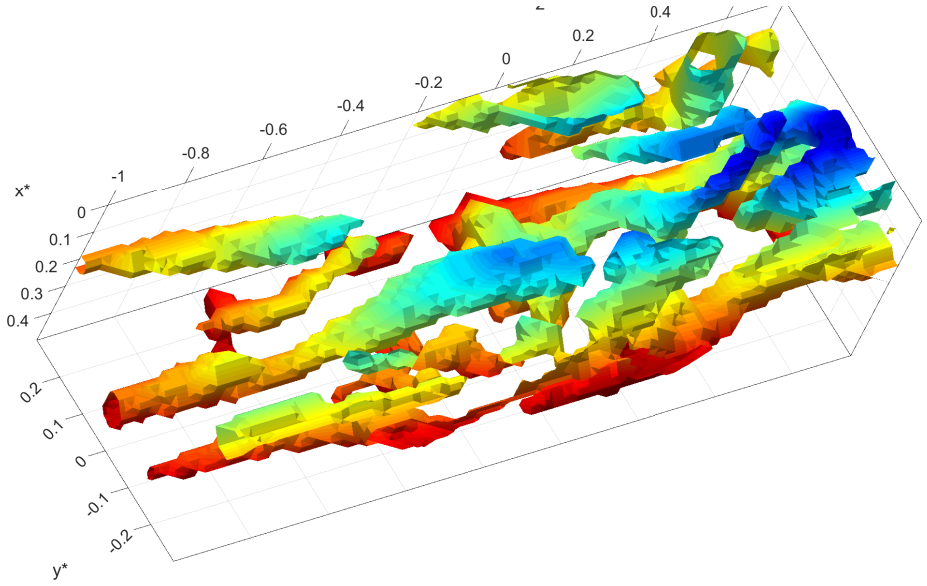

Figure C.88: Isosurfaces of swirl corresponding to $\lambda_{3D}^{*,i} > 1.5787$ within $-0.07 < z^* < 0.07$ inside Puff S-44. Colors move from red to blue with increasing wall distance.

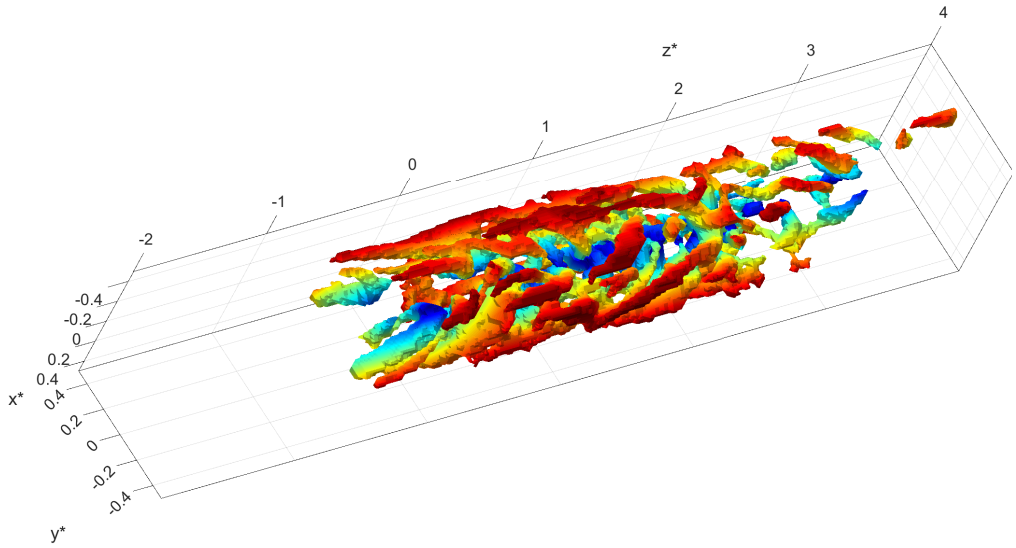

Figure C.89: Isosurfaces of swirl corresponding to $\lambda_{3D}^{*,i} > 1.5255$ inside Puff S-45. Colors move from red to blue with increasing wall distance.

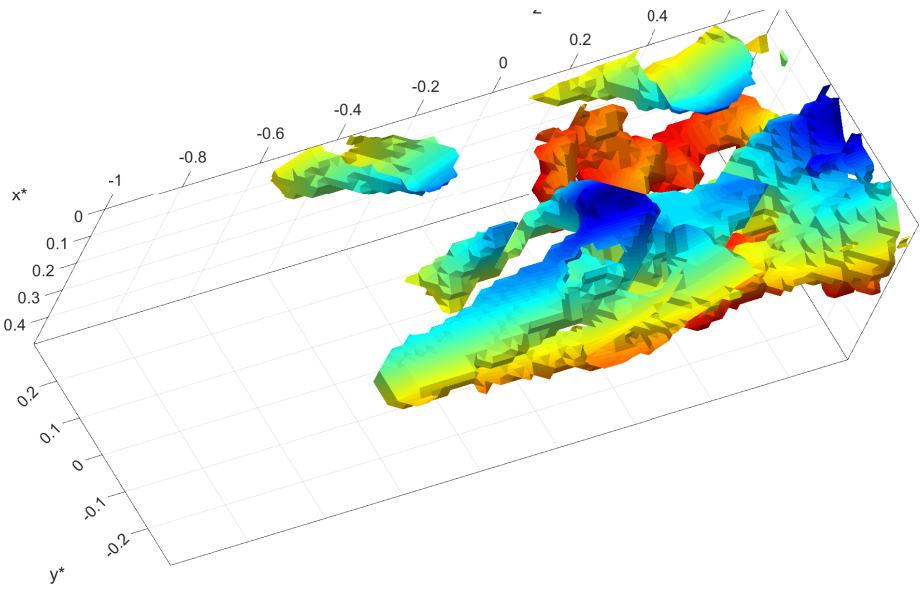

Figure C.90: Isosurfaces of swirl corresponding to $\lambda_{3D}^{*,i} > 1.5255$ within $-0.07 < z^* < 0.07$ inside Puff S-45. Colors move from red to blue with increasing wall distance.

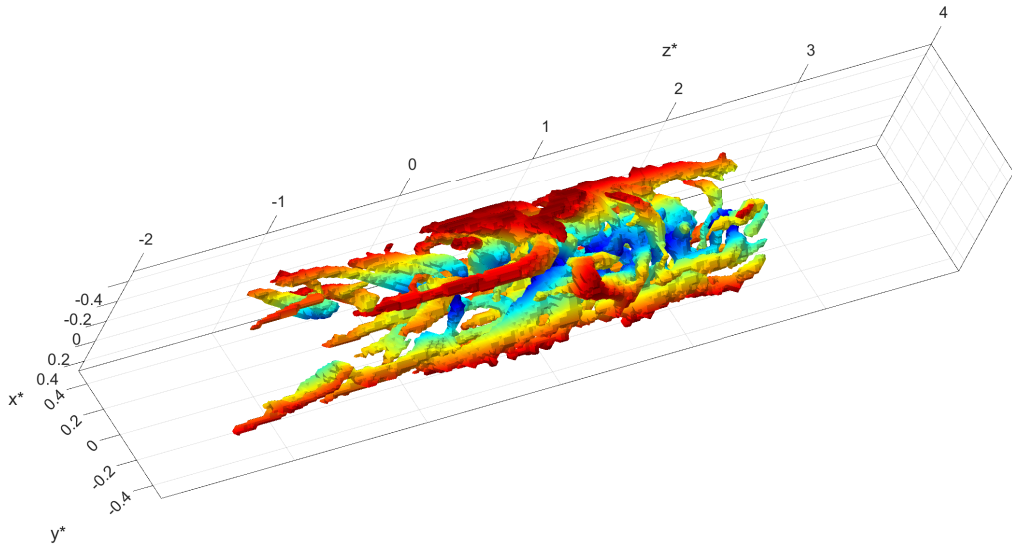

Figure C.91: Isosurfaces of swirl corresponding to $\lambda_{3D}^{*,i} > 1.5624$ inside Puff S-46. Colors move from red to blue with increasing wall distance.

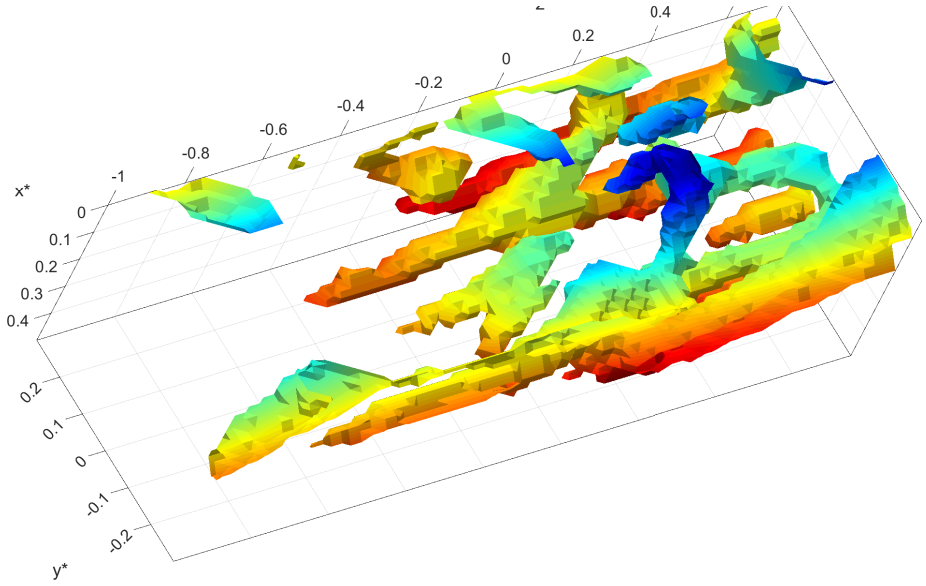

Figure C.92: Isosurfaces of swirl corresponding to $\lambda_{3D}^{*,i} > 1.5624$ within $-0.07 < z^* < 0.07$ inside Puff S-46. Colors move from red to blue with increasing wall distance.

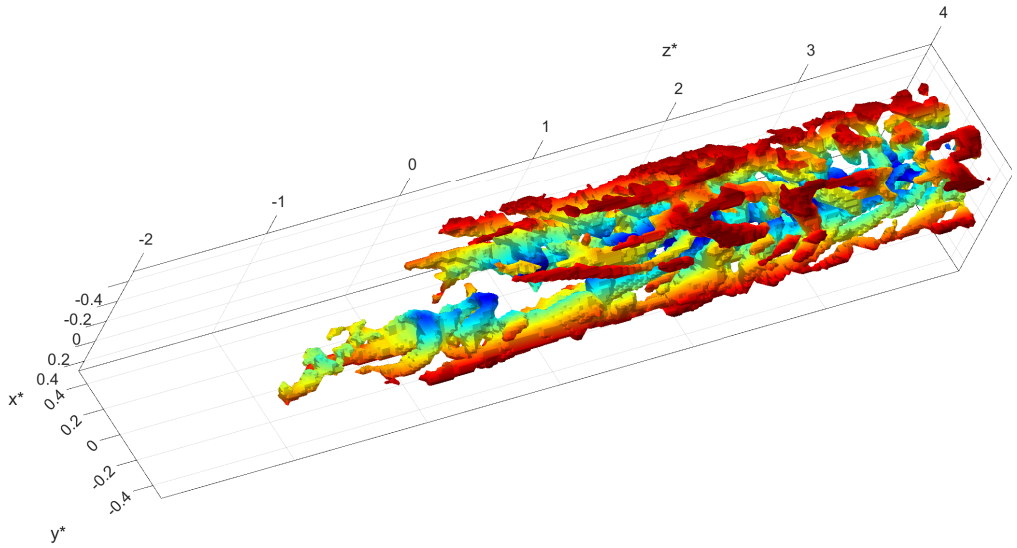

Figure C.93: Isosurfaces of swirl corresponding to $\lambda_{3D}^{*,i} > 1.3691$ inside Puff S-47. Colors move from red to blue with increasing wall distance.

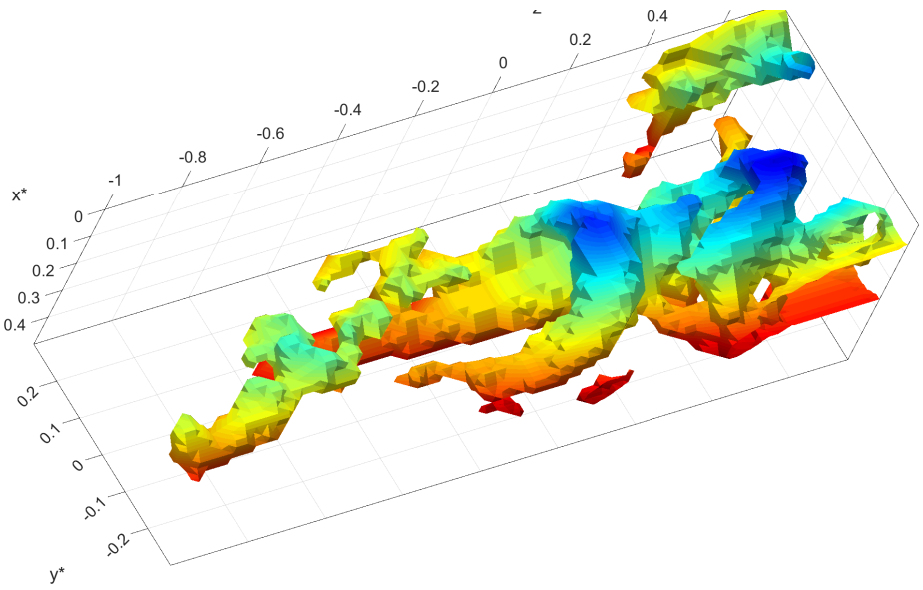

Figure C.94: Isosurfaces of swirl corresponding to $\lambda_{3D}^{*,i} > 1.3691$ within $-0.07 < z^* < 0.07$ inside Puff S-47. Colors move from red to blue with increasing wall distance.